Micro- and Macromechanics of Single Crystal and Polygranular Lamellar Block Copolymers

by

Theodora Tzianetopoulou

Submitted to the Department of Mechanical Engineering
in partial fulfillment of the requirements for the degree of

Doctor of Philosophy

at the

MASSACHUSETTS INSTITUTE OF TECHNOLOGY

June 2007

Author .....
Department of Mechanical Engineering
May 18, 2007

Certified by .....
Mary C. Boyce
Gail E. Kendall (1978) Professor of Mechanical Engineering
Thesis Supervisor

Accepted by .....
Lallit Anand
Chairman, Department Committee on Graduate Students

Micro- and Macromechanics of Single Crystal and Polygranular Lamellar Block Copolymers

by

Theodora Tzianetopoulou

Submitted to the Department of Mechanical Engineering
on May 18, 2007, in partial fulfillment of the
requirements for the degree of
Doctor of Philosophy

Abstract

Block copolymers (BCPs) are a relatively new class of thermoplastic elastomers. Their macromolecular chain consists of covalently bonded repeating blocks of thermoplastic and elastomeric molecular chains. When given the thermodynamic freedom, the chain constituents phase separate into domains of various morphologies with sizes that can range between ten to hundreds of nanometers. BCPs are in essence nanocomposites with chemically bonded interfaces. As such, their mechanical behavior is consistent both with that of elastomers, and of thermoplastics. Due to this unique behavior, BCPs are among the most popular polymeric materials with diverse commercial applications that cover a number of industries. Furthermore, BCPs are emerging as instrumental for the future of nanotechnology as an increasing number of new techniques and applications seek to utilize their nanostructural features. BCPs, whether as polycrystalline configurations or as "highly" oriented single-crystals, attract an accumulating number of applications, and the increasing demand for efficient material design and product development extends over a range of length scales. Hence, there exists a need for continuum models that will predict both the oriented as well as the polycrystalline response of block-polymer materials to generic loading conditions.

This thesis presents a general micromechanical framework for the derivation of large-strain continuum constitutive models for hyperelastic materials with layered micro- or macro-structures. The framework was implemented for the case of oriented (single-crystal) lamellar BCPs with Neo-Hookean phase behavior, and an analytical continuum model was derived for their large-strain hyperelastic response. The model was used to study the behavior of styrene-butadiene-styrene (SBS) triblock polymers, the behavior and micromechanics of which have been extensively investigated experimentally. Micromechanical unit-cell calculations were used as direct parallels to experimental (x-ray, microscopy, and stress-strain) data in order to verify the model's predictions. The presented continuum model describes the stress and deformation response of an oriented microstructure accurately, and was further implemented in multigranular numerical studies for the mechanical behavior of polycrystalline lamellar configurations. Simulations of the polycrystal structures reveal the manner in which the individual grains collectively deform and interact with each other

to accommodate the macroscopic deformation. These results reveal the key roles of inter-lamellar shearing, lamellar dilation, rotation, and buckling.

Thesis Supervisor: Mary C. Boyce
Title: Gail E. Kendall (1978) Professor of Mechanical Engineering

Contents

List of Figures

Chapter 1

Introduction: Deformation Micro- and Macromechanics of Lamellar Block Copolymers

1.1 Thermoplastic Elastomers: Historical Background and General Trends.

Thermoplastic elastomers (TPEs) emerged as a new class of polymers in the late 1960's. Since then they have taken over a large share of the plastics market which traditionally was monopolized by vulcanized rubber. The attractive properties of TPEs, combined with their ease of processing and recyclability forced a dramatic growth in TPE technology over the last 15 years. Aiming to optimize TPE products, new processing and production techniques have been invented, which boosted both the progress in the plastics industry and improved the quality of polymeric materials developed henceforth [22, 1].

With the invention of TPEs, a structural way to combine the properties of elastomers and thermoplastics was materialized. Their inherent characteristics such as resilience, thermal stability, solvent-, chemical-, creep-, and abrasive resistance, paired with their thermoplastic-like processing behavior of high processing rates, recyclability and low cost, have granted TPEs a vast number of uses [22, 1]. Major TPE markets today are the au-

tomotive, footwear, wire and cable industries. They are extremely profitable as adhesives, sealants and coatings. Finally, an area where these materials have had an enormous impact and a fast growing influence is the medical industry [23].

Styrenic block copolymers are the most widely used TPEs because they meet the hardness, stiffness, and tear resistance standards for commercial use. Block copolymers (BCPs), as the name suggests, are macromolecules containing repeating blocks of two or more different polymers, covalently bonded with each other at their block ends. What makes BCPs so successful is their ability to blend polymers with very different properties, to achieve a material possessing a tailored combination of properties. In styrenic BCPs for example, the stiffness of PS and the resilience of PB are both present, creating materials extendable far beyond the failure strain of brittle PS, and manyfold stiffer than PB. Similar results are not only achieved for mechanical properties, but also for the optical and thermal properties of BCPs [1]. These constructive combinations arise from the covalent chemical bonding between the different polymer blocks and the well-ordered microstructures they phase-separate into at the nanoscale. Phase separation in BCPs is a well studied and understood phenomenon [2, 1]. It takes place spontaneously when immiscible copolymer constituents (blocks) develop separate domains in an effort to allow enough volume for the blocks to conform to their bulk chain configuration. At the same time, minimization of the domain interface area reduces the energy penalty imposed by the repulsive forces between incompatible blocks at their domain interface. This interplay determines the volume fraction dependency of the domain shape, size and distribution in the BCP microstructure. The morphology is shown in Fig. 1-1 for a linear dual phase BCP as a function of the volume fraction. Domain sizes can range from 1-100nm depending on the molecular weights (or lengths) of the polymer blocks [1].

Owing to their wide range of nanostructural features, BCPs have attracted a lot of attention in the last decade for their potential utilization in a multitude of nanotechnological applications [24, 25, 26]. Microdomain patterns designed with long- or short-range order and engineered with specific domain orientation can be accomplished with emerging techniques via nanopatterned substrate topographies [27], or by application of an external electromagnetic field [28, 29, 30]. These hierarchically engineered materials find uses as

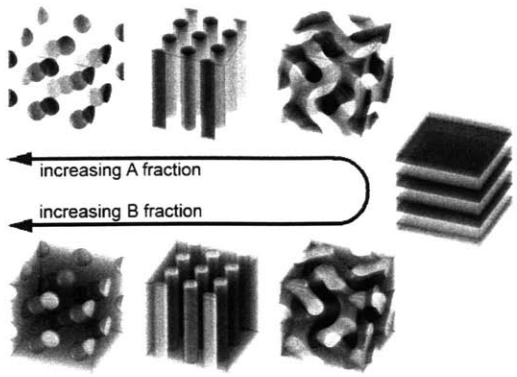

Figure 1-1: Known phase-separated morphologies for a dual phase BC as a function of the constituents' volume fraction: BCC lattice of spheres (0-20%), HCP lattice of cylinders (20-35%), bicontinuous interconnected tetrahedral arrangements of short rods in the form of a double diamond or the ordered bicontinuous double-diamond (35-40%), lamellae of about equal thickness (40-60%) [1, 2].

lithographic masks or nanoporous membranes. Furthermore, preferential positioning of nanoparticles within the nanodomain structure enables BC/inorganic nano-particle composites to be manufactured for novel photonic devices, such as mirrors and high efficiency optical wires, as well as for a new generation of storage devices with superior memory capacity [31].

Three decades after their first appearance, styrenic BCPs are already a material sector of colossal industrial, financial, and social influence. It is thus necessary to understand how their microstructure determines their mechanical behavior, and develop tools that will allow designers to predict the material response at various loading conditions. Although most of the current commercial BCP applications utilize these materials in their polycrystalline form, the nanotechnological and thin film applications outlined previously demand highly oriented microstructures. Therefore, the need for predictive models that will guide in efficient material design, selection and product development, from nano- up to macroscopic scales arises both for polycrystalline as well as oriented BCPs.

1.2 Problem Statement and Research Objectives.

The present research aims in the development of a continuum constitutive description for the large strain response of lamellar glassy-rubbery-glassy triblock copolymers, con-

structed on a knowledge of the micromechanics that govern the deformation of the underlying material nanostructure. The objectives are three-fold:

- explore the correlation between the underlying anisotropic nanostructure of the single-crystal material and its nonlinear anisotropic mechanical response,
- develop a continuum constitutive description that captures the large strain anisotropic behavior of oriented microstructures, namely that of a *"single-crystal"*,
- develop a micromechanical model for the large strain deformation behavior of random multigrain (polycrystalline) aggregates to explore and predict the underlying micromechanics of deformation and the resolving macroscopic mechanical behavior.

The following sections present a short overview, representative of experimental and modeling studies investigating the relation between the microstructure and the macroscopic mechanical behavior of lamellar SBS block copolymers.

1.3 Lamellar SBS Block Copolymers: Macroscopic Response and Deformation Micromechanics.

1.3.1 Single-Crystal (Oriented) Behavior

Early studies on BCPs, and lamellar BCPs in particular, were performed on multigrain, randomly oriented samples. Small angle X-ray scattering (SAXS) and transmission electron microscopy (TEM) were used to correlate microstructural rearrangements with characteristics of the macroscopic tensile $\sigma - \epsilon$ response. Subsequently, techniques which allowed the production of highly oriented materials aided in a systematic investigation of the single-crystal behavior.

One of the first studies performed on oriented lamellar BCPs was that of Allan *et al.* [3]. It was known from earlier studies that partially oriented microstructures of extruded BCP samples respond in an anisotropic manner when loaded at directions parallel and perpendicular to the extrusion direction [32, 33]. The anisotropy stems from the directionality of

the microstructure, analogous to oriented macroscopic composites, which exhibit a stiffer response in the direction of reinforcement.

Allan *et al.* were among the first to consider BCPs as composite materials and to invoke composite material mechanics to quantify this anisotropy of the axial modulus in oriented BCP systems. Highly oriented lamellar SBS samples were fabricated with a modified injection molding technique, which involved oscillatory shear of the melt inside the molds. The sample orientation was examined visually with inspection of surface-microcracks, and with TEM (Fig. 1-2a). The two constituent phases were assumed to be amorphous isotropic, and their elastic properties were derived using micromechanics and measurements of the (effective) axial modulus, E_θ, at five different orientations to the material microstructure. Data fitting showed a very good agreement between the experimentally measured Young's modulus and its theoretical prediction for the following constituent properties: $E_{PS} = 2$GPa, $E_{PB} = 5.91$MPa, $\nu_{PS} = 0.33$, for 46vol% in PS and assuming $\nu_{PB} = 0.44$ [1] (Fig. 1-2b).

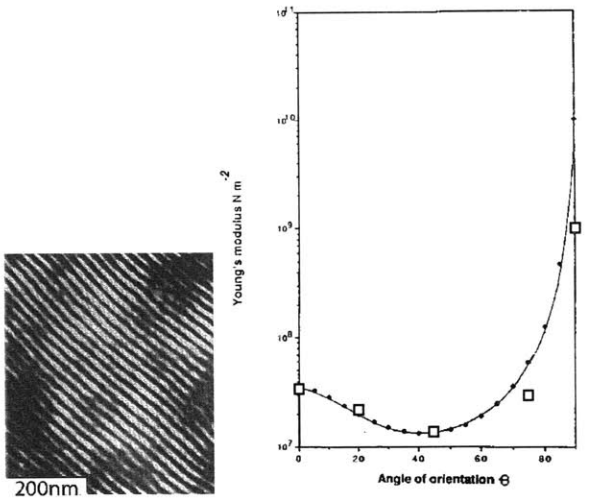

(a) (b)

Figure 1-2: (a) Oriented SBS lamellar morphology. (b) Dependency of Young's modulus on the loading direction θ. Square points correspond to actual measurements and dots on a continuous curve correspond to predicted values [3].

Allan's study concerned only the small strain uniaxial behavior of oriented BCPs, namely the anisotropy in their effective elastic modulus. The yield and large strain behavior of lamellar BCPs and their links to micromechanical deformation processes were the topics

[1] E_{PS} was taken from tensile measurements of a PS with MW comparable to the PS-block length; ν_{PS} was taken from the literature; E_{PB} and ν_{PB} were then adjusted to best fit the experimental data.

of later experimental and analytical investigations by Yamaoka [4], Cohen [5, 6, 13], and Read [14].

Yamaoka and Kimura [4] studied the effect of morphology on the mechanical-impact, tensile, and flexural–properties of star-shaped SBS lamellar triblock copolymers containing $\simeq$ 75.5wt% PS. Injection- and compression-molding were used to provide different sample microstructural orientations. Rapidly- and slowly-cooled compression-molded samples were prepared by varying the melt-cooling-rate in the molds to study the effect of the latter on the final orientation. TEM on undeformed morphologies showed that the different manufacturing routes resulted in nearly equal lamellar thickness (ranging between 15–20 and 20–25nm for PB and PS lamellae, respectively), the lattice disorder was higher for injection-molded samples, due to the different cooling and shear-flow processing conditions. The microstructure in injection-molded samples resembled a "*spinodal*" structure with curved, randomly oriented, and discontinuous PB lamellae, dispersed in a network of continuous PS-matrix lamellar domains (Fig. 1-4a). Rapidly-cooled compression-molded specimens possessed microstructure of continuous, nevertheless wavy lamellae in the plane normal to the melt flow direction, with a high degree of alignment along the melt flow direction (Fig. 1-4b).

The tensile stress-strain behaviors of injection- and compression-molded samples, shown in Fig. 1-3, exhibit striking differences. The injection-molded specimen possesses a decidedly lower strain to failure, the response is stiffer, has a distinct yield point followed by a brief constant stress-plateau, and finally, after necking has propagated through the entire specimen, failure ensues with a rapid upturn in stress at a macroscopic strain of 50% (curve (ab in Fig. 1-3). TEM on fracture surfaces showed that the microstucture deforms by orientation and stretching of the initially randomly distributed PS lamellae, in the direction of loading (Fig. 1-4). Subsequent failure of the PS microdomains, as the authors speculate, takes place after yielding and accelerates during the final rapid-stress-increase stage of deformation. On the other hand, compression molded samples were more compliant, did not develop a macroscopic neck, and their response did not show a clear yield point, but a rather gradual transition to plastic deformation with a smoothly decreasing tangent modulus (curve (a) in Fig. 1-3). Micrographs of the deformed microstructure (Fig. 1-4), revealed

continuous PS lamellae deformed into chevrons, an indication that kinking, interlamellar shear, and incidental cavitation are the prominent plastic deformation mechanisms. The relatively ordered, continuous lamellar microstructure allowed large straining through PB shearing, granting the sample its ductile behavior and larger elongation at break.

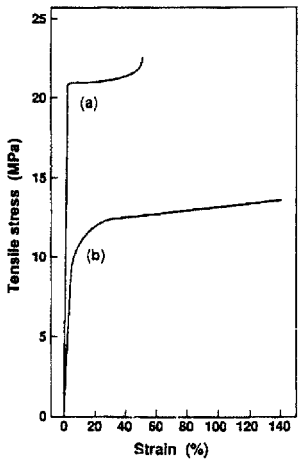

Figure 1-3: Stress-strain behavior of star-shaped lamellar SBS triblock copolymers. Injection- (a) vs. compression molded (b) material [4]. The differences between (a) and (b) are morphology related (see Fig. 1-4).

The same deformation processes of kinking and shear yielding explain the higher impact strength of rapidly-cooled compression-molded samples in comparison to injection-molded samples. In the latter, the disordered microstructure of networked PS-lamellae inhibits the free stretching of PB domains to their full extensibility, causing PS microdomains to fail earlier. Considerable anisotropy was also observed for rapidly-cooled samples depending on the direction they were machined out of compression molded plates. The mechanical anisotropy was assessed by directing pendulum strikes or the loading during tensile and flexural[2] testing at different angles to the lamellar orientation (Fig. 1-5). The highest moduli were measured for tensile specimens with lamellae oriented perpendicular to the tensile direction and for flexural samples with lamellae parallel to the loading nose[3].

The slow-cooling conditions during compression molding provided uniform cooling

[2]Three-point bending.

[3]The results appear to be inconsistent, self-contradicting and in disagreement with the well established directional dependency of composite materials' stiffness (see for example Fig. 1-2). It is possible that the sample microstructure was mapped incorrectly.

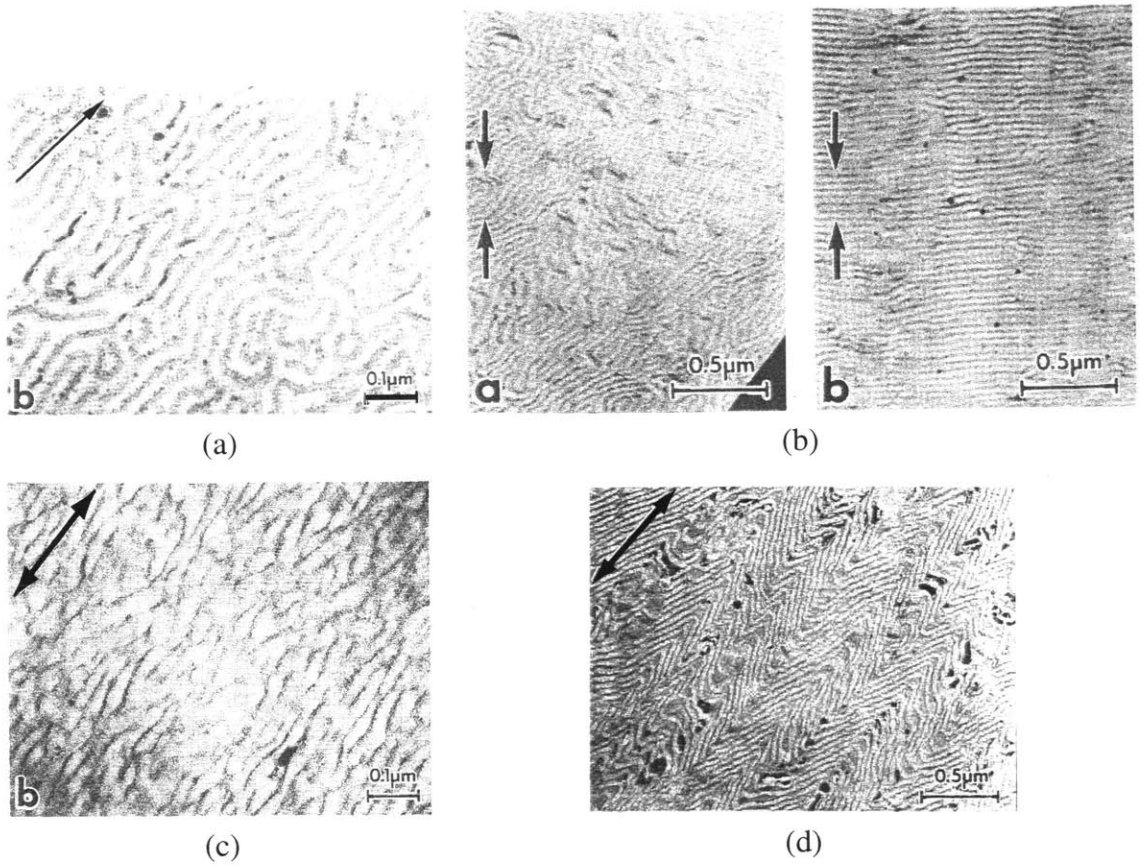

Figure 1-4: TEM micrographs of injection- and compression-molded microstructures [4]: (a) and (b) as processed (undeformed), and (c) and (d) deformed under tension. (a) Undeformed injection molded morphology as viewed for any cross-section aligned with the injection direction. (b) Undeformed compression molded morphology viewed for two orthogonal cross-sections. (d) Lamellar kinking and shearing are evident in the deformed compression-molded morphology. Different micrograph scales are chosen for display clarity. Arrows indicate: in (a) the injection flow direction, in (b) the compression direction, in (c) and (d) the deformation axis.

through the samples and sustained the melt state of the BCP longer, thus allowing sufficient time for relaxation of the lamellar disorder. The produced samples possesed highly oriented, nearly parallel lamellar microstructures in the plane of the compression molded plate. Due to this in–plane symmetry, the impact strength did not vary appreciably and no mechanical anisotropy was observed. Analogous to rapidly-cooled samples, the deformed morphology showed lamellar kinking and shearing.

Despite the clear link between anisotropic behavior and microstructural orientation that Yamaoka's study managed to establish, the samples used were quite disordered and not

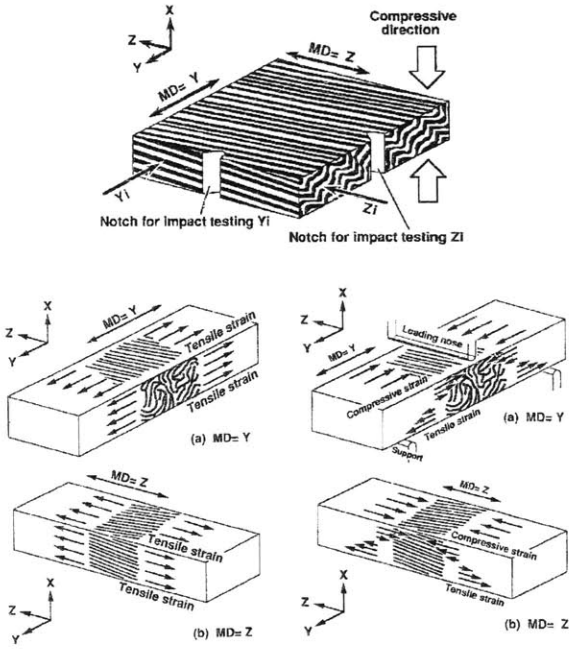

Moulding method	Injection moulding	Compression moulding	
Machine direction		*Y*	*Z*
Izod impact strength ($J\ m^{-1}$)	19.6	77.5 (*Zi*)[a]	229 (*Yi*)[b]
Tensile strength (MPa)	22.6	14.6	13.6
Tensile modulus (MPa)	1230	728	534
Elongation at break (%)	50	110	140
Flexural strength (MPa)	33.3	12.6	12.1
Flexural modulus (MPa)	1470	661	535
Deflection temperature under flexural load (°C) (Fibre stress 1820 kPa)	71	57	56

[a] Striking direction *Zi*
[b] Striking direction *Yi*

Figure 1-5: Schematic of the sample geometries used in [4] for impact, tensile and bending tests. Also shown is the relative orientation of the rapidly-cooled compression-molded morphology. The table summarizes the mechanical properties of injection- and compression molded samples.

well oriented. A more detailed and comprehensive treatment on the deformation response of lamellar SBS BCPs was recently offered by Cohen *et al.* [5] with a series of experiments on highly-oriented film specimens. The samples used were produced with the roll-casting technique, a powerful method to control the microstructural orientation and packing order of block copolymer films [34]. As shown in Fig. 1-6, this method offers the flexibility to obtain specimens with initial microstructures oriented differently relative to the deformation axis. The microstructure of an annealed roll-cast SBS specimen with a lamellar microstructure is shown in the micrograph of Fig. 1-7, aside with its 2D SAXS pattern. The lamellar period appears to be approximately 27nm.

The material used in Cohen's experiments was a commercial BC[4] containing 45wt% PS (~43vol% PS). Uniaxial tension was applied in three loading orientations relative to the lamellar microstructure: perpendicular, parallel and at 45° to the lamellae. *In-situ* SAXS during stretching and TEM were used to monitor the micromechanics of deformation. The anisotropic $\sigma - \epsilon$ response to uniaxial tension is shown in Fig. 1-8. The initial elastic response was highly anisotropic with axial moduli values that measured 180MPa, 65MPa, and 43MPa for parallel, perpendicular, and diagonal loading, respectively. After a short elastic regime, all samples exhibited yielding behavior, which for parallel loading was followed by distinct softening of the stress response and macroscopic necking, consistent with the behavior of PS, which dominates the response at this orientation. At strains higher than 300%, all samples exhibit similar rubber-like response.

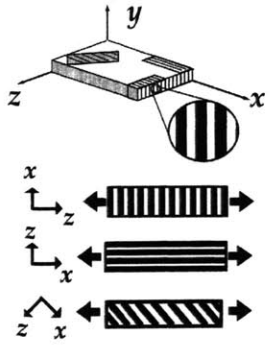

Figure 1-6: Schematic of an oriented roll-cast lamellar film and samples cut at different orientations to the roll-casting direction, which here coincides with the *x-axis*. (Roller radial direction: *y-axis*) [5].

[4]Vector 4461-D: MW_{PS}=18500, MW_{PB}=45000

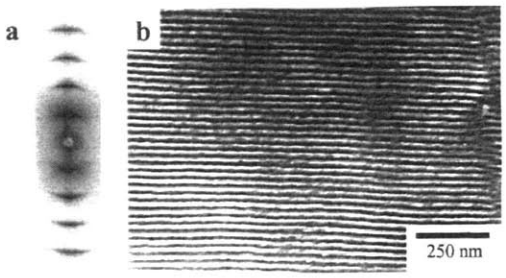

Figure 1-7: Oriented unstretched morphology from a roll-cast lamellar BC.

Samples that underwent tensile loading perpendicular to their lamellar microstructure did not develop a macroscopic neck. The evolution of SAXS scattering patterns with strain is shown schematically in Fig. 1-9. Patterns from small strains show arched azimuthal- and weak meridional reflections, which indicate layer waviness and dilation. With increasing strain, higher order reflections disappear gradually, and each arched reflection polarizes to two maxima to finally evolve into a 4-point pattern of elongated horizontal streaks. This pattern is typical to microstructures of tilted diffracting layers within elongated and narrow grains, which are separated by tilt grain boundaries that run parallel to the loading direction [35, 36]. Consistent with SAXS results, the TE micrograph of Fig. 1-9, taken from a sample strained to 300%, shows a zigzag or herringbone structure, known as *chevron*, which is observed in a variety of layered microstructures and across several length scales–from compressed geological structures [37, 38] down to liquid crystals [9, 39], nematic elastomers [40], diblock copolymers [15], and diblock copolymer melts [11, 10, 41], as well as in BCPs with cylindrical microdomains [42, 43].

The nonlinear elastic $\sigma - \epsilon$ material response to stretching and the gradual transition to plasticity differs from the linear elastic behavior and a distinct yield-point that analytical and numerical models predict [14, 9, 44]. The increasing arching of SAXS reflections and the absence of significant lamellar dilation for strains below 20%, suggest a population of increasingly undulating lamellae. Initial arching from 10° increases to 16° for 7% and to 28° for 15% strain. An "apparent" yield-point lies within this strain range. In essence, the continuous increase of undulation allows inter-lamellar shearing to dominate the micromechanical deformation response, which macroscopically is reflected in the continuously decreasing slope of the $\sigma - \epsilon$ curve. This gradually increasing, inherent and possibly

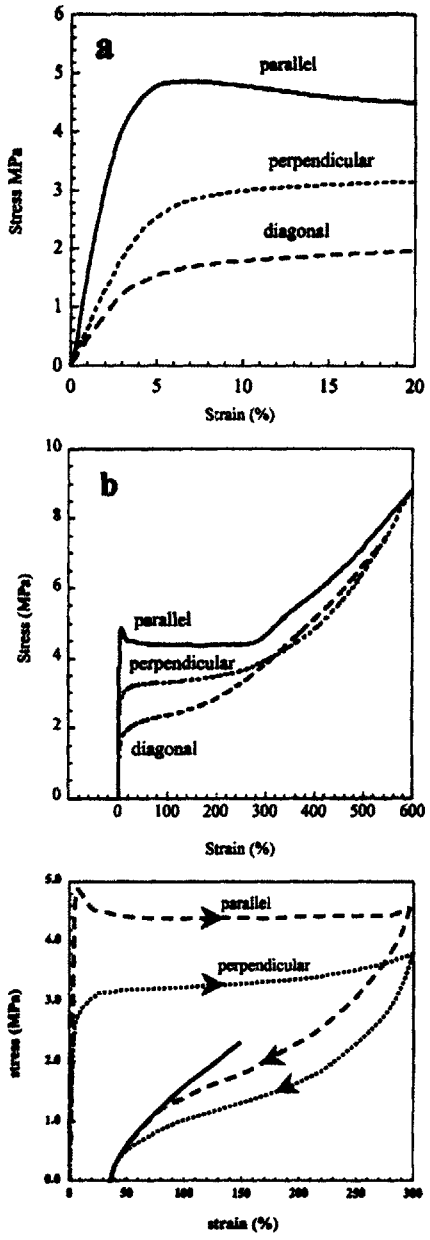

Figure 1-8: Stress-strain response of oriented lamellar SBS samples (43%volPS) for three different lamellar orientations with respect to the deformation direction: (a) small, (b) large strains, and (c) unloading behavior [5].

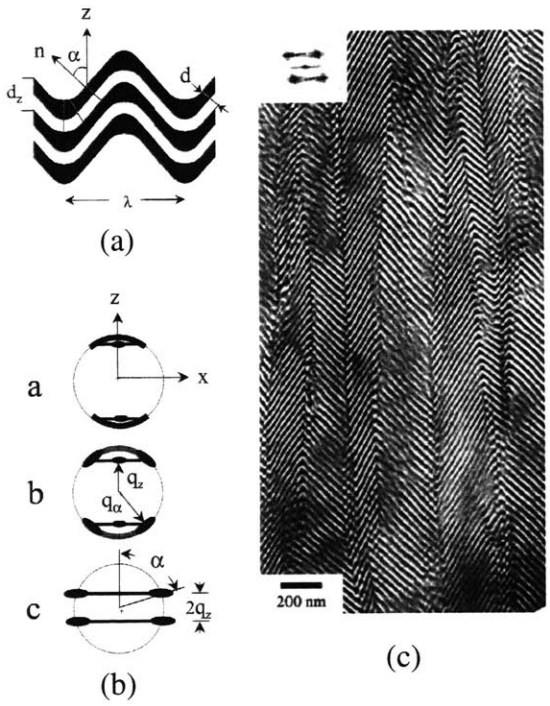

Figure 1-9: (a) Schematic of the "*chevron*" morphology from [5], where α is the tilt lamellar angle, n is lamellar normal, z is the deformation axis, d and dz are the lamellar repeat lengths in the tilted limbs and in the hinge regions, respectively, and λ is the undulation wavelength. (b) Schematic of SAXS pattern evolution during perpendicular stretching. (c) TEM micrograph of a lamellar BCP tensioned perpendicular to the lamellae. PS layers appear as white. The deformed zigzag microstructure is known as a *chevron*.

processing-induced, lamellar waviness smears out the abrupt yield behavior which buckling analysis attributes to lamellar micro-buckling, and which can be predicted to occur at strains as low as 2% when the rubber phase is modeled as strictly incompressible, and the lamellae are assumed to be perfectly aligned [14, 9].

With increasing strain, the undulations evolve into a chevron pattern of straight limbs and sharp hinges. The progressive reduction in fold-roundness has been explained in Bayly's analytical work on the compression of sedimentary rocks [37], and was simulated with micromechanical FE models by Read *et al.* [14]. Plastic deformation of PS layers and PB dilation localize at hinge areas, where eventually, either PS layer fragmentation or PB voiding occurs. This process converts hinge "trajectories" to new tilt grain boundaries, usually parallel to the loading direction. The constant, throughout the deformation, radius of the diffraction vector in both arched and 4-point reflections signifies constant lamellar spacing, which is consistent with the process of interlamellar shearing between continuously rotating lamellae, in agreement with what has been reported elsewhere [19, 17, 18, 15, 35, 36]. The stress increase in the final stages of deformation (strains >200%), and the asymptotically constant 68° azimuthal angle in SAXS patterns reflect the increasing difficulty to accommodate additional deformation by interlamellar shear alone. As this *"locking"* tilt angle is approached (Fig. 1-10c), additional stretch corresponds to dilation in both PS and PB layers, hence the increasing slope of the final upturn in the $\sigma - \epsilon$ response.

In an effort to understand the initiation of kinking, two different –according to the authors [6]– mechanisms were considered: layer misalignment around defects, and layer buckling. We note that these processes are coupled. Their view, also shared by Qiao *et al.* [10], is that layers around edge imperfections are the first to kink, and subsequently propagate the kink band to neighboring lamellae (Fig. 1-15). Different kink bands finally impinge with further deformation. This can be a reasonable explanation for the wavelength variation and kink boundary impingement observed in deformed microstructures such as the one in Fig. 1-9b. A TEM micrograph from a deformed sample taken on a cross-section perpendicular to the load (Fig. 1-11) shows that the observed irregularity in layer folds is three-dimensional in nature [45, 46, 7, 8]. This is in contrast to the regular *egg-box* or

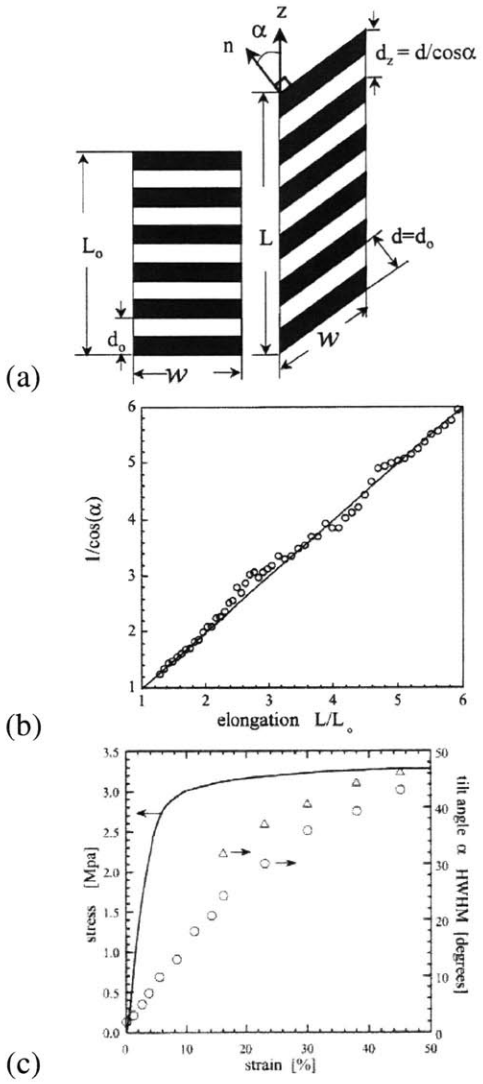

Figure 1-10: (a) RVE of a tilted lamellar morphology from [5]: α is the tilt lamellar angle, n is lamellar normal, z is the deformation axis, d and d_z are the lamellar repeat lengths in the tilted limbs measured along the lamellar normal n and along the stretching direction z, respectively, d_0 is the lamellar repeat lengths in the undeformed configuration, and $\lambda = L/L_0$ is the macroscopic stretch. (b) Tilt angle α SAXS data plotted as $1/cos(\alpha)$ versus the macroscopic elongation $\lambda = L/L_0$. The linear representation of the data with a solid line of slope equal to unity verifies the invariance of the lamellar repeat length d for stretches 1 [5]. (c) Lamellar tilt angle α evolution ($\triangle$) measured as the angle between the meridian and a peak of the SAXS four-point pattern shown against the macrocroscopic stress-strain response (solid line) [6]. The angle increases with a continuously decreasing rate as it approaches an upper limit, the "*locking tilt angle*".

checkerboard buckling pattern (Fig. 1-12) that is analytically predicted to minimize the total energy in layered liquid crystalline materials [9, 7, 8].

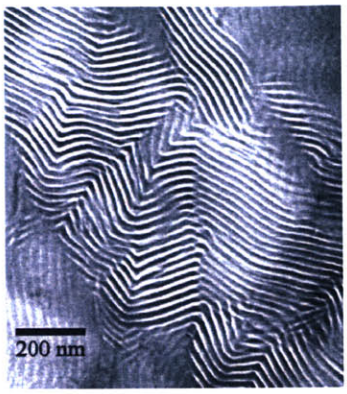

Figure 1-11: TE micrograph of a microstructure deformed under perpendicular loading. The cross-section is perpendicular to the loading direction [5].

Loading at $45°$ to the lamellae is an intermediate loading state between the extremes of perpendicular and parallel loading. The measured axial stiffness is lower in this direction, as also in Allan's experiments (Fig. 1-2b), due to the shear behavior of PB, which dominates the composite's response in this direction, as compared to the bulk modulus, which dominates the response to perpendicular loading. The tensile $\sigma - \epsilon$ behavior exhibits identical trends with those observed during perpendicular loading. As SAXS and TEM revealed, the similarities in the macroscopic behavior stems from the micromechanics of deformation, which at the microstructural length-scale are the same for both loading cases. Fig. 1-13b summarizes schematically the evolution of SAXS patterns during diagonal loading [5]. With increasing strain, the reflection streaks rotate away from the stretching direction along a circular trajectory without considerable changes in the d-spacing, even at strains as high as 500%. Similar to perpendicular deformation, a new, asymmetric 4-point SAXS pattern appears, consistent with asymmetric kinking. The kinking is due to the resultant dilative component of stress in the direction perpendicular to the layers (Fig. 1-14b), and imperfections in the lamellar microstructure (Fig. 1-15). TEM micrographs on microstructures deformed to 60% strain confirm the development of asymmetric kink bands (Fig. 1-13a). The kinks are composed of two uneven members: a long limb which with increasing strain rotates to align closer with the loading direction, and a much shorter one that tilts away towards the direction perpendicular to loading. Similar asymmetric kink bands have also

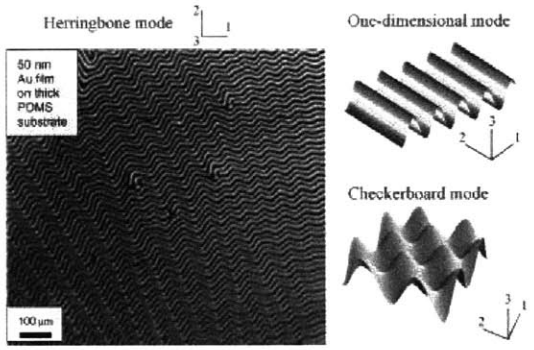

(a)

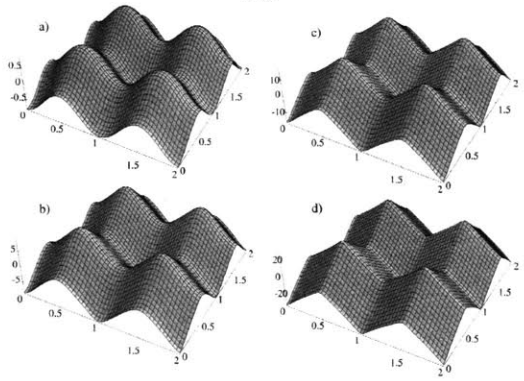

(b)

Figure 1-12: (a) Herringbone buckling mode of a thin film on a elastomeric substrate. Columnar (one-dimensional)and checkerboard buckling modes also shown [7, 8]. (b) Symmetric egg-box pattern fold evolution for a layered material in dialtive strain [9].

been observed in oriented BCP melts during shear parallel to the lamellae [11, 10, 41] (Fig. 1-14). This kinking transforms the microstructure into a striped domain of alternating short and wide bands parallel to the loading direction, which comprise of dilating and shearing layers, respectively. In the early stages of stretching, the deformation is accommodated mostly by the PB phase, by interlamellar shear parallel to the long members, and dilation perpendicular to the short limbs. With increasing strain, the layers within the short dilating bands undergo excessive deformation which leads to voiding in PB domains, and plastic deformation and fragmentation of the PS layers. As for perpendicular loading, this process generates new grain boundaries parallel to the loading direction. After unloading from 500% strain, SAXS patterns show a residual 12° tilt away from the original diagonal orientation, possibly due to plastic deformation of the PS lamellae and voids locked in the newly created grain boundaries.

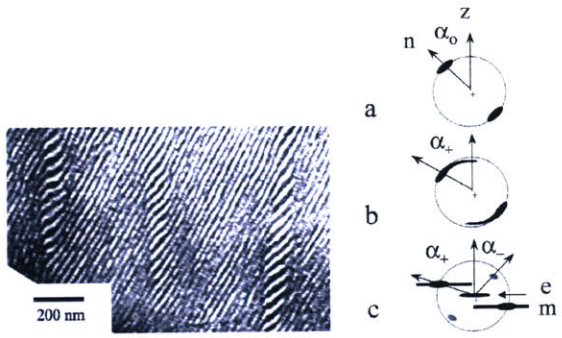

(a) (b)

Figure 1-13: (a) Asymetric kink bands in a lamellar BCP microstructure deformed in diagonsl tension. (b) Schematic of SAXS pattern evolution during diagonal tension.

Loading parallel to the lamellae yields the highest elastic modulus and yield stress, in agreement with composite material mechanics. Contrary to the observations from perpendicular and diagonal loading, the material exhibits a clear yield-point and softening for loading in this direction, as well as a macroscopic neck that progressed in a stable manner. SAXS patterns taken either outside the neck or prior to the yield-point show a reduction in the lamellar repeat distance and loss of higher order reflections (Fig. 1-16d, e). With stretching, the reflection streaks become gradually diffuse, and finally disappear for patterns taken at strains higher than 200% when the specimen has necked entirely. This indicates loss of order in the lamellar structure, due to lamellar fragmentation and material

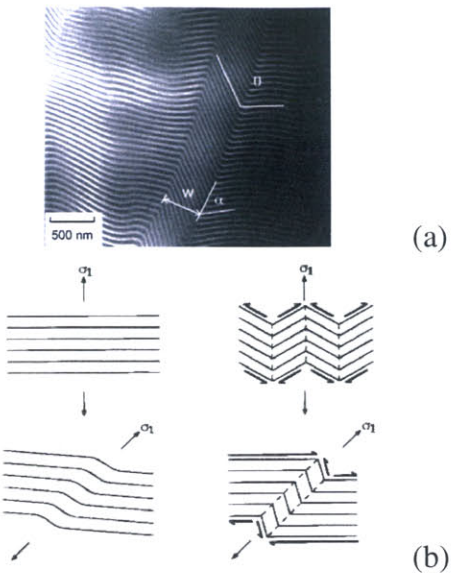

Figure 1-14: (a) Asymmetric kink bands in sheared BCP melt [10]. (b) Schamatic of kink band formation for loading perpendicular and diagonal to the lamellae [11].

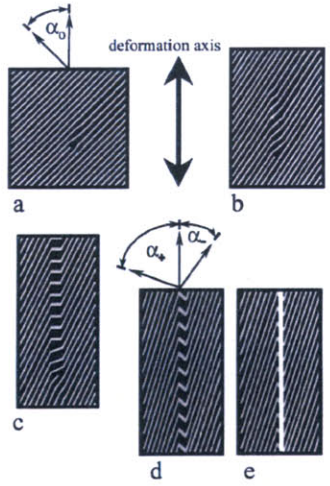

Figure 1-15: Schematic illustration of kink initiation in the vicinity of an imperfection.

voiding. The authors postulate that PS layer fragmentation occurs at the macroscopic neck front (Fig. 1-17a), and that the stress increase at strains higher that 300% results from further fracturing of already fragmented layers. Contrary to what is reported by Cohen *et al.*, my FE-based micromechanical simulations (see Section 2, Fig. 1-27) showed that the neck propagates by microneck cascading along neighbouring PS lamellae [16]. The post-yield increase in macroscopic stress is related to further drawing of the micronecked PS layers (and strain-induced chain orientation within), which eventually leads to their fragmentation, and grants the material its rubber-like response at strains larger than 300% –a process known as the "plastic-to-rubber" transition.

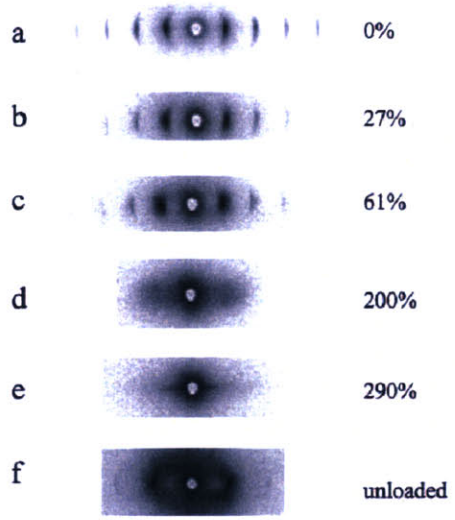

Figure 1-16: SAXS pattern evolution for loading parallel to the lamellae [5]. The elliptical diffraction pattern in (f) shows partial restructuring of the lamellar microstructure after unloading from 400% strain.

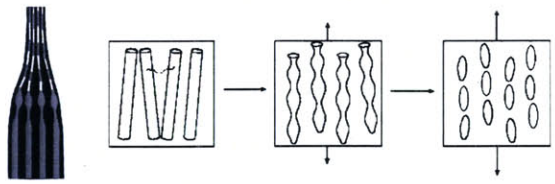

Figure 1-17: Schematic of PS layer micronecking during parallel tension. (a) Lamellar microstructure [5]. (b) Cylindrical microstructure [12]. The cascaded (diagonal) arrangement of micronecks in (b) is more realistic.

To visually and quantitatively assess the micro- and macromechanical influence of imperfections on the perpendicular deformation behavior of lamellar morphologies, iden-

tical samples with different annealing histories were also tested [13]. Annealing is expected to annihilate any processing-induced bias in the imperfection distribution and render it isotropic (Fig. 1-18a). The microstructural difference between carefully annealed and as-processed (unannealed) samples was reflected in their distinctly different necking processes, and their respective stress-strain response (Fig. 1-18b). Unannealed specimens develop a one-dimensional neck-drawn geometry (Fig. 1-19b), in contrast to annealed samples, which exhibit no necking, but a rather equibiaxial, and affine with straining, shrinking in their cross-section. SAXS patterns taken from well inside the neck region, from the neck's boundary, and outside the necked region reveal a 4-point pattern that is pronounced inside the neck and fades outwards. A similar trend was observed for the magnitude of lamellar tilt from measurements within and outside the neck region. Also, the measured tilt angle stabilizes asymptotically with increasing strain and lamellar spacing remains unaltered everywhere in the sample, in accord with results from other studies [5, 47, 15, 19]. It was concluded that if necking were a sample-geometry-induced nonlinearity, due to plane-strain conditions, then it would be independent of the annealing history. Thus, the one-dimensional necking morphology, which is observed only for unannealed samples, must be a nonlinearity induced by the material microstructure, and was ascribed to columnar buckling of the lamellar microstructure. A conceptual illustration is shown in Fig. 1-19a.

The relation between macroscopic yielding of lamellar TPEs, when these are loaded perpendicular to their lamellae, and internal buckling of their lamellar microstructure was studied by Read *et al.* [14] on the basis of a strain energy minimization approach. The analysis bridges the macro- and nano- length scales by expressing the strain energy density in terms of global and local deformation variables augmented with two additional micromechanical deformation modes: layer bending, and in-plane deformation of the soft phase (Fig. 1-21) to capture the buckling instability. The two phases are assumed to be isotropic. Minimization of the energy with respect to the local deformation variables yields the (lowest) critical buckling load and corresponding buckling wavelength as a function of the macroscopic strain. The model was used for a lamellar SBS BC, and the predicted critical buckling stress was compared to computational results from simplified micromechanical FE models. Buckling caused a sharp turnover in the calculated $\sigma - \epsilon$ curve, which

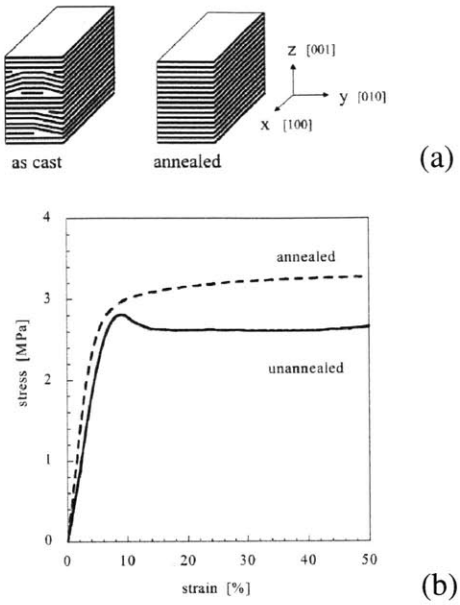

Figure 1-18: (a) Schematic representation of the morphology in as-cast (*left*) and annealed (*right*) films, with a nonuniform distribution of defects in the as-cast film. (b) Engineering stress-strain response of oriented lamellar samples to perpendicular deformation: solid line, as-cast films; dashed line, annealed films [13].

was associated with the "apparent" macroscopic yield-point for loading in this direction (Fig. 1-20). Analytical and numerical predictions converged for starker moduli contrasts between the hard and soft phases. The simulations showed that the initially sinusoidal buckling profile evolved quickly to a chevron pattern of alternating straight limbs and hinges, with the latter developing at the peaks and valleys of the sinusoid. Hinge sharpness was more pronounced when the hard layers were described as elastic-plastic (Fig. 1-20), due to localized plasticity in the hinges.

Alternative loading states were not investigated, and certainly, the model, being developed for buckling analysis, cannot predict the deformation behavior for stretching parallel to the layers. In an instability analysis, Nestorovic and Triantafyllidis [44] studied the influence of different loading orientations, material properties, and volume fractions on the material response, where the Blatz-Ko material model for porous rubbers was used to model the mechanical behavior of the rubbery phase. This eigenvalue analysis calculates the buckling load and wavelength for the lowest instability mode. Neither analysis was compared to actual data, thus the predictive aspect of these analyses is not clear, especially with the strong dependence of these instabilities on inherent material structural imperfec-

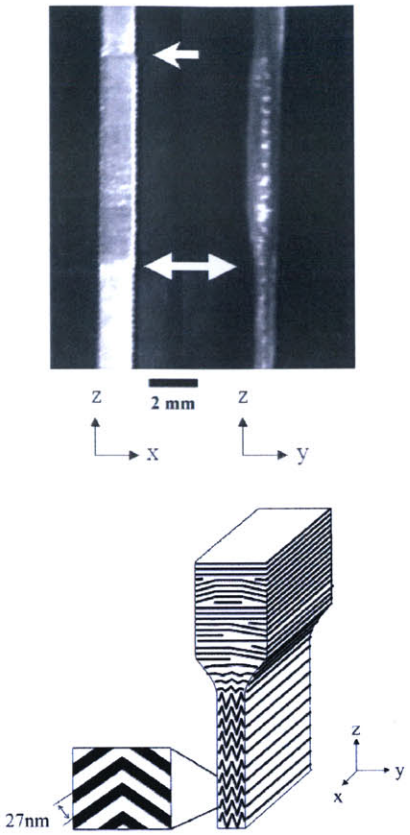

Figure 1-19: (a) Photographs of a "one-dimensional" neck (reduction of the cross-section only in the y-direction) in an as-cast sample under perpendicular deformation. Arrows indicate the neck front. (b) Schematic representation of the chevron morphology inside a "one-dimensional" neck [13].

tion content.

Hermel and coworkers [15] have investigated the effect of coupling between morphology and chain architecture on the large strain behavior of glassy/semicrystalline block copolymers with lamellar microstructures. Shear alignment was used to produce oriented samples from two molecularly different copolymers, a triblock CEC and a pentablock CE-CEC, where C and E denote polycyclohexylethynene and polyethylene, respectively. This glassy/semicrystalline lamellar BCP was observed to exhibit deformation mechanisms similar to those observed in the TPE lamellar structures when axially loaded perpendicular to the lamellae. TEM and *in-situ* SAXS showed that, similar to glassy/rubbery copolymers [5], the pentablock accommodates perpendicular deformation by layer folding and consecutive interlamellar shear. After the yield-point and until failure, the d-spacing remains constant as seen in respective SAXS 4-point patterns, and the lamellae maintain a tilt an-

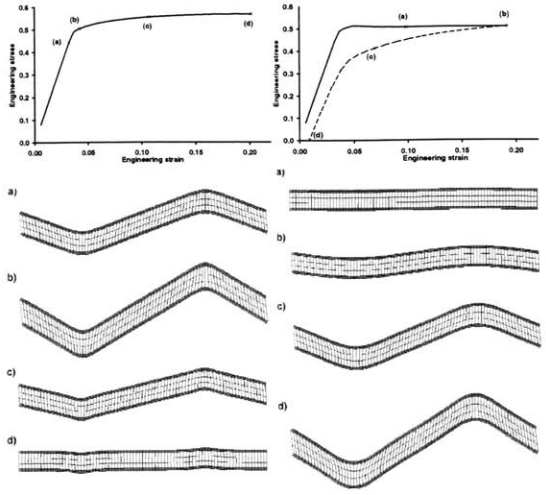

Figure 1-20: Loading/Unloading stress-strain response and the corresponding buckling profile for a lamellar SBS RVE, showing the effect of PS-layer plasticity on both [14]. *Left:* PS layers (thin) modeled as elastic-plastic. *Right:* PS layers modeled as purely elastic.

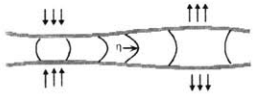

Figure 1-21: Squishing out or sucking in of the soft phase with respective dilation and compression by the transverse deformation of the hard layers [14].

gle of about 66° relative to the stretching direction, as also verified by TEM images from fractured specimens (Fig. 1-23). These results demonstrate that different materials with lamellar morphology deform with the same basic micro-mechanisms[5].

1.3.2 Finite-Element-Based Micromechanical Modeling of the Lamellar Block-Copolymer Single-Crystal

The numerous X-ray and microscopy studies of the literature aim to clarify the link between the morphology of lamellar BCPs and their mechanical properties. Such *in-situ* monitoring techniques however, collect information mostly at *discrete* time instances, and usually

[5]Hermel's study was referenced here to illustrate the universality of the deformation mechanisms met in layered polymeric materials, regardless of the nature of the different blocks present. Hermel's study however, claims a periodic void development to explain the appearance of two additional reflection pairs in SAXS patterns taken from specimens deformed at low strains (before the material yield). Even though periodic voiding seems to be an unsual and unlikely deformation pattern and (to my knowledge) has not been reported elsewhere, Helmel *et al.* offer no connection to alternative, absolutely legitimate events, such as the dilation of domains within the hinge areas, or strain induced crystallization within the domains. Thus to my opinion, this report did not unravel additional deformation micromechanisms, had there been any.

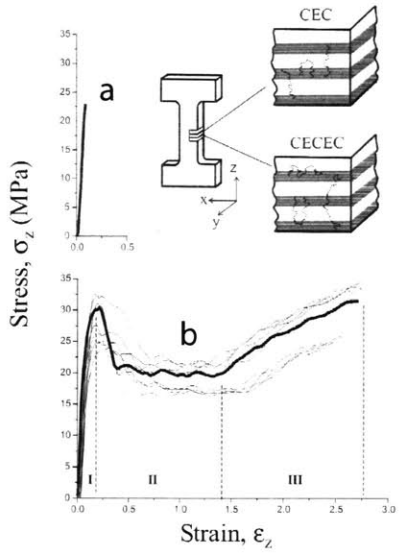

Figure 1-22: Differences in the $\sigma - \epsilon$ response between lamellar: (a) triblock CEC, and (b) pentablock CECEC glassy/semicrystalline block copolymers, for uniaxial tension perpendicular to the lamellae [15].

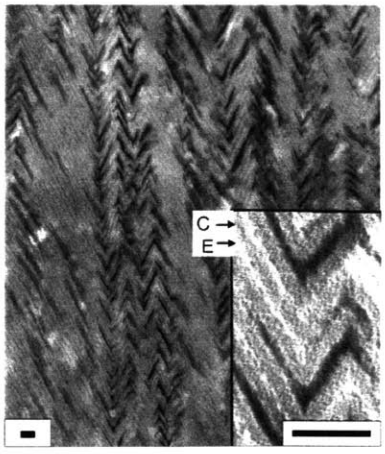

Figure 1-23: TE micrograph of a CECEC pentablock microstructure deformed in tension perpendicular to the lamellae [15]. The deformed morphology exhibits the familiar from other lamellar BCPs chevron morphology. Bar length equals 50nm.

average over a finite volume, which can be in the order of a fraction of a mm^3 or even the entire specimen, and thus cannot always be exact about the nature of the phenomena taking place. In the current research, micromechanical representative volume elements (RVEs) of the BCP microstructure are used to simulate the deformation process and to provide the undestanding and insight needed for the development of a continuum level constitutive model. The structural changes that take place during loading are recorded *continuously*, and the modeling precision is evaluated by comparing the numerical predictions with experimental data from the literature.

The lamellar BCP microstructure was modeled with a *"banded"* 2-D plane strain RVE containing 43vol% PS. The stress-strain behavior of PS is modeled as elastic-plastic with strain hardening, while PB is modeled as a neo-Hookean hyperelastic material with compressibility. The four unknown elastic constituent properties, E_{PS}, E_{PB}, ν_{PS}, and ν_{PB}, have been derived in the same manner as in Allan's composite material micromechanics study [3]. By substituting the macroscopic elastic moduli reported by Cohen [5], E_{0°, E_{90°, and E_{45°, in the expression for the effective modulus, E_θ, and assuming $\nu_{PS} = 0.3$, a system of three equations remains to be solved for the three residual unknowns[6]. The yield and post-yield behavior of PS was estimated from the BCP $\sigma - \epsilon$ response to parallel deformation. The PS and PB layers were discretized with biquadratic, plane-strain, reduced-integration and hybrid elements, respectively, with a sufficient mesh density. Periodic boundary conditions were applied on facing boundaries of the RVE. The RVEs were subjected to uniaxial tension normal and parallel to the lamellae. The simulated microstructural deformation evolution is presented in terms of the macroscopic $\sigma - \epsilon$ RVE response, and as *vonMises*-scalar-equivalent-stress contours on deformed meshes at various stages of deformation.

A variety of morphological imperfections are observed in block copolymers. Two types

[6]As commented before on Allan's work [3], the derivation of constituent properties is sensitive to the choice of directions used. Layer misalignment is associated with a large error for stiffness measurements at, or near 0° orientations relative to the lamellar plane. Even harder is the accurate estimation of PB's bulk modulus purely from stiffness measurements perpendicular to the lamellae. Depending on the degree of misalignment, the measured elastic modulus is a resultant of both bulk and shear PB response. Due to the high contrast between the bulk and shear PB moduli, large discrepancies arise between the actual and the estimated properties for the rubbery phase. Owing to this complexity, numerical simulations are also needed to verify whether the calculated constituent properties can predict the experimental $\sigma - \epsilon$ material response.

of imperfections are used here to initiate the anticipated deformation instabilities that dominate the material response in different loading orientations. For tensile loading normal to the lamellae, the initial RVE profile was perturbed with a very low amplitude sinusoidal undulation. Waviness[7] is an inherent imperfection in BCPs with a lamellar or cylindrical morphology. The wavelength was chosen to be equal to that of the 2^{nd} buckling mode for this RVE (equal here to $L/d_0 = 22$, where L is the wavelength, and d_0 the initial layer periodic spacing, equal to the combined thickness of a PS and a PB layer), such that two wavelengths span the RVE length. The imposed initial waviness is identical to that shown in Fig. 1-24, however, with a smaller amplitude ($A/d_0 = 0.08$, where A is the amplitude). The particular mode was chosen as an approximation to the average chevron wavelength observed in the TEM image of a deformed microstructure shown in Fig. 1-9b from [5], which equaled $L/t = 17.5$. This allows us to directly compare the experimental stress-strain behavior to the predicted one by the RVE simulation[8]. Various other commonly observed microstructural imperfections, such as lamellar-interface perturbations, layer misalignment, and paired edge-dislocations[9] were also studied and will be reported elsewhere. A thorough eigenmode analysis for the lamellar RVE has also been conducted. The influence of internal buckling modes on the calculated macroscopic behavior is summarized in Fig. 1-26.

During loading normal to the lamellae, the material responds initially via dilation of the soft phase (PB). The stiff PS layers constrain the desired lateral contraction of the PB layers and, therefore, the PB layers experience volumetric straining during this normal loading condition. PB being a rubber-like material is nearly incompressible. It strongly resists the volumetric strain, and thus, experiences a lateral tensile stress in addition to the imposed axial tensile stress. In turn, the PS layers experience a lateral compressive

[7]This inherent layer misalignment can be quantified by an appropriate for these materials "orientational order parameter" in terms of the arching and the intensity distribution in SAXS refelections of undeformed samples. This parameter can be used to weight material quantities, such as the modulus, which theoretical models otherwise predict for perfectly aligned microstructures.

[8]The simulated micro- and macroscopic deformation response to perpendicular loading, being determined by the buckling instability, are substantially sensitive to model size and imperfection content. Here, I directly compare simulations to experimentally observed data and thus set the imperfection to capture the average chevron wavelength observed in the corresponding experiments (see Fig. 1-9b.)

[9]Symmetric line defects.

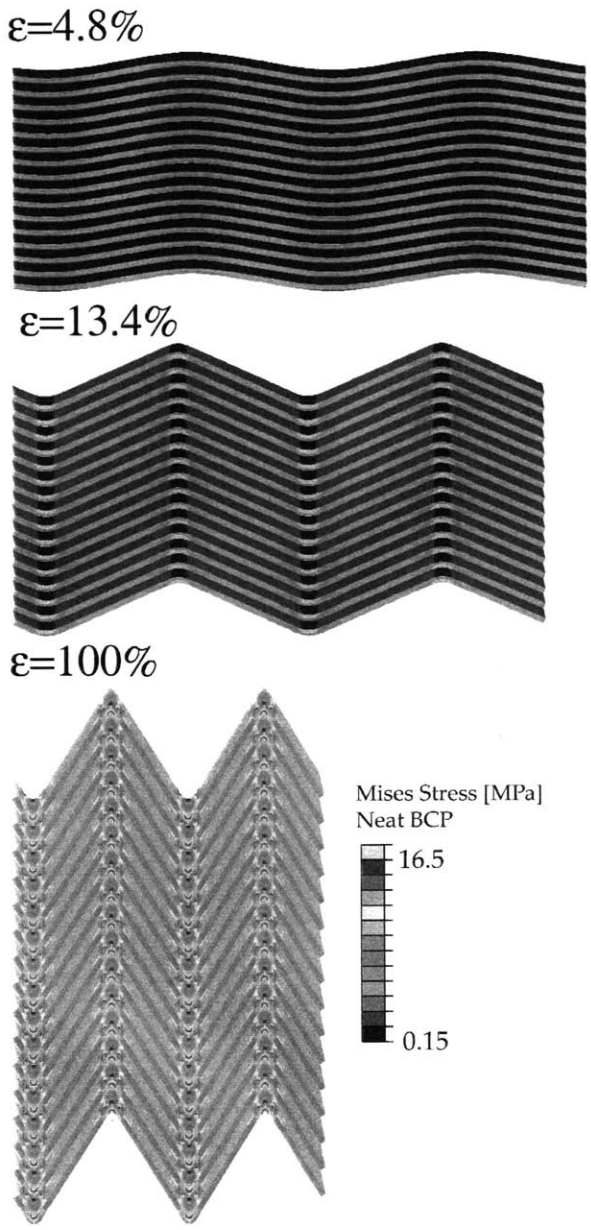

Figure 1-24: Mises-stress contour-plots for loading normal to lamellae. The initial sinusoidal buckling profile forms localized plastic hinges and evolves into a chevron pattern [16].

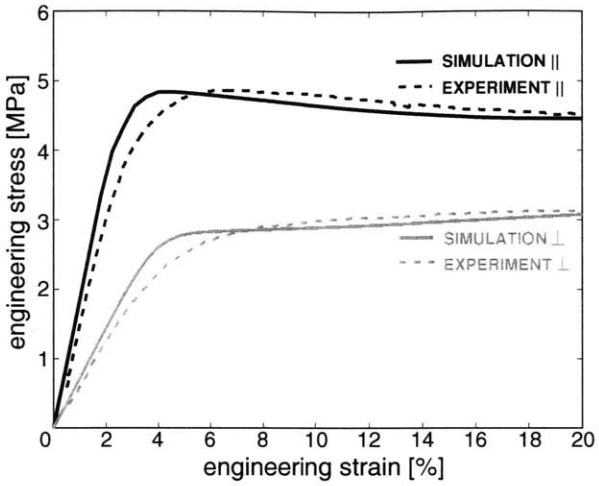

Figure 1-25: Calculated and experimental engineering $\sigma - \epsilon$ response to perpendicular and parallel loading. Constituent properties used in simulations: $E_{PS} = 385$MPa, $\nu_{PS} = 0.33$, $\sigma^y_{PS} = 9.55$MPa, $E_{PB} = 4$MPa, $\nu_{PB} = 0.487$. The experimental data are from Cohen *et al.* [5].

stress. This lateral compressive stress increases with increasing axial strain until it reaches the critical buckling stress for the PS layers. The PS layers then buckle with an initially smooth sinusoidal profile of low amplitude. This elastic buckling event corresponds to what appears as a clear rollover in the macroscopic stress-strain curve akin to the characteristic macroscopic yielding behavior in polymers. The buckled configuration enables continuing macroscopic axial deformation to be accommodated by shearing of the PB layers and tilting of the buckled PS layers. Additionally, the shear modulus of PB is orders of magnitude less than its bulk modulus and thus, shear of the PB layers is not only kinematically, but also energetically more favorable than dilation. The post-yield slope of the stress-strain curve is thus governed by the PB shear modulus and is significantly more compliant than the initial stiffness, which was governed by the PB bulk modulus.

With continuing macroscopic deformation, the sinusoidal waviness develops plastic hinges due to local yielding of the PS layers, resulting in chevron folds and kink boundaries parallel to the loading direction, consistent with microscopy images of deformed microstructures [5, 15] and analytical studies [37, 14]. Fig. 1-24 and Fig. 1-25 show this lamellar microstructure evolution and the calculated stress-strain response, respectively[10].

[10]The simulations revealed that the ratio of PB bulk to shear moduli primarily, and secondly, the stiffness and yield behavior of PS, are critical quantities for the development of plastic hinges. For example, temper-

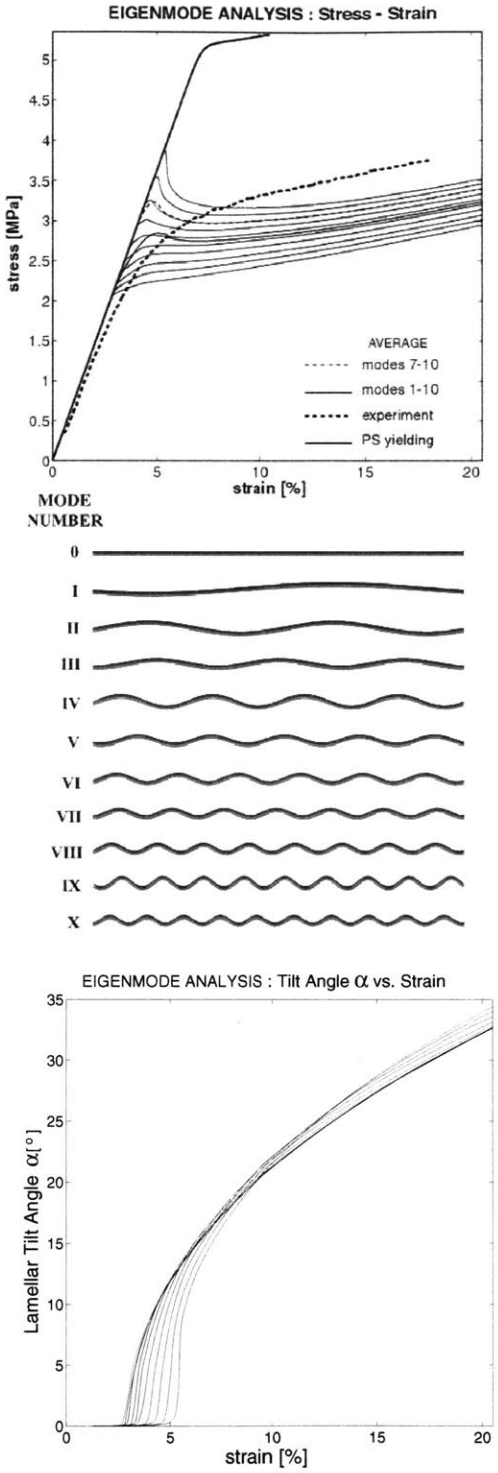

Figure 1-26: RVE buckling eigenmode analysis for perpendicular loading: stress-strain response (*top*), corresponding buckling wavelengths (*middle*), and tilt angle, α, evolution with strain (*bottom*). The lamellar tilt angle rises abruptly at the onset of the buckling instability and saturates to an upper limit as stretch increases.

Macroscopic strain hardening emanates from the increasing resistance of the formed PS plastic hinges as well as the kinematic restraint introduced by further PB dilation and shearing PB. In fact, a locking azimuthal (tilt) angle exists for the chevron folds, beyond which further tilting is difficult, and additional deformation can only happen via increased dilation of the rubbery (PB) layers. The simulations permit study of the evolution in other structural features such as the lamellar spacing, d, and the azimuthal angle, which can be directly compared to SAXS and TEM data from the literature.

The response of the BCP RVE to loading parallel to the lamellar orientation is dominated by the behavior of the PS layers. With increasing stretch, micronecks initiate in individual PS layers at imperfection sites (Fig. 1-27). The micronecks follow the basic behavior observed in macroscopic necking of polymers where the neck initiates, localizes, then stabilizes and propagates upon reaching the draw ratio. Double shear bands initiate in the immediately adjacent PB layers (Fig. 1-27). The shear bands progress from one PS/PB interface to the next and, due to perfect interface bonding, shear the neighboring PS layer and cause the initiation of a new microneck at an angle of about 45°. This produces a cascading of micronecks throughout the PS layers, which is responsible for the gradual reduction in the copolymer stiffness after the initial linear response to loading. With this deformation process, the micronecks multiply and, at a macroscopic level, form a macroscopic shear band and eventually a macroscopic neck. Once the micronecks have fully cascaded, each will locally draw through its respective layer (stress plateau on the stress-strain curve), ultimately producing the observed macroscopic strain hardening (Fig. 1-25). A similar deformation cascade has been observed in microlayered polymers where an interplay between shear bands in ductile thermoplastic layers and crazing in brittle layers results in a mutual cascading of these two deformation processes in microlayered polymer

---

ature studies by Cohen *et al.* [6] on the micromechanical response to perpendicular loading at temperatures above the T_g of PS (100°C), when the system is viscous/rubbery, have shown that the (temperature-induced) low interlayer modulus contrast eliminates the folding instability which governs the material nonlinearity at ambient temperatures. The low modulus contrast effect was partially realised by D.J. Read *et al.* [14] as well. In addition, coexistence of layer dilation in both PB and PS, as well as micro-buckling, however without the development of hinges, were observed at temperatures around the T_g of PS (80°C), when the material is rendered viscoelastic/rubbery. Thus, the influence of constituent properties on the micro/macro-mechanical behavior is an issue that deserves carefull analytical treatment, which however is lucking in the current literature.

laminates [48].

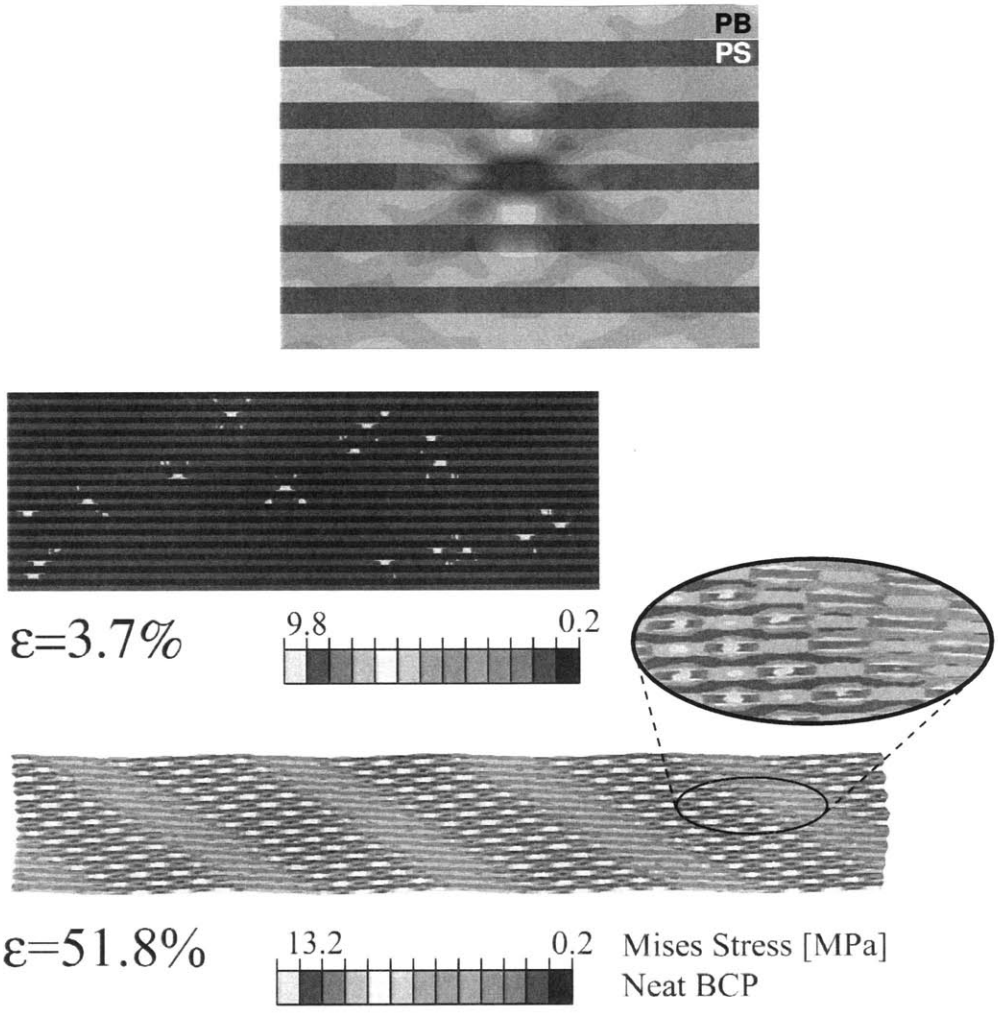

Figure 1-27: *Top*: Symmetric shear bands initiate from the PB/PS interface at the site of a PS-layer microneck, and propagate through the adjacent PB-layer to the next PB/PS interface. At that location, due to strain compatibility, the shear band acts as an imperfection that stimulates the initiation of a new microneck. With this cooperative deformation process, micronecks cascade between neighboring PS-layers to span the entire microstructure. *Bottom*: Mises stress contour-plots for loading parallel to the lammelae. PS micronecking advances through the structure by shearing adjacent PB layersc [16].

The close agreement between experimental data from the literature and the numerically predicted material response to normal and parallel loading suggests that the behavior of each constituent, as well as the physics of deformation, have been well understood and successfully reproduced. The response of multigrain copolymer morphologies can now be interpreted based on findings from the micromechanics of single-crystal lamellar morphol-

ogy. These simulations were performed on perfectly oriented, 2D microstructures and thus important effects such as processing induced disorder or line defects are not captured, yet clearly have strong influence on the micromechanics [13] and require further investigation. Three-dimensional analysis, which is lacking in the literature, is expected to offer further insights. Also, the single-crystal nonlinear response to uniaxial loading at different orientations to the initial microstructure remains to be explored, as well as the behavior when subjected to multiaxial loading conditions.

1.4 Thesis Outline

The objective of the current thesis is to develop a micromechanically-based hyperelastic continuum constitutive model for the anisotropic stress-strain response of lamellar glassy-rubbery-glassy triblock copolymers, which will be implemented for egineering applications with the finite element technique. The layered microstructure of the considered BCP combined with the well identified, both experimentally and computationally, elements that determine its anisotropic behavior from small to large strains, allow for a detailed physically-based constitutive formulation. The outline of the thesis is as follows:

Chapter 2, presents the general micromechanical framework for the development of micromechanically/physically-based continuum constitutive descriptions for the large-strain behavior of hyperlestatic materials with layered underlying morphologies. The presented framework is based on equilibrium and compatibility constraints that must be satisfied on the layer-interface, and are therefore, independent of the constituent behavior or the length-scale of the microstructure. For this reason, the presented framework can be used to describe a variety of layered materials by choice of an appropriate hyperelastic material model for each of the involved constituents. In the current thesis, the framework is applied for the lamellar SBS BCP of interest with the rubbery (PB) and glassy (PS) phases described as a neo-Hookean materials with compressibility. An analytical closed-form solution is derived, which fully describes the BCP's stress and deformation response to any type of macroscopically imposed deformation. The analytically derived continuum constitutive model is physically/micromechanically-based and thus inherently captures the

directional dependence in each layer's/phase's contribution to the overall effective material response, and hence, the orientation-dependent anisotropy in the BCP's response. The model is formulated as a FORTRAN subrutine and implemented in the commerical finite element software ABAQUS Explicit for use in numerical calculations on generic boundary value problems. The numerical predictions of the analytical model for the directional anisotropy of the BCP's single-crystal stress response and for the evolution of specific internal microdeformation quantities are validated against the corresponding results from finite-element unit-cell calculations with a 2D discrete bilayer RVE of the oriented layered morphology, under three types of applied macroscopic deformation: plane-strain axial extension, plane-strain biaxial deformation, and plane-strain simple shear, for different underlying material orientations to the respective loading axes.

In Chapter 3 the analytical constitutive model is used to study the effect of isolated boundary constraints on the deformation behavior of oriented BCP structures. Two types of tests are performed: *(i)* plane-strain iaxial extension on single-crystal tensile strip specimens with clamped-end conditions, and *(ii)* plane-strain axial extension of bicrystal strip specimen configurations, also with clamped-end conditions. The results from the micro- and macromechanical study of the anisotropic single-crystal behavior in Chapter 2 are used to elucidate the differences in the force/displacement response of the extended specimens and the nature and spatial extent of the boundary influence on the deformed specimen configurations, based on the underlying material orientation with respect to the loading axis and the specimen geometry/dimensions. The deformation results from both oriented and bicrystal specimens are qualitatively compared to existing experimental data.

In chapter 4, the developed continuum constitutive model is further utilized for numerical studies on the mechanical behavior of lamellar BCP polycrystals. 2D finite-element-based micromechanical models containing a sufficiently large number of randomly oriented grains are developed to represent the multigrain lamellar aggregate. The continuum model is used to assign the behavior of the invidual grains, and to predict intergranular compatibility and equilibrium interactions among them, which collectively result in the effective macroscopic stress and deformation response of the polycrystal configuration. The model enables a thorough investigation of the occurring micromechanical deformation

modes within each individual grain, based on single-crystal results and the specific grain orientation and boundary influences. In order to evaluate its capability to capture complex micro-deformation/stress processes and intergranular interactions at the length scale of the microstructure in an accurate and physically consistent manner, contour plots of homogenized and layer-specific stress/deformation quantities are counter examined and correlated to RVE-calculated macroscopic stress-strain curves. Furthermore, histograms of the evolving distribution of grain orientation within the RVEs are compared to corresponding SAXS data from the literature. To gain insight for the development of physically-based continuum constitutive descriptions for the behavior of polycrystalline lamellar BCPs or analogous lamellar morphologies, histograms depicting the evolution of deformation gradients within the deforming RVEs are studied and the calculated macroscopic stress-strain curves are compared to corresponding Taylor/Sachs predictions.

Finally, Chapter 5 summarizes key conclusions, and suggests directions for future work.

Chapter 2

Micromechanically-based Constitutive Model for the Mechanical Response of Lamellar Block Copolymers

Block copolymers (BCPs) are a relatively new class of thermoplastic elastomers (TPEs). Over the last three decades, modern copolymerization techniques have enabled covalent bonding between repeating chain blocks of two or more, otherwise chemically incompatible, thermoplastics and elastomers to produce a single (BCP) macromolecule. Due to their incompatibility, when given the freedom the constituents spontaneously phase separate into domains of various shapes, morphologies and sizes from tens to hundreds of nanometers. In essence, BCP TPEs are nanocomposites (with perfectly bonded interfaces), and as such exhibit behavior consistent with both that of elastomers and of thermoplastics. Due to this unique behavior and despite their novelty, BCP TPEs have become today some of the most commonly used polymeric materials counting numerous commercial applications over diverse industries[1]. Furthermore, block copolymers are emerging as instrumental in future directions of nanotechnology as an increasing number of new nano- techniques and applications seek to utilize their nanostructural features[24, 25, 26, 31]. BCPs, whether as polycrystalline configurations or as "highly" oriented single-crystals, attract an accumulating number of applications, and the inquiry for efficient material design and product develop-

[1]Automotive, footwear, wire and cable, adhesives and sealants, coatings, medical[22, 1, 23].

ment extends over a range of length scales, from nano up to macro. Hence, there exists a need for continuum models that will predict both the oriented as well as the polycrystalline response of block-polymer materials to generic boundary value problems.

This chapter presents a micromechanically-based hypereslastic continuum constitutive description for the large strain response of oriented (single-crystal) block copolymers with lamellar microstructures. Here we offer a specific application to styrene-butadiene-styrene (SBS) triblock polymers, the behavior and micromechanics of which have been extensively investigated by experimental means [5, 6, 13][2]. Micromechanical finite-element-based unit cell models, representative of the underlying material microstructure -noted as representative volume elements (RVEs)- are used to reproduce the deformation processes, which take place at the inherent length scale of the microstructure during loading, and to monitor the concomitant evolution of the microstructure. The micromechanical simulation results are direct parallels to experimental (x-ray, microscopy, and stress-strain) data from the literature, and are a toll to provide the insight needed for the development of a physically-based continuum constitutive model. Operationally, the continuum model is derived from equilibrium and compatibility considerations along the lamellar interface. Hence the constitutive model is length-scale independent and general enough to describe point-wise hyperelastic materials with layered microstructures. A similar framework has been implemented in a numerical iteration scheme by vanDomellen *et al.* [49] to describe the elastic-plastic behavior of semi-crystalline polymers.

The material presented here is organized in the following manner. First we describe the BCP microstructure in order to introduce the micromechanical RVE, which is used: *(i)* to derive the continuum constitutive model analytically, and *(ii)* in unit-cell finite-element simulations to study the deformation micromechanics of the microstructure and how these relate to the macroscopic material response. Second, using the RVE, we describe the generic micromechanical framework for the hyperelastic continuum model: *(a)* we give the generalized form for the hyperelastic strain energy density of a dual-phase lamellar

[2]Styrenic block polymers are among the most utilised TPE classes. Their mechanical response combines the stiffness (stuctural robustness) of the styrenic component and the hyperelasticity (resilience) of the elastomeric blocks. In addition, in comparison other TPEs they appear as more chemically stable in relatively aggressive enviroments.

material, which will be used to derive the stress-strain relationship, and *(b)* we state the equilibrium and compatibility requirements that must be satisfied at every material point within a layered continuum. Third, the framework is applied in the case of lamellar SBS BCPs and an analytical continuum model is derived assuming Neo-Hookean behavior for both phases - styrene and butadiene. Finally, for different loading cases the predictions of the analytical continuum model are verified against results from finite-element unit-cell calculations[3].

2.1 Continuum Modeling.

2.1.1 The Oriented Lamellar Block Polymer Microstructure.

The microstructural morphology of block copolymers has been studied extensively in the past. Microphase separation in block copolymers results in well-defined morphologies including a BCC lattice of spheres within a matrix, HCP cylinders within a matrix, bicontinuous double-diamond networks, and lamellae. The formed microstructure depends on the relative volume fraction of the constituent blocks. Initial volume fractions ranging between 40-60% result in layered lamellar microstructures. The microstructural features are on the order of a few nanometers in thickness with perfect bonding between domains, due to the covalent chemical bonds between the constituent blocks. An oriented lamellar microstructure of a styrene-butadiene-styrene (SBS) triblock is shown in the TEM of Fig.1-7. This highly ordered ("near single-crystal") morphology has been induced by the shear-aligning process of roll-casting[5]. In the absense of an alignment factor, a polygranular aggregate is found consisting of lamellar structures of grains at different orientaions. For completeness, a polycrystalline configuration of the triblock is also presented in Fig. 4-5. Distinct grains containing highly oriented lamellae are visible clearly in the micrograph. The sharp grain boundaries are narrow regions across which the lamellae reorient abruptly without generally disrupting their continuity.

[3]The model can be implemented in multigrain finite-element simulations to reproduce the isotropic response of polycrystalline lamellar BCPs, and to investigate the deformation micromechanics of individual grains.

2.1.2 Micromechanically-based Continuum Model.

Microstructurally-based Represenatative Volume Element.

To study the mechanical response of lamellar block polymers, the microstructure of a *"single crystal"* is modeled with the *representative volume element* (RVE) shown in Fig. 2-1, which consists of two layers, each corresponding to a constituent phase, which are mechanically coupled at their interface. The initial volume fraction of the copolymer is replicated by appropriate adjustment of each layer's thicknesses as $h_r = \phi_o H$ and $h_g = (1 - \phi_o)H$, where ϕ_o is the initial volume fraction of phase r and H the total RVE thickness. Notionally, the RVE extends to infinity in all directions and in a repeating manner, such that it can be considered a representative material point.

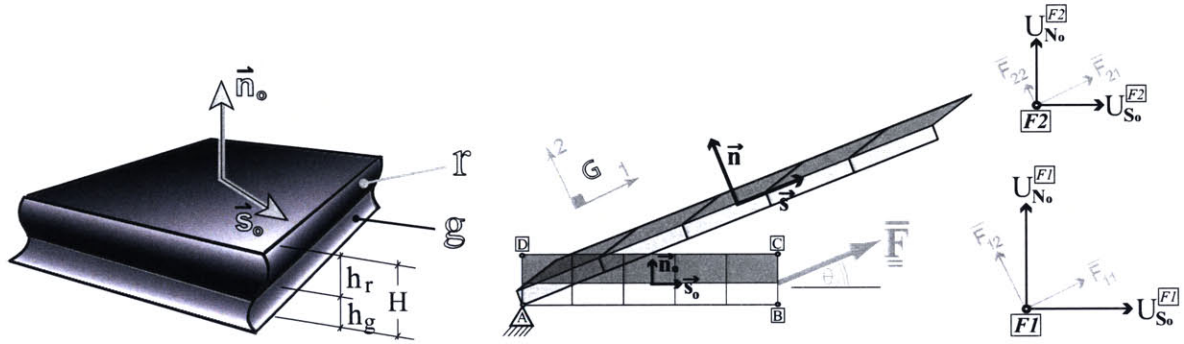

Figure 2-1: *(a)* 3D Schematic illustration of the bi-layer representative volume element (RVE) and *(b)* the RVE counterpart used in 2D analysis.

Microstructurally-informed 2D Continuum-level Constitutive Model.

We seek to develop a microstructurally-informed hyperelastic constitutive description for the anisotropic, hyperelastic, mechanical behavior of lamellar block copolymers. Using the given RVE, a hyperelastic strain energy density function for a lamellar material will be developed in terms of the applied macroscopic deformation gradient. The stress-strain response of the material will follow by simple derivation of its strain energy function with respect to the macroscopic deformation gradient. The model will account for large rotations of the microstructure and for the non-affine distribution of deformation and stress within the constituent phases.

The macroscopic deformation is accommodated inhomogeneously between the two phases, however, within each layer it is considered to be piecewise homogeneous. Ma-

terial continuity is satisfied by the imposed mechanical coupling at the layer interface. In agreement with Hill's lema, the effective response of the material is the volume-weighted average of each phase's individual contribution. The structure has to be in equilibrium with the traction boundary condition and maintain compatibility with boundary displacements. For the current model, these conditions correspond to the volume-weighted average in the RVE's true (Cauchy) stress,$\overline{\boldsymbol{\Sigma}}$, and deformation gradient, $\overline{\mathbf{F}}$:

$$\overline{\boldsymbol{\Sigma}} = \phi \cdot {}^{\mathrm{r}}\boldsymbol{\sigma} + (1-\phi) \cdot {}^{\mathrm{g}}\boldsymbol{\sigma} \tag{2.1}$$

$$\overline{\mathbf{F}} = \phi_o \cdot {}^{\mathrm{r}}\mathbf{F} + (1-\phi_o) \cdot {}^{\mathrm{g}}\mathbf{F} \tag{2.2}$$

where $\overline{\mathbf{F}}$ denotes the macroscopic deformation gradient and and $\overline{\boldsymbol{\Sigma}}$ the macroscopic Cauchy Stress, ${}^{w}\mathbf{F}$ is the microdeformation gradient and ${}^{w}\boldsymbol{\sigma}$ the Cauchy Stress within phase w, while ϕ_o and ϕ are the initial and current volume fraction of the rubbery phase. Since deformation gradients are defined with respect to the reference (undeformed) configuration (of the RVE), the initial volume fraction ϕ_o of phase r is used to average the microdeformation gradients. True (Cauchy) stress is defined in the current (deformed) configuration, therefore, the current volume fraction, ϕ, is appropriate for averaging the stress contributions. At each instance of the deformation, the volume, and thus the volume fraction, of each phase is changing due to dilatation. The current volume fraction for the rubbery phase is given by:

$$\phi = \frac{\phi_o \cdot J_r}{\phi_o \cdot J_r + (1-\phi_o) \cdot J_g} \tag{2.3}$$

where $J_r = det({}^{\mathrm{r}}\mathbf{F})$ and $J_g = det({}^{\mathrm{g}}\mathbf{F})$ are the volume ratios of the constituents. Mechanical integrity is maintained by enforcing compatibility and equilibrium on the interface. If $\vec{\mathbf{n}}_o$ is the unit normal on the interface in the undeformed configuration (Fig. 2-1), and $\vec{\mathbf{s}}_o$ a unit vector in the plane of the interface (normal to $\vec{\mathbf{n}}_o$), then compatibility at the interface is expressed by enforcing compatibility on the microdeformation gradients of the constituents:

$$\left.\begin{aligned} {}^{\mathrm{g}}\mathbf{F} \cdot \vec{\mathbf{s}}_o = {}^{\mathrm{r}}\mathbf{F} \cdot \vec{\mathbf{s}}_o = \overline{\mathbf{F}} \cdot \vec{\mathbf{s}}_o \\ (1-\phi_o) \cdot {}^{\mathrm{g}}\mathbf{F} \cdot \vec{\mathbf{n}}_o + \phi_o \cdot {}^{\mathrm{r}}\mathbf{F} \cdot \vec{\mathbf{n}}_o = \overline{\mathbf{F}} \cdot \vec{\mathbf{n}}_o \end{aligned}\right\} \text{ Compatibility} \tag{2.4}$$

Likewise, in the current configuration, with $\vec{n}$ and $\vec{s}$ denoting the respective unit vectors normal to- and in the plane of the interface, stress continuity (equilibrium) across the interface has the form:

$$\left.\begin{aligned} {}^{g}\boldsymbol{\sigma}\cdot\vec{n} = {}^{r}\boldsymbol{\sigma}\cdot\vec{n} &= \overline{\boldsymbol{\Sigma}}\cdot\vec{n} \\ (1-\phi)\cdot{}^{g}\boldsymbol{\sigma}\cdot\vec{s} + \phi\cdot{}^{r}\boldsymbol{\sigma}\cdot\vec{s} &= \overline{\boldsymbol{\Sigma}}\cdot\vec{s} \end{aligned}\right\} \quad \text{Equilibrium} \tag{2.5}$$

In the indicial notation introduced in Fig. 2-1, the above averaging laws and continuity restrictions are reduced to:

$$\begin{aligned} \overline{F}_{s_o s_o} &= {}^{r}F_{s_o s_o} = {}^{g}F_{s_o s_o} & \overline{F}_{s_o n_o} &= \phi_0\cdot{}^{r}F_{s_o n_o} + (1-\phi_0)\cdot{}^{g}F_{s_o n_o} \\ \overline{F}_{n_o s_o} &= {}^{r}F_{n_o s_o} = {}^{g}F_{n_o s_o} & \overline{F}_{n_o n_o} &= \phi_0\cdot{}^{r}F_{n_o n_o} + (1-\phi_0)\cdot{}^{g}F_{n_o n_o} \end{aligned} \tag{2.6}$$

$$\begin{aligned} \overline{\Sigma}_{nn} &= {}^{r}\sigma_{nn} = {}^{g}\sigma_{nn} & & \\ \overline{\Sigma}_{sn} &= {}^{r}\sigma_{sn} = {}^{g}\sigma_{sn} & \overline{\Sigma}_{ss} &= \phi\cdot{}^{r}\sigma_{ss} + (1-\phi)\cdot{}^{g}\sigma_{ss} \end{aligned} \tag{2.7}$$

In the above relations, the components of the macroscopic deformation gradient, $\overline{\mathbf{F}}$, need to be expressed in terms of the local orthonormal basis $\mathcal{R}$, defined in the reference frame by vectors $\vec{s}_o$ and $\vec{n}_o$. It will also be useful to define the components of the macroscopic deformation gradient in the global orthonormal basis $\mathcal{G}$. To distinguish between the two equivalent expressions for $\overline{\mathbf{F}}$, we denote by $\overline{\mathbf{F}}_{\mathcal{G}}$ the tensor presented in the global basis, and $\overline{\mathbf{F}}_{\mathcal{R}}$ denotes the expression w.r.t.the local reference basis. Thus a simple basis transformation between $\mathcal{G}$ and $\mathcal{R}$ is required:

$$\overline{\mathbf{F}}_{\mathcal{R}} = \mathbb{Q}_{\mathcal{GR}}\ \overline{\mathbf{F}}_{\mathcal{G}}\ \mathbb{Q}^{\mathbf{T}}_{\mathcal{GR}}\ , \tag{2.8}$$

where $\mathbb{Q}_{\mathcal{AB}}$ is a proper orthogonal rotation from frame $\mathcal{A}$ to frame $\mathcal{B}$.

Using Eqn. 2.6 one of the unknown micro-deformation gradients, here ${}^{g}\mathbf{F}$, can be eliminated from all subsequent expressions, which will then depend only on $\overline{\mathbf{F}}$ and ${}^{r}\mathbf{F}$.

For hyperelastic materials, the true stress is calculated from a strain energy density function by derivation w.r.t. to the deformation gradient.

Assuming hyperelastic behavior for both phases, the total strain energy density of the RVE can be expressed as the volume-weighted average of the individual hyperelastic strain energy densities:

$$\mathcal{U} = \phi_o \cdot \mathcal{U}_r({}^r\mathbf{F}) + (1-\phi_o) \cdot \mathcal{U}_g({}^g\mathbf{F}) \tag{2.9}$$

Since the each constituent's deformation gradient is a function of the specified macroscopic deformation gradient, the strain energy density of the composite can be completely described in terms of $\overline{\mathbf{F}}$:

$$\begin{aligned} \mathcal{U} &= \phi_o \cdot \mathcal{U}_r({}^r\mathbf{F}) + (1-\phi_o) \cdot \mathcal{U}_g({}^g\mathbf{F}) && (2.10) \\ &= \phi_o \cdot \mathcal{U}_r(\overline{\mathbf{F}}) + (1-\phi_o) \cdot \mathcal{U}_g(\overline{\mathbf{F}}) \implies \mathcal{U} = \widehat{\mathcal{U}}(\overline{\mathbf{F}}) && (2.11) \end{aligned}$$

We can use a variational argument to solve for the unknown quantities ${}^r\mathrm{F}_{s_on_o}$ and ${}^r\mathrm{F}_{n_on_o}$; the resulting strain energy of the composite should be minimized for the applied macroscopioc deformation gradient, $\overline{\mathbf{F}}$:

$$\frac{\partial \mathcal{U}}{\partial(\overline{\mathrm{F}}_{s_on_o})} = 0 \quad (2.12) \qquad \text{and} \qquad \frac{\partial \mathcal{U}}{\partial(\overline{\mathrm{F}}_{n_on_o})} = 0 \quad (2.13)$$

These lead to:

$$\begin{aligned} \frac{\partial \mathcal{U}}{\partial(\overline{\mathrm{F}}_{s_on_o})} = 0 \quad &= \quad \phi_o \cdot \frac{\partial \mathcal{U}_r}{\partial({}^r\mathrm{F}_{s_on_o})} + (1-\phi_o) \cdot \frac{\partial \mathcal{U}_g}{\partial({}^r\mathrm{F}_{s_on_o})} \\ &= \quad \phi_o \cdot \underbrace{\frac{\partial \mathcal{U}_r}{\partial({}^r\mathrm{F}_{s_on_o})}}_{{}^r\mathrm{P}_{s_on_o}} + (1-\phi_o) \cdot \underbrace{\frac{\partial \mathcal{U}_g}{\partial({}^g\mathrm{F}_{s_on_o})}}_{{}^g\mathrm{P}_{s_on_o}} \cdot \underbrace{\frac{\partial({}^g\mathrm{F}_{s_on_o})}{\partial({}^r\mathrm{F}_{s_on_o})}}_{-\frac{\phi_o}{1-\phi_o}} \\ \implies {}^r\mathrm{P}_{s_on_o} &= {}^g\mathrm{P}_{s_on_o} \end{aligned} \tag{2.14}$$

and similarly for the other in-plane direction: ${}^r\mathrm{P}_{k_on_o} = {}^g\mathrm{P}_{k_on_o}$.
Likewise:

$$\begin{aligned} \frac{\partial \mathcal{U}}{\partial(\overline{\mathrm{F}}_{n_on_o})} = 0 \quad &= \quad \phi_o \cdot \frac{\partial \mathcal{U}_r}{\partial({}^r\mathrm{F}_{n_on_o})} + (1-\phi_o) \cdot \frac{\partial \mathcal{U}_g}{\partial({}^r\mathrm{F}_{n_on_o})} \\ \implies {}^r\mathrm{P}_{n_on_o} &= {}^g\mathrm{P}_{n_on_o} \ . \end{aligned} \tag{2.15}$$

This is the equivalent form of stress equilibrium on the interface (Eqn. 2.7), albeit in the undeformed configuration and in terms of the 1^{st} *Piola-Kirchhoff* stress tensor, ${}^{\mathrm{w}}\mathbf{P}$. As before, $\vec{\mathrm{n}}_{\mathrm{o}}$ denotes the unit vector normal to the undeformed interface, and stress continuity in the reference configuration follows as [4]:

$$ {}^{\mathrm{r}}\mathbf{P}\cdot\vec{\mathrm{n}}_o \;=\; {}^{\mathrm{g}}\mathbf{P}\cdot\vec{\mathrm{n}}_o \;\Longrightarrow\; \begin{cases} {}^{\mathrm{r}}\mathrm{P}_{\mathrm{n_o n_o}} \;=\; {}^{\mathrm{g}}\mathrm{P}_{\mathrm{n_o n_o}} \\ {}^{\mathrm{r}}\mathrm{P}_{\mathrm{s_o n_o}} \;=\; {}^{\mathrm{g}}\mathrm{P}_{\mathrm{s_o n_o}} \\ {}^{\mathrm{r}}\mathrm{P}_{\mathrm{k_o n_o}} \;=\; {}^{\mathrm{g}}\mathrm{P}_{\mathrm{k_o n_o}} \end{cases} . \tag{2.16} $$

The reader should be cautioned here, that stress continuity can only be enforced on these stress components, whose definition is tied to the layer interface, *i.e.,* the normal, ${}^{w}\mathrm{P}_{\mathrm{n_o n_o}}$, and the in-plane shear stress components, ${}^{w}\mathrm{P}_{\mathrm{s_o n_o}}$. The thicknesses of the RVE layers are not changing affinely because the phases dilate by different amounts. Thus, the 1^{st} *Piola-Kirchhoff* stress tensor is not symmertic and shear stress equilibrium cannot be used for the 1^{st} *P-K* shear stress components, ${}^{w}\mathrm{P}_{\mathrm{n_o s_o}}$.

Hence, the compatibility conditions as expressed in Eqn.2.6 and the equilibrium equations as expressed in Eqn.2.7 provide the equations needed to determine the deformation gradients of each constituent, ${}^{\mathrm{r}}\mathbf{F}$ and ${}^{\mathrm{g}}\mathbf{F}$, in terms of the macroscopic deformation gradient, $\overline{\mathbf{F}}$. As a point of clarity, writing the equilibrium constraints in terms of the 1^{st} *Piola-Kirchhoff* stress, ${}^{\mathrm{w}}\mathbf{P}$, as opposed to in terms of the Cauchy stress, ${}^{w}\boldsymbol{\sigma}$, was found to greatly simplify the algebraic solution process.

The Cauchy stress, ${}^{w}\boldsymbol{\sigma}$, within each layer follows from the corresponding 1^{st} *Piola-Kirchhoff* stress, ${}^{w}\mathbf{P}$, and the micro-deformation gradient, ${}^{w}\mathbf{F}$, as: [5]

---

[4] This approach could have been used from start instead of describing equilibrium in terms of true stresses. However, we believe that this presentation of the micromechanical framework is more insightfull for the reader.

[5] Alternatively, the Cauchy stress, ${}^{w}\boldsymbol{\sigma}$, for a material w with neo-Hookean behavior can be calculated as:

$$ \begin{aligned} {}^{w}\boldsymbol{\sigma} = \left(\frac{1}{J_w}\,{}^{w}\mathbf{P}\,{}^{w}\mathbf{F}^{\mathrm{T}}\right) &= \frac{2}{J_w}\left[{}^{w}\mathrm{I}_3\frac{\partial \mathcal{U}_{\mathrm{i}}}{\partial\,{}^{w}\mathrm{I}_3}\,\mathbf{I}+\left(\frac{\partial \mathcal{U}_w}{\partial\,{}^{w}\mathrm{I}_1}+{}^{w}\mathrm{I}_1\frac{\partial \mathcal{U}_w}{\partial\,{}^{w}\mathrm{I}_2}\right){}^{w}\mathbf{B}-\frac{\partial \mathcal{U}_w}{\partial\,{}^{w}\mathrm{I}_2}\,{}^{w}\mathbf{B}^2\right] \\ &= \frac{\mathrm{c}_w}{2\,J_w}\left({}^{w}\mathbf{B}-\mathbf{I}\right)+\mathrm{k}_w\left(J_w-1\right)\mathbf{I} \end{aligned} \tag{2.17} $$

where ${}^{w}\mathbf{B} = {}^{w}\mathbf{F}\,{}^{w}\mathbf{F}^{T}$ is the left *Cauchy-Green* deformation tensor. The copolymer's effective stress follows

$$ {}^{w}\boldsymbol{\sigma} \;=\; \frac{1}{J_w}\,{}^{w}\mathbf{F}\,{}^{w}\mathbf{P}^{\mathrm{T}} \;=\; \frac{1}{J_w}\,{}^{w}\mathbf{P}\,{}^{w}\mathbf{F}^{\mathrm{T}} \quad . \tag{2.18} $$

The effective true stress response of the RVE is calculated as the volume-weighted average of each constituent's stress contribution:

$$ \boldsymbol{\sigma} \;=\; \phi\cdot{}^{r}\boldsymbol{\sigma} \;+\; (1-\phi)\cdot{}^{g}\boldsymbol{\sigma} \;=\; \frac{\phi}{J_r}\cdot{}^{r}\mathbf{P}\,{}^{r}\mathbf{F}^{\mathrm{T}} \;+\; \frac{(1-\phi)}{J_g}\cdot{}^{g}\mathbf{P}\,{}^{g}\mathbf{F}^{\mathrm{T}} \quad . \tag{2.19} $$

Since both ${}^{w}\mathbf{F}$ and ${}^{w}\mathbf{P}$ are defined in the reference frame, the Cauchy stress tensor calculated above is expressed in terms of the local reference basis. Expression in terms a different orthogonal coordinate system requires a simple change of basis transformation:

$$ \boldsymbol{\sigma}_{\mathcal{B}} \;=\; \mathbb{Q}_{\mathcal{AB}}\,{}^{w}\boldsymbol{\sigma}_{\mathcal{A}}\,\mathbb{Q}_{\mathcal{AB}}^{T} \quad , \tag{2.20} $$

where $\mathbb{Q}_{\mathcal{AB}}$ is a proper rotation from frame $\mathcal{A}$ to frame $\mathcal{B}$.

2D Plane-Strain Application for Neo-Hookean Materials with Compressibility.
For ease of showing the solution process, the 2D plane-strain case is chosen as an example. We assume that both the rubbery and the glassy phase are amorphous and we model their stress-strain behavior as a hyperelastic neo-Hookean solid with compressibility[6]. The strain energy density function for a hyperelastic neo-Hookean material with compressibility is given by:

$$ \mathcal{U}_w = \mathrm{c}_w\,(\,{}^{w}\mathrm{I}_1 - 3\,) - \frac{\mathrm{c}_w}{2}\,\ln(J_w) + \frac{\mathrm{k}_w}{2}\,(\,J_w - 1\,)^2\,, \tag{2.21} $$

---

then as:

$$ \begin{aligned} \boldsymbol{\sigma} \;&=\; \frac{\phi}{J_r}\cdot\frac{\mathcal{U}_{\mathrm{r}}}{\partial\,{}^{r}\mathbf{F}}\,{}^{r}\mathbf{F}^{T} \;+\; (1-\phi)\cdot\frac{\mathcal{U}_{\mathrm{g}}}{\partial\,{}^{g}\mathbf{F}}\,{}^{g}\mathbf{F}^{T} \\ &=\; \phi\cdot\left[\frac{c_{\mathrm{r}}}{2\,J_{\mathrm{r}}}\,({}^{\mathrm{r}}\mathbf{B}-\mathbf{I}) + k_{\mathrm{r}}\,(J_{\mathrm{r}}-1)\,\mathbf{I}\right] + \frac{(1-\phi)}{J_g}\cdot\left[\frac{c_{\mathrm{g}}}{2\,J_{\mathrm{g}}}\,({}^{\mathrm{g}}\mathbf{B}-\mathbf{I}) + k_{\mathrm{g}}\,(J_{\mathrm{g}}-1)\,\mathbf{I}\right] \end{aligned} $$

[6]By assigning rubbery behavior to both materials, we neglect plasticity effects in the deformation of the glassy phase. However, this approximation should be sufficient up to moderate strains and for deformation modes that evolve without buckling or necking instabilities.

where w denotes the material (here $w = \mathrm{r}, \mathrm{g}$ for rubber and glass, respectively), $\mathrm{c}_w = \mu_w/2$ is one half of the shear modulus and k_w is the bulk modulus. ${}^{w}\mathrm{I}_1$ is the first invariant of the stretch tensor[7]

$$\begin{aligned} {}^{w}\mathrm{I}_1 &= trace[\,{}^{w}\mathbf{B}\,] = trace[\,{}^{w}\mathbf{F}\,{}^{w}\mathbf{F}^{T}\,] \\ &= ({}^{w}\mathrm{F}_{\mathrm{s_o s_o}})^2 + ({}^{w}\mathrm{F}_{\mathrm{s_o n_o}})^2 + ({}^{w}\mathrm{F}_{\mathrm{n_o s_o}})^2 + ({}^{w}\mathrm{F}_{\mathrm{n_o n_o}})^2 + 1\,, \end{aligned} \tag{2.22}$$

and J_w, is the volume ratio between the current and reference configurations:

$$J_w = {}^{w}\mathrm{I}_3{}^{1/2} = \det[\,{}^{w}\mathbf{F}\,] = \frac{{}^{w}\mathrm{V}}{{}^{w}\mathrm{V}_\mathrm{o}} = {}^{w}\mathrm{F}_{\mathrm{s_o s_o}} \cdot {}^{w}\mathrm{F}_{\mathrm{n_o n_o}} - {}^{w}\mathrm{F}_{\mathrm{s_o n_o}} \cdot {}^{w}\mathrm{F}_{\mathrm{n_o s_o}}\ , \tag{2.23}$$

where ${}^{w}\mathrm{I}_3$ is the third invariant of the stretch tensor. As stated, the composite strain energy density is the volume-weighted average of the individual constituents' strain energy densities:

$$\begin{aligned} \mathcal{U} &= \phi_o \cdot \mathcal{U}_\mathrm{r} + (1-\phi_\mathrm{o}) \cdot \mathcal{U}_\mathrm{g} \\ &= \phi_\mathrm{o} \cdot \left[\mathrm{c_r}\,({}^{\mathrm{r}}\mathrm{I}_1 - 3) - \frac{\mathrm{c_r}}{2}\ln(J_\mathrm{r}) + \frac{\mathrm{k_r}}{2}\,(J_\mathrm{r}-1)^2 \right] \\ &\quad + (1-\phi_\mathrm{o}) \cdot \left[\mathrm{c_g}\,({}^{\mathrm{g}}\mathrm{I}_1 - 3) - \frac{\mathrm{c_g}}{2}\ln(J_\mathrm{g}) + \frac{\mathrm{k_g}}{2}\,(J_\mathrm{g}-1)^2 \right], \end{aligned}$$

with ϕ_o the initial volume fraction of the rubbery component, and

$$J_\mathrm{r} = \overline{\mathrm{F}}_{\mathrm{s_o s_o}} \cdot {}^{\mathrm{r}}\mathrm{F}_{\mathrm{n_o n_o}} - {}^{\mathrm{r}}\mathrm{F}_{\mathrm{s_o n_o}} \cdot \overline{\mathrm{F}}_{\mathrm{n_o s_o}} \quad , \quad J_\mathrm{g} = \overline{\mathrm{F}}_{\mathrm{s_o s_o}} \cdot {}^{\mathrm{g}}\mathrm{F}_{\mathrm{n_o n_o}} - {}^{\mathrm{g}}\mathrm{F}_{\mathrm{s_o n_o}} \cdot \overline{\mathrm{F}}_{\mathrm{n_o s_o}}\ . \tag{2.24}$$

[7]For plane-strain conditions ${}^{w}\mathrm{F}_{\mathrm{k_o k_o}} = 1$ and ${}^{w}\mathrm{F}_{\mathrm{s_o k_o}} = {}^{w}\mathrm{F}_{\mathrm{n_o k_o}} = {}^{w}\mathrm{F}_{\mathrm{k_o s_o}} = {}^{w}\mathrm{F}_{\mathrm{n_o k_o}} = 0$.

Using Eqn. 2.6, two unknown components, ${}^{g}\mathrm{F}_{s_o n_o}$, ${}^{g}\mathrm{F}_{n_o n_o}$, and the corresponding determinant, $J_w = \det[{}^{g}\mathbf{F}]$, are eliminated by rewriting:

$$ {}^{g}\mathrm{F}_{s_o n_o} = \frac{\overline{\mathrm{F}}_{s_o n_o} - \phi_o \cdot {}^{r}\mathrm{F}_{s_o n_o}}{1-\phi_o} \tag{2.25} $$

$$ {}^{g}\mathrm{F}_{n_o n_o} = \frac{\overline{\mathrm{F}}_{n_o n_o} - \phi_o \cdot {}^{r}\mathrm{F}_{n_o n_o}}{1-\phi_o} \tag{2.26} $$

$$ J_g = \frac{\bar{J} - \phi_o \cdot J_r}{1-\phi_o} \, . \tag{2.27} $$

The two remaining unknowns, ${}^{r}\mathrm{F}_{s_o n_o}$ and ${}^{r}\mathrm{F}_{n_o n_o}$, are determined from Eqns. 2.14 and 2.15. The 1^{st} *Piola-Kirchhoff* stress tensor, ${}^{w}\mathbf{P}$, for a hyperelastic material w with strain energy density $\mathcal{U}_w$ is given by:

$$ {}^{w}\mathbf{P} = \frac{\partial \mathcal{U}_w}{\partial\, {}^{w}\mathbf{F}} \qquad \text{or} \qquad {}^{w}\mathrm{P}_{ij} = \frac{\partial \mathcal{U}_w}{\partial\left({}^{w}\mathrm{F}_{ij}\right)} \, , \tag{2.28} $$

which for the neo-Hookean strain energy function of Eqn. 2.21 yields:

$$ {}^{w}\mathrm{P}_{s_o s_o} = \frac{\partial \mathcal{U}_w}{\partial\, {}^{w}\mathrm{F}_{s_o s_o}} = 2\,\mathrm{c}_w \cdot \overline{\mathrm{F}}_{s_o s_o} - {}^{w}\mathrm{F}_{n_o n_o} \cdot \left[\frac{2\,\mathrm{c}_w}{J_w} + \mathrm{k}_w \cdot (J_w - 1) \right] \tag{2.29} $$

$$ {}^{w}\mathrm{P}_{n_o s_o} = \frac{\partial \mathcal{U}_w}{\partial\, {}^{w}\mathrm{F}_{n_o s_o}} = 2\,\mathrm{c}_w \cdot \overline{\mathrm{F}}_{n_o s_o} + {}^{w}\mathrm{F}_{s_o n_o} \cdot \left[\frac{2\,\mathrm{c}_w}{J_w} - \mathrm{k}_w \cdot (J_w - 1) \right] \tag{2.30} $$

$$ {}^{w}\mathrm{P}_{s_o n_o} = \frac{\partial \mathcal{U}_w}{\partial\, {}^{w}\mathrm{F}_{s_o n_o}} = 2\,\mathrm{c}_w \cdot {}^{w}\mathrm{F}_{s_o n_o} + \overline{\mathrm{F}}_{n_o s_o} \cdot \left[\frac{2\,\mathrm{c}_w}{J_w} - \mathrm{k}_w \cdot (J_w - 1) \right] \tag{2.31} $$

$$ {}^{w}\mathrm{P}_{n_o n_o} = \frac{\partial \mathcal{U}_w}{\partial\, {}^{w}\mathrm{F}_{n_o n_o}} = 2\,\mathrm{c}_w \cdot {}^{w}\mathrm{F}_{n_o n_o} - \overline{\mathrm{F}}_{s_o s_o} \cdot \left[\frac{2\,\mathrm{c}_w}{J_w} - \mathrm{k}_w \cdot (J_w - 1) \right] \tag{2.32} $$

$$ {}^{w}\mathrm{P}_{k_o k_o} = \frac{\partial \mathcal{U}_w}{\partial\, {}^{w}\mathrm{F}_{k_o k_o}} = 2\,\mathrm{c}_w \cdot {}^{w}\mathrm{F}_{k_o k_o} = 2\,\mathrm{c}_w \tag{2.33} $$

Applying equibrium Eqns. 2.14 and 2.15 we obtain:

$$ {}^{r}\mathrm{P}_{s_o n_o} = {}^{g}\mathrm{P}_{s_o n_o} \implies $$

$$2\,c_r \cdot {}^{r}F_{s_o n_o} + \overline{F}_{n_o s_o} \cdot \left[\frac{2\,c_r}{J_r} - k_r \cdot (J_r - 1) \right] = 2\,c_g \cdot {}^{g}F_{s_o n_o} + \overline{F}_{n_o s_o} \cdot \left[\frac{2\,c_g}{J_g} - k_g \cdot (J_g - 1) \right] \tag{2.34}$$

$$ {}^{r}P_{n_o n_o} = {}^{g}P_{n_o n_o} \implies$$

$$2\,c_r \cdot {}^{r}F_{n_o n_o} - \overline{F}_{s_o s_o} \cdot \left[\frac{2\,c_r}{J_r} - k_r \cdot (J_r - 1) \right] = 2\,c_g \cdot {}^{g}F_{n_o n_o} - \overline{F}_{s_o s_o} \cdot \left[\frac{2\,c_g}{J_g} - k_g \cdot (J_g - 1) \right] \tag{2.35}$$

This is a 3rd order system of nonlinear equations in ${}^{r}F_{s_o n_o}$ and ${}^{r}F_{n_o n_o}$, with the two unknowns coupled due to denominator terms J_r and J_g. The system is thus intractable and an analytical closed-form solution for the unknowns is unwieldy, unless a realistic assumption is made to decouple the unknowns and reduce the order in the equations.

For the majority of deformations these materials undergo a minimal volume change and J_w's are not expected to differ from unity considerably[8]. Thus, we can assume that $c_w/J_w \approx c_w$. The following approximation can be made with little compromising in the accuracy of numerical calculations:

$$\frac{c_w}{J_w} - k_w \cdot (J_w - 1) \approx c_w - k_w \cdot (J_w - 1) \ . \tag{2.36}$$

Hence, the system is reduced to a linear one with two equations and two unknowns, which can be solved by simple substitution. We arrive at the forthcoming closed-form solution

[8]As will be shown in the results section, this is true even up to moderate strains, and in particular, up to strain levels at which instabilities begin to occur.

for the distribution of deformation within each phase[9][10]:

$$
\begin{aligned}
{}^{r}F_{s_o s_o} &= \overline{F}_{s_o s_o} & {}^{g}F_{s_o s_o} &= \overline{F}_{s_o s_o} \\
{}^{r}F_{n_o s_o} &= \overline{F}_{n_o s_o} & {}^{g}F_{n_o s_o} &= \overline{F}_{n_o s_o} \\
{}^{r}F_{n_o n_o} &= \frac{G \cdot A + B \cdot C}{E \cdot A - B^2} & {}^{g}F_{n_o n_o} &= \frac{\overline{F}_{n_o n_o} - \phi_o \cdot ({}^{r}F_{n_o n_o})}{1 - \phi_o} \\
{}^{r}F_{s_o n_o} &= \frac{C + B \cdot ({}^{r}F_{n_o n_o})}{A} & {}^{g}F_{s_o n_o} &= \frac{\overline{F}_{s_o n_o} - \phi_o \cdot ({}^{r}F_{s_o n_o})}{1 - \phi_o}
\end{aligned}
\tag{2.37}
$$

where:

$$
\begin{aligned}
B &= \left[k_r + k_g \left(\frac{\phi_o}{1 - \phi_o} \right) \right] \cdot \overline{F}_{s_o s_o} \cdot \overline{F}_{n_o s_o} \\
A &= 2 \left[c_r + c_g \left(\frac{\phi_o}{1 - \phi_o} \right) \right] + \left[k_r + k_g \left(\frac{\phi_o}{1 - \phi_o} \right) \right] (\overline{F}_{n_o s_o})^2 \\
E &= 2 \left[c_r + c_g \left(\frac{\phi_o}{1 - \phi_o} \right) \right] + \left[k_r + k_g \left(\frac{\phi_o}{1 - \phi_o} \right) \right] (\overline{F}_{s_o s_o})^2 \\
C &= \left(\frac{2 c_g}{1 - \phi} \right) \cdot \overline{F}_{s_o n_o} - \left\{ k_g \left(\frac{\overline{J} - 1}{1 - \phi_o} \right) + \left[k_r + k_g \left(\frac{\phi_o}{1 - \phi_o} \right) \right] + 2 (c_r - c_g) \right\} \cdot \overline{F}_{n_o s_o} \\
G &= \left(\frac{2 c_g}{1 - \phi_o} \right) \cdot \overline{F}_{n_o n_o} + \left\{ k_g \left(\frac{\overline{J} - 1}{1 - \phi_o} \right) + \left[k_r + k_g \left(\frac{\phi_o}{1 - \phi_o} \right) \right] + 2 (c_r - c_g) \right\} \cdot \overline{F}_{s_o s_o}
\end{aligned}
$$

In 2D, the coordinate system rotation of Eqn. 2.8 corresponds to:

$$
\begin{aligned}
\overline{F}_{s_o s_o} &= \overline{F}_{11} \cdot \cos^2\theta + (\overline{F}_{12} + \overline{F}_{21}) \cdot \cos\theta \cdot \sin\theta + \overline{F}_{22} \cdot \sin^2\theta \\
\overline{F}_{s_o n_o} &= \overline{F}_{12} \cdot \cos^2\theta - (\overline{F}_{11} - \overline{F}_{22}) \cdot \cos\theta \cdot \sin\theta - \overline{F}_{21} \cdot \sin^2\theta \\
\overline{F}_{n_o s_o} &= \overline{F}_{21} \cdot \cos^2\theta - (\overline{F}_{11} - \overline{F}_{22}) \cdot \cos\theta \cdot \sin\theta - \overline{F}_{12} \cdot \sin^2\theta \\
\overline{F}_{n_o n_o} &= \overline{F}_{22} \cdot \cos^2\theta - (\overline{F}_{12} + \overline{F}_{21}) \cdot \cos\theta \cdot \sin\theta + \overline{F}_{11} \cdot \sin^2\theta
\end{aligned}
$$

[9]Note that due to the aforementioned assumption, in expressions C and G term $(c_r - c_g)$ appears in place of the term $\left(\frac{c_r}{J_r} - \frac{c_g}{J_g} \right)$, which depends on the unknowns.

[10]The solution precedure presented above was based on equilibrium requirements on the interface in terms of the 1st *Piola-Kirchhoff* stress. True stress equilibrium could have been used instead as stated in Eqns. 2.7. The true stress expression though, is far more complex than that of the 1st *P-K* stress. The extra multiplications required in calculating the true stress (see eqn. 2.17) increase the coupling among the unknowns and the order of the nonlinear system that needs to be solved. It is doubteful that the given assumption alone can render the resulting system tractable. A solution is therefore much less cumbersome to obtain as presented here in terms of 1st *P-K* stress considerations in the reference frame.

where θ, the angle of rotation from the fixed global frame, $\mathcal{G}$, to the interface-tied local frame in the reference (undeformed) configuration, $\mathcal{R}$, corresponds here to the initial orientation of the undeformed microstructure w.r.t. a reference axis. As anticipated, the distribution of deformation between the layers and the relevant intralyer deformation trade-offs (*i.e.*, layer shear *vs* dilation) depend on the initial volume fractions $\phi_{\mathrm{r}} = \phi_o$ and $\phi_{\mathrm{g}} = (1 - \phi_o)$, and on the interlayer property contrast between shear and bulk moduli, c_w and k_w .

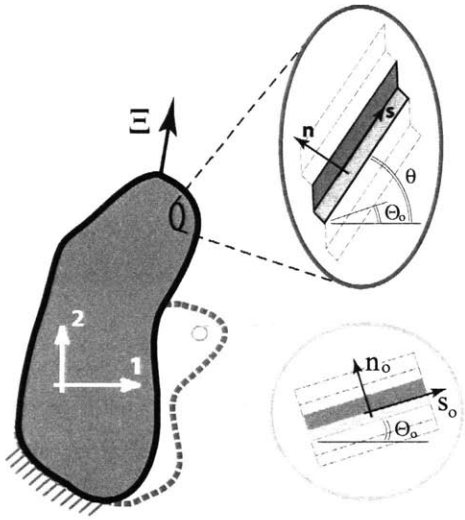

Figure 2-2: Schematic of a generic boundary value problem.

The analytical constitutive model was numerically implemented as a user subroutine (VUMAT) in ABAQUS Explicit for single-element calculations on the BCP's mechanical response to different types of loading. The analytical model's predictions are compared to corresponding micromechanical unit-cell calculations. The results and the details of unit-cell modeling are presented in the following section

2.2 Finite Element-based Micromechanical Modeling and Results for Neo-Hookean phase behavior

The constitutive model is used to describe the BCP response at different loading orientations to the undeformed lamellae under three types of plane-strain loading: uniaxial tension, isochoric biaxial deformation, and simple shear. The constitutive model was implemented

in ABAQUS through a user subrutine (vumat) and its numerical predictions from single-element calculations are compared to FE-based micromechanical unit-cell results. The quantities used to compare the two models are: the effective BCP stress response, the microdeformation gradient and the stress of each constituent, the evolution of volume ratios, and the lamellar tilt angle.

2.2.1 Unit-cell calculations

The Representative Volume Element (RVE)

We are interested in monitoring microstructural kinematic quantities in the absense of structural instabilities (*i.e.*, no layer buckling or necking), and thus it suffices to model the oriented lamellar microstructure of Fig.1-7 with a 2-D plane-strain *bilayer* RVE such as the one shown in Fig. 2-1. Since no layer buckling is present it is both sufficient and computationally efficient to use one element per layer to capture the evolution of microdeformation gradients ${}^{r}\overline{\mathbf{F}}$ and ${}^{g}\overline{\mathbf{F}}$[11]. The relative volume fractions of the constituents is determined by the thickness of each layer. Here, the BCP of interest contains 43vol% PS in its undeformed state. Both constituents are modeled as a neo-Hookean hyperelastic material and for this reason are discretized with biquadratic, plane-strain, hybrid elements.

To verify numerically that the developed continuum description reproduces the distribution of the deformation field between the engaged layers, the finite-element unit-cell RVE was subjected to various characteristic deformation modes and the calculated micromechanical deformation quantities are compared to corresponding predictions from the analytical continuum model in the next section. In the following two subsections we describe: the type of perodic boundary conditions that enforced on the RVE, the application of a generic macroscopic deformation, and the process to calculate the effective stress-stretch

[11]The deformation micromechanics are particularly sensitive to material and structural instabilities. It has been shown that, depending on the loading orientation either cascade micronecking or columnar microbuckling of the glassy lamellae are the dominant material and structural instabilities responsible for the nonlinearity in the macroscopic stress response of the given materials. In order to capture the particular material and structural instabilities which for different loading conditions dominate the deformation at the microstructural level , the height-to-length RVE-aspect-ratio and the mesh density are critical. Depending on the anticipated instability, a single long bi-layer RVE might sufficient or an RVE with several layer repetitions might be necessary.

response of the RVE.

Boundary Conditions for Different Loading Cases.

Periodic boundary conditions were enforced on opposite facing boundaries of the RVE (Fig.2-1):

$$\begin{aligned} \mathbf{u}|_{BC} - \mathbf{u}|_{AD} &= \mathbf{u}|_B - \mathbf{u}|_A \\ \mathbf{u}|_{DC} - \mathbf{u}|_{AB} &= \mathbf{u}|_D - \mathbf{u}|_A \\ \mathbf{u}|_A &= \mathbf{0} \end{aligned} \qquad \begin{aligned} u_1|_{BC} - u_1|_{AD} &= u_1|_B - u_1|_A \\ u_2|_{BC} - u_2|_{AD} &= u_2|_B - u_2|_A \\ u_1|_{CD} - u_1|_{AB} &= u_1|_D - u_1|_A \\ u_2|_{CD} - u_2|_{AB} &= u_2|_D - u_2|_A \\ u_1|_A = u_2|_A &= 0 \end{aligned} \tag{2.38}$$

Given any generic macroscopic deformation gradient $\overline{\mathbf{F}}$, the displacement of RVE node C should follow the relation:

$$\mathbf{x}|_C = \overline{\mathbf{F}}_{\mathcal{R}}\,\mathbf{X}|_C \Longrightarrow \mathbf{u}|_C = \left(\overline{\mathbf{F}}_{\mathcal{R}} - 1\right)\mathbf{X}|_C = \overline{\mathbf{H}}_{\mathcal{R}}\,\mathbf{X}|_C$$

Noting that here u_1 corresponds to the displacement in direction s_o, and u_2 to the diplacement in direction n_o, the above relation can be rewritten as:

$$\begin{aligned} u_1|_C &= (\overline{F}_{s_o s_o} - 1)\cdot X_C + \overline{F}_{s_o n_o}\cdot Y_C \\ u_2|_C &= \overline{F}_{n_o s_o}\cdot X_C + (\overline{F}_{n_o n_o} - 1)\cdot Y_C \end{aligned} \tag{2.39}$$

For the simple parallelogram RVE geometry used here, $X_C = L$ (RVE length) and $Y_C = H$ (RVE height).

Operationally, the evolving components of the macroscopic deformation gradient $\overline{\mathbf{F}}_{\mathcal{R}}$ can not be applied directly to the RVE nodee. Instead, two dummy nodes $\mathcal{N}_1$ and $\mathcal{N}_2$ with no physical connection to the material are used as a vehicles on which to apply the components of $\overline{\mathbf{F}}_{\mathcal{R}}$ as displacements:

$$\begin{aligned} u_1|_{\mathcal{N}_1} &= \overline{F}_{s_o s_o} \\ u_2|_{\mathcal{N}_1} &= \overline{F}_{s_o n_o} \end{aligned} \qquad \begin{aligned} u_1|_{\mathcal{N}_2} &= \overline{F}_{n_o s_o} \\ u_2|_{\mathcal{N}_2} &= \overline{F}_{n_o n_o} \end{aligned} \tag{2.40}$$

where the components of $\overline{\mathbf{F}}_{\mathcal{R}}$ are given in Eqn. 2.38. The dunmmy node displacements are then tied to the displacements of RVE node C through the following equations:

$$\begin{aligned} \mathrm{u}_1|_C &= (\mathrm{u}_1|_{\mathcal{N}_1} - 1) \cdot \mathrm{X}_C + \mathrm{u}_2|_{\mathcal{N}_1} \cdot \mathrm{Y}_C \\ \mathrm{u}_2|_C &= \mathrm{u}_1|_{\mathcal{N}_2} \cdot \mathrm{X}_C + (\mathrm{u}_2|_{\mathcal{N}_2} - 1) \cdot \mathrm{Y}_C \end{aligned} \tag{2.41}$$

The last set of equations (eqns.4.2.1) combined with eqns.2.38 tie the macroscopic deformation gradient $\overline{\mathbf{F}}$ to the displacements of every node within the RVE, and thus, drive the RVE deformation.

The RVE is subjected to three types of plane-strain loading: tension, isochoric extension, and simple shear. The macroscopic deformation gradients for these three loading conditions, expressed in a fixed global reference frame $\mathcal{G}$, are:

- *Plane-strain Tension:*

$$\overline{\mathbf{F}}_{\mathcal{G}} = \lambda\, \mathbf{e}_1 \otimes \mathbf{e}_1 + 1\, \mathbf{e}_3 \otimes \mathbf{e}_3 \tag{2.42}$$

  The plane-strain condition is enforced in direction-3 and λ is the applied stretch in the direction of tension. Direction-2 is traction-free and its stretch is calculated from the boundary constraints.

- *Plane-strain Isochoric (Volume Preserving) Extension:*

$$\overline{\mathbf{F}}_{\mathcal{G}} = \lambda\, \mathbf{e}_1 \otimes \mathbf{e}_1 + \lambda^{-1}\, \mathbf{e}_2 \otimes \mathbf{e}_2 + 1\, \mathbf{e}_3 \otimes \mathbf{e}_3 \tag{2.43}$$

- *Plane-strain Simple Shear:*

$$\overline{\mathbf{F}}_{\mathcal{G}} = 1\, \mathbf{e}_1 \otimes \mathbf{e}_1 + \tan(\gamma)\, \mathbf{e}_1 \otimes \mathbf{e}_2 + 1\, \mathbf{e}_2 \otimes \mathbf{e}_2 + 1\, \mathbf{e}_3 \otimes \mathbf{e}_3 \tag{2.44}$$

  where γ is the applied shear angle.

Eqn. 2.8 is used to transform the components of the applied macroscopic deformation gradient $\overline{\mathbf{F}}_{\mathcal{G}}$ from the global fixed frame of reference $\mathcal{G}$ to the local (layer-tied) frame $\mathcal{R}$ (Eqn. 2.8), as needed for the application of deformation.

Application of Deformation.

Given the various periodic boundary conditions described above for different loading cases, the next step is to operationally specify the imposed macroscopic deformation gradient, $\overline{\mathbf{F}}$, within this finite element analysis. $\overline{\mathbf{F}}$ is imposed following the precedure introduced by Danielsson *et al.* [50]. The components of the macroscopically applied displacement gradient, $\overline{\mathbf{H}} = \overline{\mathbf{F}} - 1$, are entered in the finite-element RVE models as displacements applied on two "*dummy*" nodes[12]. The schematic of Fig.2-1 illustrates this approach. The *dummy* nodes are external to the RVE and do not correspond material points, but their displacements are tied to the displacements of the RVE nodes through specific equation contraints (Eqns. 2.38). The RVE's reaction to the applied deformation is in this way concentrated in *reaction forces* at the dummy nodes, $[\Xi]_{ij}$, in the directions of the imposed displacements (with i denoting the dummy node and j the direction of the reaction force). The reaction forces are monitored and used to calculate the effective true-stress response of the RVE using the *"Principle of Virtual Work"*. According to the *PVW*, any increment of *virtual* work supplied to the material externally must equal the corresponding change in the internal *virtual* energy stored in the material:

$$\delta(\mathcal{W}^{\text{ext}}) = \delta(\mathcal{W}^{\text{int}}) \quad . \tag{2.45}$$

The external virtual work here is equal to:

$$\delta(\mathcal{W}^{\text{ext}}) = \sum_{i,j=1}^{2} \Xi_{ij} \cdot \delta(\overline{\mathrm{H}}_{ij}) = \sum_{i,j=1}^{2} \Xi_{ij} \cdot \delta(\overline{\mathrm{F}}_{ij} - 1_{ij}) = \sum_{i,j=1}^{2} \Xi_{ij} \cdot \delta(\overline{\mathrm{F}}_{ij}) \quad , \tag{2.46}$$

where $\overline{\mathrm{H}}_{\mathrm{ij}} = \frac{\partial u_i}{\partial X_j}$ is the displacement gradient, Ξ_{ij} the reaction force on dummy node i in the j-direction, and $\mathbf{1} = \delta_{\mathrm{ij}}$ the identity matrix.

The internal virtual work is calculated as the volume integral of the product between a

[12]For 3D RVEs the deformation gradients consist of nine elements. Thus, three *dummy* nodes are needed to apply all nine deformation components. For *dummy* node-1 for *e.g.*, the imposed displacements in the x-, y-, and z-directions, respectively, are: $u_1 = \overline{\mathrm{H}}_{11} = \overline{\mathrm{F}}_{11} - 1$, $v_1 = \overline{\mathrm{H}}_{12}$, and $w_1 = \overline{\mathrm{H}}_{13}$.

work conjugate pair of stress and strain measures:

$$\delta(\mathcal{W}^{\text{int}}) = V_o \cdot \overline{\mathbf{P}} : \delta(\overline{\mathbf{F}}) = \sum_{i,j=1}^{2} \overline{\mathrm{P}}_{ij} \cdot \delta(\overline{\mathrm{F}}_{ij}) \quad , \tag{2.47}$$

here using the work conjugate pair of the applied macroscopic deformation gradient, $\overline{\mathbf{F}}$, and the 1st *Piola-Kirchhoff* stress, $\overline{\mathbf{P}}$, both of which are defined in the reference configuration where the RVE's volume is V_o.

Substitution in Eqn.2.45 gives the relation between reaction forces on dummy nodes and the corresponsing 1st *Piola-Kirchhoff* stress response of the RVE:

$$\overline{\mathbf{P}} = \frac{1}{\mathrm{V_o}} \boldsymbol{\Xi} \qquad \text{or} \qquad \overline{\mathrm{P}}_{ij} = \frac{1}{V_o} \cdot \Xi_{ij} \quad . \tag{2.48}$$

The true stress response of the RVE, which represents the effective BCP stress response, $\overline{\boldsymbol{\sigma}}$, follows then as:

$$\overline{\boldsymbol{\sigma}} = \frac{1}{\bar{J}} \overline{\mathbf{P}}\, \overline{\mathbf{F}}^T = \frac{1}{\mathrm{V}} \boldsymbol{\Xi}\, \overline{\mathbf{F}}^T \quad . \tag{2.49}$$

where $\bar{J} = \det[\overline{\mathbf{F}}] = V/V_o$ is the volume ratio between the deformed and undeformed configurations[13]. The macroscopic logarithmic strain tensor is calculated from $\overline{\mathbf{E}} = ln\overline{\mathbf{U}}$, with $\overline{\mathbf{U}} = \sum_{i=1}^{2} \lambda_i\, \mathbf{e}_i \otimes \mathbf{e}_i$, the right stretch tensor calculated from the polar decomposition of the macroscopic deformation gradient, $\overline{\mathbf{F}} = \overline{\mathbf{R}}\,\overline{\mathbf{U}}$ [14].

2.2.2 Results:

Constitutive Model and Numerical Micromechanical Model

The analytically derived constitutive model for the lamellar BCP is now used to predict the mechanical behavior when subjected to various macroscopic loading conditions. Three types of loading conditions will be studied: plane-strain tension, plane-strain isochoric extension, and plane-strain simple shear. These loading conditions will be applied to the BCP

[13]For 2D analyses, $\bar{J}$ simply corresponds to the change in area.

[14]For the loading cases we will explore here -plane-strain tension, plane-strain biaxial deformation, and plane-strain simple shear- $\overline{\mathbf{R}} = \mathbf{I}$.

lamellar material at different angles with respect to the lamellae plane. The constitutive model results will be compared to results obtained for the same loading conditions applied to the finite element based discrete micromechanical model. Results will be presented in terms of macroscopic quantities (the effective stress-strain behavior of the lamellar material) and microscopic quantities (the micro-deformation gradient in each phase as a function of applied macroscopic strain, the stress components within each phase as a function of macroscopic strain, the lamellar tilt angle as a function of macroscopic strain). Results will be reported in detail for three cases: imposing the macroscopic loading with lamellae at initial orientations of 0^o, 45^o, and 90^o, followed by overall comparisons which include additional off-axis loading conditions.

Plane-Strain Extension

Plane-strain tension is enforced by imposing a stretch in a prescribed direction, while restraining the through-thickness deformation of the RVE ($\overline{F}_{33} = 1$) and leaving the third orthonormal face to be traction-free. The stretch in the traction-free direction is then calculated by satisfying the applied boundary conditions[15].

Plane-Strain Extension Normal to the Lamellar Plane: As seen from the components of the microdeformation gradients in Fig. 2-3, for loading normal to the underlying microlayers, deformation is accommodated at the microstructural level solely by layer dilatation since the only non-zero component in both microdeformation gradients is the component coresponding to deformation normal to the layer-plane, ${}^{w}F_{n_o n_o}$. Dilation within rubber is however much higher than in the glassy phase, due to the property (bulk modulus) contrast between the two phases, and is in fact maximized at this orientation. No layer tilting is observed (${}^{w}F_{n_o s_o} = 0$) and hence, no layer shear (${}^{w}F_{s_o n_o} = 0$). Due to the mismatch in the Poisson effect between the two layers, rubber layers are contrained in their lateral iso-

[15]The model predicts accurately the deformation micromechanics and the stress response for the case of uniaxial tension. However, only component $\overline{F}_{11}$ is specified in the applied macroscopic deformation gradient, $\overline{\mathbf{F}}$,, while the remaining components are solved for. This results in minor discrepancies between the predicted from the constitutive model $\overline{F}_{12}$, $\overline{F}_{21}$, and $\overline{F}_{22}$ components and those calculated with the unit-cell. For both of the other two studied cases of plane-strain tension and plane-strain simple shear, the macroscopically imposed deformation gradient, is fully prescribed. Therefore, the corresponding calculated components overlap completely with the continuum model's predictions.

choric contraction by the glassy layers, thus experiencing a state of volumetric extension, while glassy layers experience contraction. This is evidenced quantitatively by the tensile in-plane deformation component for the rubber phase, ${}^{r}F_{s_o s_o} > 1$, and the compressive corresponding component for the glassy phase, ${}^{g}F_{s_o s_o} < 1$. The effective BCP stress response (Fig. 2-4) for loading in this direction is therefore dominated by the bulk modulus of rubber.

Plane-Strain Extension Tangential to the Lamellar Plane: For loading in a direction tangential to the underlying morphology, the microdeformation gradient component which correspond to in-plane deformation for the underlying layers is maximized and equals the macroscopically applied stretch ${}^{g}F_{s_o s_o} = {}^{r}F_{s_o s_o} = \overline{F}_{11} = \lambda$. No layer tilting or shear occur (${}^{w}F_{n_o s_o} = 0$ and ${}^{w}F_{s_o n_o} = 0$, respectively), and deformation is accommodated by layer extension alone. For this orientation, the stress contribution of glassy layers to the effective BCP resposne is maximized, thus resulting in the stiffest among orientations stress response, since the tensile modulus of glass is much higher than both the shear and bulk moduli of rubber. The isochoric deformation of rubber is not constrained in this case; as can be seen in Fig. 2-3, ${}^{r}F_{n_o n_o} = ({}^{r}F_{s_o s_o})^{-1}$ continuously.

Plane-Strain Extension at 45° to the Lamellar Plane: Loading diagonally to the underlying layers results in layer tilting (${}^{w}F_{n_o s_o} > 0$) and gradual alignment of the microstructure with the loading axis, as seen for the evolution of θ in Fig. 2-6. The off-axis orientation in this case results in the accommodation of applied deformation by a combination of layer extension, shear, and dilation, as can respectively be inferred from the numerical values of components ${}^{w}F_{s_o s_o}$, ${}^{w}F_{s_o n_o}$, and ${}^{w}F_{n_o n_o}$. The stress response is therefore due to the combined contribution of the previous deformation modes. By comparing the shear deformation components in the microdeformation gradients of the two phases, the shear response of rubber is much more prominent than that of glass (${}^{r}F_{s_o n_o} > {}^{r}F_{s_o n_o}$). The same holds for the normal components ${}^{r}F_{n_o n_o} > {}^{g}F_{n_o n_o}$, while extension is minimal for both phases (${}^{w}F_{n_o n_o} \approx 1$). Deformation is therefore accommodated by rubber shear and dilation. The shear modulus of the rubber phase is much less than both its bulk modulus and the tensile modulus of the glassy phase. Therefore, the effective stress response of the BCP for this loading orientation appears more compliant than for loading normal or tangentially to the

underlying layers as seen in Fig. 2-4.

Plane-Strain Extension at various angles to the Lamellar Plane: Similar to what has been described for diagonal loading, for off-axis loading orientations (other than normal or coaxial with the underlying morphology), the imposed displacement causes layer tilting, which gradually aligns the underlying morphology with the loading direction. As a result, the imposed deformation is accommodated by different amounts of layer shear, dilation and extension, depending on the initial orientation of the underlying layers. Three orientation-dependent micromechanical deformation mechanisms can be identified from the studied micromechanics and as can be identified by the orientation dependent-stiffness of the BCP in Fig. 2-5: *(i)* for loading orientations between 0^o and 30^o, *(ii)* for loading orientations in the $30^o - 70^o$ range, and *(iii)* for loading at angles in the range of $75^o - 90^o$ to the underlying layers.

For orientation angles less than 30^o to the loading direction, the least rotations are required to align the underlying microstructure with the loading axis. Thus, for orientations between 0^o and 30^o a high degree of alignment is achieved (the final orientation θ (Fig2-6) is the lowest among all orientations) much earlier than for other orientations. Due to this alignment with the loading axis, the BCP accommodates the imposed deformation through layer tension as seen from the in-plane tensile microdeformation components ${}^{w}F_{s_o s_o}$ in Fig.2-3, which for these orientations attain positive (tensile) values. The glassy layer's contribution to in-plane shear is the least observed among all orientaions as seen from the ${}^{g}F_{s_o n_o}$ plots in Fig. 2-3, while rubber layers undergo the highest observed shear deformation as the corresponding shear component ${}^{r}F_{s_o n_o}$ attains the highest values among all orientations (Fig.2-3). The dilatation component for rubber, ${}^{r}F_{n_o n_o}$, even though substantial, is for small angles the least observed (Fig.2-3). Thus, for orientations in the range $0^o - 30^o$ the BCP accommodates deformation predominantly through glassy layer tension and rubber layer shear. The stiffer for these orientations BCP stress response, Σ_{11}^{BCP}, (also see Fig.2-5 for the tensile modulus E_{BCP}) can therefore be attributed to the glassy phase's tensile behavior, which is far stiffer and thus more prominent than the shear and tensile contribution of rubber.

The 30^o-direction to loading is the *"break-even"* point for the projected local tensile

component; no layer tension corresponds to this orientation (${}^{w}F_{s_o s_o} \approx 1$), while at angles higher than 30^o the in-plane deformation component ${}^{w}F_{s_o s_o}$ turns compressive. Layer tilting is higher as can be seen from the corresponding ${}^{w}F_{n_o s_o}$ components, but high alignment with the loading direction -as for $0^o - 30^o$ orientations- is not attained as seen from the final orientation θ in Fig.2-6. For orientations within the $30^o - 75^o$ range, the imposed deformation is accommodated by increasing layer rotation and shear, and rubber dilation (increasing ${}^{w}F_{n_o s_o}$, ${}^{w}F_{s_o n_o}$, and ${}^{r}F_{n_o n_o}$ values). The additional tilting results in further layer shear for both phases (see${}^{w}F_{s_o n_o}$ components in Fig. 2-3). However, accommodating additional deformation by glassy layer shear is energetically costlier than by rubber dilatation. The tilting rate is thus gradually decreasing, as seen from the tilting component ${}^{w}F_{n_o s_o}$, and layer rotation saturates at earlier stretches for this orientation range (see Fig. 2-6). Therefore, the determining deformation mechanism for the given range of material orientations is such that the stress response results from a trade-off between the shear contribution of both phases and the volumetric response of rubber. The possible combinations of these deformation modes result in equally compliant combinations. Hence, any observed variations in the initial tensile modulus, E_{BCP}, and the overall effective stress response, Σ_{11}^{BCP}, are minimal for the given orientations.

For orientations higher than about 70° ($\rightarrow 90^o$), large layer rotations to achieve alignment with the loading axis are not possible, and the imposed deformation is thus accommodated mainly by dilation of the rubber layers as can also be inferred from the microdeformation components ${}^{w}F_{n_o n_o}$. As already described, for the extreme case of loading at 90^o, layer tilting does not occur and dilation within rubber is maximized.

The constitutive model predicts accurately the orientation-dependent BCP deformation micromechanics and the resulting anisotropy in the BCP effective stress-stretch response as shown in Fig.2-4. The initial slopes of the $\Sigma_{11}^{BCP} - \lambda$ curves correspond to the effective tensile modulus E_{θ}^{BCP}. The predicted θ-dependence is in excellent agreement with the numerical unit-cell results and with experimental data from Allan and Arridge []. For orientations in the range of 25° – 75° the initial deformation is accommodated primarily through shear in the softer rubbery layers. This results in the most compliant initial stress responses. Similarly, for loading in close alignment with the BCP microstructure ($\theta \rightarrow 0^o$),

the effective material stiffness reduces to the volume-fraction-weighted stiffness of the hard glassy layers (with a negligible contribution from rubber). With increasing misalignment the deformation ceases to be completely tensile and the stiffness modulus decreases dramatically due to the increasing participation of rubber shear in the deformation response. For loading near-normal to the layers deformation occurs through volumetric expansion of the rubber phase, due to the lateral constraint imposed by glassy layers on the isochoric deformation of rubber. Therefore, the effective composite modulus depends highly on the bulk modulus of the rubber phase. Since the rubber is modeled as near-incompressible, its resistance to volumetric deformation is much higher than that to shear; hence, the increased effective modulus for loading directions near normal to the layers ($\theta \rightarrow 90^o$).

The model also predicts accurately the large strain response of the material (Fig.2-4). For intermediate orientations the evolution in layer tilting allows for additional shear in the rubber layer, hence the tangent modulus gradually reduces with increasing stretch. On the other hand, for loading directions near-parallel to the lamellae, layer rotation results in firmer alignment between the load and the glassy constituent, which results in a gradually increasing tangent modulus and a stiffer stress response. The model's predictions are excellent for all loading orientations, but for perfect or near perfect alignment of the microstructure with the stretching direction (0^o). In this case the model overpredicts the reduction in layer thickness for both phases (${}^{r}\mathrm{F}_{n_o n_o}$ and ${}^{g}\mathrm{F}_{n_o n_o}$). This is an inherent handicap, due to the approximation of negligible volume change ($J_w \approx 1$) used in an intermediate stage during model-derivation. Volume changes are not however negligible for stretch values higher than $\lambda = 1.2$, as seen from unit-cell calculations in Fig.2-7, while the projected local tensile component ${}^{g}\mathrm{F}_{s_o s_o}$ is maximized at 0^o. For loading parallel to layers, the volume change reduces to: $J_w = {}^{w}\mathrm{F}_{s_o s_o} \cdot {}^{w}\mathrm{F}_{n_o n_o}$. Neglecting the significant volume increase is equivalent to enforcing $J_g = 1$. This causes the largest (among orientations) error in calculating ${}^{g}\mathrm{F}_{n_o n_o}$. With J_g underestimated, the predicted in-plane stress contribution of the glassy layers, ${}^{g}\sigma_{11}$, (Eqn.2.17) is exaggerated. This in turn compromises the model's prediction for the effective BCP stress response at 0^o-loading, which depends on the tensile response of the glassy phase. A similar discussion is valid for loading orientations at 90^o to the layers. The effect however, is not as detrimental because the effective stress response in

this case is determined by the volumetric behavior of the rubber phase, which is far more compliant than the response of glassy layers to in-plane tension. Thus, for 90^o loading the model's predictions remain very reasonable [16]

Plane-Strain Isochoric Biaxial Deformation

Isochoric plane-strain biaxial deformation is applied by imposing a macroscopic stretch $\overline{F}_{11} = \lambda$ in one direction and a stretch of $\overline{F}_{22} = \lambda^{-1}$ in the transverse direction, as shown in Fig.??, while restraining the through-thickness deformation of the RVE ($F_{33} = 1$ or $\epsilon_{33} = 0$), such that the total composite volume is kept constant during deformation ($\overline{J} = 1$). This deformation condition will necessarily result in a multiaxial macroscopic stress. The current case study offers additional verification for the constitutive model's performance. However, it is more interesting to contrast isochoric deformation results to observations from plane-strain extension in order to evaluate how the imposed lateral deformation component λ^{-1} affects the microdeformation mechanisms.

Plane-Strain Isochoric Biaxial Deformation with Principal Stretch Direction Normal to the Lamellar Plane: The response to uniaxial extension in the direction normal to layers is distinctly characterized by rubber's response to volumetric extension. The lateral BCP contraction under uniaxial plane-strain extension is not entirely isochoric due to the glassy constituent's contrain on the deformation of rubber layers. Therefore, the applied isochoric component, $\overline{F}_{22} = \lambda^{-1}$, corresponds to imposing a larger -and for this reason compressive- lateral contraction than what would occur naturally under axial tension (compare the coresponding in-plane deformation components ${}^{w}F_{s_o s_o}$ in Figs. 2-3 and 2-8). In addition, plane-strain unidirectional extension results in volumetric expansion for the composite ($\bar{J} > 1$), and thus, an isochoric deformation gradient alleviates the (normal) dilative pressure which would develop otherwise due to the volumetric extension of rubber layer. It should also be noted that for loading normal to layers (90^o) $\sigma_{nn} = \Sigma_{11}$. The result

[16]It should be noted here that beyond stretches of 1.2 ($\epsilon = 20\%$), instabilities such as microbuckling and micronecking change the microstructure. Thus the current model would a-priori be an inaccurate description of the morphology and the behavior at such stretch levels. However, the post-buckling deformation behavior is shear-based, and therefore, the assumption for negligible volume change is still a valid approximation. Thus, the constitutive model remains a very good description, however it may be enhanced with a criterion for the initiation of layer buckling.

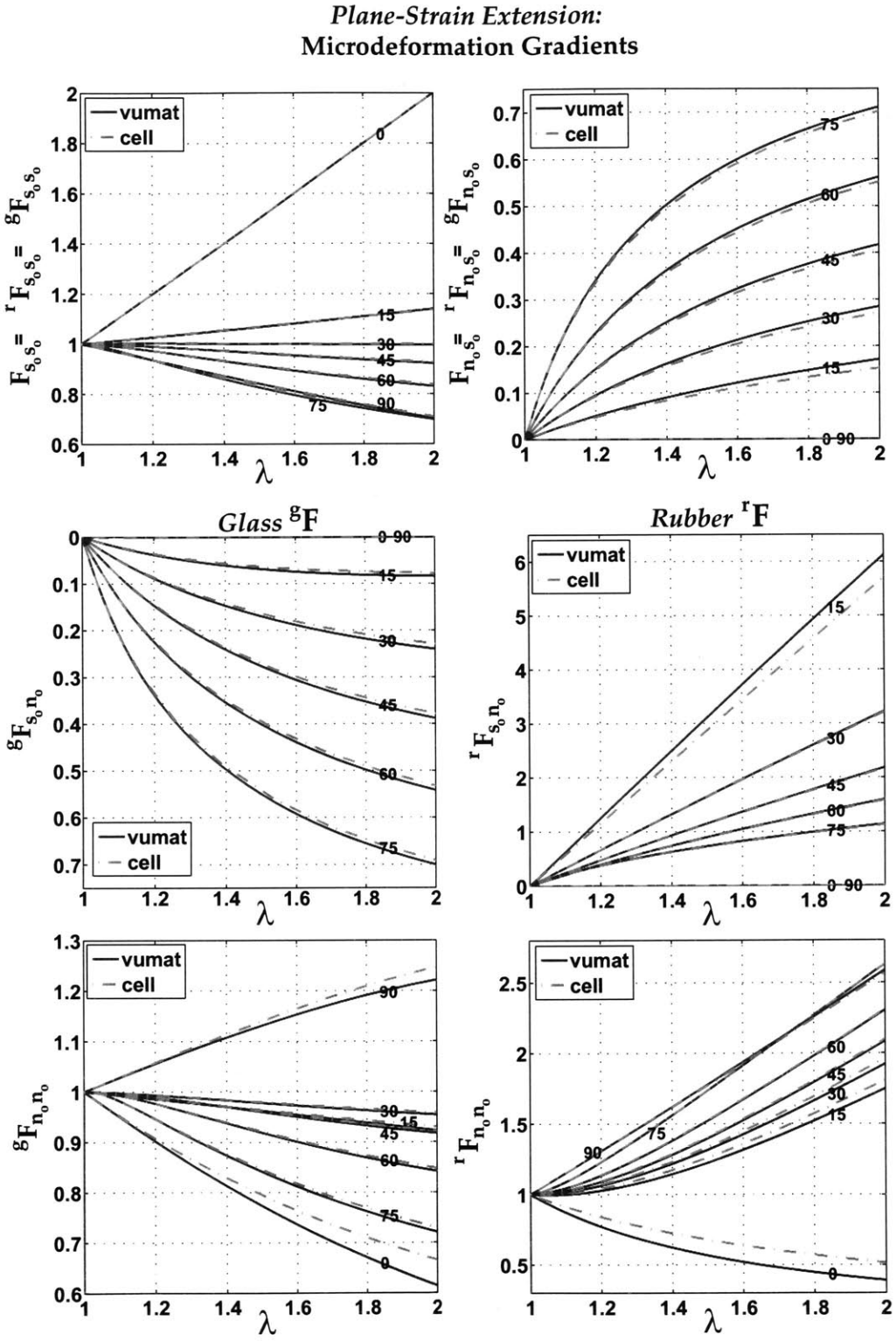

Figure 2-3: *Plane-strain Extension*: Constitutive Model predictions (–) and Unit-Cell calculations (- -) for the microdeformation gradients ${}^{r}\mathbf{F}$ and ${}^{g}\mathbf{F}$.

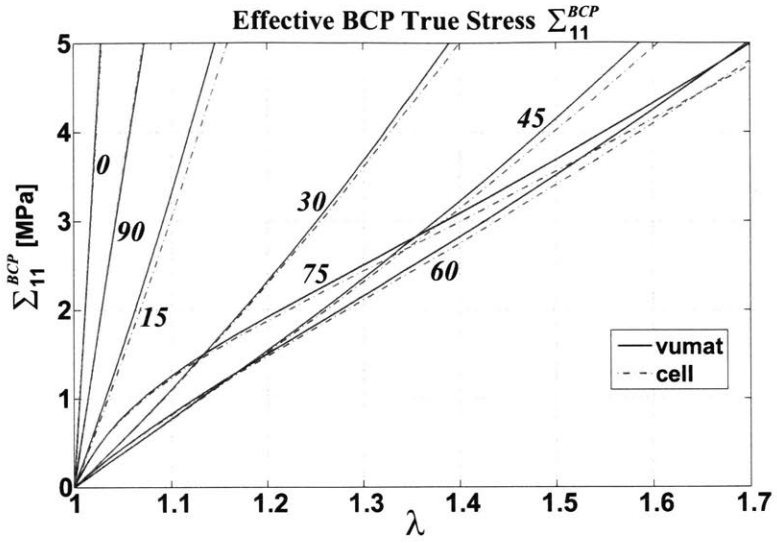

Figure 2-4: *Plane-strain Extension:* Constitutive Model predictions (–) and Unit-Cell calculations (- -) for the effective stress response in the direction of loading, Σ_{11}. Details of the stress response at small stretches are easier to view in the bottom figure.

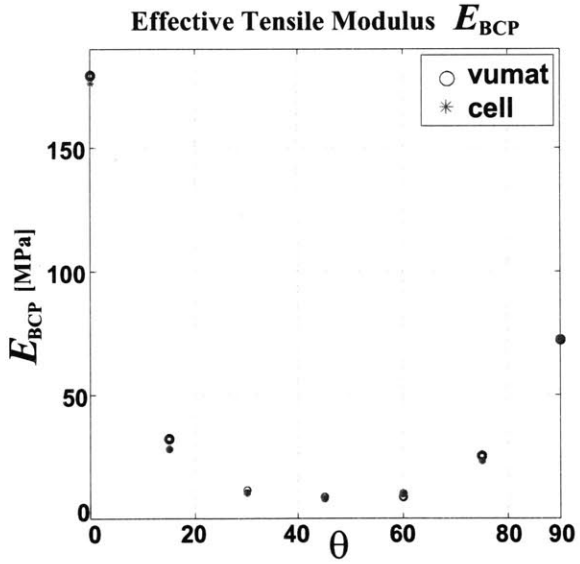

Figure 2-5: *Plane-strain tension:* Constitutive Model predictions (–) and Unit-Cell calculations (- -) for the effective tensile modulus, E_θ, for different loading directions to the microstructure.

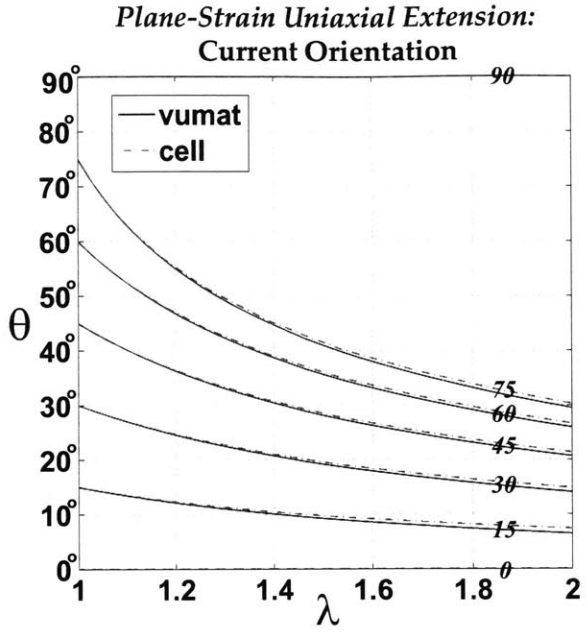

Figure 2-6: *Plane-strain Extension:* Constitutive Model predictions (–) and Unit-Cell calculations (- -) for the evolving orientation of the microstructure, θ.

from the reduced dilative component is two-fold: (i) less volume increase J_r for the rubber phase, and thus less local axial tension ${}^{\mathrm{r}}\sigma_{\mathrm{ss}}$; (ii) higher volume reduction J_g for the glassy phase, mainly due to the increased imposed local axial compression through the resulting ${}^{\mathrm{w}}\mathrm{F}_{\mathrm{s_o s_o}}$ component.

Plane-Strain Isochoric Biaxial Deformation with Principal Stretch Direction Tangential to the Lamellar Plane: For perfect alignment between the principal stretch direction and the microstructure (0^o), the BCP's lateral contraction to uniaxial plane-strain extension is almost entirely due to the unrestricted isochoric reduction in the thickness of rubber layers. The appliction of the lateral isochoric stretch component should not alter the micromechanics for this material orientation. It is verified by comparing the evolution of the microdeformation gradient components in Figs. 2-8 and 2-3, that the deformation characteristics for plane-strain uniaxal extension tangential to the layers (0^o orientation) are essentially preserved by isochoric biaxial deformation with principal stretch direction tangential to the layers.

Plane-Strain Isochoric Biaxial Deformation with Principal Stretch Direction at 45^o to the Lamellar Plane: Both extreme loading orientations at 0^o and 90^o cause no layer

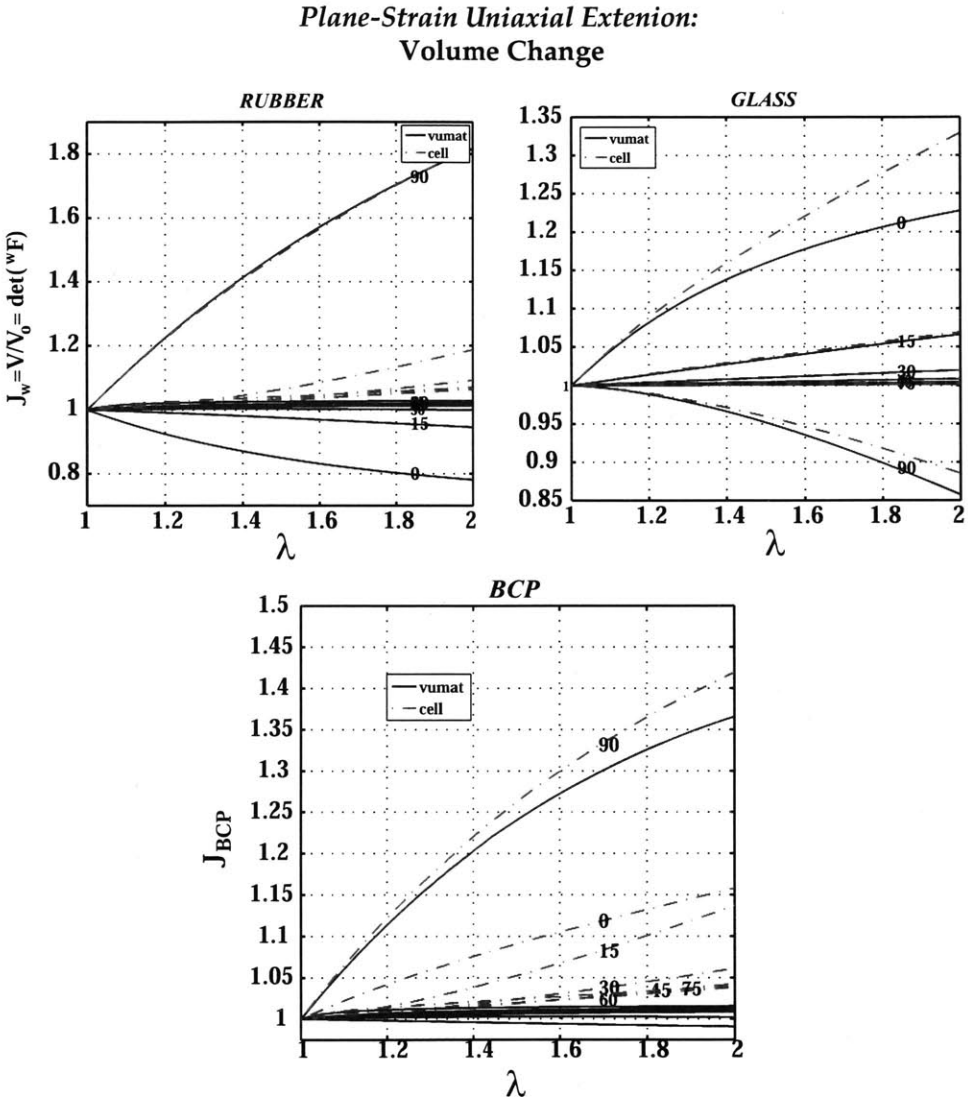

Figure 2-7: *Plane-strain Extension:* Constitutive Model predictions (–) and Unit-Cell calculations (- -) for the constituent volume ratios, J_r and J_g, and for the BCP material, $\overline{J}$.

rotation or shear. For all other material orientations, the fundamenatal mechanism to accommodate deformation is by increasing layer tilting in order to facilitate the lower energy deformation mode of shear within rubber layers. Plane-strain isochoric biaxial deformation with principal stretch direction at 45^o to the underlying morphology, results in a larger rotation component than the one observed for uniaxial plane-strain extension (compare component ${}^{w}F_{n_o s_o}$ between Figs. 2-8 and Figs. 2-3). Increased layer tilting results in a higher alignment between the underlying BCP morphology and the principal loading axis. Thus, the in-plane deformation component is now tensile, *i.e.* ${}^{w}F_{n_o s_o} > 1$, and glassy (as well as rubbery) layers are for this deformation state under extension (as opposed to compression in the case of uniaxial extension). Deformation is thus accommodated, in this case, mainly by layer extension. Due to the higher alignment, glass dilation is reduced (*i.e.* lower ${}^{w}F_{n_o n_o}$ component). In addition, the volume change for both phases is isochoric, therefore the dilative pressure experienced by glass is reduced. (Even though rubber dilation is unaffected, this is due to the compressive effect of the isochoric lateral stretch component.)

Plane-Strain Isochoric Biaxial Deformation with Principal Stretch Direction at various angles to the Lamellar Plane: Similar to what has been described for plane-strain isochoric biaxial deformation with principal stretch direction at 45^o to the underlying morphology, isochoric deformation influences the microstructural rotation and concurrent layer shearing mechanism by which layered materials with off-axis orientations accommodate the applied deformation. During uniaxial plane-strain extension, layer tilting increases with increasing orientation angles as indicated by the rotation component ${}^{w}F_{n_o s_o}$ in Fig. 2-3. On the other hand, the layer rotations imposed by the isochoric biaxial deformation gradient are symmetric about 45^o; the local rotation component ${}^{w}F_{n_o s_o}$ (Fig. 2-8) is the same for orienttion pairs $30^o/60^o$ and $15^o/75^o$. Comparing the results in Figs. 2-8 and 2-3 for ${}^{w}F_{n_o s_o}$, we deduce that: *(i)* for orientations up to about 70^o the imposed tilt is higher than what is naturally attained under uniaxial plane-strain extension, and *(ii)* for orientations higher than 70^o the imposed isochoric component places a limitation on the natural tilting of the microstructure.

For orientations higher than 30^o in the case of uniaxial tension, the resolved in-plane stretch component, ${}^{w}F_{s_o s_o}$, is compressive (Fig. 2-3), and deformation proceeds through in-

creasing rubber dilation (${}^{r}F_{n_o n_o}$). The isochoric deformation state has altered the micromechanics completely. The increased rotation component ${}^{w}F_{n_o s_o}$ implies additional layer tilting toward higher alignment with the principal direction of deformation. The shear and dilation components of the rubber phase have been significantly reduced, while the in-plane deformation component ${}^{w}F_{s_o s_o}$ has turned tensile. Thus, deformation is accommodated mainly through layer extension. Furthermore, the isochoric constraint has significantly perturbed the shear and dilation response of rubber. This is an additional indication that rubber accomodates most of the deformation during plane-strain uniaxial extension.

As mentioned, isochoric stretching hinders layer tilting, which for deformation orientations $> 70^o$ to the underlying morphology is the strongest observed during uniaxial plane-strain extension. Since layer rotation and therefore layer shear are constrained by the orthonormal stretch component, deformation can only be accomodated by layer dilation. Layer tilting combined with shear was more prominent for glass, thus this phase will be influenced more by the isochoric constraint. It is interesting to observe that only glass experiences such a significant increase in dilation by comparing the normal deformation component in Figs. 2-3 and 2-8. The micromechanics of rubber layers' deformation -being naturally determined by isochoric volumetric deformation- have shown minimal sensitivity. Also, due to the isochoric deformation requirement, both phases exhibit a reduced volume increase when compared to uniaxial extension results, however the reduction is mostly observed for rubber.

Plane-Strain Simple Shear

As will be evident from the analysis in Chapter 4, for polycrystalline materials deformed under uniaxial plane-strain extension shear is the predominant microdeformation mechanism for most grains. Experimental studies both on the deformation micromechanics of polycrystalline lamellar aggregates[19] as well as on isolated grain boundaries[51] have verified that grains gradually rotate with increasing deformation in a manner that allows individual layers to convert their corresponding deformation state from a combination of tension and dilation to that of shear. Biaxiality will develop in grains whose tilting motion is kinematically constrained by neighboring material. Such grains will buckle even

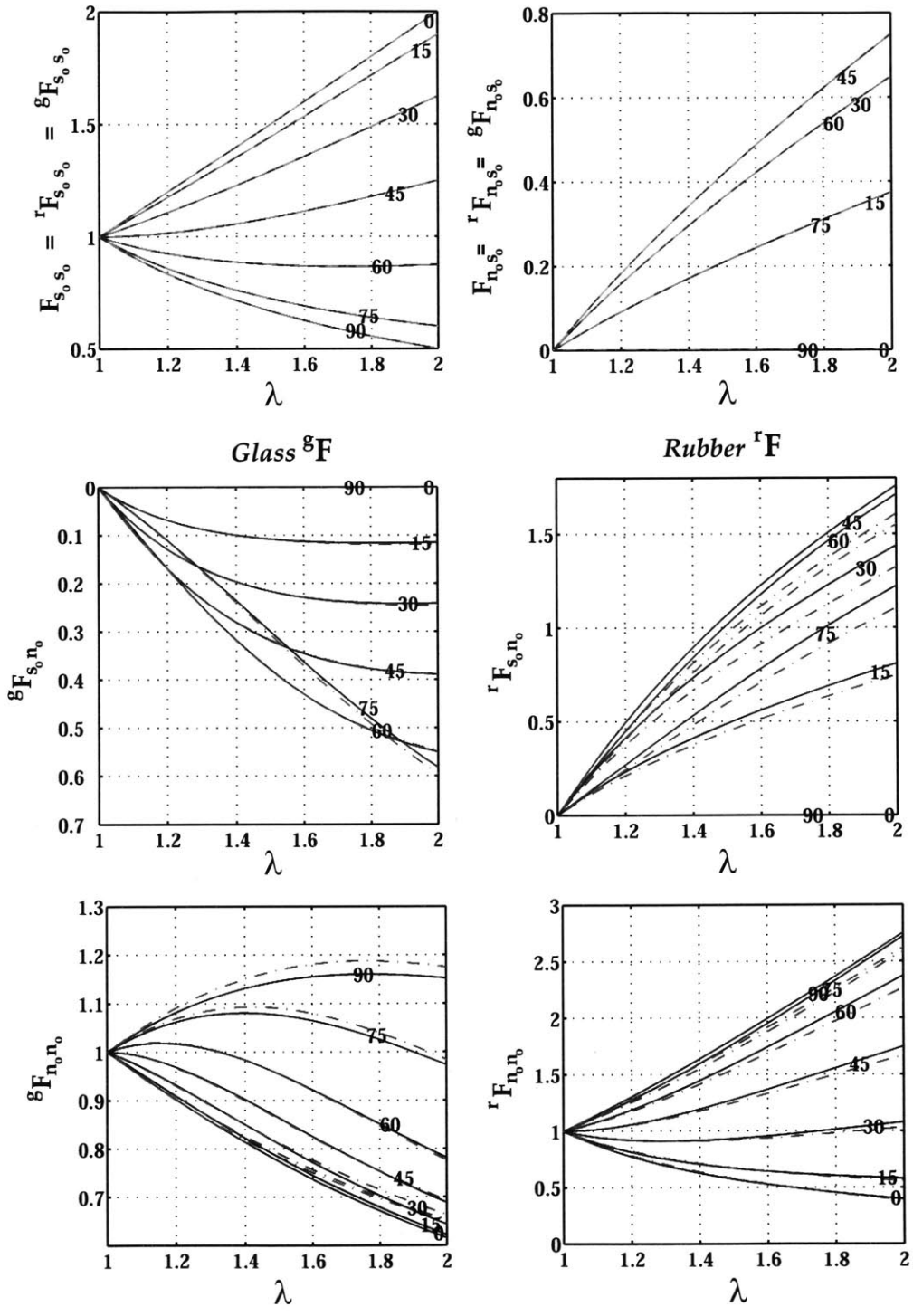

Figure 2-8: *Plane-strain Isochoric Deformation*: Constitutive Model predictions (–) and Unit-Cell calculations (- -) for the microdeformation gradients ${}^{r}\mathbf{F}$ and ${}^{g}\mathbf{F}$.

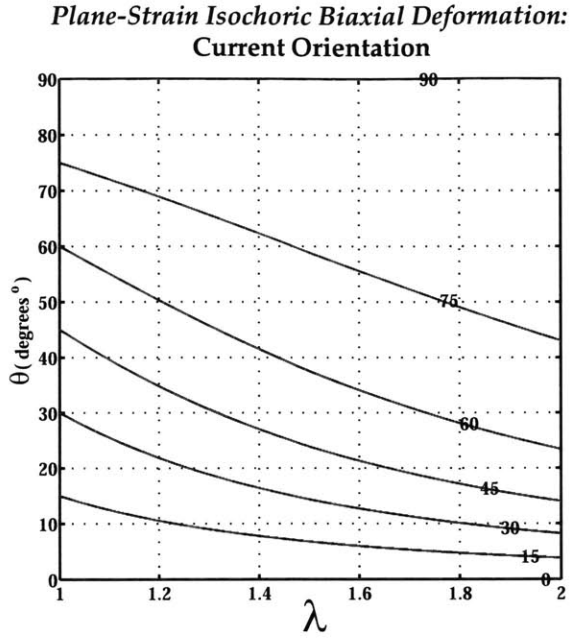

Figure 2-9: *Plane-strain Isochoric Deformation:* Constitutive Model predictions (–) and Unit-Cell calculations (- -) for the evolving orientation of the microstructure, θ.

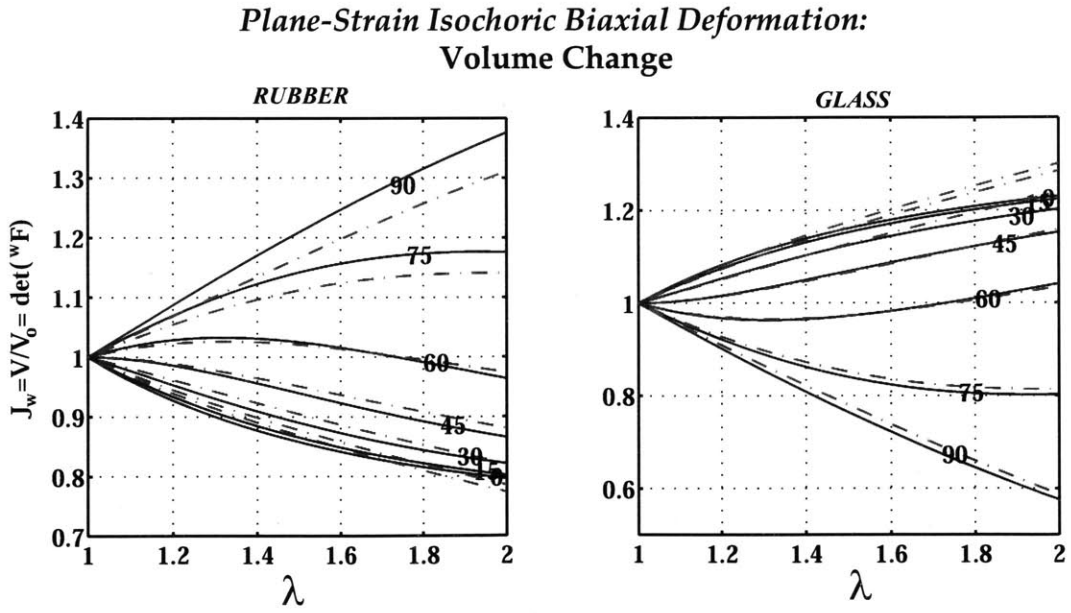

Figure 2-10: *Plane-strain Isochoric Deformation:* Constitutive Model predictions (–) and Unit-Cell calculations (- -) for the constituent volume ratios, J_{r} and J_{g}. For the BCP material, $\overline{J} = 1$ for isochoric deformation.

at very small strains to subdue to shear deformation as well. As a result, biaxial loading will have little influence on the effective response of a polycrystalline aggregate, unless *(i)* the imposed macroscopic deformation is already biaxial in nature, or *(ii)* the glassy layers are too thick, and therefore too stiff to allow buckling and the associated shear. Therefore, for biaxiality to matter the grain size has to be decidedly small (comparable to the layer thickness)[17]. In this section we present the continuum model's predictions for the case of plane-strain simple-shear deformation for different orientations of the underlying lamellar microstructure.

Macroscopic plane-strain simple shear is applied by restraining the through-thickness and lateral deformations of the RVE ($F_{33} = 1$ and $F_{22} = 1$ or $\epsilon_{22} = 0$ and $\epsilon_{33} = 0$), while imposing a macroscopic shear angle γ in the transverse direction such that $F_{12} = tan(\gamma)$.

Two different behaviors can be identified for each phase's kinematic response and their relative microdeformations: *(a)* for loading directions at angles higher than 45^o, and *(b)* less than 45^o to the underlying material orientation. For orientations up to 45^o, the macroscopic shear deformation is mostly accommodated by the rubbery layer, due to its significant shear compliance ($G_r << G_g$), as manifested in the relative magnitudes of the in-plane shear microdeformation components ${}^{r}F_{s_o n_o} > {}^{g}F_{s_o n_o}$ (Fig.2-11).

The level of shear deformation each layer assumes depends on the shear moduli contrast between layers and the direction of loading. For higher alignments between the underlying layers and the shearing direction (angles $\rightarrow 0^o$), the amount of shear deformation the rubbery layer accommodates increases, rendering the effective BCP response to shear more compliant. This is reflected in the composite's effective shear stress response, Σ_{12}, (Fig2-12) and effective shear modulus, G_{BCP}, (Fig2-13).

For less aligned deformation situations, the deformation each layer must undergo is no longer shear alone. Instead macroscopic simple shear translates into both shear and biaxial stretching in the local frame of the layered microstructure. The stiffer initial BCP stress response and modulus stem primarily from the increasing tensile contribution of the glassy layers. As seen in the tensile component of the microdeformation gradients, ${}^{w}F_{s_o s_o}$

[17]For polycrystalline aggregates of such grain sizes the present RVE would not describe a typical material point, because it assumes infinite layer extension and repetition in all directions

(Fig.2-11), the level of tension imposed on layers increases with the misalignment between the underlying layers and the shear direction (*i.e.* increasing θ). The second contribution to the increasingly stiffer initial BCP shear stress response derives from the increasing shear deformation of glassy layers (component ${}^{g}F_{s_o n_o}$) with increasing misalignment θ. The orientation-dependent tensile effect is maximized at 45^o, consistent with the trends manifested in the effective BCP's initial shear stress response and modulus (Figs. 2-13 and 2-12, respectively). (Tension of course is followed by a reduction in layer thickness as indicated by microdeformation components ${}^{w}F_{n_o n_o}$.)

For loading angles $> 45^o$, the characteristic symmetry which shear loading possesses for this composite about 45^o orientations is also inherent in the model's initial, small-deformation shear stress response and effective modulus. The initial effective shear stress appears to be decreasing for loading directions higher than $> 45^o$ since the projected local tensile component ${}^{w}F_{s_o s_o}$ is decreasing. As the imposed shear angle increases, this decreased projection is counterbalanced by: (i) the increased shear contribution of the glassy layer (increasing ${}^{g}F_{s_o n_o}$), and (ii) the layer rotation (increasing ${}^{g}F_{n_o s_o}$), the subsequent increasing alignment of glassy layers with the direction of loading, and the resulting in-plane layer extension. This is the main cause for the upward trend in the tangent shear modulus and the reduction in glassy layer's thickness (${}^{g}F_{n_o n_o}$) as shear deformtion progresses. The trend is more prominent for 90^o material orientation, because in this case, layer alignment with the loading requires larger rotations.

The volume change for each phase can be well explained in accord with the previous description for the evolution of microdeformation within each layer. The overall agreement with unit-cell results is excellent in Fig.2-15, but for loading directions in the vicinity of 45^o degrees, where the tensile deformation component is maximized, and this only for shear strains higher than $\gamma \approx 0.6$. Beyond this level of shear strain the volume changes for these loading orientations are in the order of 10%. Hence, the negligible volume change approximation breaks down and the model's performance is somewhat compromised.

The constitutive model's predictions for the BCP's shear stress response is in excellent agreement with numerical unit-cell results for shear strains even up to $\gamma = tan(\theta) = 1$. For all orientations however the model predicts an increasingly stiffer response than does the

unit-cell, due to the gradual tilting and increasing alignment of the layers with the loading direction, which promotes layer extension. Consistent with the disagreement observed for uniaxial tensile deformation tangential to the lamellar plane, the error in the constitutive model's predictions is increasing as orientations appoach 45°, where layer extension is maximized.

2.3 Conclusions.

This work presents a micromechanical framework for the derivation of large-stain continuum constitutive models for hyperelastic materials with layered microstructures. The lamellar morphology is represented by a planar bi-layer RVE, which is used to derive the appropriate continuity and equilibrium arguments that must be satisfied at every material point. A generic description for the strain energy function of the composite and the resulting system of equilibrium and continuity equations, complete the micromechanical framework.

The strain energy function was presented here as an (initial-)volume weighted average of the constituents' strain energies. The framework of micromechanical constraints was applied for the case of contituents with hyperelastic Neo-Hookean behavior. An analytical closed-form solution was elaborated for the distribution of macroscopic deformation within the individual layers. The solution for each phase's microdeformation gradient was a function of the applied macroscopic deformation gradient. The composite strain energy density can then be fully described in terms of the macroscopic deformation gradient, and the material stress-strain response is simply obtained by deriving the strain energy function with respect to the macroscopic deformation gradient. The effective composite stress response follows as a (current-)volume weighted average of each constituent's stress contribution.

Stress and microdeformation predictions from the constitutive model were in excellent agreement with micromechanical finite element calculations on a 2D bilayer unit-cell. The constitutive model describes the stress and deformation response of the oriented microsctructure accurately, and it will be used in multigrain calculations to study the mechanical behavior of polycrystalline lamellar aggregates. The model predicts the rotation and large deformations of the underlying lamellae, however, it does not account for critical mi-

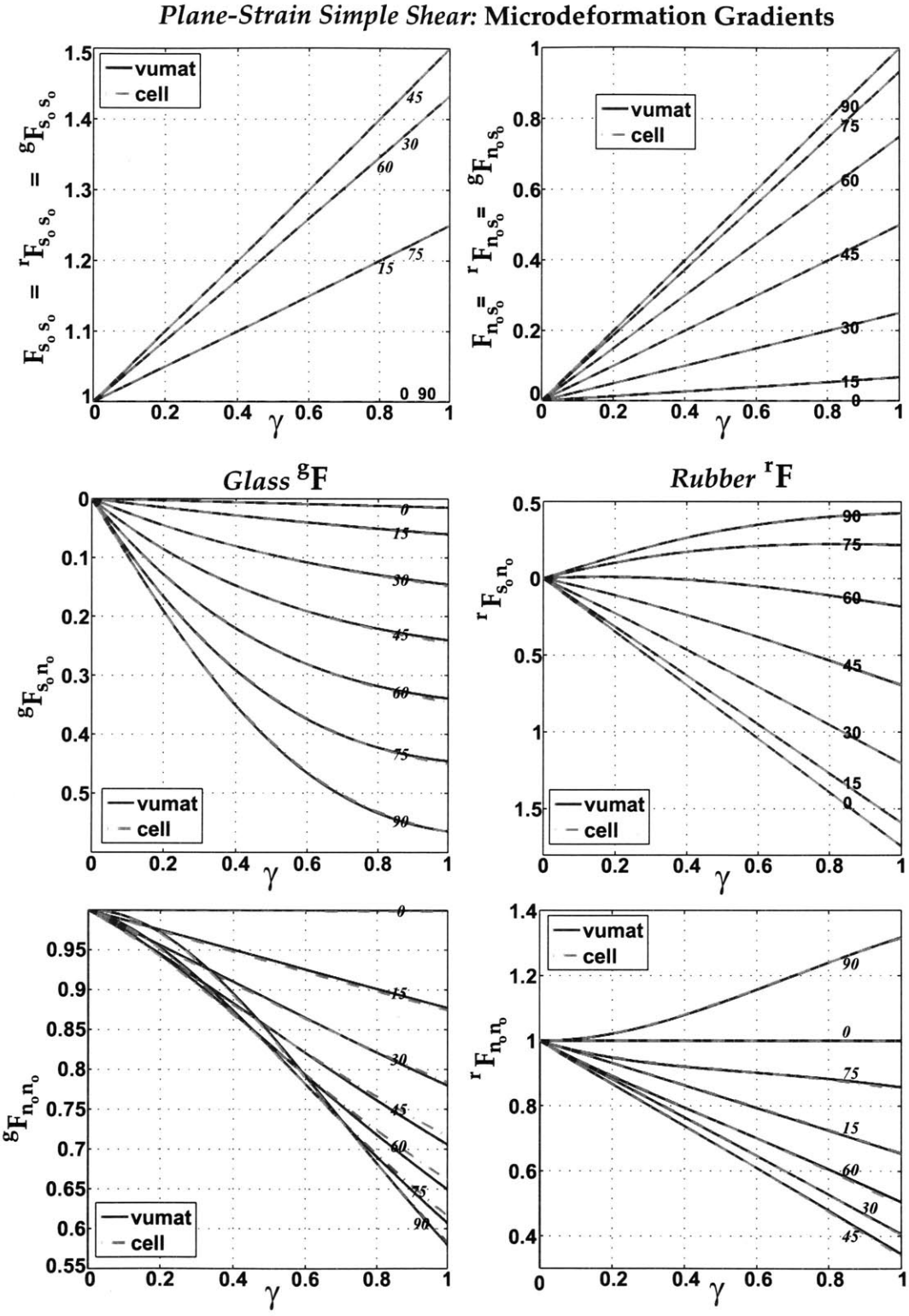

Figure 2-11: *Plane-strain Simple Shear*: Constitutive Model predictions (–) and Unit-Cell calculations (- -) for the microdeformation gradients ${}^{r}\mathbf{F}$ and ${}^{g}\mathbf{F}$.

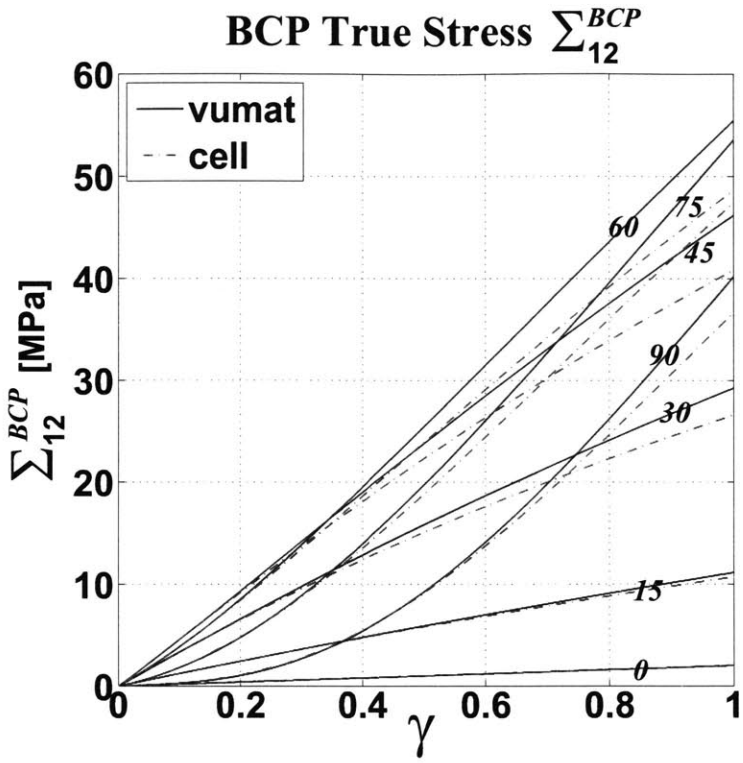

Figure 2-12: *Plane-strain Simple Shear:* Constitutive Model predictions (–) and Unit-Cell calculations (- -) for the effective shear stress response, Σ_{12}.

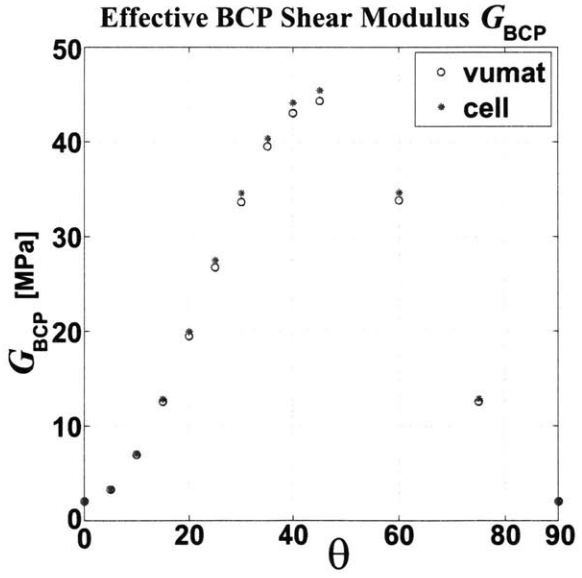

Figure 2-13: *Plane-strain Simple Shear:* Constitutive Model predictions (–) and Unit-Cell calculations (- -) for the effective shear modulus, G_θ, for different shearing directions with respect to the microstructure.

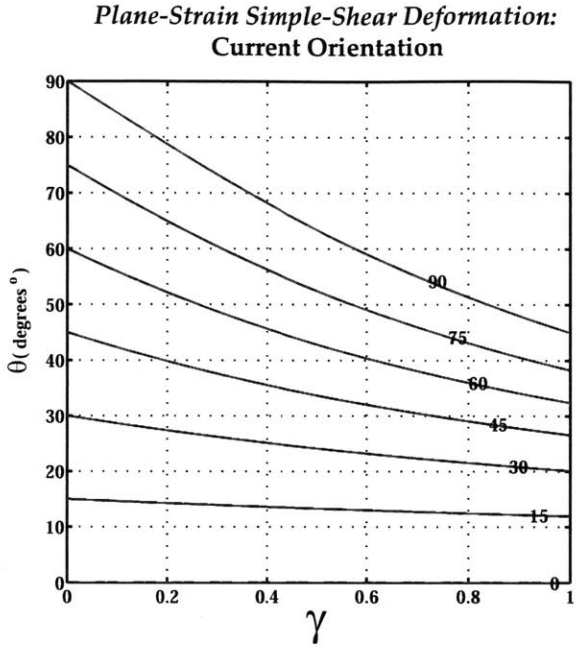

Figure 2-14: *Plane-strain Simple Shear:* Constitutive Model predictions (–) and Unit-Cell calculations (- -) for the evolving orientation of the microstructure, θ.

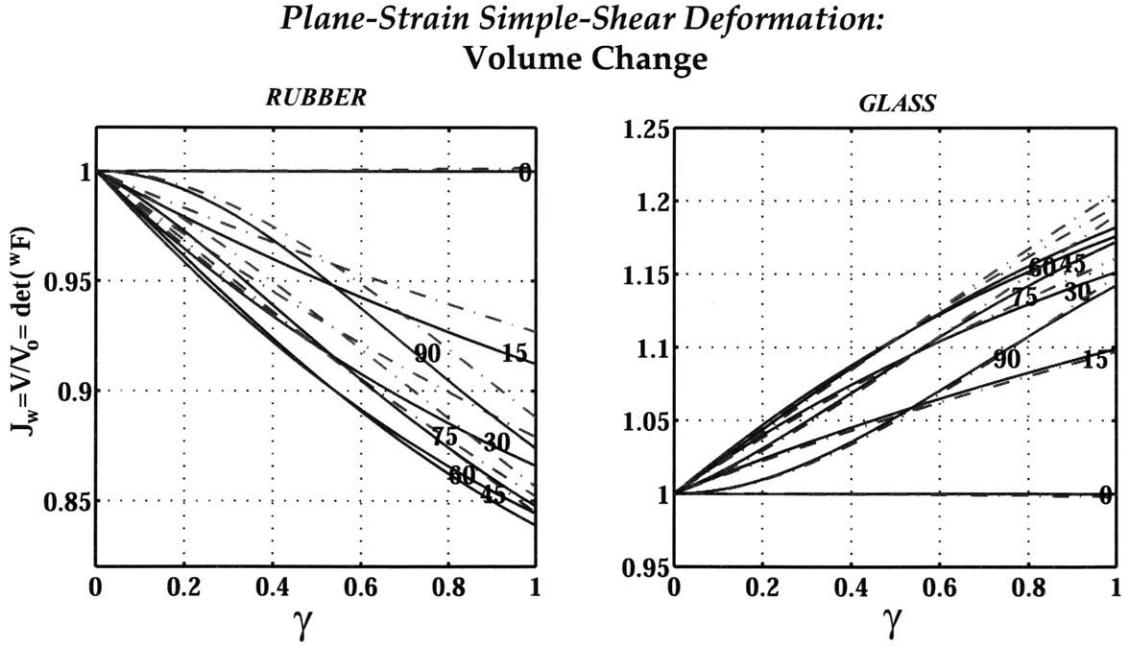

Figure 2-15: *Plane-strain Simple Shear:* Constitutive Model predictions (–) and Unit-Cell calculations (- -) for the constituent volume ratios, J_{r} and J_{g}. For the BCP material, $\overline{J} = 1$ for Plane-Strain simple shear deformation.

crostructural instabilitites such as lamellar microbuckling and micronecking. To describe such microstructural transformations the constitutive model needs to be augmented with appropriate criteria for the initiation of instabilities, and should account for plasticity-related localization phenomena. Even though these are decisive mechanisms for the large strain response of an oriented structure (single-crystal), we expect the model to be accurate enough for numerical studies on polycrystals.

The presented framework is general and the solution precedure can be followed for any choise of hyperelastic phase behavior. It is very possible that a numerical scheme will be needed to reach a solution for other material descriptions. Nevertheless, the neo-hookean behavior is an excellent approximation, pending on a judicious choise of material properties for the constituents.

Chapter 3

Mechanics of Single and BiCrystal Lamellae Structures during Tensile Testing

The layered structure of the lamellar block copolymer materials together with the strong contrast in mechanical properties of the constituent layers provides the highly anisotropic stress-strain behavior of the material. In this chapter, we study the effect of isolated deformation constraints on the deformation behavior of these lamellar block copolymers. The first study examines the plane strain tensile extension of the lamellar structures when the lamellar normal is at various angles to the tensile axis; the strip specimen is constrained from lateral deformation at its ends in order to emulate the grip constraint during a test. The second study examines the plane strain tensile extension of bicrystal configurations where a specimen tensile strip now consists of two crystals at different orientations perfectly adhered to one another at the center of the strip along a plane normal to the tensile axis; this centrally located adhesion plane constitutes an isolated grain boundary. Again, strips are subjected to tensile extension with the lateral deformation constrained on the strip ends (capturing the grip effect on specimen deformation) and each grain will now also contain an additional separate deformation constraint due to the grain boundary enabling a study of the influence of the orientation of neighboring grains on the deformation of differently oriented lamellae.

3.0.1 Model Description

The plane strain tensile strips of single crystals were of relative dimensions of width =1 and length =10. The tensile strips of single and bicrystal lamellar block copolymers were modeled using plane strain finite elements (ABAQUS type CPE4R) with 20 elements across the width and 140 elements along the length. The lateral displacement of the top and bottom edges were both constrained. The bottom edge was also constrained in the axial direction; the top edge was subjected to a uniform, monotonically increasing axial displacement giving the imposed axial extension. The bicrystal strips were of width w = $2.25mm$, but total length L = $9.5mm$ with each crystal of length l = $4.75mm$ (with the grain boundary located midway along the specimen length). The elements were assigned the lamellar block copolymer stress-strain behavior detailed in Chapter Two where the constitutive model was formulated as a Fortran VUMAT subroutine for use with the ABAQUS Explicit nonlinear finite element code. Elements were assigned different initial lamellar orientations depending on the particular crystal orientations under investigation.

Results: Tensile Testing of Single Crystals

The simulation results for the tensile testing of single crystal lamellar block copolymers are depicted in Figures 3-1 through 3-4. Figure3-1 depicts the simulated axial force versus axial displacement behavior for different lamellae orientations. The gradual reduction in initial stiffness as the initial lamellae orientation moves away from the tensile axis is observed until reaching an initial orientation of 45 degrees. The 60 degree orientation is initially stiffer than the 45 degree orientation and the 75 degree orientation is initially stiffer than the 60 degree (and it is even initially stiffer than the 30 degree orientation). The relatively high initial stiffness of the 75 degree case is a result of the initial sampling of the bulk stiffness of the rubbery layer as a result of the lower resolved shear stress on the lamellae plane (and hence the initially relatively lower sampling of the shear behavior of the lamellae). We also note that the 75 degree and the 60 degree cases are rather nonlinear - this is a direct result of the tilt of the lamellae orientation towards the tensile axis as the strip is axially strained; the tilting increases the resolved shear stress on the lamellae plane and hence gradually

increases the relative shear contribution as opposed to dilation contribution of the rubbery lamellae deformation to accommodate the imposed extension.

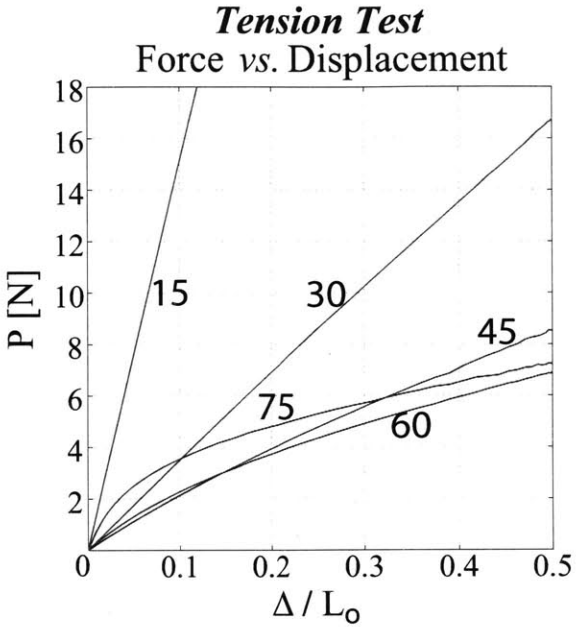

Figure 3-1: Force-Displacement curves for different specimen microstructure orientations.

The nature of the deformations for each initial orientation can be seen in greater detail by looking at contours of axial strain and shear strain in each strip (Figures 3-2, 3-3 and 3-4). The imposed extension is seen to be accommodated by both shear and axial stretching, with relative contributions of shear and extension depending on the initial orientation as well as the imposed strain level. The grip boundary is also seen to have a very strong influence on the homogeneity of the deformation field. The spatial extent of the influence of the boundary constraint is seen to strongly depend on the initial lamellae orientation. These results begin to show the strong interaction between the lamellae strain and any boundary constraints.

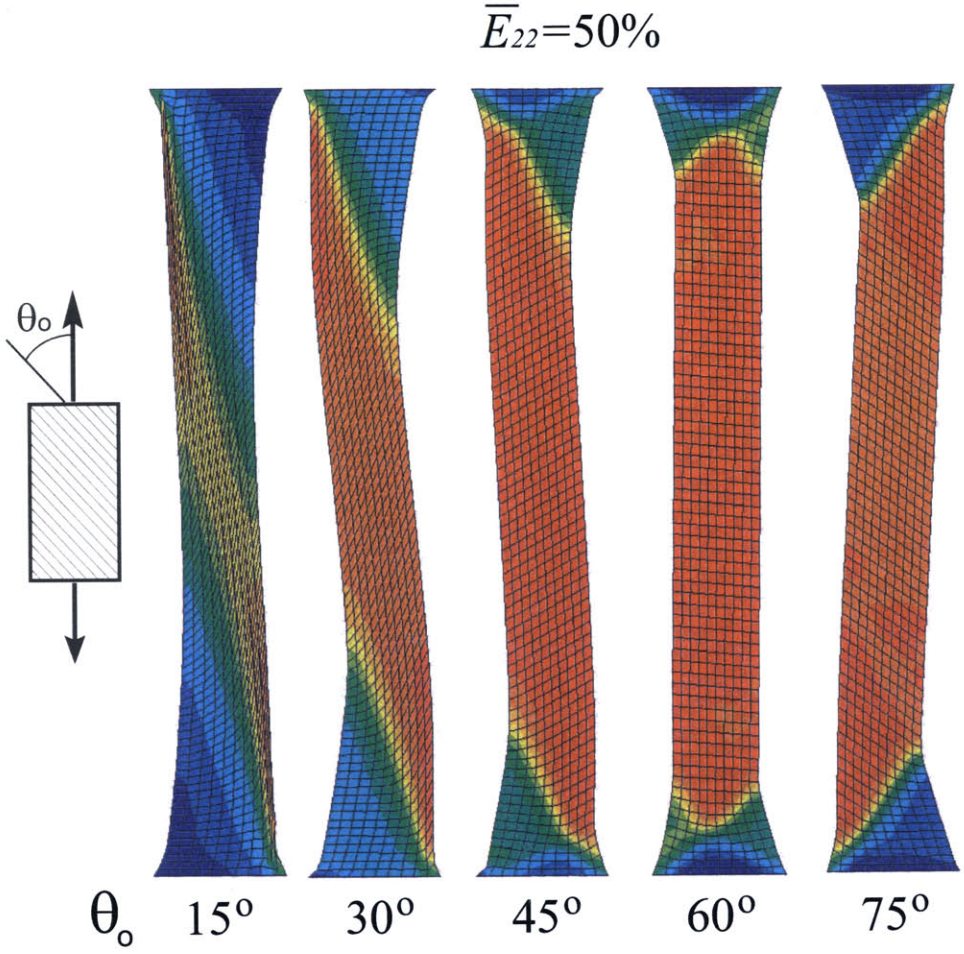

Figure 3-2: Deformed meshes at 50% macroscopic strain and axial strain contours for specimens with different initial microstructure orientations to the loading direction. The imposed extension is accommodated by both shear and axial stretching, with relative contributions of shear and extension depending on the initial orientation as well as the imposed strain level. The grip boundary also has a very strong influence on the homogeneity of the deformation field. The spatial extent of the influence of the boundary constraint depends strongly on the initial lamellae orientation.

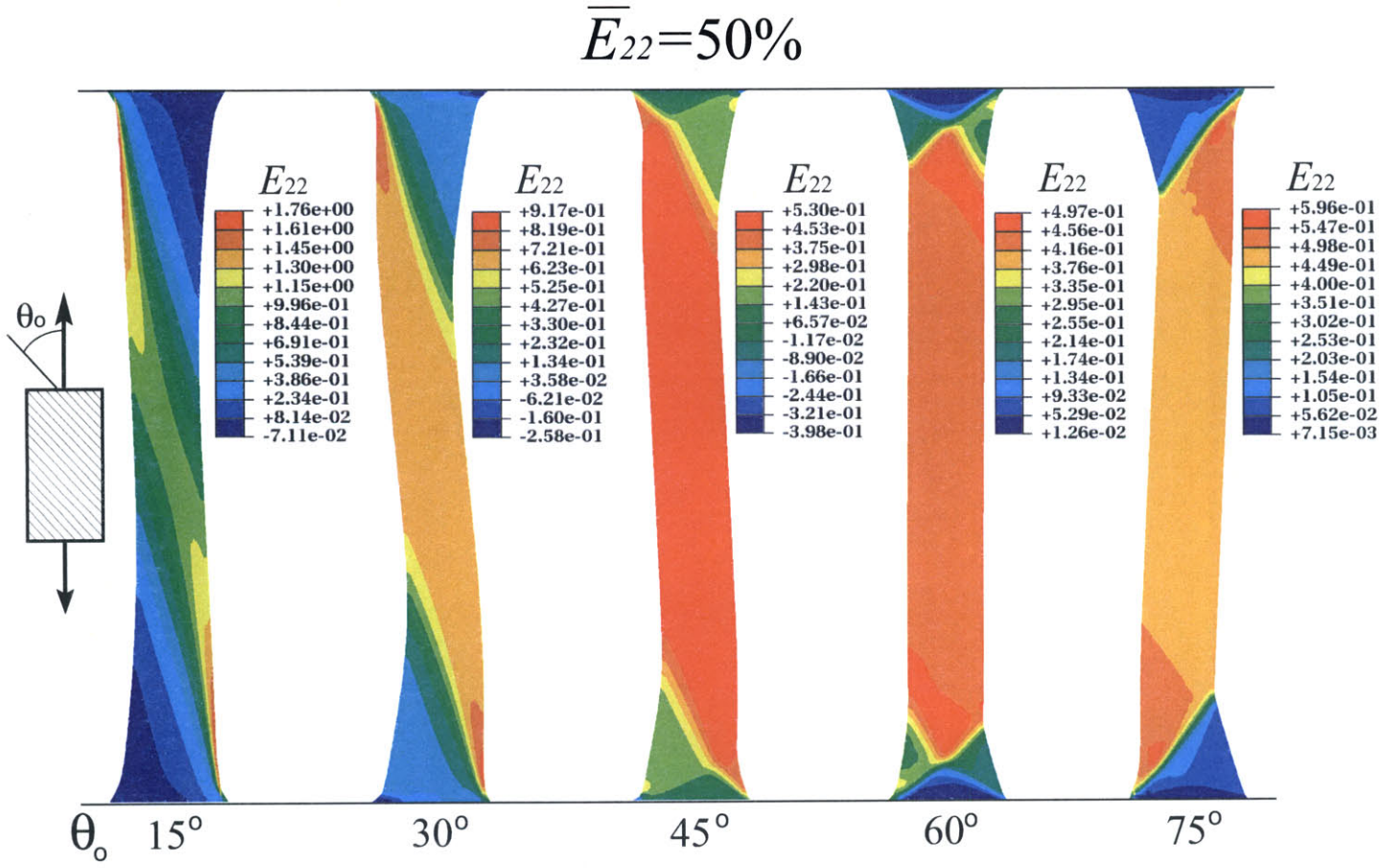

Figure 3-3: Axial strain contours at 50% macroscopic strain for specimens with different initial microstructure orientations to the loading direction.

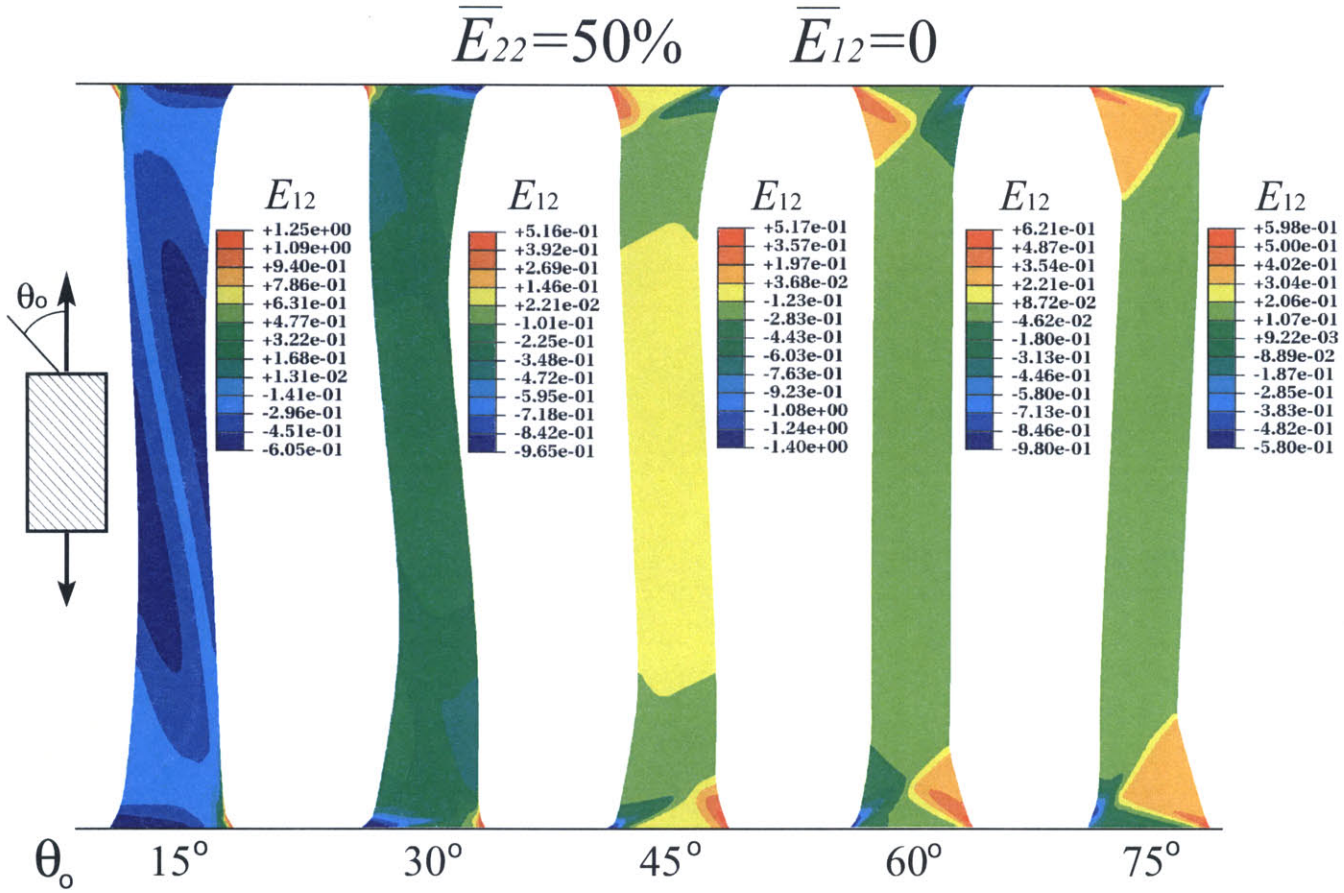

Figure 3-4: Shear strain contours at 50% macroscopic strain for specimens with different initial microstructure orientations to the loading direction.

3.0.2 Tensile Testing of Bicrystals

Background

The mechanical behavior of polycrystalline block copolymers depends largely on the influence of grain boundaries on deformation micromechanics. To investigate the effect of different grain boundary structures Wanakamol[51] fabricated tensile strip specimens containing isolated grain boundaries by joining oriented film strips of a glassy-rubbery (SIS) cylindrical block copolymer material. The morphology in the vicinity of the structured grain-boundary between the two single-crystals was examined using atomic force microscopy (AFM). The model bicrystal specimens were then extended to 100% nominal strain and the microstructural evolution within the grain boundary region and within each grain was monitored using small angle x-ray scattering (SAXS). In addition, the specimens were marked with a fine grid of small square cells to allow for quantitative measurements of the developing strain field with optical microscopy. Three grain boundary geometries were tested: a symmetric tilt grain-boundary with grains oriented at 45° and $-45°$ to the loading direction (grains oriented normal to each other), and two asymmetric tilt boundaries with grain orientations at 90°/45° and 90°/0°. The type of deformation patterns which evolve through the specimen illustrate the effects of the property mismatch between the grains and the spatial extent of the grain boundary influence.

The bicrystal behavior is studied here numerically using the developed analytical constitutive model to describe the deformation behavior of each grain. The same model which was used to study the plane-strain extension of oriented BCP samples will be adopted to investigate the bicrystal's response to extension with a minor (from a modeling standpoint) modification to account for the existence of two different material orientations. The specimen area is divided into two equal regions which represent the two grains in the bicrystal, and the constitutive model is used to assign the grain orientation and the mechanical behavior to each of the two corresponding element sets. The nodes in the left face of the model are encastred, while those on the right face are not permitted any motion in the 2-direction. Specimen extention is applied by translation of the right face's nodes along direction-1. In accord to Wanakamol's experimental work, the model is $9.5mm$ in length and $2.25mm$ in

width, and is used to test three bicrystal configurations: the symmetric, with grains oriented at 45° and −45° to the loading axis-1, and two asymmetric specimens with grains oriented at 90°/45° and at 90°/0° to the loading direction (1-axis).

In the following subsection we present the experimental results from each bicrystal configuration's extension and compare them to the corresponding results from numerically simulated bilayer extension experiments using the constitutive model. The comparison is qualitative between optical observations and strain measurements from the deformed bicrystal specimen and strain contours and deformed mesh grids calculated from the numerical model. The intention is twofold: *(i)* to interpret the bicrystal deformation and the influence of the grain boundary based on knowledge from the previously described deformation behavior of oriented single-crystal specimens under uniaxial extension, and *(ii)* to demonstrate the model's capability to reproduce the deformation fields observed during the extension of bilayer specimens in a micromechanicanically and physically accurate manner.

Apart from macroscopic strain measures, the constitutive model also calculates all the layer-related micromechanical quantities that describe the microstructural evolution anywhere within the bicrystal model. However, the current constitutive model describes layered morphologies. Its microstructural predictions, although relevant, will not be presented here because they cannot be directly compared to the corresponding x-ray measurements from cylindrical morphologies presented in P. Wanakamol's thesis [51].

3.0.3 Symmetric Bicrystal: 45°/45° Grain Boundary

Experimental Results Optical images of the deformed grid are shown in Fig. 3-5 for a symmetric specimen at different macroscopic nominal strains. Polarized transmitted light was used to take advantage of the optical anisotropy between the two grains and locate the grain boundary, which is here denoted with a dashed line. The overall specimen deformation is inhomogeneous, however symmetric about the grain boundary, due to the microstructural symmetry. As observed in the optical images, the grain boundary remains straight and normal to the stretching direction; however, there is a triangular region of

constrained deformation extending across the grain boundary (giving a grain boundary influence zone), which influence zone translates upwards in a direction normal to the loading axis. A constrained triangular region is also seen to emanate from the grip boundary. Material between these two zones experiences the more homogeneous shear and dilation response of a single-crystal (with no boundary effects).

The schematic in Fig. 3-6 replicates the specimen deformation. Each grain deforms as a specimen under uniaxial extension oriented at 45° to the loading direction (Figs. 3-2 and 3-3). The triangular regions denoted by letters "a" and "c", located at the grip and adjacent to the grain boundary, are influenced in their deformation behavior by the applied boundary conditions. Similar to the case of a single-grain under uniaxial extension, blocks "a" and "b" exhibit negligible deformation and behave as almost rigid. In between these boundary influenced regions, the specimen portion denoted by "b" extends by shear as revealed by the shape of the deformed grid. The difference between the two experiments, that of uniaxial extension of the 45^o single-crystal and that of bicrystal extension, is that in the latter case the rigid grip on side "c" is allowed to translate freely in the vertical direction as if the grip was on rollers. The lack of this degree of freedom in the case of uniaxial extension and the compatibility constraint between sections "b" and "c" result in a rotated "b" region as seen in Fig.3-2. Rotation is not needed in this case in order for the two symmetric grains to satisfy deformation compatibility on the grain-boundary. Instead, compatibility is attained with a "rigid" upward translation of the grain boundary and of each grain's boundary affected region "c". Local strains within regions "a", "b", and "c" at different levels of macroscopic specimen stretch were measured using the deformed grid. The locally measured axial strain, ϵ_{xx}, and lateral contraction, ϵ_{yy}, for these three regions are shown in Fig. 3-7 as functions of the overall axial strain imposed on the specimen. It can be seen from the graph that the extension in region "b" is nearly affine but slightly higher than the overall imposed extension, because it has to compensate for the limited extensibility of regions "a" and "c". The deformation in region "c" reaches a plateau after a macroscopic strain of 25%, which indicates that region "c" does not extent beyond that point. The grain boundary acts as a rigid grip for both the oriented grains of the bicrystal, and thus, deformation in region "c" corresponds to rubber dilation between the glassy rods.

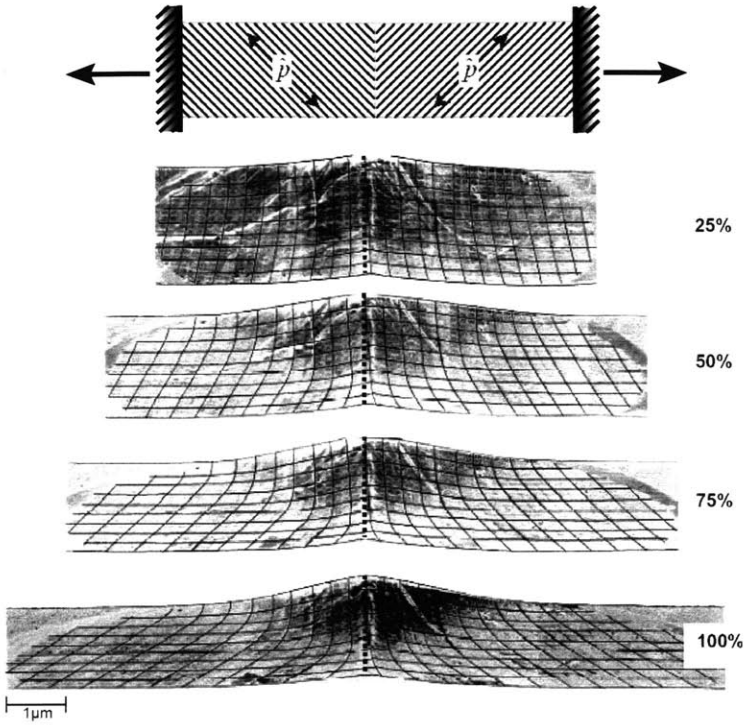

Figure 3-5: Schematic of the symmetric bicrystal 45°/45° specimen configuration and optical images of the deformed specimen grid at 25%, 50%, 75% and 100% macroscopic specimen strain.

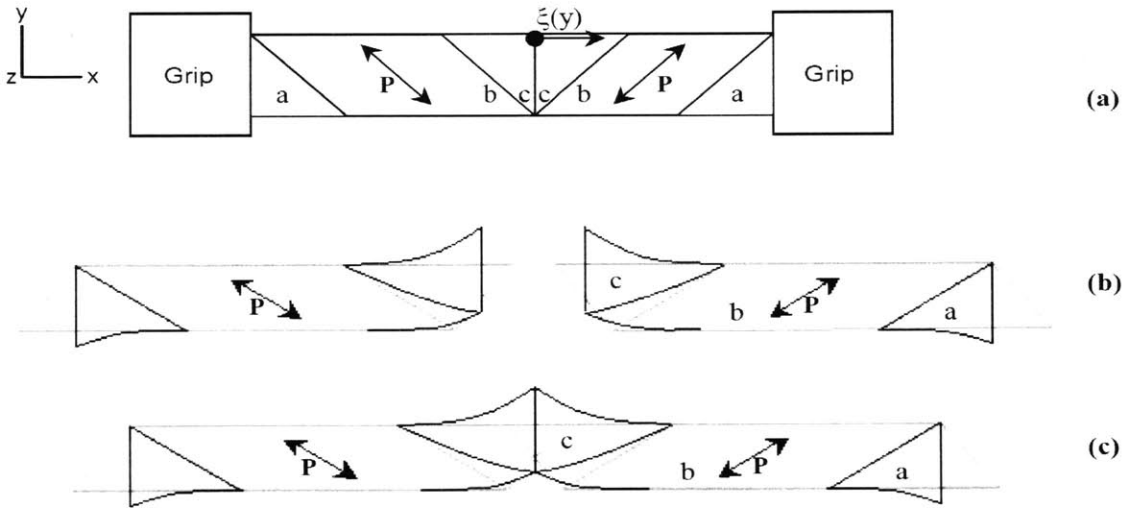

Figure 3-6: Schematic illustration of how specimen deformation is accommodated between grains of incompatible deformation modes in the symmetric 45°/45° bicrystal configuration.

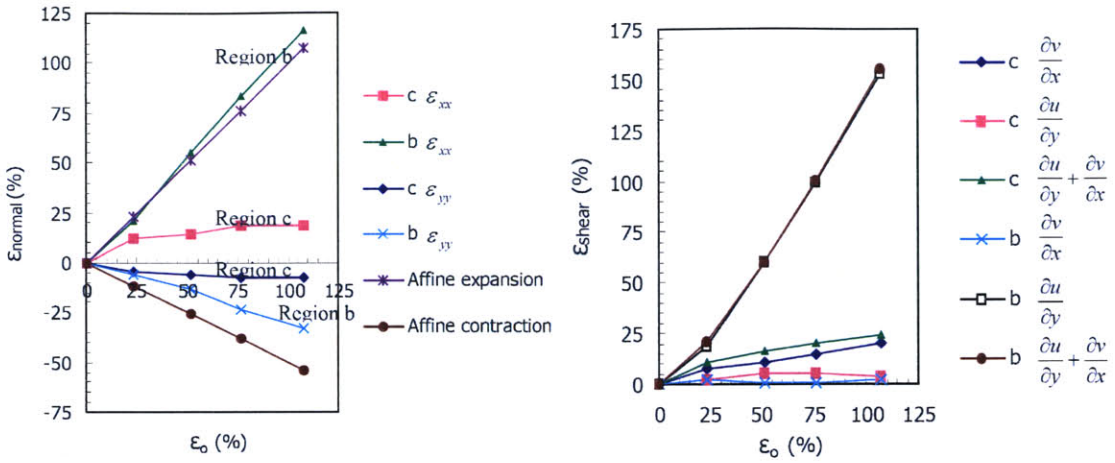

Figure 3-7: Axial and Shear Strains from regions "a" and "c from the symmetric $45^{o}/45^{o}$ bicrystal as functions of the applied macroscopical strech.

Beyond the strain of 25%, the cylindrical morphology within region "b" has rotated to a configuration which allows for uninhibited rubber shear between the glassy rods. Therefore, any additional deformation is accommodated entirely by each grain's compliant "b region rather than by additional dilation of the rigid blocks "c". Due to the Poisson effect, the highest contraction, ϵ_{yy}, is observed in region "b", which experiences the highest axial stretch. Region's "c" contraction is significantly less and ceases beyond the macroscopic strain of 25%, in correspondence to the plateauing observed in its local axial strain.

The shear strains measured locally within regions "b" and "c" are also shown in Fig.3-7. There is a stark contrast between the levels of shear strain observed within the two regions. It is more important to note however, that the shrear strain of region "b" corresponds to a simple shear deformation, since there is no rotation observed ($\partial v/\partial x \approx 0$). As already discussed, this kinematic condition results to the vertical shift of the grain boundary.

Simulation Results The simulation results for the deformed specimen and the axial strain within the bicrystal are shown in Fig. 3-8. Despite the differences in the microstructure between experiments (cylindrical) and numerical calculations (layered), the deformed mesh is in perfect agreement with optical images of the deformed specimen grid. Each diagonal grain is seen to deform by shear, and macroscopic deformation appears to be accommodated almost entirely by the shearing "b" region in each grain. Regions of limited

deformation are seen at the grip ends and at the grain boundary. In particular, the grain boundary influence region ("c") has the same characteristic shape, spatial extent, and upward motion as has been observed in experiments.

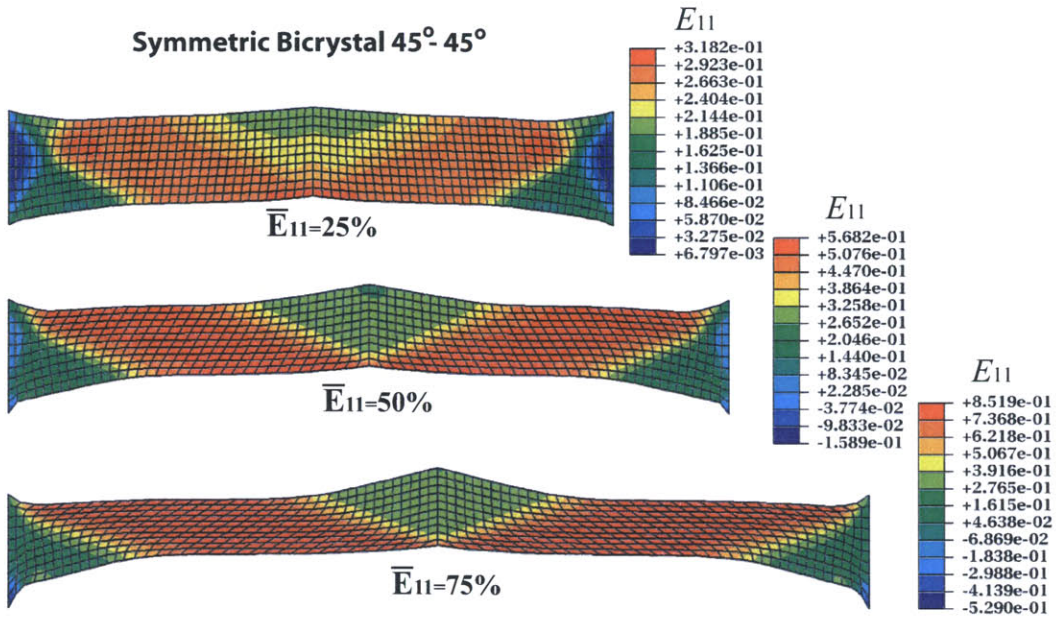

Figure 3-8: *Symmetric* 45°/45° *Bicrystal:* Axial strain contours at different macroscopic specimen extensions.

3.0.4 Asymmetric Bicrystal: 90°/45° Grain Boundary

Experimental Results Fig. 3-9(*top*) shows a schematic of the specimen morphology for an asymmetric bicrystal configuration with grains oriented at 90° and 45° to the 1-axis. Also shown in the figure are optical images of the deformed specimen grid at 25% and 100% nominal macroscopic strains. The deformed grain boundary is denoted by a dashed line. The schematic of Fig. 3-10 illustrates how each grain's deformation, constrained by the required compatibility at the grain boundary, result in the overall deformed specimen configuration. The crystal on the right, oriented at 45° to the horizontal, deforms by shear. The grain on the left, oriented normal to the stretching direction, deforms by dilation of the rubbery matrix around the glassy cylinders. Deformation compatibility at the grain boundary results in the latter's rotation in the direction of shear for the diagonal grain. At 25% nominal extension, the grain boundary appears also slightly shifted downwards in agreement

to the corresponding translation observed for the grain boundary of the symmetric bicrystal. The lateral motion in this case is restrained by the normal grain, which act as a grip, however not entirely encastred. This effect vanishes at larger strains, when the cylindrical morphology within the normal grain, right at the grain boundary, has rotated enough to deform by shear and not only by dilation of the microstructure, such that both grains shear in tandem. Shear deformation within the diagonal grain results in a higher lateral contraction than the resulting contraction in the dilating normal grain. Thus, the cylidrical domain in the 90° grain experiences a contraction imposed by the diagonal grain, due to deformation compatibility at the g'rain boundary. This compression is visible in the horizontal lines of the deformed specimen grid, which tapped down as they approach the grain boundary. This compression results in asymmetric kinking of the oriented cylindrical microstructure near the grain boundary as SAXS patterns from that vicinity have shown[1]. SAXS patterns have shown that the spatial extent of the grain boundary influence is minimal for this bicrystal configuration, since for the given orientations both grains have very compliant behaviors, and in essence allow each other to deform as the corresponding single-crystal in isolation.

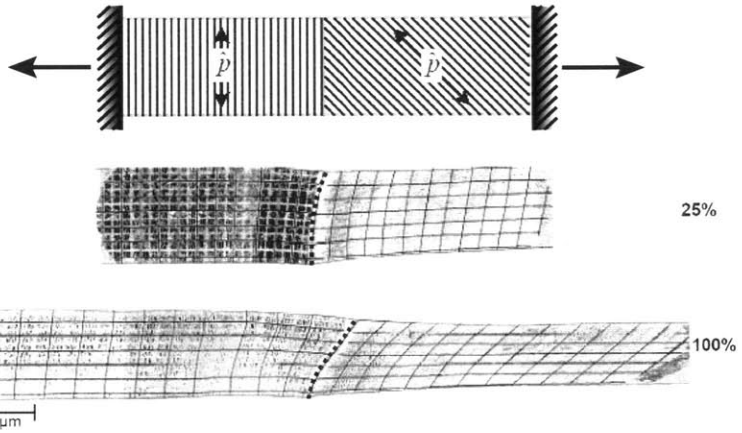

Figure 3-9: Schematic of the asymmetric bicrystal $90^{\circ}/45^{\circ}$ specimen configuration and optical images of the deformed specimen grid at 25% and 100% macroscopic specimen strain.

Simulation Results The deformation results for the 90°-45° bicrystal are presented in

[1]For the cylindrical morphology, microstructural buckling occurs at high stretches of about 80% because the rubbery matrix is relatively free to deform around the glassy rods before sufficient dilative pressure builds up to compress and to buckle the cylindrical microstructure. In the case of lamellar morphologies, the glassy layers impose a much stronger constraint on the almost isochoric deformation of rubbery layer, and thus the compressive stress exerted on glassy layers is already high enough to cause their buckle at quite small strains.

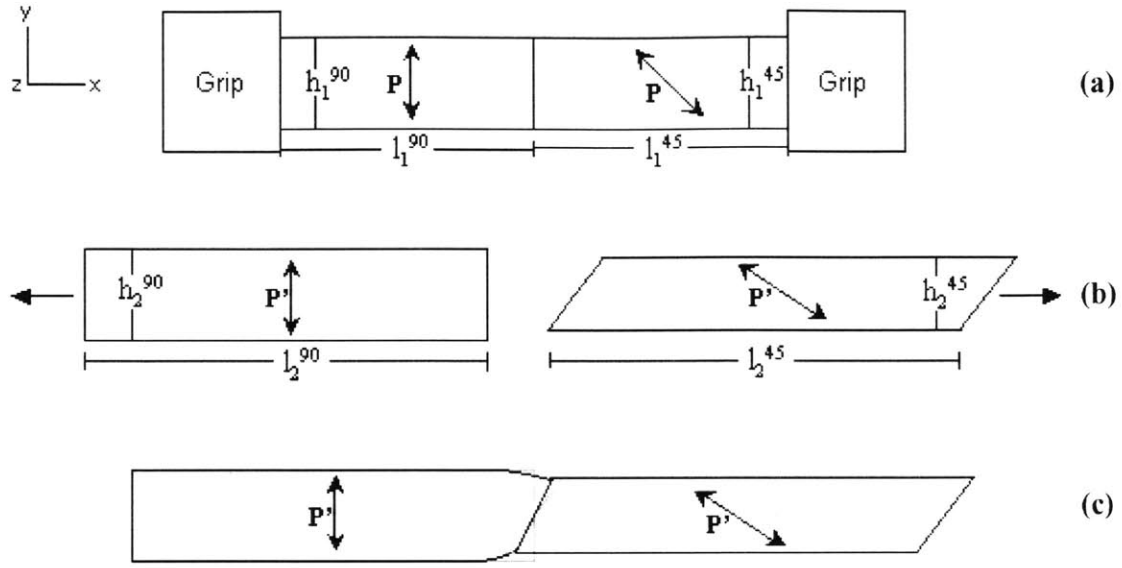

Figure 3-10: Schematic illustration of how specimen deformation is accommodated between grains of incompatible deformation modes in the 90°/45° bicrystal specimen configuration.

Fig.3-11. The axial strain contour and the deformed mesh at 12.5% nominal specimen strain show that deformation in the diagonal grain is accommodated by shear. The stress contour for the axial stress in glassy layers, σ_{ss}, shows that the glassy layers experience compressive forces at the grain boundary due to the mismatch in the lateral contraction of the two grains. Due to the compression, buckling initiates in the 90° grain at 15% macroscopic strain. Buckling initiation is easier viewed in the shear strain (E_{12}) contour plot of Fig. 3-11 (*bottom*), where opposite shearing, due to buckling, element rows are colored differently (red and blue). Due to the constitutive model's inherent capability to capture the initiation of buckling, hourglassing instabilities are excited in the numerical calculations for strains higher than 15%. For this reason, numerical results from beyond this strain level are not presented. These results are in agreement with the previously discussed experimental observations. The model captures the relative differences in the deformation across the grain boundary and is capable of reproducing critical microstructural rearrangements. Initiation of microstructural kinking within the 90° grain at the grain boundary occurs at much smaller strains than observed in the experiments, because the constitutive model describes

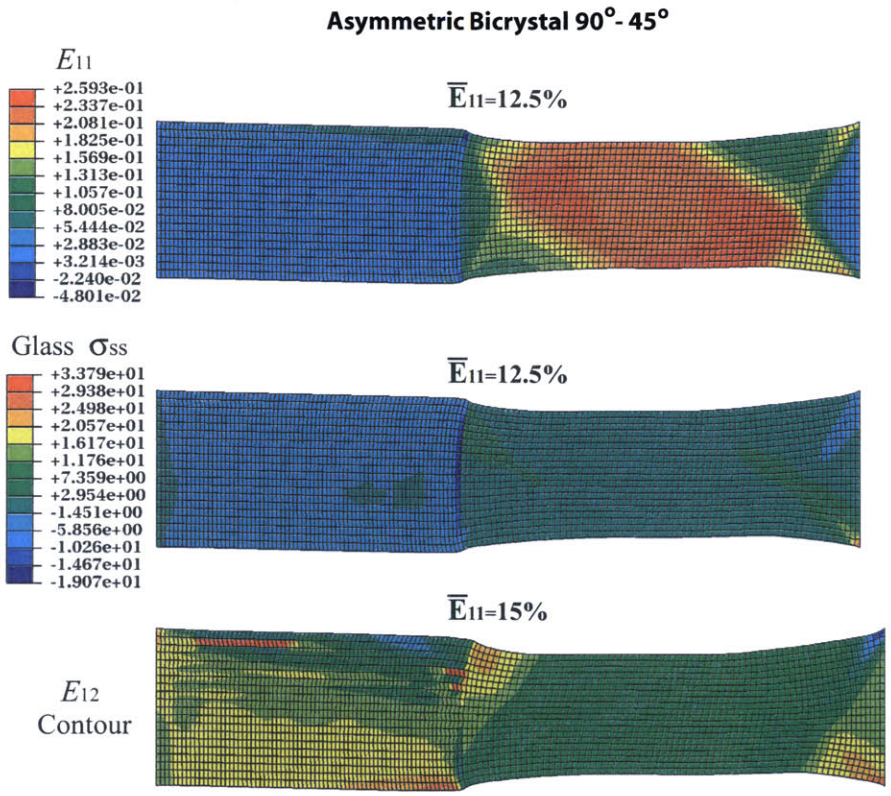

Figure 3-11: *Asymmetric* 90°/45° *Bicrystal:* Strain and microstructural stress contours.

layered and not cylindrical morphologies.

3.0.5 Asymmetric Bicrystal: 90°/0° Grain Boundary

Experimental Results Fig. 3-12 presents a schematic of an asymmetric bicrystal configuration with grains oriented at 90° and 0° to the 1-axis, named the *"T"*-grain bicrystal. For materials with cylindrical morphologies, single-crystal morphologies oriented parallel to the stretching direction exhibit the stiffest response to loading, while those oriented normal to the stretching direction are the most compliant. Therefore, the *"T"*-bicrystal is the configuration which combines grains with the highest possible stiffness contrast for the cylindrical morphology.

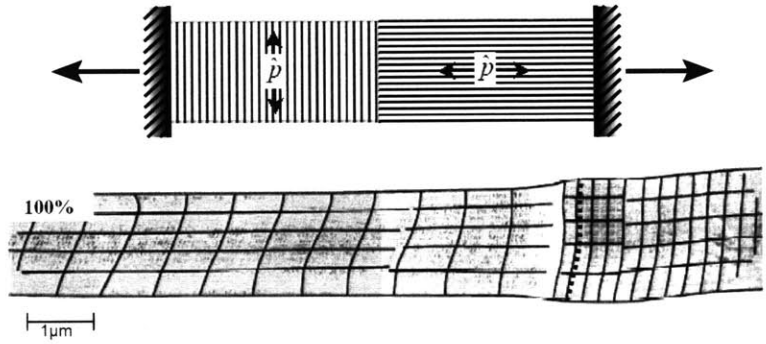

Figure 3-12: Schematic of the asymmetric 90°/0° bicrystal and deformed specimen grid at 100% nominal specimen strain.

The grid of the *"T"*-grain bicrystal is shown in Fig. 3-12 deformed at 100% nominal strain. In the undeformed specimen both grains have equal lengths. Due to the high stiffness contrast between the two grains, with the 0° (parallel) grain being 25-fold stiffer than the 90° (normal) grain, deformation concentrates entirely in the compliant normal grain. As can be viewed in cell snapshots taken from the deformed grid within each grain at equal overall specimen deformations, the stretch in the normal grain is twice the macroscopically imposed stretch to compensate for the relative inextensibility of the parallel grain. For specimen strains higher than about 50% (about 100% extension for the normal grain) the morphology of the normal grain has kinked and deformation in this grain proceeds not only by dilation of the rubber matrix, but also by cylinder rotation and rubber shear. Due to this restructuring, the lateral contraction in the normal grain becomes prominent enough and a

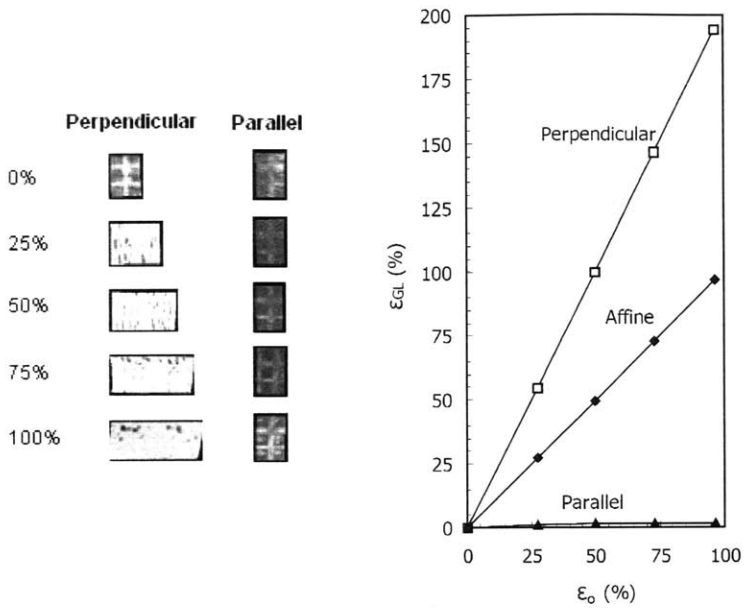

Figure 3-13: *Left:* Deformed grid cells from within the two grains. *Right:* Axial strains in the two grains *vs.* the macroscopically imposed strain.

deformation mismatch occurs at the grain boundary. At high stretches shear bands develop in the parallel grain due to cylinder fragmentation, and extend through the grain boundary causing the slight waviness of the grain boundary visible in Fig. 3-12.

The spatial influence of the grain boundary is minimal. Due to the high stiffness contrast between the two grains, each one deforms as a single-crystal in isolation, with the parallel grain acting as a rigid grip for the compliant normal grain[2].

3.0.6 Simulation Results

The deformation results for the 90°-0° bicrystal are shown in Fig.3-11. The figure presents contours of the in-plane stress within the glassy layers at very early stages of the deformation. The vertical grain deforms by dilation of rubbery layers in the microstructure. Due to the nearly incompressible behavior of rubber, the glassy layers experience a distributed compressive stress. The contours correctly indicate that the glassy layers in the parallel grain are extended, while glassy layers in the normal grain are under compression, which causes microbuckling. It can be seen in the contour legends that the compression exerted

[2]There is also minimal spatial influence from the grain boundary in the case of the 90°-/45° bicrystal. The reason there being the high compliance of both grains.

on the glassy layers in the normal grain is relieved as microbuckling initiates. Subsequent deformation is accomodated by the normal grain through interlamellar shear. The onset of shear deformation due to microbuckling is clearly indicated by the coloring in the shear strain contour plot, where alternating rows of elements are seen to shear in opposite directions within the normal grain. Hourglassing instabilities do not permit the study at strains

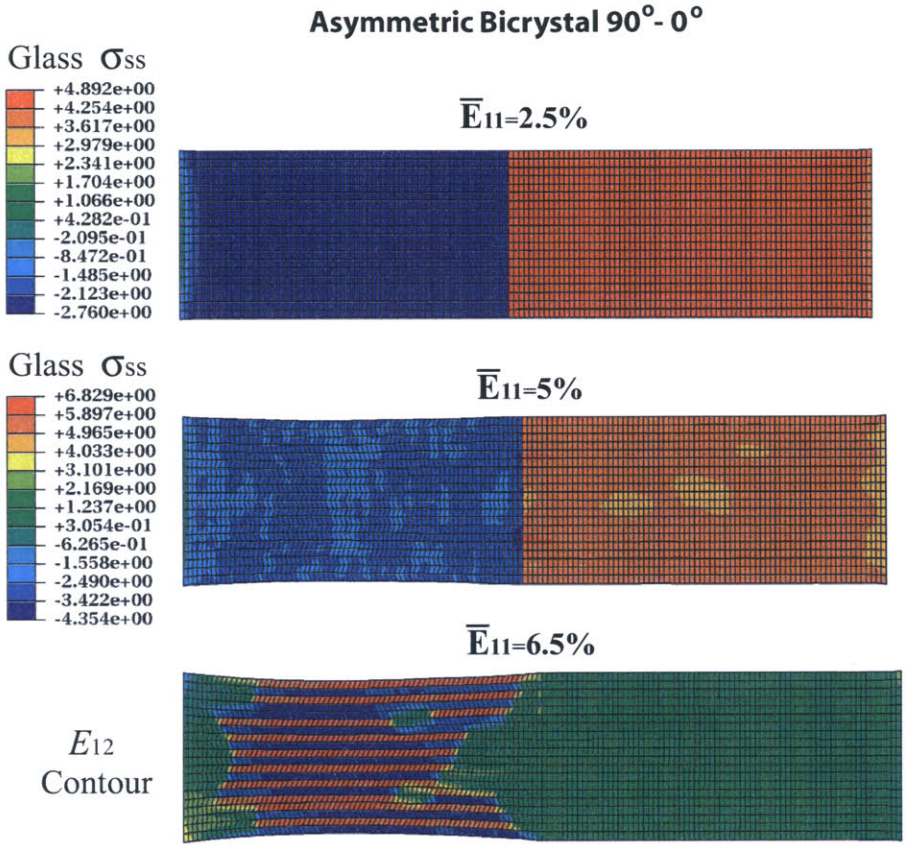

Figure 3-14: *Asymmetric* 90°/0° *Bicrystal:* Contours of in-plane stress within the glassy layers.

higher than 7%. Also, as described before, microbuckling initites at smaller strains for layerd morphologies. However, the presented results qualitatively agree with the micromechanical experimental findings from cylindrical morphologies.

Conclusions

The effect of isolated deformation constraints on the deformation behavior of lamellar block copolymers was examined with plane-strain numerical calculations of the tensile

behavior of oriented and bicrystal strip specimens, when grip constraints are imposed at the specimen ends.

The simulations have shown that the imposed extension on oriented material strips is accommodated by both shear and axial stretching, with relative contributions of shear and extension depending on the initial orientation as well as the imposed strain level. The grip boundary constraint and the specimen length have a very strong influence on the homogeneity of the deformation field. The spatial extent of the boundary influence depends strongly on the initial lamellae orientation and the specimen length.

For the case of bicrystal specimens, three bicrystal grain arrangements were examined. The resulting deformation patterns across the boundary and throughout the entire specimen are in excellent agreement with the experimental findings by Wanakamol and Thomas [51]. The nature and spatial extend of the grain boundary influence on the deformations of such bicrystal configurations strongly depends on the relative orientations of the neighboring grains and on the nature of the imposed loading. Micromechanical observations from the plane-strain extension tests on tensile strip specimens closely correlate to micro- and macrodeformation modes present during the extension of bicrystal strip speciens. The constitutive model was able to capture buckling instabilities which occur due to deformation incompatibilities at the grain boundary. A buckling criterion has not been rigorously implemented in the model, and due to the models inherent tendency to capture lower energy deformation modes, the finite element models used to calculate the deformation field within the asymmetric bicrystals exhibited hourglassing instabilities during the analysis.

Chapter 4

Deformation Mechanics of PolyCrystalline Lamellar Block Copolymers

4.1 Background

Unless an orientation technique is used during BCP solidification, BCPs develop polygranular structures analogous to the polycrystalline structure of metals. Fig. 4-5 depicts a micrograph of a polygrain lamellar BCP structure. Some of the earliest *in-situ* studies on the microstructural evolution of lamellar SBS triblock copolymers during tensile stretching were conducted on polygrain microstructures by Fujimura and Hashimoto *et al.* [17, 18]. TEM and SAXS were used to investigate the micromechanics that govern the softening behavior, and the stress rise observed after the stress-plateau region, termed the *"plastic-to-rubber transition"*. The specimens were polycrystalline spin cast films of various PS contents, some of which possessed a lamellar morphology with lamellar thickness $d = 26.9$nm.

The $\sigma - \epsilon$ response and SAXS pattern evolution during two loading cycles is shown in Fig. 4-1b for samples of SBS and SBS-PS blends. Akin to ductile polymer behavior, the response to first loading exhibits an initial linear region, followed by a distinct yield-

point and rapid softening, a subsequent constant-stress plateau during neck-drawing, and finally a rapid increase in stress prior to failure. Unloading takes place with substantial strain recovery, while reloading reveals a rubber-like material response devoid of yielding and necking phenomena. As it appears from deformed microdomain micrographs (Fig. 4-1a), yielding and neck-drawing are governed by lamellar reorientation, kinking, shearing, dilation, and finally, at very large strains, fragmentation mechanisms. Consistent with the diffuse SAXS patterns and the rubber-like behavior observed at strains higher than 200%, micrographs from that strain range displayed fragmented PS lamellae dispersed in PB. The schematic of Fig. 4-1c illustrates the micromechanical deformation processes that take place at different stages of the deformation response.

Further quantitative analysis on small strain ($< 30\%$) SAXS data verified that lamellae originally oriented perpendicular to the load direction exhibit an increase in their lamellar repeat distance but lose their packing order by micromechanical mechanisms such as lamellar rotation, shearing, kinking, and fragmentation. On the contrary, at the early deformation stage, lamellae originally oriented parallel to the stretching direction do not reorient and their lamellar spacing does not vary appreciably; thus, they retain their packing order. This is a consequence of their increased stiffness with respect to abutting grains, which renders them to be far less extensible, and thus behave as "hard grains/fillers" at these low macroscopic strain levels. Upon further stretching, the equatorial SAXS maxima corresponding to these particular grains disappear, indicating that the packing order in the specimen microstructure has been destroyed by aforementioned deformation micromechanisms, due to compatibility issues and grain interactions with neighboring grains. During neck-drawing, the evolution of the 4-point SAXS pattern indicates further lamellar tilting of grains initially oriented off-axis toward the stretching direction with constant lamellar spacing along the lamellar normal.

The yield and post-yield deformation behavior and micromechanics of polycrystalline lamellar SBS triblocks were studied in detail by Seguela and Prud'homme [19]. The specimens were solvent cast films containing 29vol% PS. During uniaxial tension, *in-situ* small angle X-ray scattering analysis was coupled with local strain-ellipsoid measurements from the neck region to monitor grain orientation and interlamellar shear at different strain in-

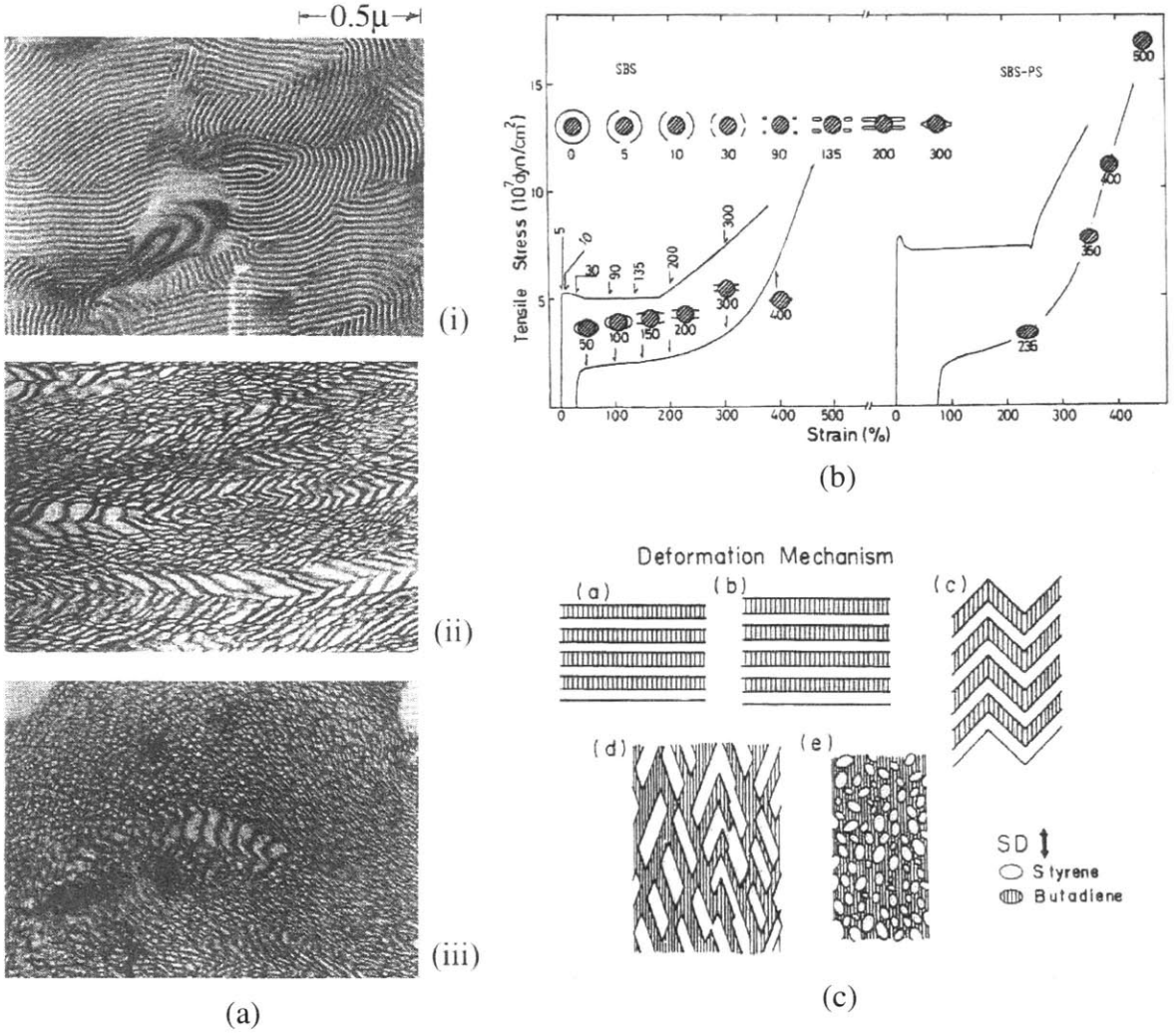

Figure 4-1: *(a)* Deformed microstructures of multigrain lamellar SBS block copolymers at different macroscopic strains: (i) 0%, (ii) 85%, and (iii) 500%. *(b)* Stress-strain response for the 1^{st} and 2^{nd} tensile cycle shown without the unloading curve. Superposed are schematics of the corresponding SAXS pattern at each strain. *(c)* Schematic illustration of the micromechanical deformation processes within an isolated grain, initially oriented normal to the loading axis, during the deformation of lamellar block copolymers [17, 18].

stances. As the local measurements verified, the deformation inside the neck was volume preserving and the lateral contraction isotropic, leading to the conclusion that strain was mostly accommodated by the rubbery domains. The first-order SAXS diffraction maxima formed the characteristic four-point pattern, which corresponds to symmetric grain rotation about the stretching direction. The pattern evolution suggests that, despite the random orientation in the as-cast material, grains gradually attain a favorable orientation of $\sim 22^\circ$ and accommodate additional deformation only by interlamellar shear. Grains with a different initial orientation, either lost their stacking order, or rotated to assume this preferential configuration. The kinematics of this deformation process involve large grain elongations along the stretching direction by rotation and shearing of the rubber layers, a process that preserves d-spacing (see schematic in Fig. 4-2)[1]. The dominant grain inclination of 22° results from an energetic competition between: *(i)* the energetically inexpensive deformation mode of grain rotation toward the loading direction and concurrent shearing of the rubbery layers (Fig. 4-3a), and *(ii)*, the counterbalancing increase in stiffness for continuous grain rotation toward orientations parallel to that of loading (Fig. 4-3b).

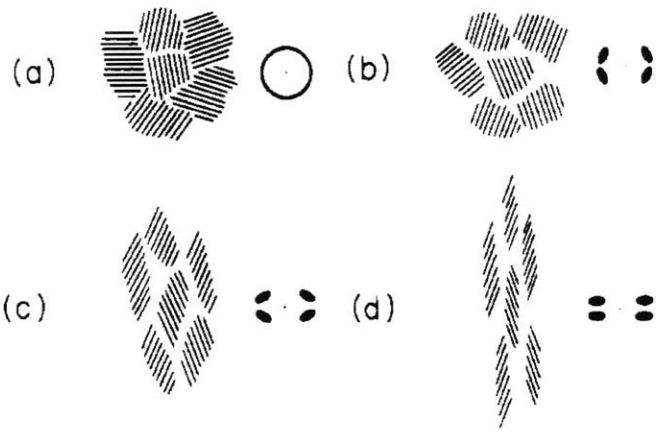

Figure 4-2: Schematic of grain reorganization and corresponding SAXS patterns at different levels of tensile strain for a multigrain lamellar microstructure [19].

It is known that the mechanical behavior of poly-crystal aggregates is determined by the collective response of individual grains. In turn the behavior of each grain is determined

[1]In contrast to the previously desribed interpretation of the micromechanics by Fujimura and Hashimoto [17, 18], Seguela and Prud'homme do not consider intragranular lammelar kinking in their reasoning of deformation kinematics. The dominance of kinking in polycrysatlline BCP deformation micromechanics has however been established by several TEM studies.

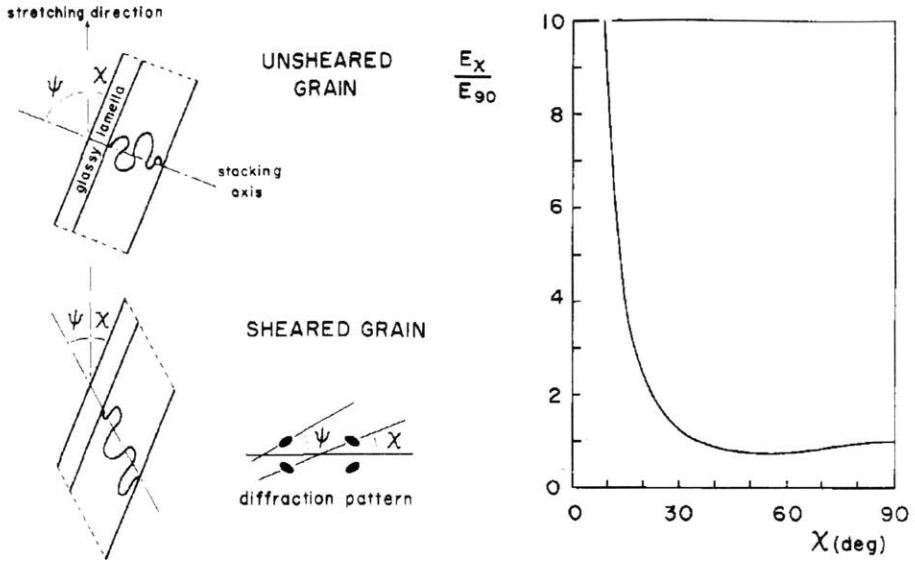

(a) (b)

Figure 4-3: (a) Accommodation of strain by rotation and shear in a lamellar glassy/rubbery microstructure. (b) Increasing grain stiffness for lamellar orientations near parallel to the direction of loading [19].

by the deformation modes excited through interactions with neighboring grains through the influence of grain boundaries. The effect of grain size and grain boundaries on the stiffness, yield, and post-yield behavior of lamellar SBS triblock copolymers was studied by Myers and Cohen [20]. Styrene- and butadiene rich triblock samples[2], containing 75 and 45wt% PS, respectively, with multi-grain lamellar microstructures[3] of various grain sizes were compared under uniaxial tension. Grain sizes ranged between 0.27 and 3.31μm for the PS rich-, and between 3.72 and 5.80μm for the PB rich copolymer. In addition, extruded (*"highly textured"*) samples of the styrene rich BCP were deformed in tension at various orientations to their textured microstructure to establish stiffness bounds (Fig. 4-4a).

An interesting trend was established for the styrene rich material, for which the yield stress was reported to increase with increasing grain size (Fig. 4-4b). The trend was reversed for the PB rich samples with the yield strength being higher for smaller grain sizes (Fig. 4-4c). For all but one of the materials tested, the elastic modulus appeared to be

[2]Commercial name for styrene rich (75wt% PS) triblock copolymer: KK31, MW=187,000, lamellar spacing d$\simeq$35nm. Commercial name for butadiene rich (45wt% PS) triblock: 4461, MW=82,000, d$\simeq$28nm.

[3]A lamellar microstructure for 75wt% PS is surprising.

grain-size independent[4]. Also, as can be seen in Fig. 4-4b, the multigrain material yield-stress for KK31 is between the respective *maximum* (at 90°) and *minimum* (at 30°) values measured for extruded samples (Fig. 4-4a)[5]. The authors attribute these differences to higher PS and PB concentration at the grain boundaries for PS- and PB-rich samples, respectively. They offer however no proof of this related to their data, neither do they report the amount of the suggested material excess. Since the two triblocks tested had different molecular weights and non-overlapping grain sizes (not to mention that the grain variation is in fact quite small), and due to the increased complexity introduced by the chosen molecular architecture of the polymer blocks used (which also strongly affects the response), it is unclear whether the coupling between the grain size and the mechanical response of polycrystalline BCPs was succesfully isolated[6]. Grain boundaries have been early realized as a controlling factor in the mechanical properties of multigrain BCPs. The morphology of grain-boundary defects has been studied both experimentally via TEM and analytically with interphase-area minimizing theories by Gido *et al.* [52, 53, 54, 55], and experimentally with TEM by Cravalho *et al.* [21]. Various grain-boundary structures are shown in Fig. 4-5. All but T-junctions maintain phase connectivity across grain-boundaries

[4]Only a 3-arm star BCP (KRO3, MW=217,000) containing 79wt%PS showed appreciable stiffness increase with increasing grain size.

[5]The lowest axial stiffness is expected for loading at 45° to the plane of the lamellae. In Mayer's study the lowest stiffness is measured at 30° (or 0°; the reported data data and the corresponding $\sigma - \epsilon$ curves appear to be very inconcistent!), either because extrussion did not produce perfectly oriented microstructures, or due to incorrect measurement of the sample's microstructural orientation.

[6]In the absence of other relevant experimental and/or FE-based micromechanical studies, one can only be cautious and very reluctant in offering alternative explanations to Myers' results. With this in mind, an extrapolation based solely on single-crystal micromechanical studies will be attempted here. Depending on the grain-size and BCP composition, different micromechanical deformation modes are expected to dominate, with a different impact on the macroscopic response. Namely, grain rotation is more difficult for large as opposed to small grains. Small grains can immmediately tilt and assume a configuration that encourages interlamellar shear in the rubbery domains. Large grains overcome the rotation constraint by accomodating deformation initially through dilation and subsequently by kinking. On the other hand, kinking is energetically expensive for short lamellae, due to their high bending resistance. Thus, by immediately commencing to PB shear, small grains respond to deformation with a mode of reduced micromechanical resistance and result in lower macroscopic yield-stresses. Analogously, large grain polycrystalline structures, due to the nearly incompressible response of PB to dilatation, exhibit a higher deformation resistance at the microstructural level, and consequently, higher macroscopic yield-stresses. Previous experimental studies on polycrystalline lamellar SBS BCPs [17, 18, 19] lend support to both conjectures. It was shown that the favorable deformation mechanism was that of interlamellar shear, which all grains try to achieve by tilting toward the loading direction. Grains for which rotation was impeded resorted to kinking in order to accomplish a configuration that would finally allow them to shear. These conjectures however, remain to be evaluated with future multigrain FE-based micromechanical models.

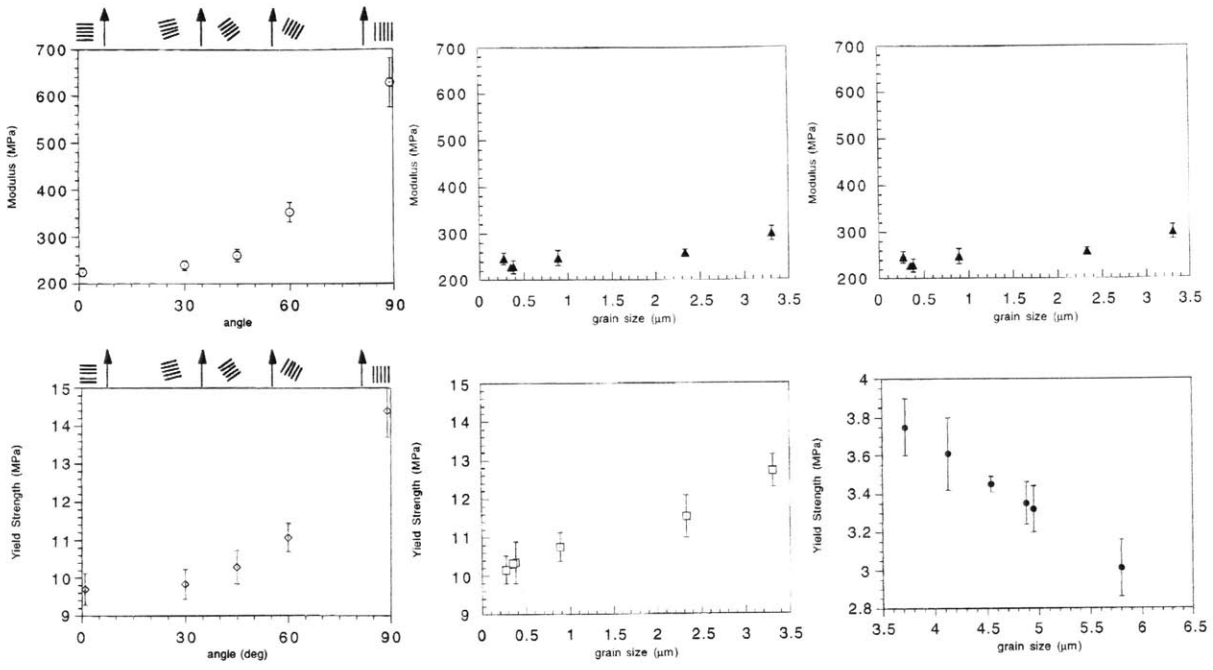

Figure 4-4: Modulus and yield strength variation versus grain size [20] for: *(a)* Extruded (textured) lamellar KK31 samples (75wt% PS). *(b)* Cast (multigrain) lamellar KK31 samples (75wt% PS), and *(c)* Cast (multigrain) lamellar 4461 samples (45wt% PS).

by a gradual change of lamellar orientation. This microstructural grain-boundary feature might be important for multigrain micromechanical modeling. It is not known whether specific defects are related to particular grain sizes, constituent compositions, or molecular architectures. Furthermore, despite on-going efforts [51], no research yet has isolated the influence of specific defects on the overall mechanical behavior. Thus, we cannot correlate the influence of specific grain boundary imperfections with Myers' findings on the grain-size-dependency of the mechanical behavior.

4.2 Polycrystal Simulations

Polycrystal simulations aim to investigate and predict how the interactions and collective response of individual grains determine the effective mechanical behavior of the polycrystalline lamellar BCP aggregate. The analytical constitutive model was shown to predict accurately the highly anisotropic stress-strain behavior of the single-crystal lamellar material

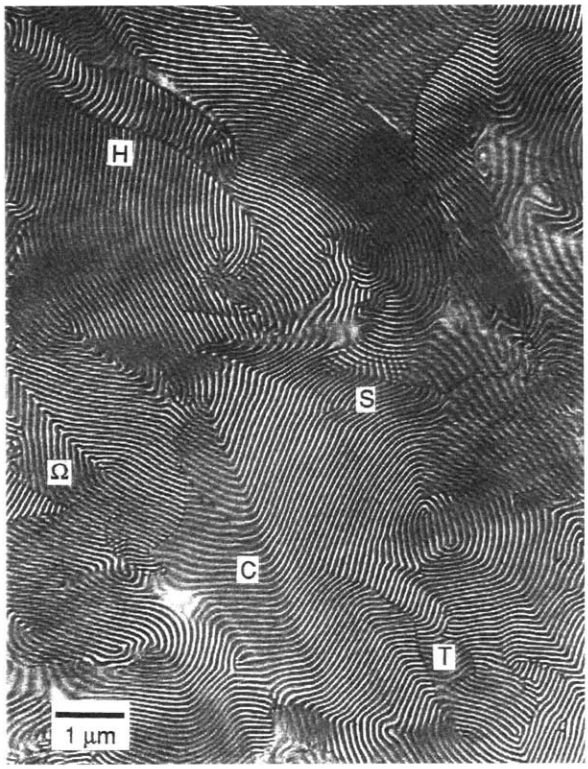

Figure 4-5: Multigrain lamellar morphology and grain boundary types: *Chevron* (*C*) and *Omega* (Ω) (*tilt boundaries*), *Scherk* (*S*) and *Helicoid* (*H*) (*twist boundaries*), and *T-junction* (*T*) defects [21].

and will be used to assign the behavior of individual grains within polygranular finite-element-based representative volume elements (RVEs). During tensile experiments on polycrystalline lamellar BCP samples, it has been observed that small macroscopically imposed deformations are accommodated by dilatation of rubbery layers within grains which are oriented normal to the deformation axis, and by rubber layer shear within grains oriented other than normally or tangentially to the loading direction. With increasing deformation, the increase in rubber layer dilation within grains oriented normal to the loading direction results in lamellar buckling and subsequent accommodation of deformation by increasing layer tilting and rubber layer shearing. On the other hand, grains originally aligned with the loading axis exhibit minimal extensibility. For all grains, a tendency to gradually align with the loading direction has been observed until a universal locking orientation is attained for all grains, beyond which deformation occurs mostly by additional dilatation of rubber layers. These deformation micromechanisms have been schematically outlined in Figs.4-1c and 4-2.

The objective of the polycrystalline numerical simulations presented in this chapter is to reproduce the observed micromechanics accurately, and allow for a detailed investigation of the polycrystalline lamellar BCP response. It is shown in the results section that the numerical polycrystalline RVEs predict microstructural evolutions which are in successful correspondence with the fine details from the above experimental observations. In addition, stress- and strain-field information from such polycrystalline studies provide insight as to whether simple homogenization schemes such as the Taylor and Sachs models for polycrystalline materials can reproduce accurately the mechanical behavior of the polycrystal, and suggest directions for averaging schemes which are appropriate and physically meaningfull for these, as well as for analogous, highly anisotropic materials.

4.2.1 The Polygranular Representative Volume Element

The representative volume element used to calculate the mechanical response of a polycrystalline microstructure is depicted in Fig. 4-6. The RVE is a simple parallelogram divided into 56 identically shaped, hexagonal regions, each one of which represents a single

grain. For the current analysis, all hexagonal grains have been identically discretized with 400 four-noded, reduced integration, plane-strain elements (type CPE4R in ABAQUS Explicit). Each grain is assigned a randomly chosen orientation with respect to the 1-direction, and its response to loading is described with the analytical constitutive model for lamellar BCPs. For a periodic RVE, grains that appear discontinued at one RVE boundary (face), actually continue as mirror images across the opposite facing boundary, should be assigned the same material orientation across the associated boundary. This assignment imposes material periodicity. Geometric periodicity is guaranteed by imposing periodic displacement boundary conditions on opposite faces of the RVE, such that the deformations these attain are always compatible for RVE stacking. Using the notation of Fig. 4-6, the periodic displacement boundary conditions applied on opposite facing boundaries of the RVE are as follows:

$$\begin{aligned} \mathbf{u}|_{BC} - \mathbf{u}|_{AD} &= \mathbf{u}|_{B} - \mathbf{u}|_{A} \\ \mathbf{u}|_{DC} - \mathbf{u}|_{AB} &= \mathbf{u}|_{D} - \mathbf{u}|_{A} \\ \mathbf{u}|_{A} &= \mathbf{0} \end{aligned} \qquad \begin{aligned} u_1|_{BC} - u_1|_{AD} &= u_1|_{B} - u_1|_{A} \\ u_2|_{BC} - u_2|_{AD} &= u_2|_{B} - u_2|_{A} \\ u_1|_{CD} - u_1|_{AB} &= u_1|_{D} - u_1|_{A} \\ u_2|_{CD} - u_2|_{AB} &= u_2|_{D} - u_2|_{A} \\ u_1|_{A} &= u_2|_{A} = 0 \end{aligned} \tag{4.1}$$

Using the RVE of Fig. 4-6, the behavior of the polycrystalline microstructure was studied under two loading situations: plane-strain extension and plane-strain simple-shear deformation.

Plane-strain Extension: Plane-strain extension is imposed by restraining deformation in the 3-direction, prescribing a stretch in one direction, and leaving the remaining third orthonormal direction traction-free. A hexagonal grain has inherent anisotropy, due to its geometry. In the global frame of Fig. 4-6, loading along direction-1 translates in loading along grain boundaries while extension in direction-2 results in loading normal to grain boundaries. The behavior of the RVE is thus studied under extension both along the 1-direction (with direction-2 being traction-free), and along direction-2 (with direction-1 left traction-free)[7]. The *imposed* macroscopic deformation gradients for these two loading

[7]The calculation results show that the layered material's anisotropy is more influencial for the RVE response than the anisotropy induced by the grain shape. However, the considerable variation observed for

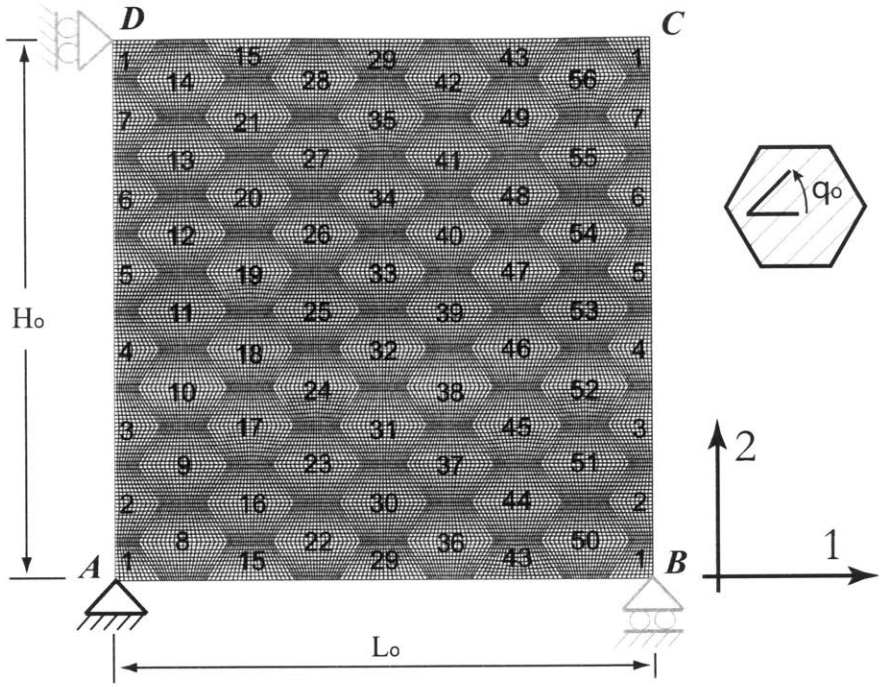

Figure 4-6: Undeformed Polygranular RVE mesh containing 56 hexagonal grains.

orientations are, respectively:

$$\overline{\mathbf{F}}_1 = \lambda\, \mathbf{e}_1 \otimes \mathbf{e}_1 + 1\, \mathbf{e}_3 \otimes \mathbf{e}_3 \tag{4.2}$$

$$\overline{\mathbf{F}}_2 = \lambda\, \mathbf{e}_2 \otimes \mathbf{e}_2 + 1\, \mathbf{e}_3 \otimes \mathbf{e}_3 \tag{4.3}$$

The plane-strain condition is enforced in direction-3, and λ is the applied stretch in the direction of extension. The resulting stretches (contractions) in the traction-free directions are calculated by satisfying the traction boundary conditions.

The imposed displacement on node C for a given macroscopic deformation gradient $\overline{\mathbf{F}}$, follows from Eqn. 4.2.1. Noting with u_1 the diplacement in the 1-direction and u_2 the diplacement in the 2-direction, extension in direction-1 is imposed by:

$$\mathrm{u}_1|_C = (\overline{\mathrm{F}}_{11} - 1) \cdot \mathrm{X}_C = (\lambda - 1) \cdot \mathrm{L}_o \tag{4.4}$$

ten calculated stress-strain curves indicates that 56 grains might not be a large enough grain population to decouple these two effects.

The stretch in the traction-free direction, $\overline{\mathrm{F}}_{22}$, is calculated from the boundary conditions. For the simple parallelogram RVE used here, $\mathrm{X}_C = \mathrm{L}_\mathrm{o}$ (RVE length) and $\mathrm{Y}_C = \mathrm{H}_\mathrm{o}$ (RVE height). Likewise, extension in direction-2 is applied as:

$$\mathrm{u}_2|_C = (\overline{\mathrm{F}}_{22} - 1) \cdot \mathrm{Y}_C = (\lambda - 1) \cdot \mathrm{H}_\mathrm{o} \tag{4.5}$$

and the stretch in the traction-free direction, $\overline{\mathrm{F}}_{11}$ in this case, remains to be calculated by satisfying the traction boundary conditions.

The applied deformation, boundary conditions, and the deformed meshes for the above two extension directions are shown in Fig. 4-7 at 20% nominal extension.

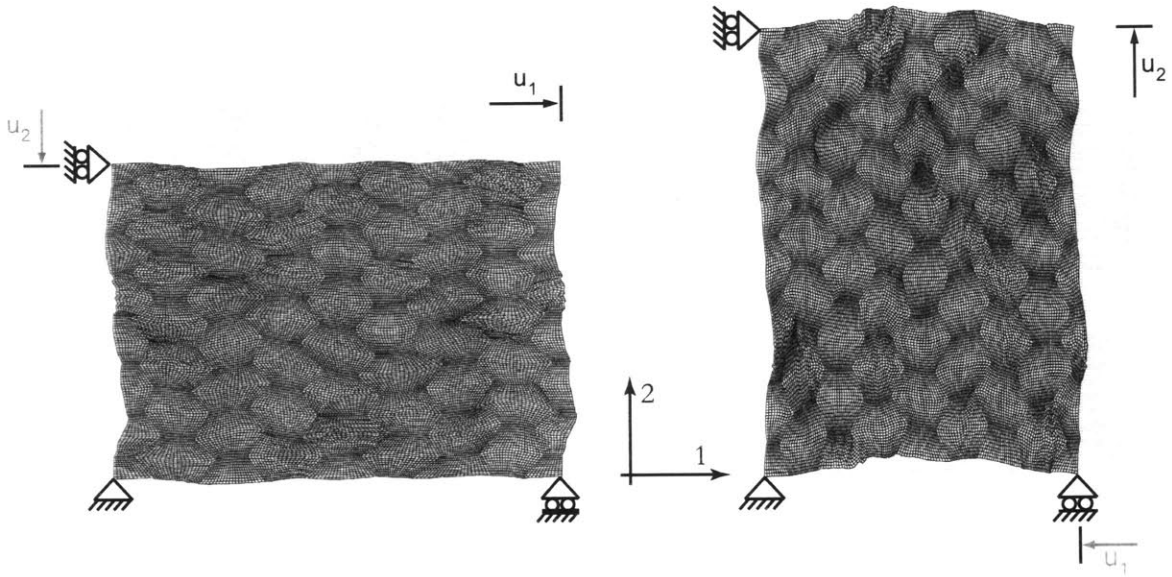

Figure 4-7: *Plane-strain Extension:* Deformed Polygranular RVE mesh. Displacements in the respective traction-free directions are shown in gray.

Plane-strain Simple Shear: Macroscopic plane-strain simple-shear is applied by restraining the through-thickness ($\overline{\mathrm{F}}_{33} = 1$ or $\epsilon_{33} = 0$) and lateral deformations of the RVE, while imposing a macroscopic shear angle γ in the transverse direction. Shear was imposed tangentially in two different orthonormal directions: direction-1, and direction-2.

The respective macroscopic deformation gradients are:

$$\overline{\mathbf{F}}_1 = 1\,\mathbf{e}_1 \otimes \mathbf{e}_1 + \tan(\gamma)\,\mathbf{e}_1 \otimes \mathbf{e}_2 + 1\,\mathbf{e}_2 \otimes \mathbf{e}_2 + 1\,\mathbf{e}_3 \otimes \mathbf{e}_3 \tag{4.6}$$

$$\overline{\mathbf{F}}_2 = 1\,\mathbf{e}_1 \otimes \mathbf{e}_1 + \tan(\gamma)\,\mathbf{e}_2 \otimes \mathbf{e}_1 + 1\,\mathbf{e}_2 \otimes \mathbf{e}_2 + 1\,\mathbf{e}_3 \otimes \mathbf{e}_3 \tag{4.7}$$

where γ is the applied shear angle.

The displacement imposed on node C for simple shear applied in direction-1 with macroscopic deformation gradient $\overline{\mathbf{F}}_1$, follows from Eqn. 4.2.1:

$$\mathrm{u}_1|_C = \overline{\mathrm{F}}_{12} \cdot \mathrm{Y}_C = \tan(\gamma) \cdot \mathrm{H}_\mathrm{o} \tag{4.8}$$

$$\mathrm{u}_2|_C = 0 \tag{4.9}$$

Likewise, for simple shear applied in direction-2 with macroscopic deformation gradient $\overline{\mathbf{F}}_2$, the imposed displacement on node C equals:

$$\mathrm{u}_1|_C = 0 \tag{4.10}$$

$$\mathrm{u}_2|_C = \overline{\mathrm{F}}_{21} \cdot \mathrm{X}_C = \tan(\gamma) \cdot \mathrm{L}_\mathrm{o}\ . \tag{4.11}$$

Fig. 4-8 illustrates the boundary conditions, the imposed deformation, and the deformed RVE meshes for the given shear direction at $\sim 50\%$ macroscopic shear strain.

4.2.2 Results

Using the derived analytical continuum model to describe the deformation behavior of grains within the multigranular RVE allows us to investigate in detail the different micromechanical mechanisms by which individual grains respond to the imposed loading and interact with neigboring grains. Contour plots of deforming RVEs monitor the evolving contrours of various field quantities including the distribution in axial strain, the distribution in "'microdeformation" gradient components (mainly the normal, shear and in-plane components of deformation gradients of the glassy and rubbery layers) as well as the lamellar orientations at three different levels of macroscopic stretch. Stress-related field quan-

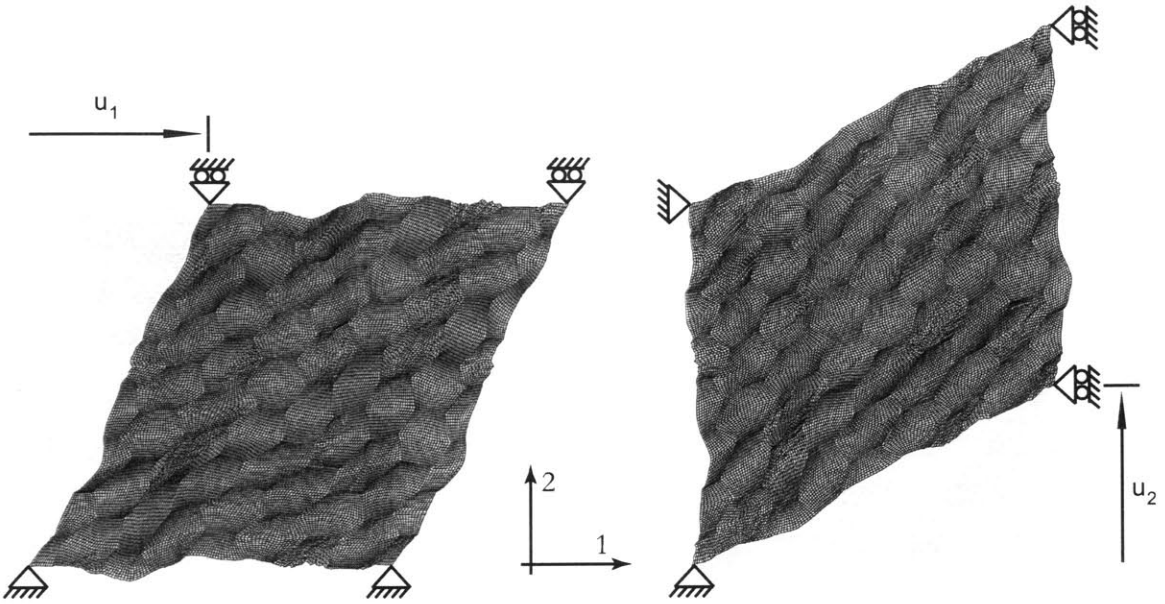

Figure 4-8: *Plane-strain Simple Shear:* Deformed Polygranular RVE.

tities are also contoured, including the axial stress and the micro-stress components of glassy and rubbery layers. The constitutive model maps the laminated single-crystal to a homogenized anisotropic medium. In order to understand the underlying deformation micromechanisms behind the effective behavior of the homogenized grain, its deformation needs to be decomposed into the deformation of its constituents[8] (hence, the contours of "'micro-deformation" components are provided). Therefore, cross-examination between layer-specific and grain-related kinematic quantities is necessary to interpret simulation results.

At the given macroscopic stretch levels, the calculated results are presented in contour plots and histograms. To allow qualitative cross examinations of kinematic and stress quantities, the contour plots are organized in two sets, each one of which correlates the initial, θ_o, and current (deformed) grain orientation, θ, to:

(a) rubber layer shear (component ${}^{r}F_{s_o n_o}$), rubber layer dilatation (component ${}^{r}F_{n_o n_o}$), glassy layer in-plane stretch (component ${}^{g}F_{s_o s_o}$), and effective grain strain in the stretch direction, E_{22}.

(b) rubber layer shear stress, ${}^{r}\sigma_{s_o n_o}$, rubber layer dilative (normal-to-layers) stress, ${}^{r}\sigma_{n_o n_o}$,

[8]The same change in the shape of a grain can, for example, occur through layer shear, dilation, extension, or any possible combination of these.

glassy layer axial (in-plane) stress, ${}^{g}\sigma_{s_o s_o}$, and effective grain stress, Σ_{22}, (the grain stress component which is coaxial with the imposed stretch).

The micromechanical observations from contour plots are verified quantitatively with histograms that track the evolving distribution of grain orientations -as these have been calculated at every element (integration point) throughout the RVE-, and the distributions of effective grain-deformation quantities.

Plane-strain extension: RVE-3 is chosen to present the micromechanical details of polycrystalline calculations. The results for plane-strain extension are given in Figs. 4-9 through 4-25. Fig. 4-9 gives the RVE's stress-stretch response to plane-strain extension in two different orthonormal directions, and the distribution of initial grain orientations, θ_0, within the RVE. The uniform distribution of initial grain orientations results in a highly isotropic RVE behavior. The calculated response is nonlinear isotropic with an initial linear regime and a departure from linearity at macroscopic stretch $\overline{F}_{22} \sim 1.03$, beyond which the stress response continues to increase monotonicaly, however with a reduced tangent modulus. Rough Taylor- and Sachs predictions for the small strain response of the given polycrystalline lamellar BCP material are superposed to the RVE's stress-stretch response. Taylor approximations determine a volume averaged response assuming all grains are subjected to the macroscopic deformation gradient. Sachs approximation computes a volume averaged stress-strain response assuming all grains experience the macroscopic stress state. It is already evident, and will be discussed in detail later, that simple Taylor and Sachs approximations give very wide bounds for the effective response of the given polycrystalline material, and thus, neither one can represent the polycrystalline behavior accurately. This motivates examining the micromechanical details of how the grains are deforming in order to gain insight that can lead to the development of appropriate micromechanically-based models for materials with such highly anisotropic single-crystal behavior.

Figs. 4-10 and 4-11 present deformation and stress contours from RVE-3 for extension in direction-2 and at macroscopic stretch $\overline{F}_{22} = 1.01$. At this very early stage of deformation, lamellar rotations are insignificant. Grains with initial orientations normal to the loading direction ($\theta_o = 0°$, $180°$), colored in the θ_o-contour as blue and red, accommodate deformation by rubber layer dilatation as can be seen from the high ${}^{r}F_{n_o n_o}$ values in the

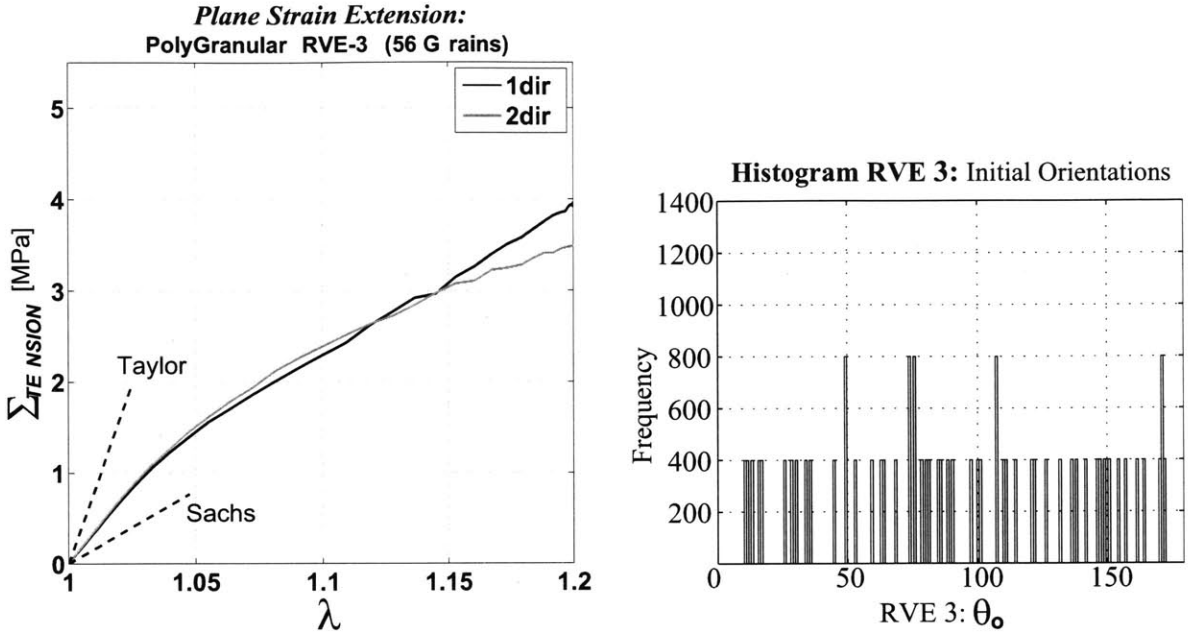

Figure 4-9: *Plane-strain extension* - RVE3*:* Stress-Stretch response and histogram of initial grain orientations, θ_0.

corresponding contour (see grains "*A*" and "*B*"). Likewise, the normal to layers (dilative) stress is higher for grains oriented normally to the loading axis as seen in the ${}^{r}\sigma_{nn}$-contour of Fig. 4-11. Consistently, glassy layers in these grains experience compression as shown by stress contours of ${}^{g}\sigma_{ss}$ in Fig. 4-11.

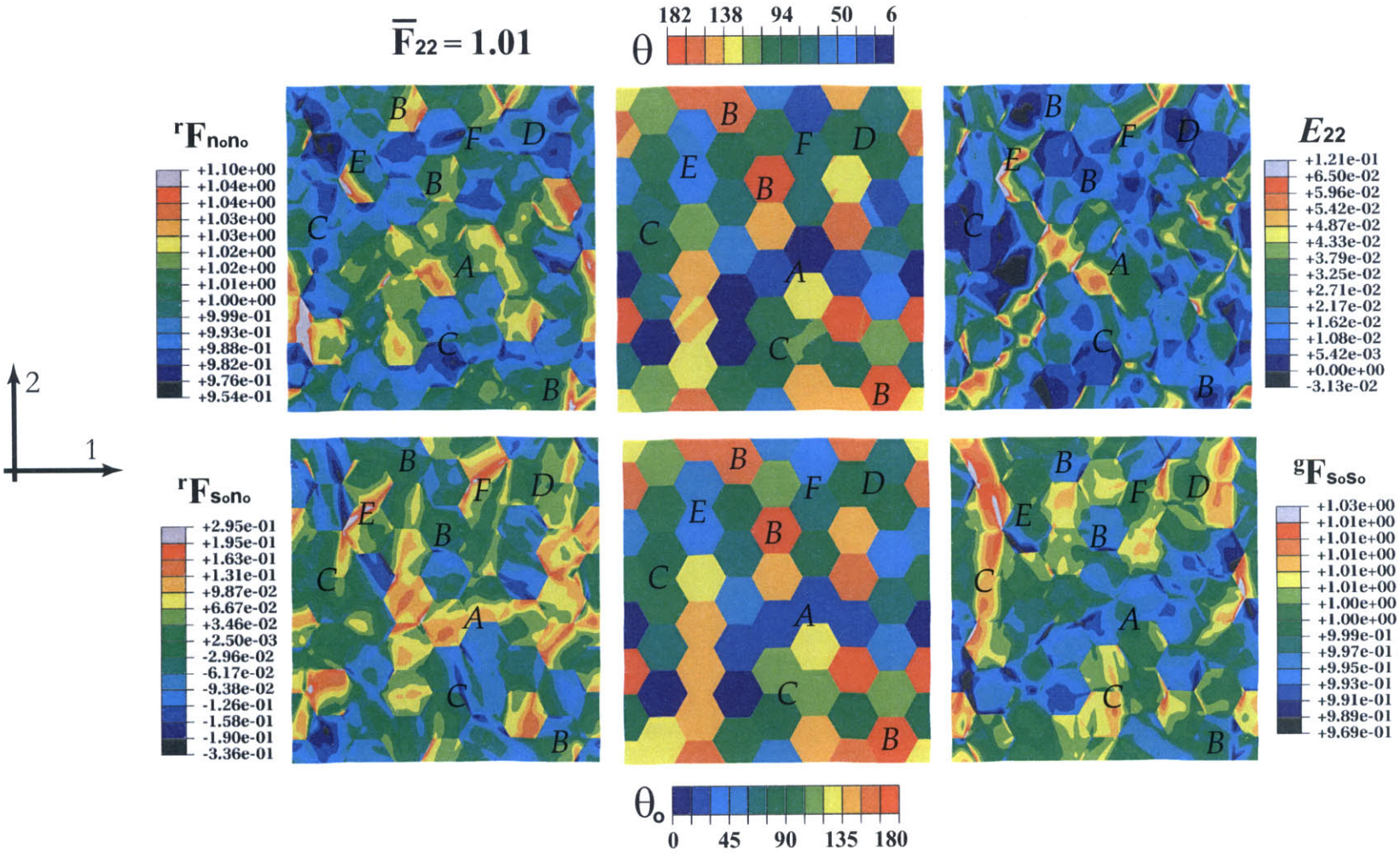

Figure 4-10: *Plane-strain extension* - RVE3*:* Strain contours at macroscopic stretch $\overline{F}_{22} = 1.01$.

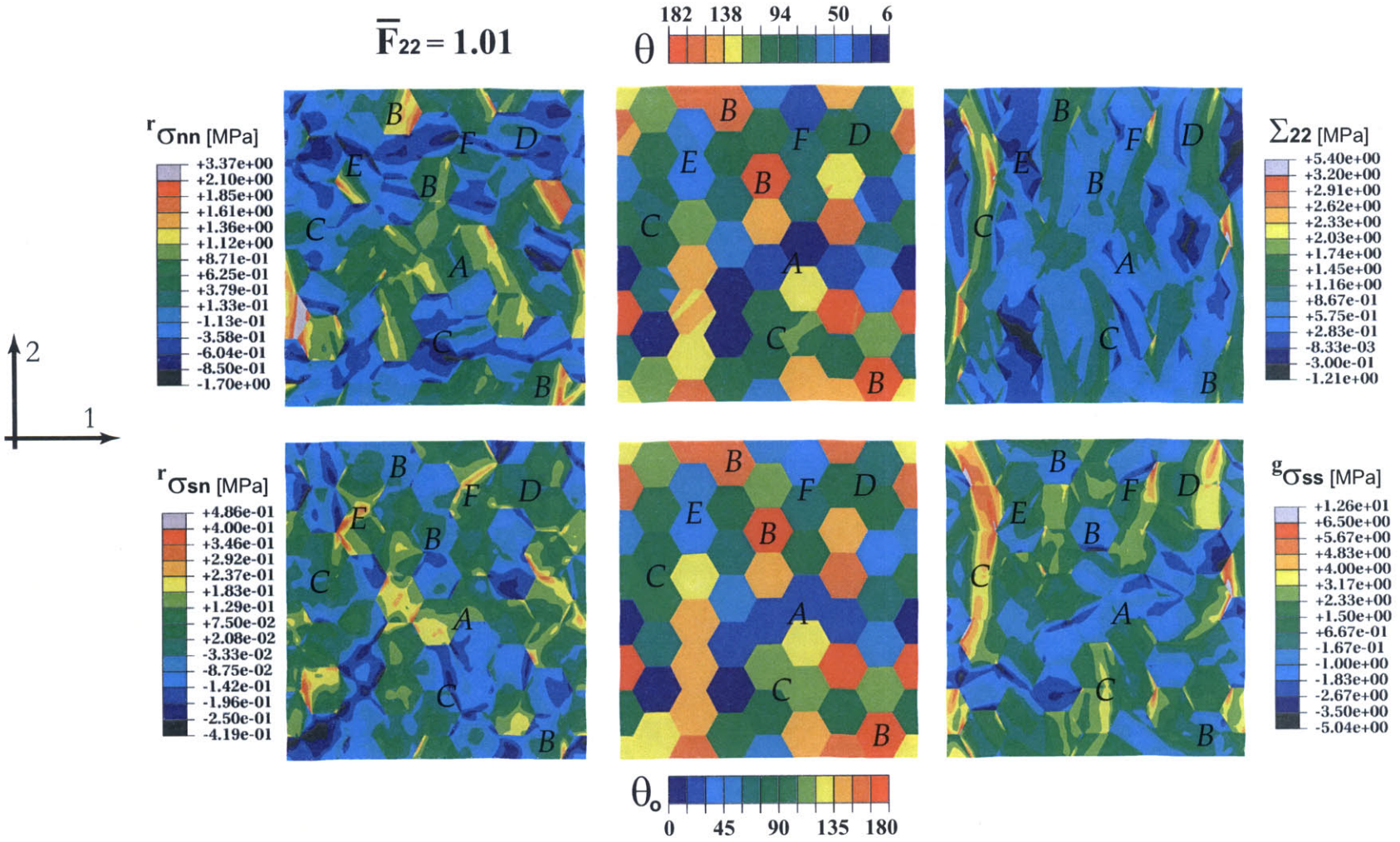

Figure 4-11: *Plane-strain extension* - RVE3*:* Stress contours at macroscopic stretch $\overline{F}_{22} = 1.01$.

Grains with their morphologies initially aligned or nearly-aligned to the loading axis ($\theta_o \sim 90°$; appearing green in θ_o-contours) show limited extension in the E_{22} strain contour (grains *"C"* and *"D"* in Fig. 4-10), due to the high stiffenss contrast with grains of other orientations, and act similar to hard fillers. Grains "C" even shield their highly compliant grain neighborhood. Due to the alignment with the load, the axial stress on glassy layers, ${}^{g}\sigma_{ss}$, within these grains is tensile (Fig. 4-11).

Grains with intermediate initial orientations with respect to direction-2 deform mostly by interlamellar rubber shear. Some of the highest values of shear deformation and stress with the rubber layers (${}^{r}F_{s_o n_o}$ and ${}^{r}\sigma_{s_o n_o}$, respectively) are seen within grains initially oriented at $\theta_o \approx 45°$, $135°$ to the loading direction. Grains *"E"* and *"F"* in the contours are characteristic.

The homogenized stress (Σ_{22}) and strain (E_{22}) contours in Figs. 4-10 and 4-11 show that stress and strain values vary considerably from grain to grain throughout the RVE, due to the high anisotropy in the single-crystal behavior. Strain is accommodated by the most compliant grains, while stress is balanced by the stiffest ones. It is therefore physically incorrect to map an affine, homogeneous stress or strain field to the respective fields within the polycrystal body. Hence, the Sachs and Taylor models are inappropriate descriptions for these polycrystalline configurations.

Figs. 4-12 through 4-15 give micromechanical contours at macroscopic stretches $\overline{F}_{22} = 1.1$ and $\overline{F}_{22} = 1.2$. It is evident from all contours that significant micromechanical restructuring has occurred between a stretch of $\overline{F}_{22} = 1.01$ and $\overline{F}_{22} = 1.1$. These deformation processes are visible in the evolution of θ-contours. Also, Fig. 4-16 summarizes the interrelated micromechanics, and presents among others the layer tilt angle, α, contour in reference to initial grain orientations, θ_o. Grains initially oriented parallel to direction-2 experience limited or no rotation at all; their tilting is negligible in Fig. 4-16 (grains *C* and *D*). Grains with initial orientations belonging to color-regions adjacent to green, have gradually tilted to the $90^o \pm 20^o$ regime, thus rendering the current orientations contour (θ) mostly green. Grains with inital orientations nearly normal to the loading axis whose glassy layers were under compression (negative values for the stress component ${}^{g}\sigma_{ss}$) due to the dilatation in rubber, appear *"crumpled"*. Grains *A* and *B* clearly undergo this microstruc-

tural reconfiguration. Orientation contours within these grains show columnar striations of alternating color shades, which coincide with regions of large antisymmetric tilting (see Fig. 4-16). Microstructural buckling is a mechanism by which these grains can rotate and increasingly accommodate deformation by interlamellar rubber shear, rather than by dilation alone. This is verified by the evolution of ${}^{r}\mathrm{F}_{s_o n_o}$, ${}^{r}\mathrm{F}_{n_o n_o}$, and E_{22} contours within these grains. Between $\overline{\mathrm{F}}_{22} = 1.1$ and $\overline{\mathrm{F}}_{22} = 1.2$ macroscopic stretch, both rubber layer shear and dilatation concentrate within the narrow buckling striations. These buckled configurations are locked in place by the neighboring material without much freedom for rotation, and thus can continue to deform only by increasing shear and dilation. Finally, grains of intermediate initial orientation have tilted towards the stretching axis, and extended their shape by interlamellar shear (see grains *E* and *F*). Many of the prominent shear bands (circled in Fig. 4-12) have formed through grains initially oriented at 45° or 135° in the direction of the rubbery layers, which effectively act as *"slip planes"* in lamellar BCPs.

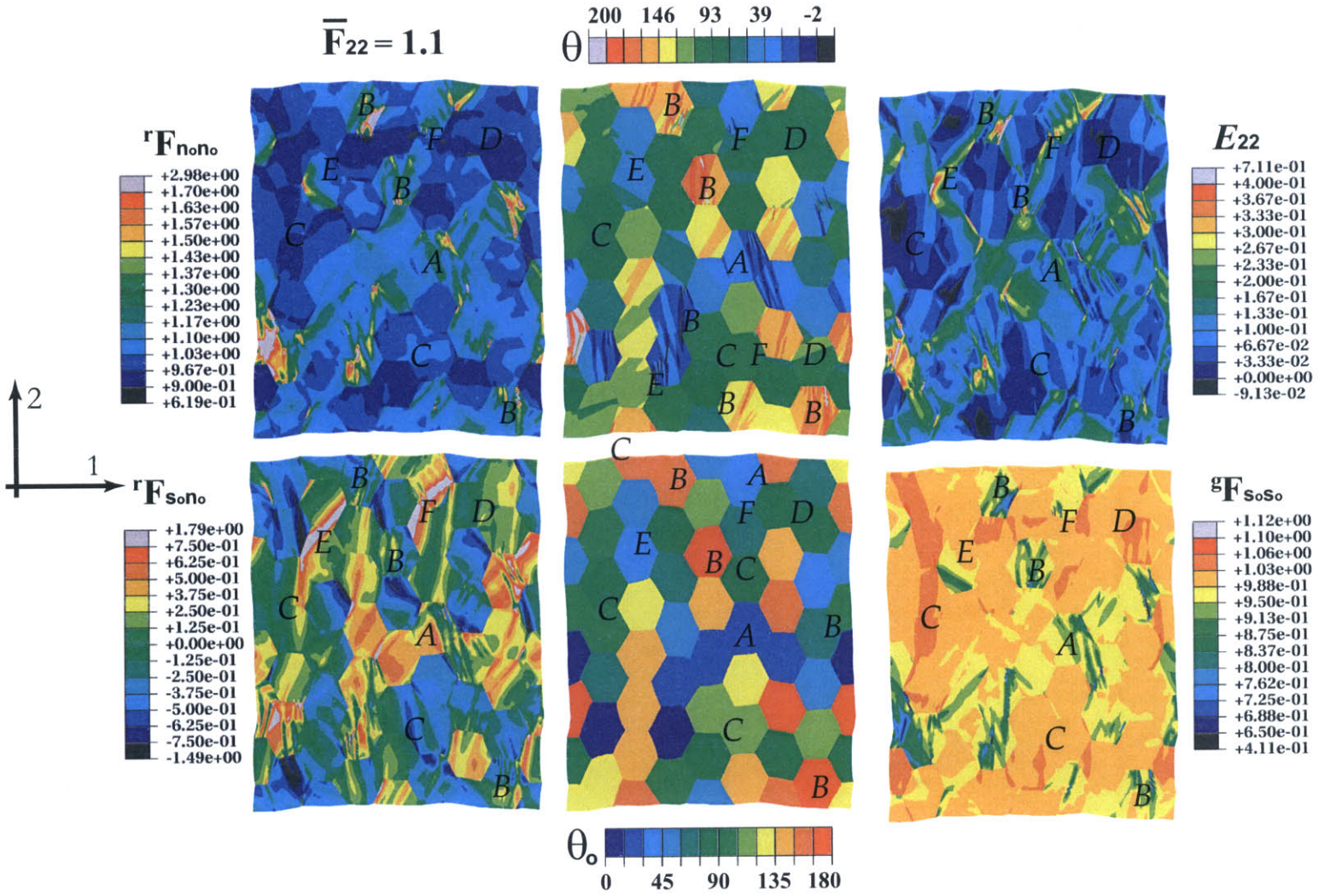

Figure 4-12: *Plane-strain extension* - RVE3*:* Strain contours at macroscopic stretch $\overline{F}_{22} = 1.1$.

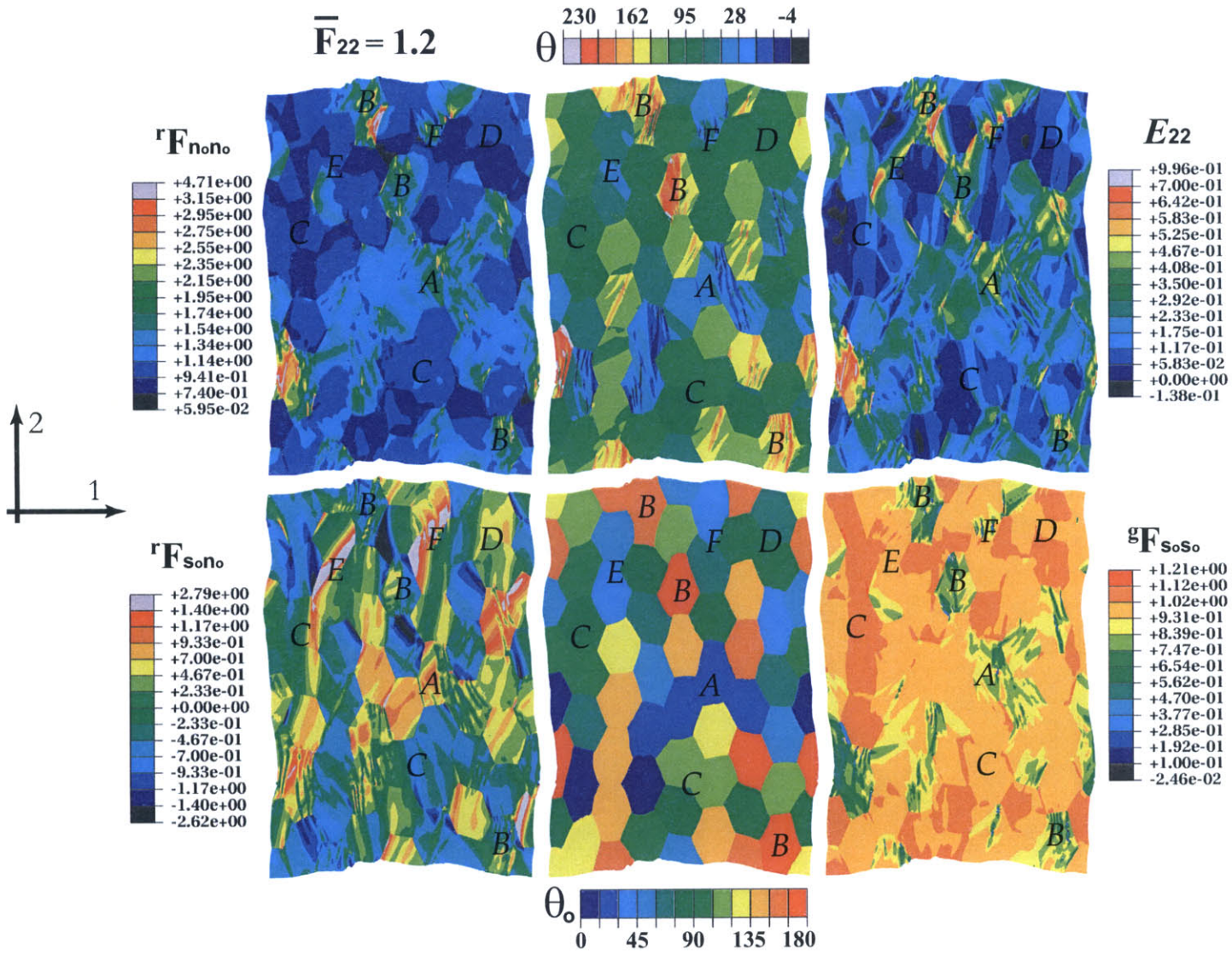

Figure 4-13: *Plane-strain extension* - RVE3*:* Strain contours at macroscopic stretch $\overline{F}_{22} = 1.2$.

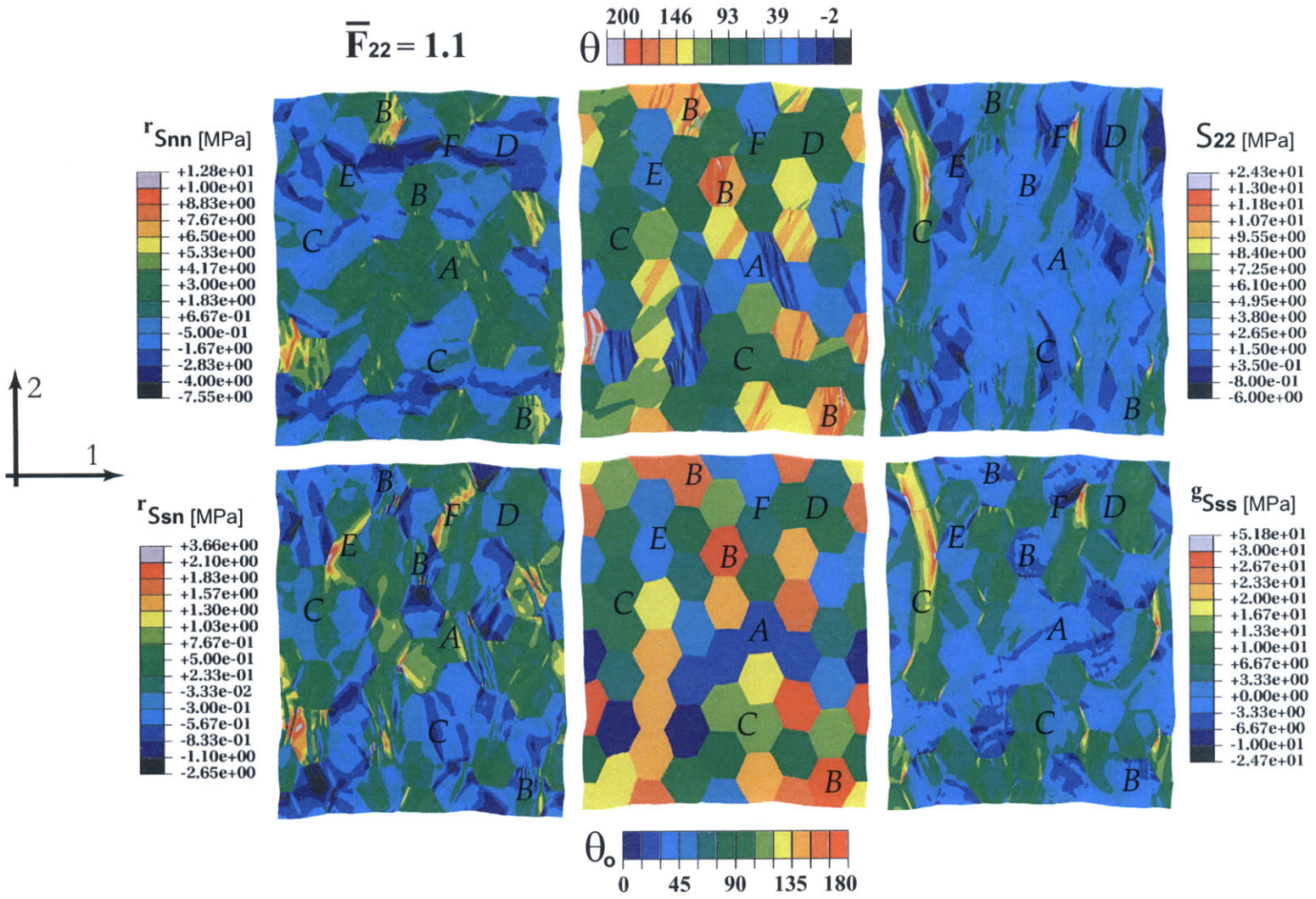

Figure 4-14: *Plane-strain extension* - RVE3*:* Stress contours at macroscopic stretch $\overline{F}_{22} = 1.1$.

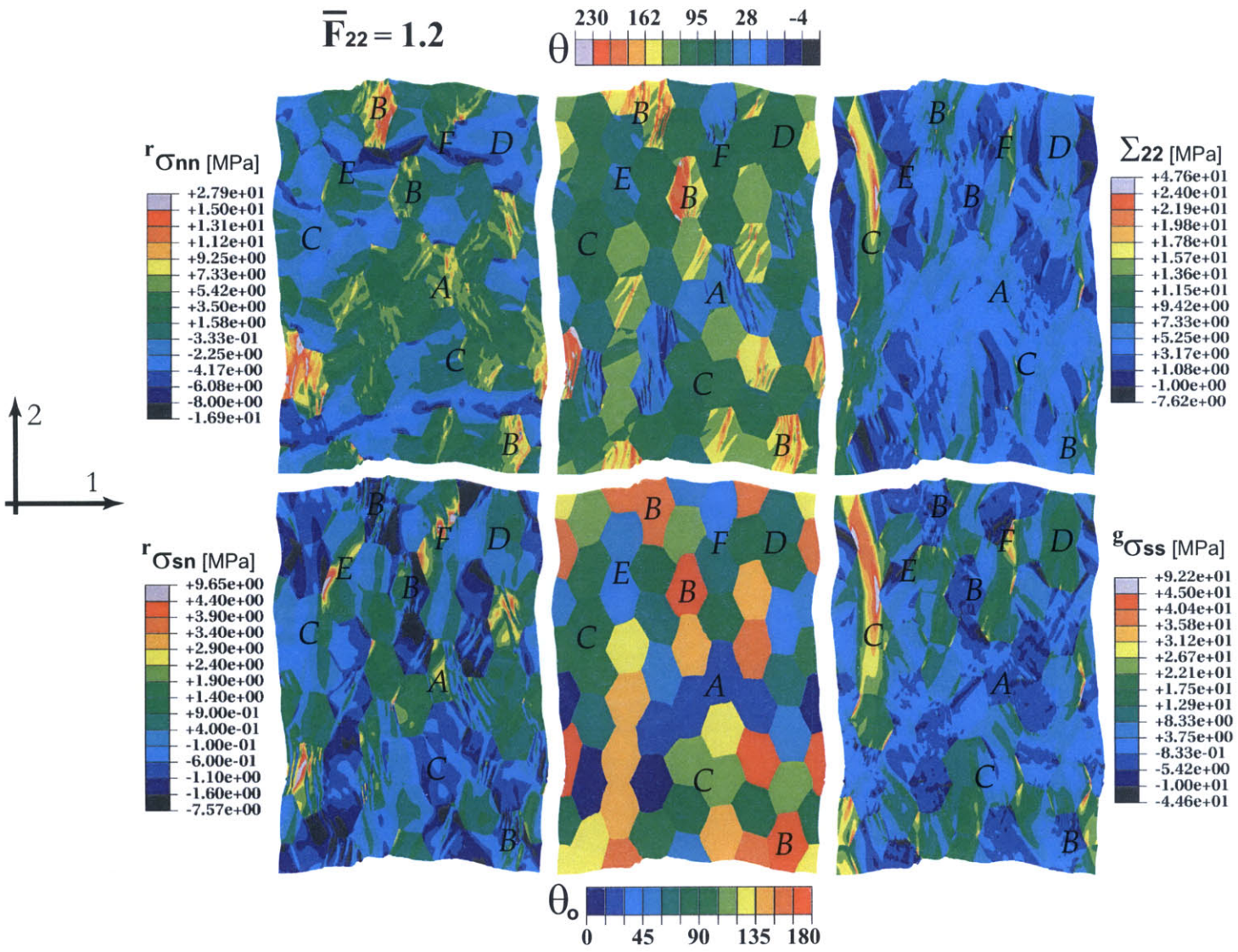

Figure 4-15: *Plane-strain extension* - RVE3*:* Stress contours at macroscopic stretch $\overline{F}_{22} = 1.2$.

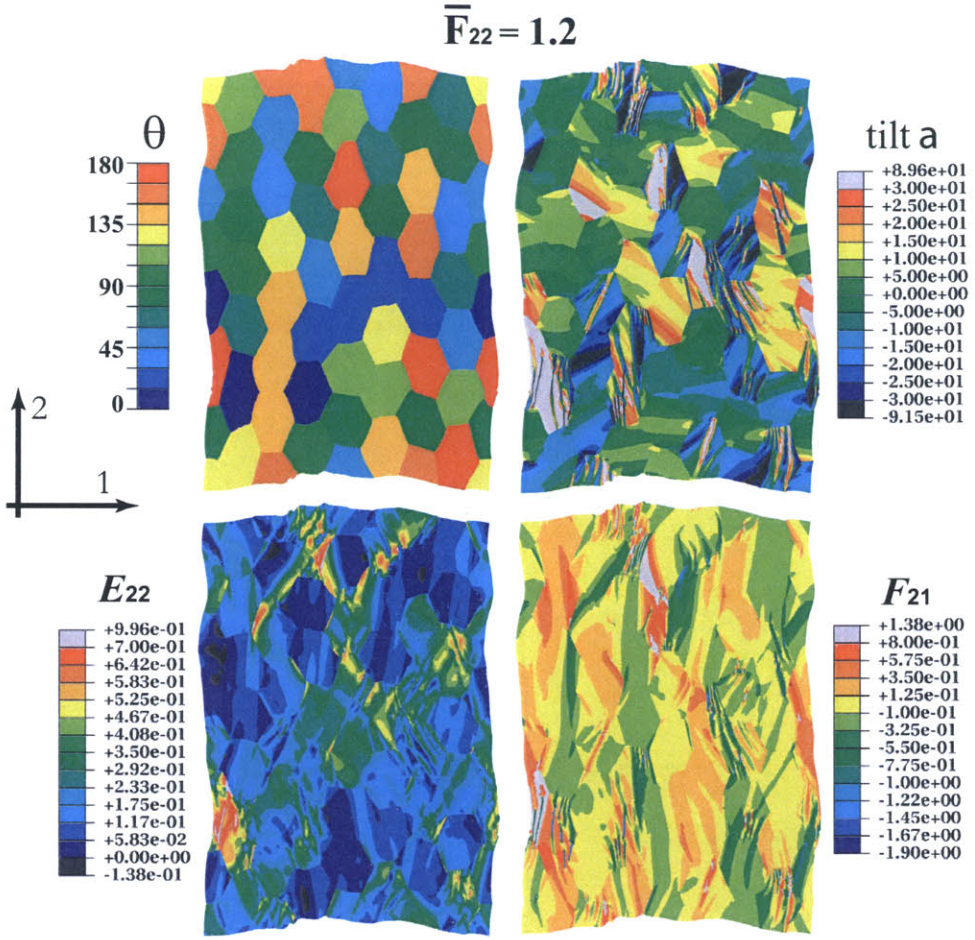

Figure 4-16: *Plane-strain Extension* - All RVEs*:* Summary of deformation micromechanics at macroscopic stretch $\overline{F}_{22} = 1.2$.

The gradual tilting and close alignment of grains with the loading direction is manifested dramatically in histograms of current grain orientations, which are taken at different deformation instances. The histograms in Fig.4-17 illustrate the evolving distribution of grain orientations, θ's, within RVE-3 for the same instances of macroscopic stretch as those for the presented contours. The initially uniform distribution of grain orientations in the undeformed RVE-3 were given in Fig. 4-9. With increasing deformation the distribution of grain orientations tends to coalesce towards 90^o. For macroscopic stretches higher that $\overline{F}_{22} = 1.1$ very distinct peaks have formed over the orientation spectrum: at 90^o, at $90^o \pm 25^o$, and at 250^o and -65^o with respect to direction-2. The orientation of 90^o corresponds to the loading direction (axis-2). Grains initially aligned with direction-2 experience minimal rotations and only as a result of maintaining compatibility with neighboring

grains. Between histograms, the 90^o frequency is increasing, augmented by grains that rotated in order to attain a higher alignment with the direction of stretching. Peaks observed at $250^o/70^o$, and $-65^o/115^o$, correspond to symmetric orientations of $\pm 25^o$ about the loading axis (90^o). This trend, as described in this chapter's introduction, has been observed by Seguela and Prud'homme [19] during tensile experiments on 3D lamellar BCP polycrystals, and is also consistent with the single-crystal behavior of gradual tilting towards the stretching direction and deformation by the shearing of rubber layers.

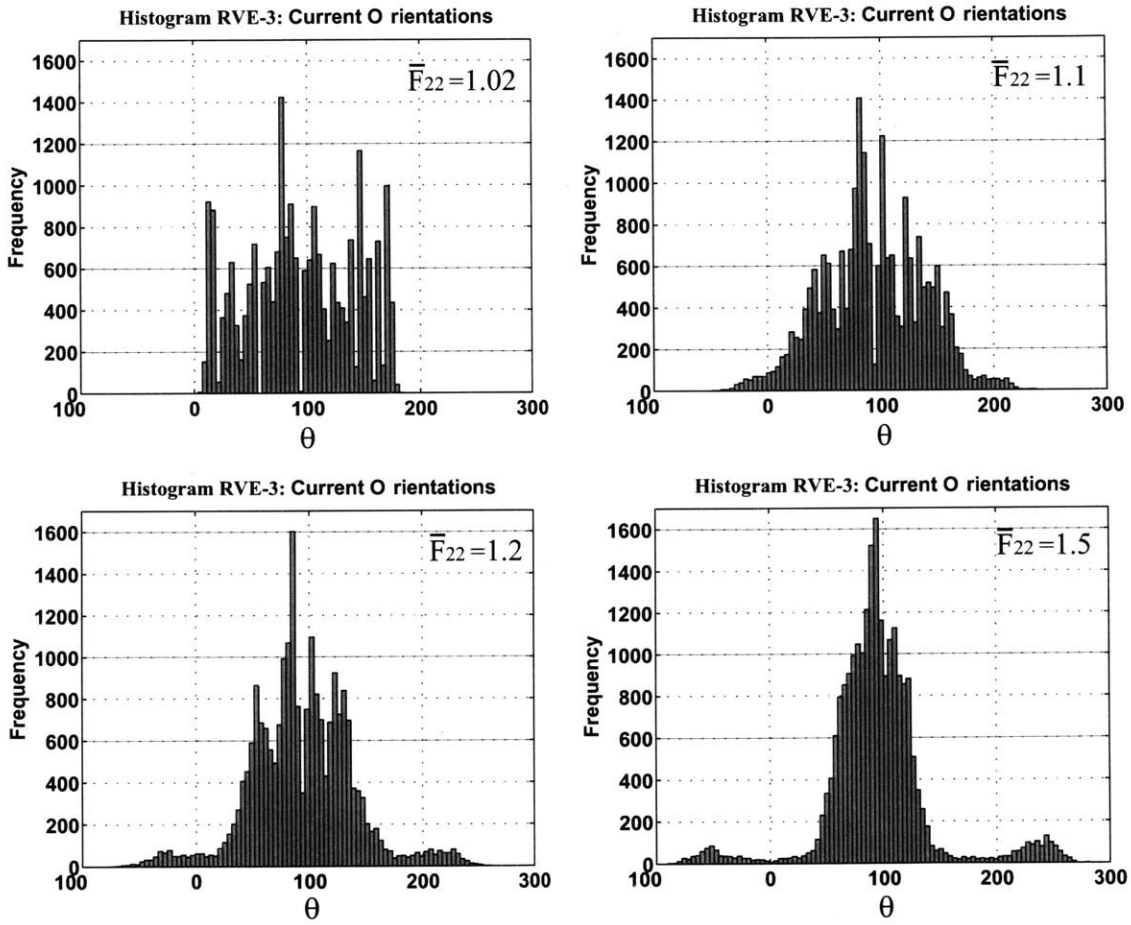

Figure 4-17: *Plane-strain Extension* - RVE3*:* Histogram of current grain orientations, θ, at different levels of macroscopic stretch $\overline{F}_{22}$.

The histograms in Figs. 4-18 and 4-19 present grain orientation results from all RVEs during plane-strain extension. The results for extension along direction-1 are shown in Fig. 4-19. The exact same trend of gradual grain restructuring and tilting toward the loading axis is being observed in θ-histograms from all RVEs, independent of the loading direction.

Care should be taken however to reference orientations with respect to the correct loading direction, which for extension along direction-1 corresponds to the $0°/180°$-orientation. Apart from the slow shifting of oriention peaks towards the appearing preferred orientation of $\pm 20^o$ to the stretching direction, there is no other variation observed in the shape of θ-distributions for stretches higher than $\overline{F}_{22} \approx 1.1$. This verifies that all the "restructuring" in the granular arrangement takes place at a stretch less than $\overline{F}_{22} = 1.1$, and is manifested in the RVE's stress-stretch response as a macroscopic "yield" point at $\overline{F}_{22} \approx 1.03$ (Figs. 4-17 and 4-20). Before "yielding", much of the imposed deformation is accommodated by the rubber layers through their dilation. Beyond this microstructural reconfiguring, deformation is accommodated mostly by interlamellar shear within rubbery layers. The reduction observed in the tangent modulus at the "yield" point is attributed to this shift in the underlying micromechanical deformation mechanisms. As grains get locked in their new spatial configurations by neigboring grains, their tilting becomes increasingly harder. Deformation is thus increasingly accommodated by rubber layer dilation and less by rubber shear, a transition which results in the steady increase in the stress response. The polygranular RVE calculation predictions of the underlying micromechanical processes are in stunning agreement with the experimental observations of Fujimura and Hashimoto *et al.* [17, 18] and of Seguela and Prud'homme [19] summarized in Figs. 4-1c and 4-2, despite the fact that the experiments refer to 3D polycrystals.

The stress-stretch response of all RVEs for plane-strain extension are given in Fig.4-20. RVE-1 and RVE-5 exhibit the most anisotropic response between the two loading directions. Histograms for the initial grain orientations within all five RVEs are shown in Fig.4-21. In the histograms describing the initial distributions of grain orientations within the five different RVEs, it is apparent that RVE-1 and RVE-5 have a relatively higher density of grains with close initial alignment to the 1-axis. Their response is bound to be biased when compared to RVEs 2, 3, and 4 -the stiffest for extension in direction-1, and the most compliant when extended in direction-2. Grains in RVEs 2,3 and 4 are unifomly oriented, and their stress response to deformation is isotropic.

Considering the relatively small number of grains used to discretize the RVEs, all RVEs behave in a reasonably isotropic manner. All ten responses are similarly nonlinear, and all

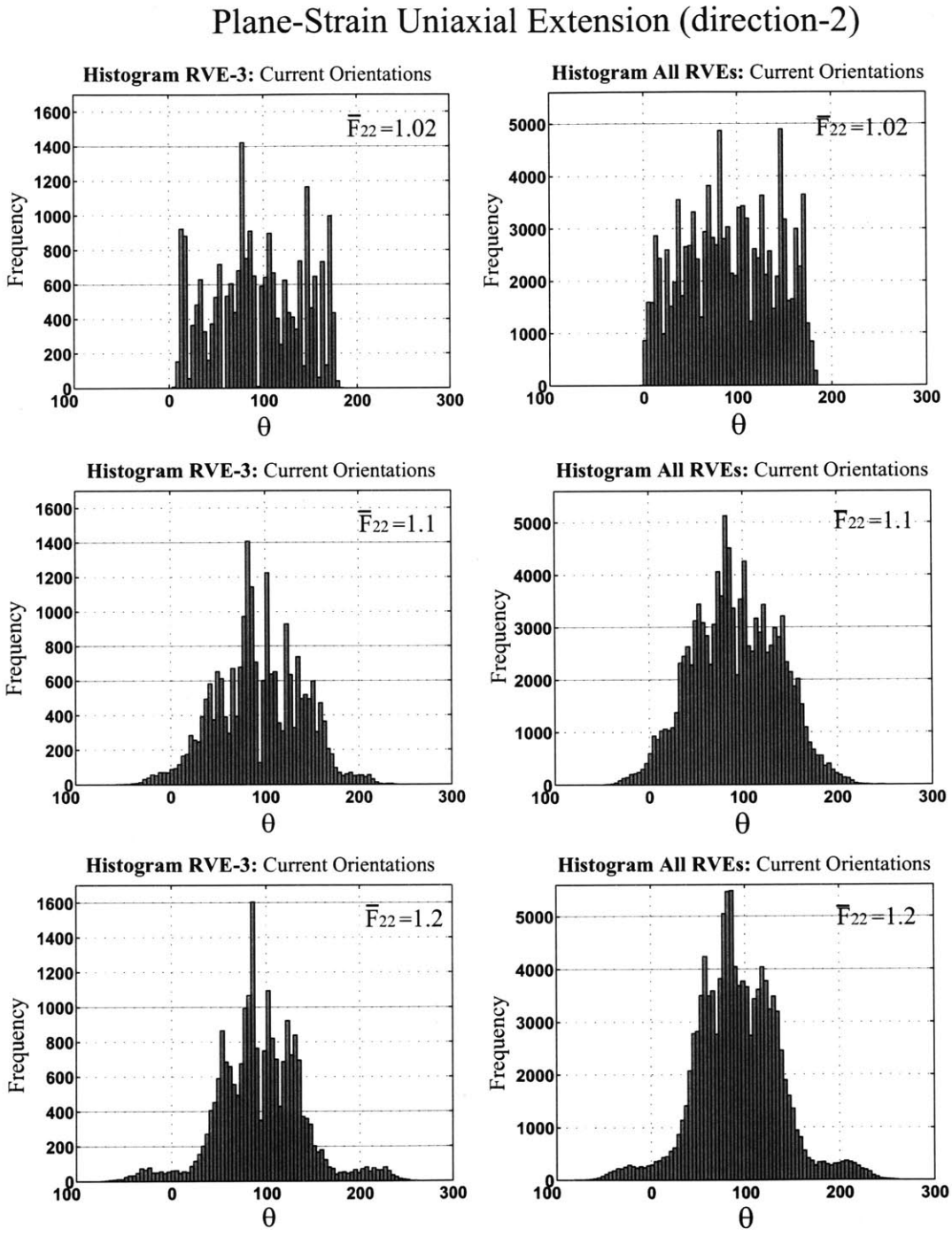

Figure 4-18: *Plane-strain Extension* - All RVEs*:* Histogram of current grain orientations, θ, for RVE-3 and for all polygranular RVEs, at different levels of macroscopic stretch $\overline{F}_{22}$.

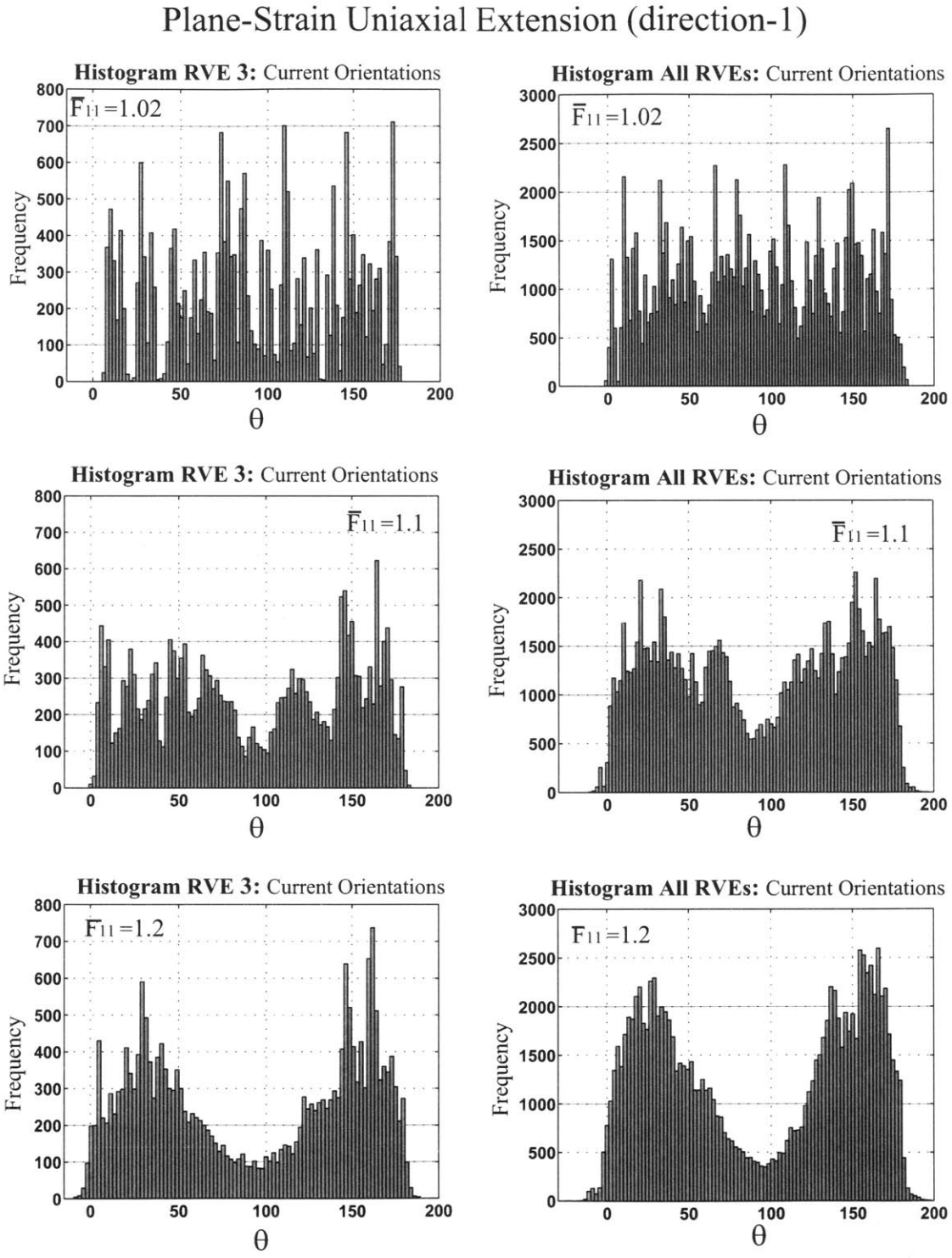

Figure 4-19: *Plane-strain Extension* - All RVEs*:* Histogram of current grain orientations, θ, for RVE-3 and for all polygranular RVEs, at different levels of macroscopic stretch $\overline{F}_{11}$.

exhibit a "yield" point at a macroscopic stretch of ~ 1.02. The derived analytical constitutive model, which described the behavior of grains does not account for plasticity effects. The "yield"-like nonlinearity stems from internal grain tilting and buckling, such that the oveall imposed deformation can be collectively accommodated by interlamellar rubber shear, a deformation mode of reduced stiffness for the overall response of the polygranural assembly. An overall grain-shape induced anisotropy is present in the stress

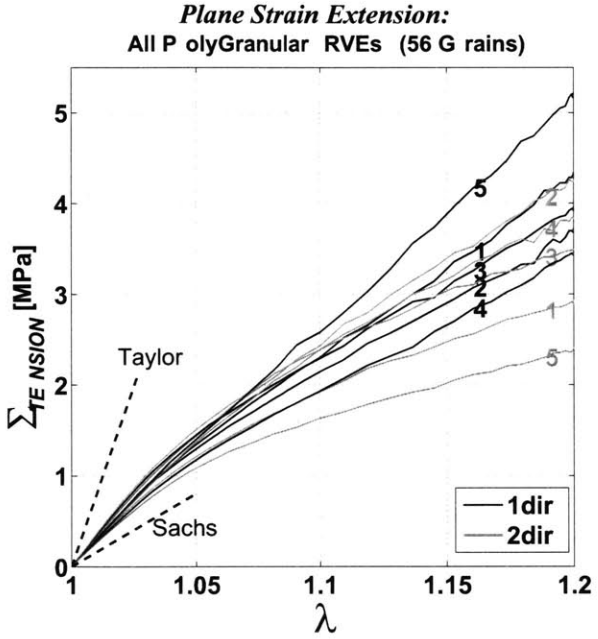

Figure 4-20: *Plane-strain Extension* - All RVEs: Stress-Stretch response of all multigranular RVEs.

response of RVEs between stretching in direction-1 and stretching in direction-2. With the given arrangement of hexagonal grains in the RVEs (Fig.4-6), stretching in direction-1 corresponds to loading along grain boundaries (the bases of the hexagon), while extension along direction-2 results in grain stretching normal to grain boundaries. Thus, the RVE is expected to have a slightly stiffer response when loaded along direction-1. Such a trend is observed in all ten stress-strain curves presented here. However, the current RVEs are not discretised with a sufficiently large number of grains and the observed anisotropy is mostly an influence of the inherent anisotropy of the single-crystal and the distribution bias in initial grain orientations. The RVEs' stress-stretch curves are bounded in Fig.4-20 by the Taylor (upper-bound) and Sachs (lower-bound) approximations for the polycrystal's small

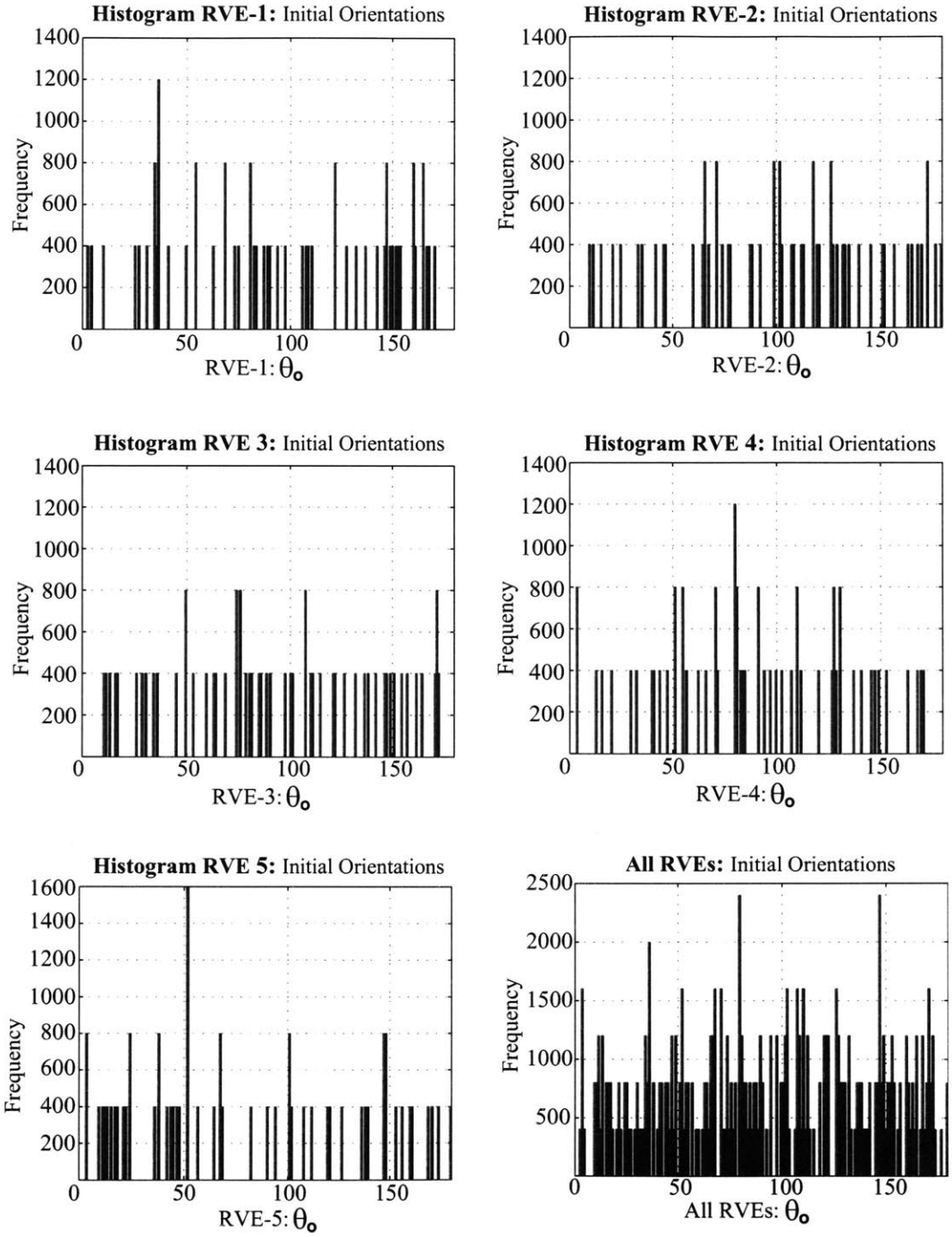

Figure 4-21: Histogram of initial grain orientations, θ_o, for all multigranular RVEs.

strain response. As described above for RVE-3, for highly anisostropic materials such as the lamellar BCP studied here, these bounds are very wide and neither one can represent the response of the polycrystal with reasonable accuracy. The Taylor prediction is very stiff as seen in Fig.4-20, because it overweights the contribution of aligned grains, which are found to experience little axial strain, and underweights off-axis grains which are found to accommodate most of the imposed deformation through shear and rotation. The contours of axial strain show the large distribution of axial strain in the structure, and identify the axial strain experienced in each grain, which can be compared to that of the macroscopic strain to reveal the non-Taylor response. In fact, the axial strain within grains varies considerably throughout the RVE even at very small macroscopic strains, due to the high, orientation-dependent anisotropy of the single-crystal behavior. Assuming a uniform stress field throughout the polycrystalline aggregate in accord with the Sachs approximation, is equally unrealistic. The Sachs model largely underpredicts the effective stress response in Fig.4-20, because it assumes the same stress in each grain, and therefore overweights the deformation (compliance) contribution of off-axis grains and underweights the effect of the aligned grains. The contours of axial stress show the stress distribution and identify the stress within each grain, which can be compared to the macroscopic stress, further showing the non-Sachs response.

For completeness in this discussion, the distributions of the effective grain deformation components F_{11}, F_{22}, F_{12}, and F_{21} at the previously used macroscopic stretches are presented in histograms given in Figs. 4-22 through 4-25. Similar to the large variation which was observed throughout the RVE for the calculated effective grain stress and strain values -Σ_{22} and E_{22},respectively-, all histograms demonstrate a large, and increasing with macroscopic stretch, variance for these kinematic quantities. The distributions of the calculated values are, however, physically meaningful; despite the variance, the quantities are always centered at the value of the corresponding macroscopic quantity. For the case of extension, the shear and rotation deformation components, F_{12} and F_{21} are normally distributed about the corresponding macroscopic values $\overline{F}_{12} = \overline{F}_{21} = 0$. Components F_{11} and F_{22} on the other hand follow a Γ-type distribution (*Erlang*) skewed in the direction of macroscopic stretch. The variance in all cases is increasing with increasing deformation. It is evident

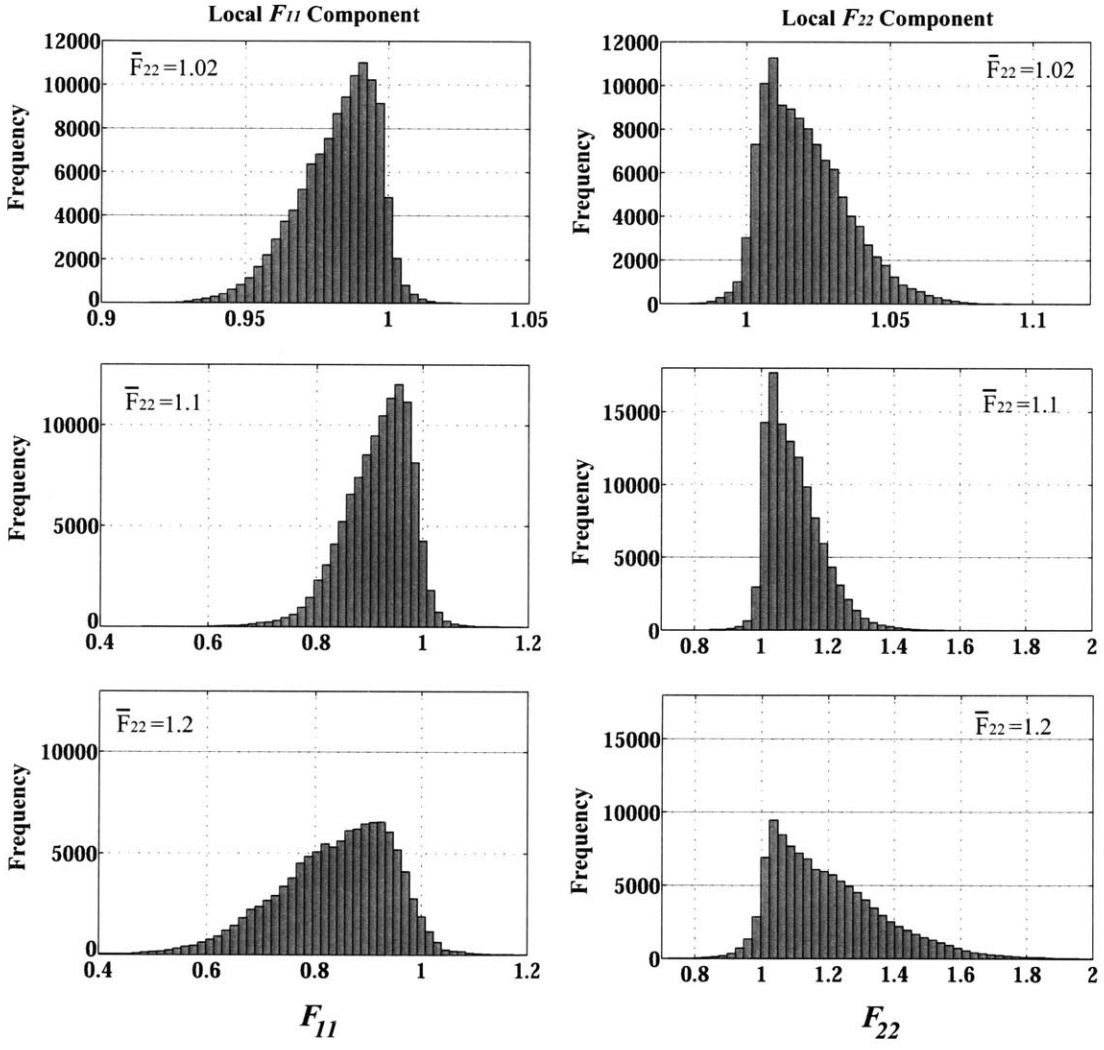

Figure 4-22: *Plane-strain Uniaxial Extension (Direction-2)* - All RVEs: Histograms of deformation gradient components F_{11} and F_{22}.

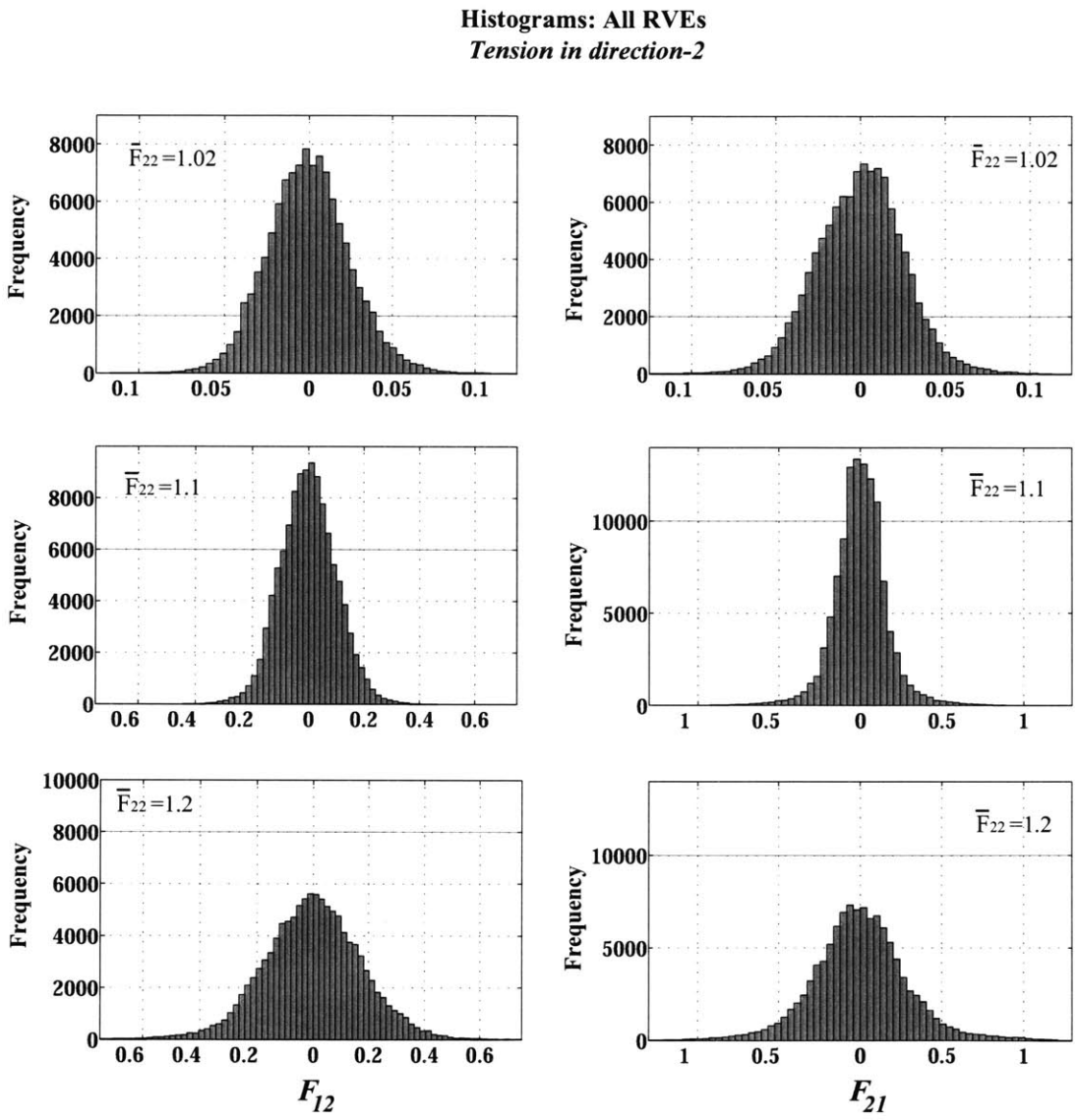

Figure 4-23: *Plane-strain Uniaxial Extension (Direction-2)* - All RVEs: Histograms of deformation gradient components F_{12} and F_{21}.

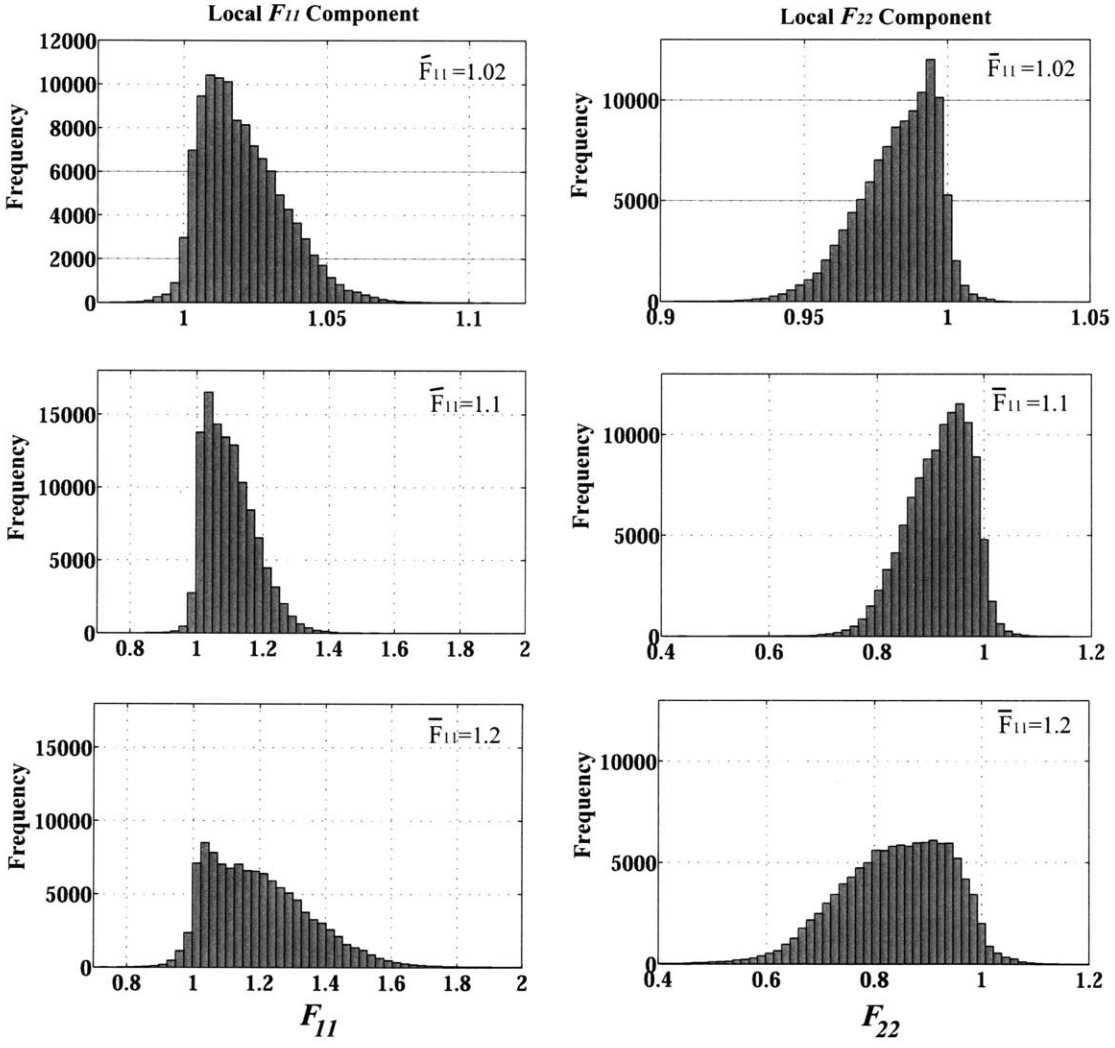

Figure 4-24: *Plane-strain Uniaxial Extension (Direction-1)* - All RVEs: Histograms of deformation gradient components F_{11} and F_{22}.

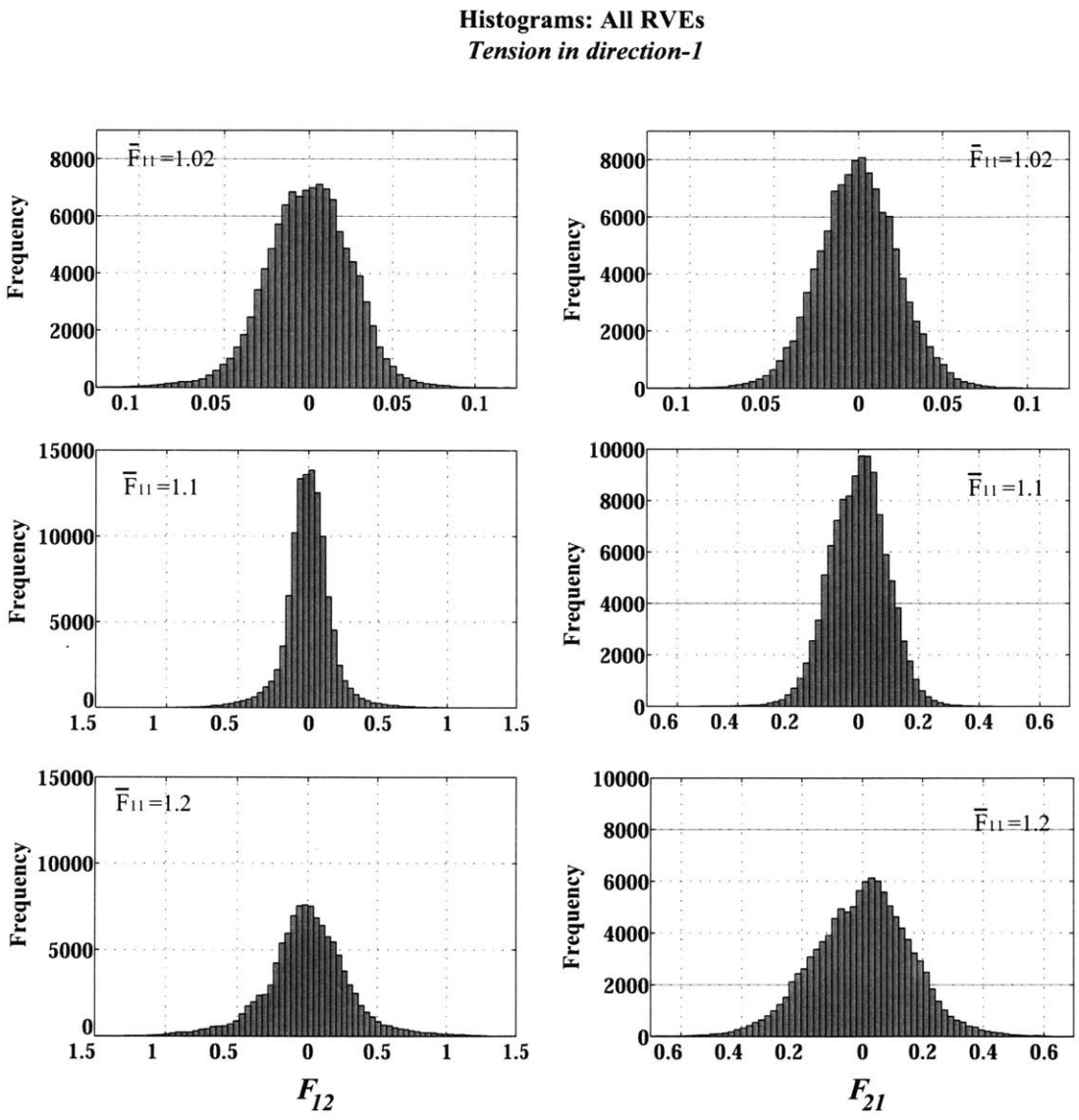

Figure 4-25: *Plane-strain Uniaxial Extension (Direction-1)* - All RVEs: Histograms of deformation gradient components F_{12} and F_{21}.

that the assumption for a homogeneous deformation or stress field throughout the RVE cannot be a physically correct approximation for the response of this polycrystal. For this reason, neither the Taylor nor the Sachs model can capture the polycrystalline response. The observed distributions can be used to develop micromechanically-based *"statistical"* Taylor/Sachs models, to map a statistically and micromechanically correct varying kinematic/stress field to grains in the polycrystalline configuration and/or hybrid Taylor/Sachs models such as the model developed by VanDommelen *et al* [56] for semi-crystalline polymers.

Plane-Strain Simple Shear: The results for simple shear deformation under plane-strain conditions are given in Figs. 4-26 through 4-36. The shear stress-strain response of RVE 3 as well as the responses of all RVEs are shown in Fig. 4-28. Also shown are the Taylor and Sachs predictions for the initial stress-strain response to simple-shear deformation under plane-strain conditions for the given BCP polycrystal. Contour plots of strain and stress measures from RVE-3 are shown in Figs. 4-26 and 4-27 at 30% macroscopic shear deformation.

The stress-strain response of all RVEs to plane-strain simple-shear deformation exhibits similar trends to their response during plane-strain extension. The behavior is overall non-linear with an almost linear initial region, followed by a "yield" point beyond which the stress response continues to increase monotonically with a reduced, tangent modulus, which gradually increases with deformation. As captured by the contour plots, deformation micromechanics similar to those observed during plane-strain extension determine the effective deformation and stress response of the polygranular configuration in the case of simple-shear deformation. The initial linear response at small macroscopic shear strains stems predominantly from rubber layer shearing combined with small rotations of individual grains, which are mostly affine with the macroscopically applied rotation due to the inposed shear angle. With increasing deformation, grains tend to configurations which are favorable for interlammelar shear. This is facilitated either by the rotation of grains whose tilting is not limited by the surrounding material, or by micromechanical deformation mechanisms such us layer buckling for those grains with otherwise limited rotational freedom. By definition, buckling entails large rotations and enables grain shearing. This

reconfiguration which takes place at the microstructural level is manifested macroscopically as a clear departure from linearity (interestingly occuring at the same macroscopic shear strain for all RVEs). The two prominent shear bands which are visible through the RVE contour plots coincide with the locations of grains that have internally buckled (initially at 135° and thus experience compression), and grains oriented at 90°, 180°, or 0°, which exhibit the least resistance to shear. Similar to the single-crystal behavior at higher shear strains, the gradual increase in the post-yield tangent stiffness results from the gradual alignment of grains with the stretching component of the macroscopic deformation gradient (orientations approacing 45°). For most RVEs the post-yield stress response is anisotropic and depends on the direction of the imposed shear. Here, the hexagonal grain shape is not the determining factor, but the anisotropty arises from the distribution of initial grain orientations and the anistropy of the single-crystal behavior. Even though initial grain orientations were uniformly distributed within most RVEs, larger grain populations should be used for future multigranural RVEs to achieve *"uniform"* interactions between grains as well, as grain interactions seem to be more influential for shear-type deformations.

As seen in the contour plots, the macroscopically applied shear deformation is accommodated by the collective shearing of grains whose orientations are less resistant to shear deformation, as for example those with 90° initial orientation. Grains with 0° and 180° initial orientations rotate in an affine manner with the bottom/top faces of the RVE (to which they are parallel), and shear along their rubbery layers without considerable resistance. Grains initially at 90° to axis-1 (aligned with the shearing direction) deform entirely by shearing of their rubber layers (highest ${}^{r}F_{s_o n_o}$ component), and similarly to single-crystal analysis results, appear as the most compliant grains. Their locations within the RVE coincide with the highest E_{12} and the lowest Σ_{12} values in the contour plots. Grains with initial orientations between 0° and 90° rotate in an affine manner with the faces of the RVE as well, and their glassy layers gradually align with the stretching component of the macroscopic deformation gradient. Consistent with the single-crystal shear results, ${}^{g}\sigma_{ss}$ takes the highest tensile values for grains initially oriented at 0°. This gradual alignment with the tensile axis results in the gradually increasing post-yield tangent modulus in the RVE response. On the other hand, grains initially oriented between 90° and 180° experience

compression for the given shear direction as seen from the corresponding ${}^{g}\sigma_{ss}$ contour. As seen in contours from 30% macroscopic shear, these grains appear to have attained buckled configurations in order to achieve less compliant orientations and accommodate further deformation by shear deformation of their rubber layers.

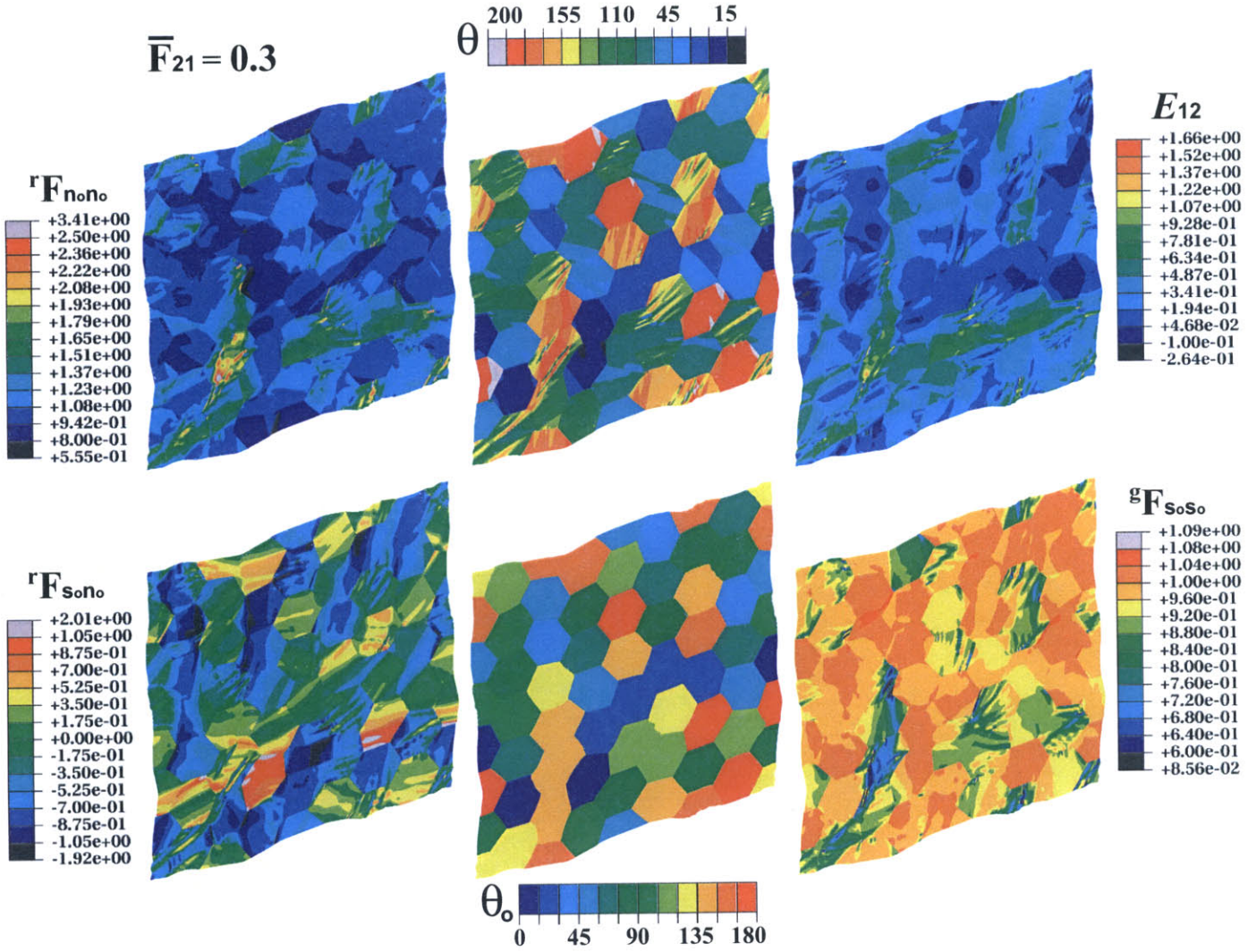

Figure 4-26: *Plane-strain Extension:* Strain contours.

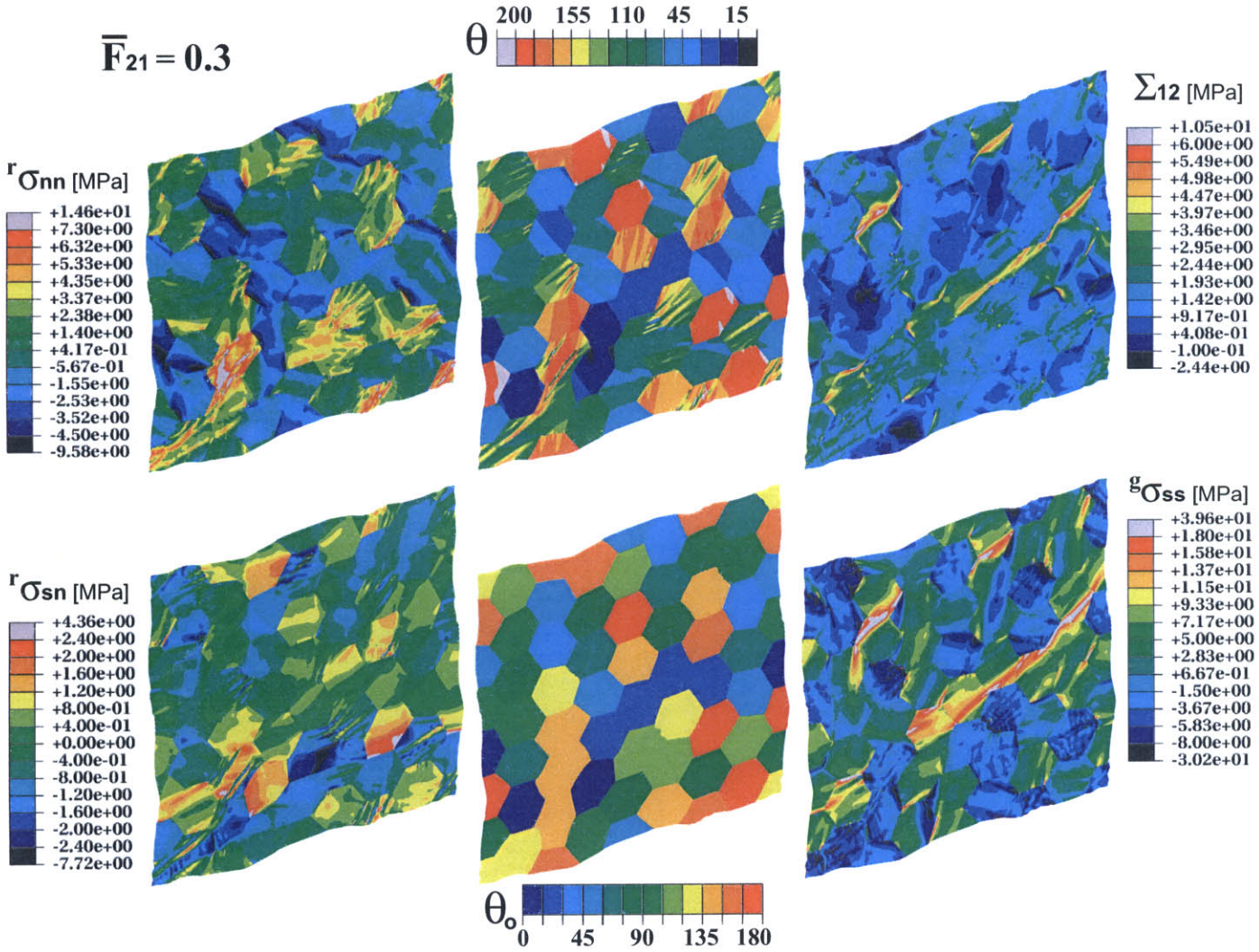

Figure 4-27: *Plane-strain Simple Shear:* Stress contours.

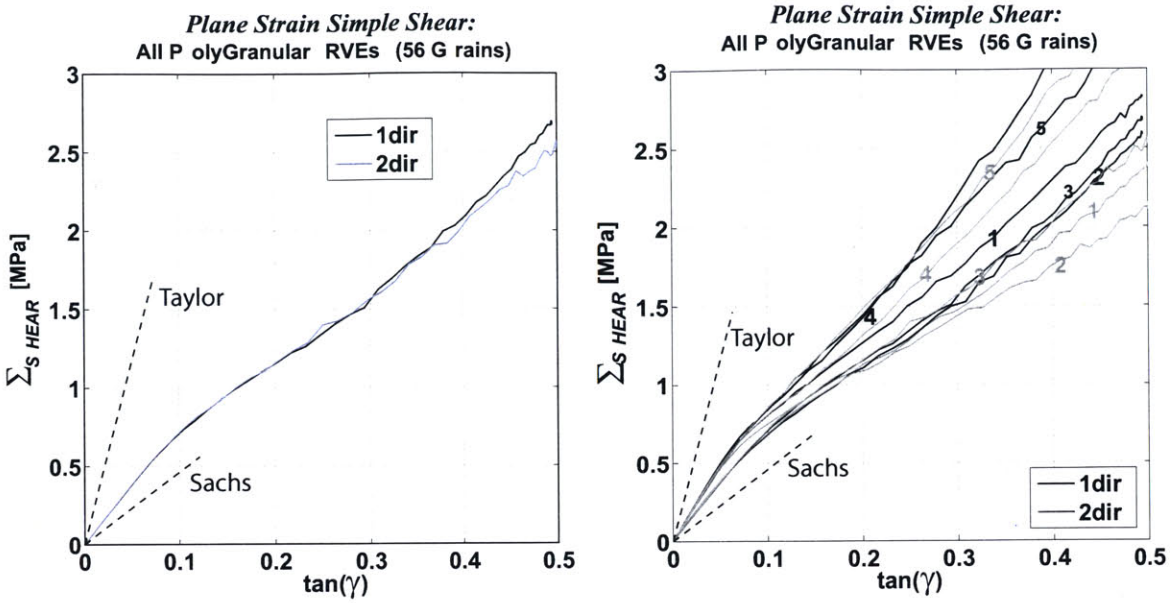

Figure 4-28: *Plane-strain Simple Shear:* RVE Stress-strain responses; on left for RVE-3, and for all RVEs on the right.

The contour observations are quantitatively supported by the histograms in Figs. 4-29 and 4-30, which monitor the evolution of grain orientations (θ's) with increasing macroscopic shear. Grain orientation distributions are shown for RVE-3 in Fig. 4-29, and for all five RVEs in Fig. 4-30. The histograms indicate a gradual shift of the distribution to the right, due to the overall RVE rotation, and three orientation peaks: at 45^o, 200^o, and 90^o w.r.t. the horizontal. The frequency of the 90^o peak is steadily augmented and remains constant located at 90^o. As described before, grains aligned with the shear direction are the easiest to shear, hence the 90^o orientation seems to be an asymptotic limit (a preferable final orientation). The peak at 200^o (or 20^o w.r.t. direction-1) is due to nearly horizontal grains (180^o), which have rotated affinely with the imposed shear angle (and thus have gradually shifted to higher angles). The 45^o orientation is the stiffest for shear deformation. Grains that attain this orientation experience minimal additional deformation, hence the corresponding peak at 45^o. It is interesting to note that the 135^o orientation is being eliminated from early on, since grains with this orientation undergo compression and buckle to attain more compliant configurations.

The corresponding histograms for shear along direction-1 are given in Fig. 4-33 for RVE-3, and in Fig. 4-34 for all five RVEs. The distribution trends are identical to those

observed for shear along direction-2 (when grain orientations are appropriately referenced to direction-1 (0°)). Two distinct peaks appear equally spaced about 45°, which is the stiffest orientation for this type of deformation and and thus, acts again as a boundary. The 65° peak corresponds to grains with almost vertical orientations, which rotate affinely with the entire RVE. The most compliant grain orientation to shear deformation is that of 180° (or 0°). Grains initially aligned with the shear direction (180°) do not rotate, while others gradually tend to this favorable orientation; hence the prominent correposnding peak. The stiffest orientation is again at 135°. Since grains with this orientation experience compression and buckle, the frequency of 135° is strongly reduced.

As for the predicted material behavior in the case of plane-strain extension, the Taylor and Sachs models fail to predict adequatly narrow bounds for the stress-strain response of the polycrystalline BCP structure. Histograms in Figs. 4-31 through 4-36 quantify the mismatch between an approximately uniform stress/strain distribution through the RVEs, and the actual (calculated) field. The histograms present the distribution of the calculated (homogenized) deformation gradient components at four different levels of macroscopic shear strain for RVE-3, as well as for all the five studied RVEs. As for plane-strain extension, all the components appear distributed in a physically meaningful manner; normally centered at the corresponding macroscopic value, however with large variances which increase even more with increasing macroscopic deformation. It is evident that the occuring distributions cannot be treated as uniform, and therefore simplistic assumptions such as the Taylor and Sachs models will be inefficient for materials of such highly anisotropic single-crystal behavior.

4.3 Conclusions

The analytical continuum constitutive model was utilized in 2D finite element based calculations to study the mechanical behavior of polycrystalline lamellar BCP microstructures under conditions of plane-strain deformation. 2D multigranular RVEs were developed, each containing 56 identically shaped hexagonal grains -an aggregate size sufficiently large to represent the material microstructure without being computationally expensive-, and the

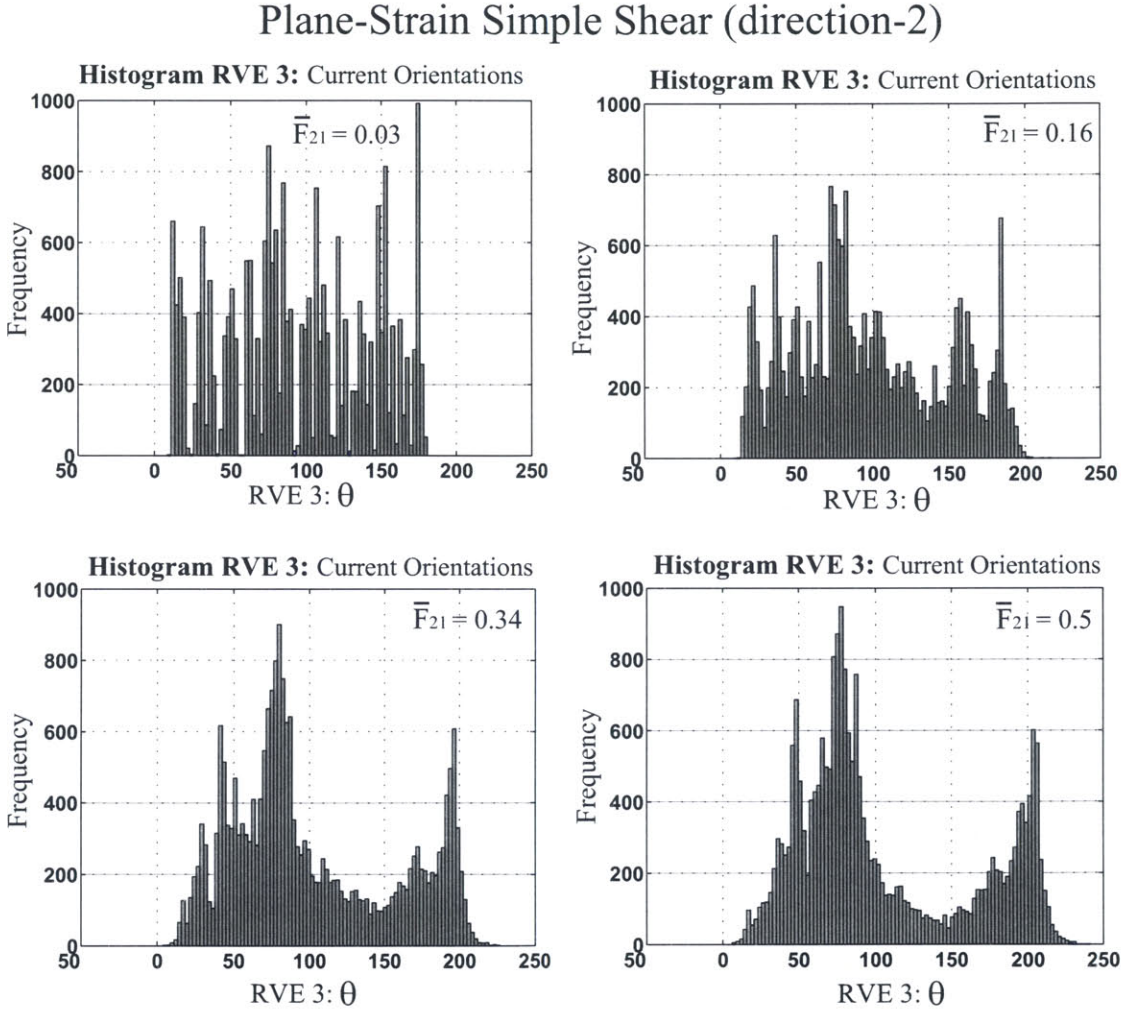

Figure 4-29: *Plane-strain Simple-Shear Deformation* - RVE-3*:* Histogram of current grain orientations, θ, for RVE-3 at different levels of macroscopic shear deformation $\overline{F}_{21}$.

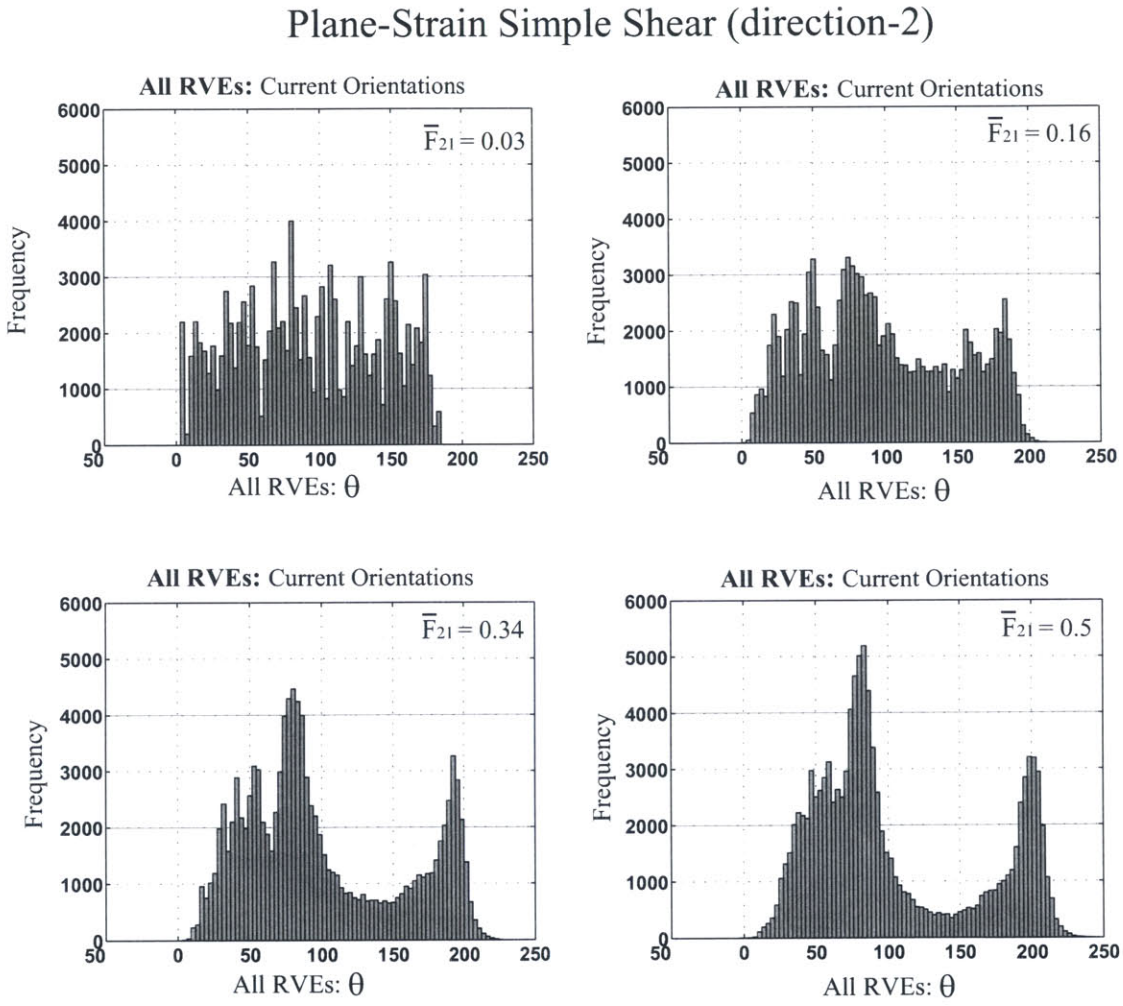

Figure 4-30: *Plane-strain Simple-Shear Deformation* - All RVEs: Histogram of current grain orientations, θ, for all RVEs at different levels of macroscopic shear deformation $\overline{F}_{21}$.

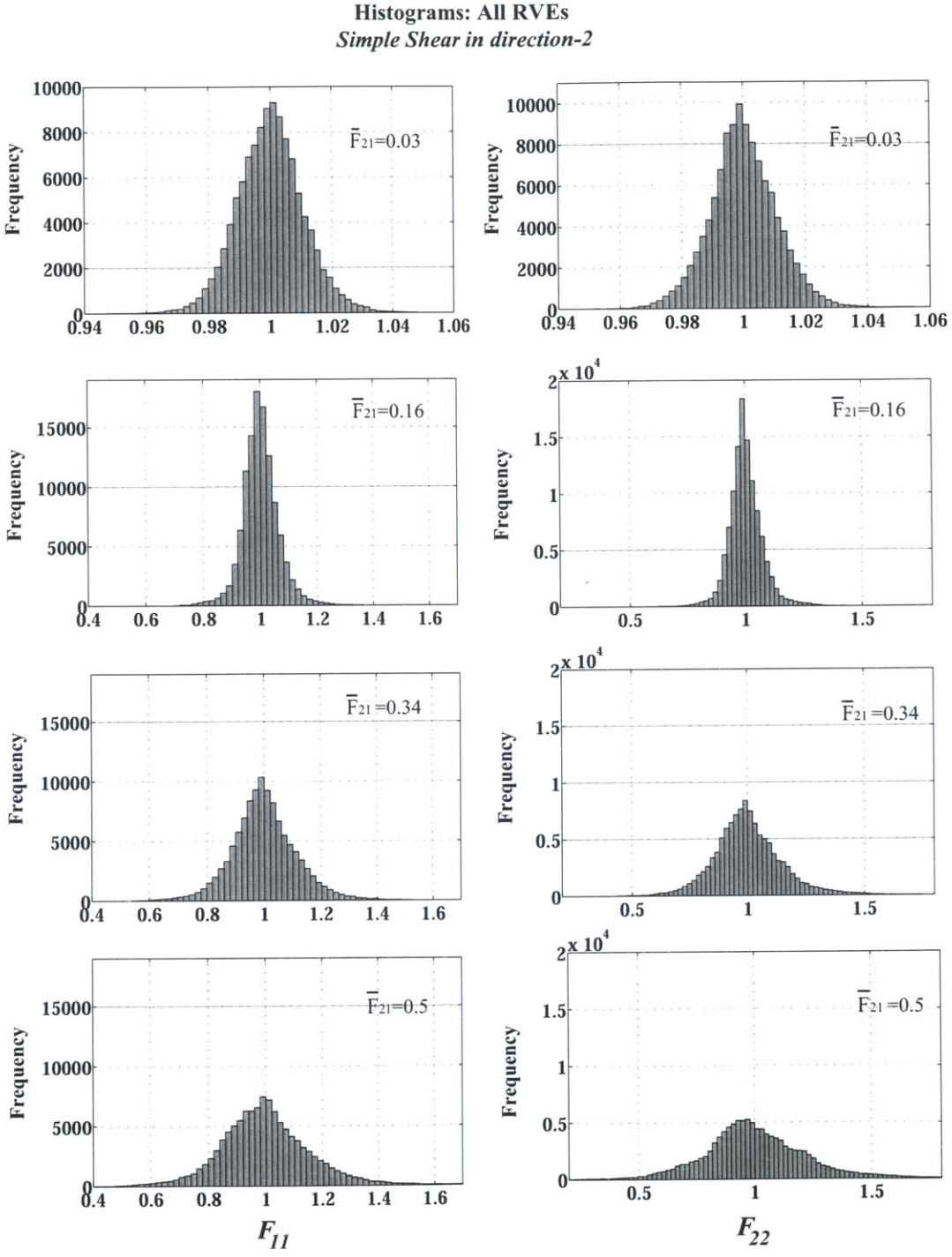

Figure 4-31: *Plane-strain Simple Shear (Direction-2)* - All RVEs: Histograms of deformation gradient components F_{11} and F_{22}.

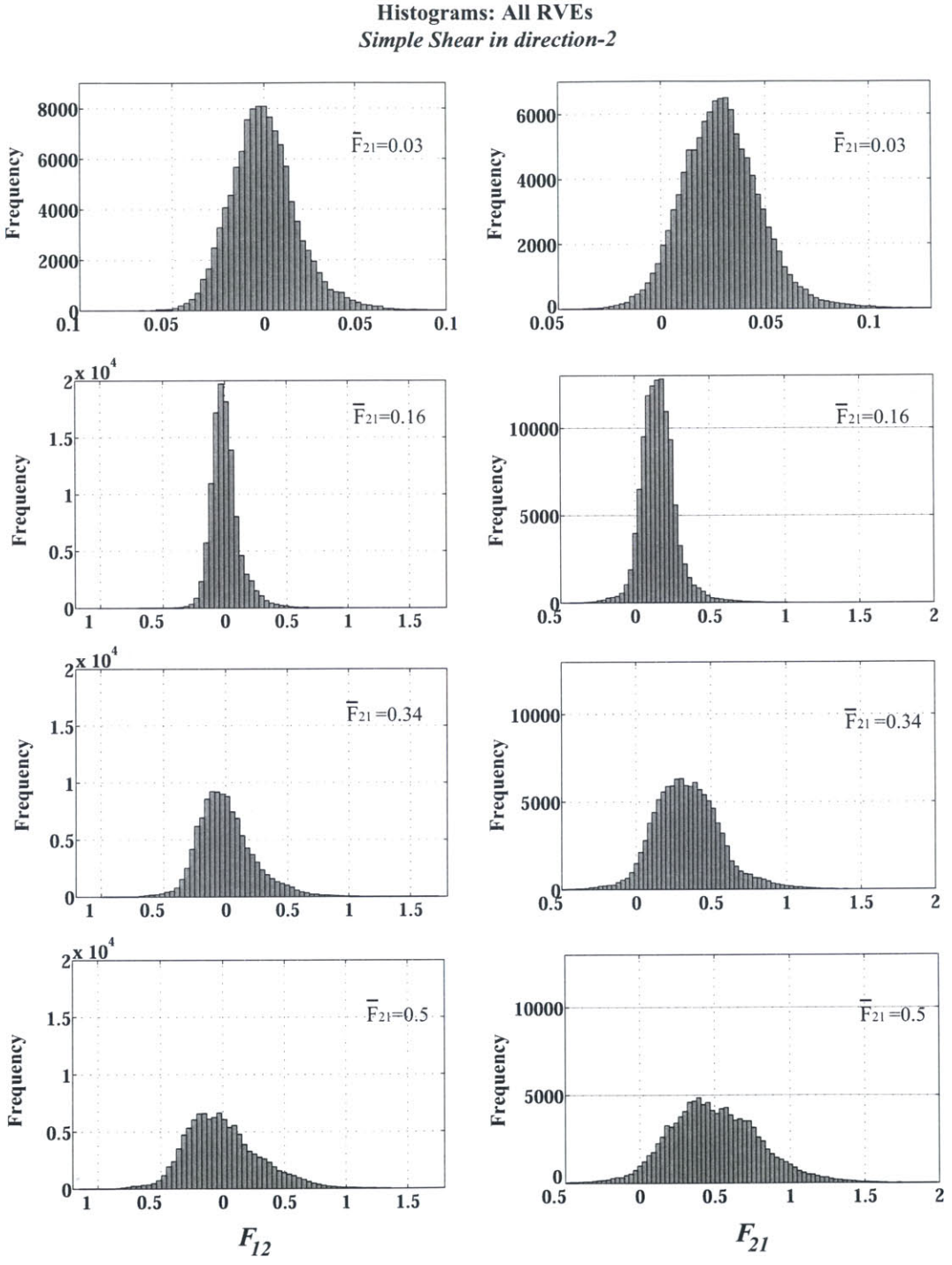

Figure 4-32: *Plane-strain Simple Shear (Direction-2)* - All RVEs: Histograms of deformation gradient components F_{12} and F_{21}.

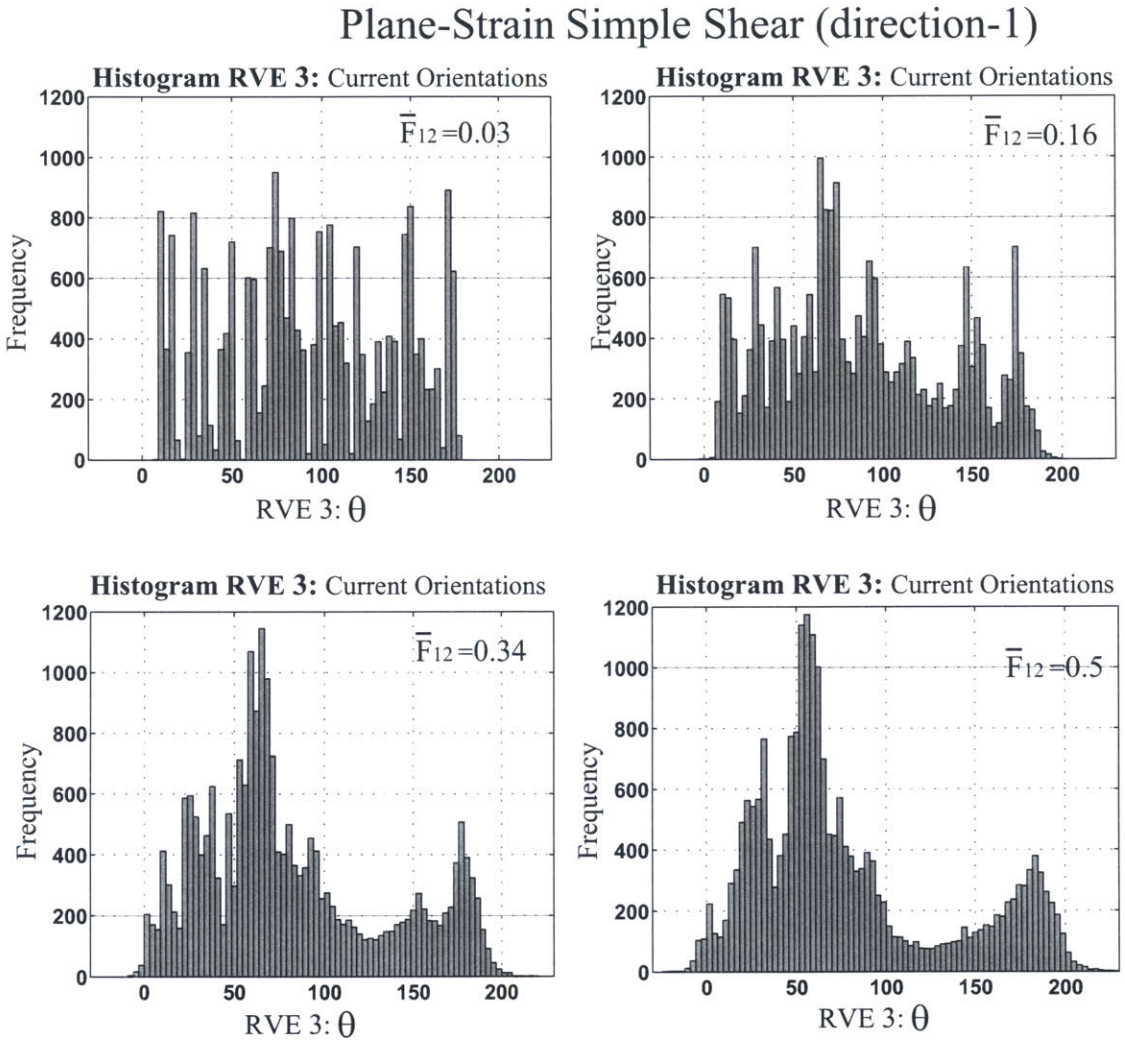

Figure 4-33: *Plane-strain Extension* - RVE-3*:* Histogram of current grain orientations, θ, for RVE-3 at different levels of macroscopic shear deformation $\overline{F}_{12}$.

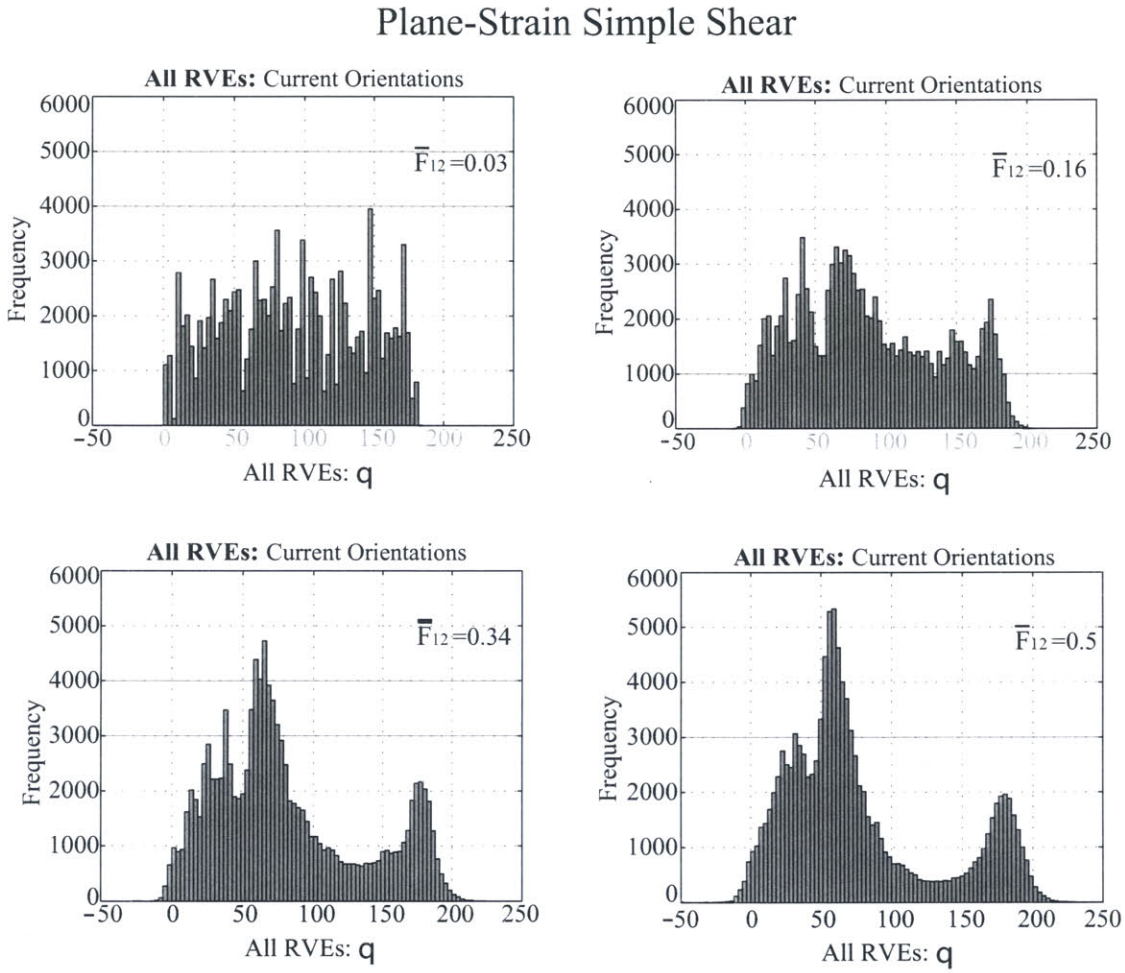

Figure 4-34: *Plane-strain Extension* - All RVEs: Histogram of current grain orientations, θ, for all RVEs at different levels of macroscopic shear deformation $\overline{F}_{12}$.

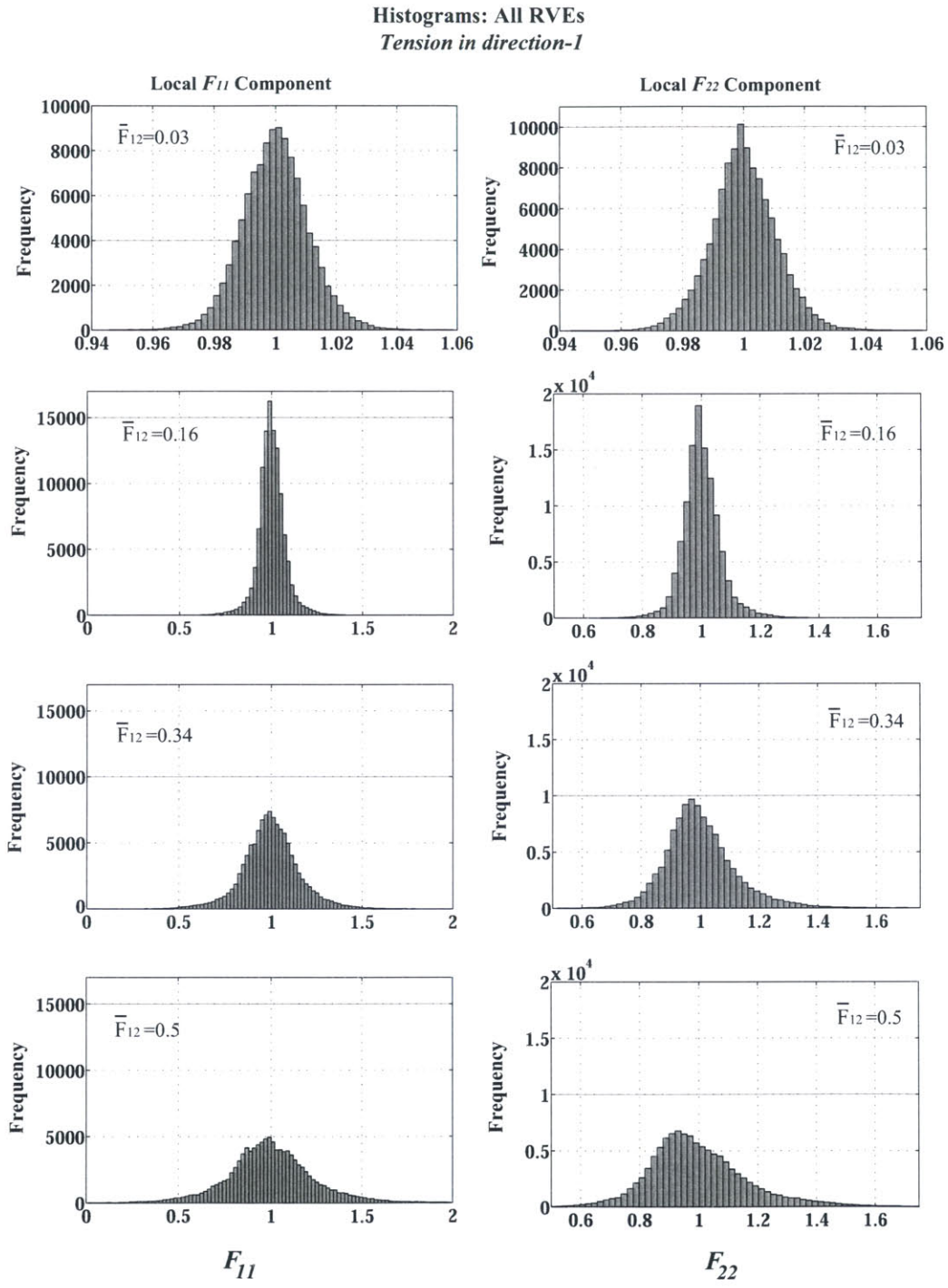

Figure 4-35: *Plane-strain Simple Shear (Direction-1)* - All RVEs: Histograms of deformation gradient components F_{11} and F_{22}.

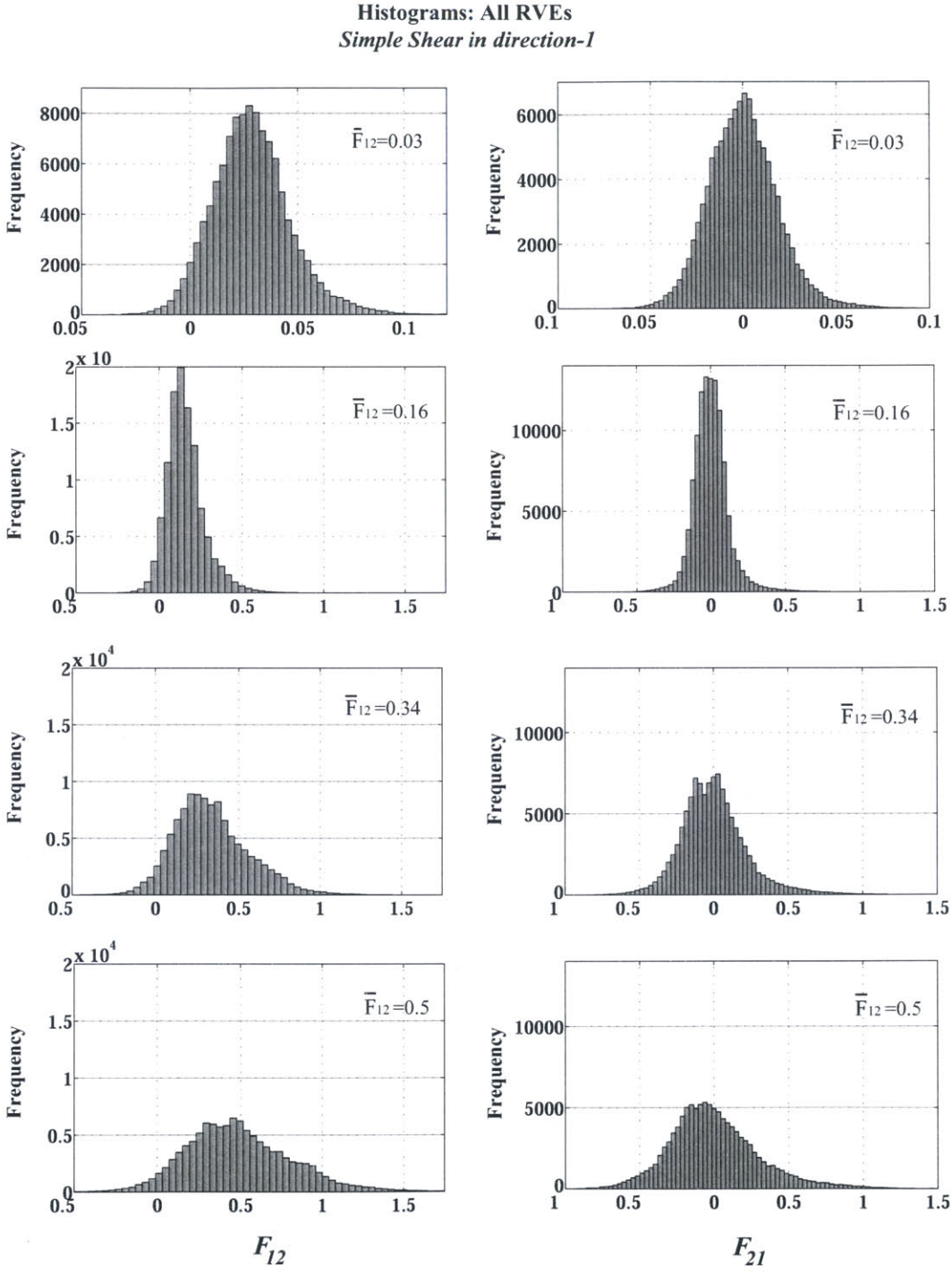

Figure 4-36: *Plane-strain Simple Shear (Direction-1)* - All RVEs*:* Histograms of deformation gradient components F_{12} and F_{21}.

constitutive model was used to describe the behavior of the individual grains according to their specific microstructural orientation. Five different assignments were randomly chosen for the inital grain orientations within RVEs, and two different types of macroscopic deformation were applied: plane-strain uniaxial extension, and plane-strain simple-shear.

The constitutive model is micromechanically/physically based, and thus it provides information both about the effective (homogenized) response at every material point, and about microstructural kinematic/stress quantities within each of the BCP's constituent phases, rubber (PB) and glass (PS). Therefore, a thorough investigation of both the macro- and microscopic stress and deformation field within a polycrystal RVE was possible, which motivates the development of a physically-based continuum constitutive description for the polycrystalline BCP material, and indicates the level of micromechanical detail needed for polycrystalline continuum modeling (whether, for example, kinking and grain size are necessary modeling quantities). The micromechanical deformation evolution in each grain was continuously monitored during the polycrytalline FE calculations. Deformation events occurring at the grain level, such as layer dilatation, shear, buckling, and rotation, were related to numerical and experimental macroscopic stress-strain characteristics such as the "yield" point and the gradual reduction in tangent stiffness, and compared to experimental SAXS data for the internal evolution of grain orientations. The physical validity of numerical predictions was verified by counter-examining contour plots of microdeformation and microstress fields at the length scale of individual grains. The contour snapshots show that the constitutive model is inherently able to capture complex intergranular interactions and characteristic local modes of micromechanical deformation -such as the synergy between lamellar buckling and interlayer shear within a grain- in a physicaly consistent manner, even though the analytical constitutive model is not informed about critical microstructural instabilities that drive such phenomena. Contour plots and histograms of the evolving grain orientations agree both qualitatively and quantitatively with the corresponding trend of gradual grain tilting towards the loading axis up to a "'locking" tilt angle that has been observed in past x-ray studies. In addition, histograms of deformation gradient components, as these are calculated within the inividual grains, depict distributions which were both micromechanically realistic and in accord with the imposed macroscopic deformation

gradient. The large, and increasing with deformation, variances observed for these distributions show that the simple Taylor/Sachs models, even though successful when describing polycrystal aggregates of metals, are innaccurate for materials with highly anisotropic single-crystal behavior.

The performance of the developed constitutive model in the presented analysis proves its utility as a powerful and very promising tool for finite element calculations on generic boundary value problems. However, the current model is developed for 2D plane-strain applications and should be extended to describe the mechanical behavior of a full 3D lamellar single-crystal and polycrystal morphology. The constitutive model can be used to predict the material behavior under different deformation histories, with RVEs containing larger grain populations, and also up to macroscopic strains higher than in the present analysis with the help of remeshing techniques. Additional experimentation on polycrystalline BCP samples up to moderate strains is still needed to complete the study of lamellar BCP polycrystals, as the existing literature concentrates on the large strain behavior, when the microstructural order is completely destroyed due to layer fragmentation. In addition, and as described in Chapter 5, length-scale issues such as the effect of layer thickness (relative to the grain size) can now be revisited with multigranular RVEs containing both "homogenized" grains (grains described by the constitutive model), and grains with a discretely modeled lamellar microstructure. Finally, apart from being used to analyze existing microstructural configurations, the constitutive model can aid in designing/suggesting materials with application-specific optimal microstructures.

Chapter 5

Research Contributions and Future Directions

5.1 Research Contributions

5.1.1 Constitutive Model for Single-Crystal Lamellar Structures

This thesis presents a micromechanical framework for the derivation of large-strain continuum constitutive models for hyperelastic materials with layered microstructures. The lamellar morphology is represented by a planar bi-layer RVE, which is used to derive the appropriate continuity and equilibrium arguments that must be satisfied at every material point. A generic description for the strain energy function of the composite and the resulting system of equilibrium and continuity equations, complete the micromechanical framework.

The strain energy function was presented here as an (initial-)volume weighted average of the constituents' strain energies. The framework of micromechanical constraints was applied for the case of contituents with hyperelastic Neo-Hookean behavior. A analytical closed-form solution was elaborated for the distribution of macroscopic deformation within the individual layers. The solution for each phase's microdeformation gradient was a function of the applied macroscopic deformation gradient. The composite strain energy density can then be fully described in terms of the macroscopic deformation gradient, and the ma-

terial stress-strain response is simply obtained by deriving the strain energy function with respect to the macroscopic deformation gradient. The effective composite stress response follows as a (current-)volume weighted average of each constituent's stress contribution.

The model was implemented as a subroutine (vumat) for use within the commercial FE-code ABAQUS Explicit. Stress and microdeformation numerical predictions from single element calculations using the constitutive model were in excellent agreement with micromechanical finite element calculations on a discrete 2D bilayer model of the layered microsctructure. The constitutive model describes the stress and deformation response of the oriented microsctructure accurately, and can also be used in multigrain calculations to study the mechanical behavior of polycrystalline lamellar aggregates. The model predicts the rotation and large deformations of the underlying lamellae, however, it does not account for critical microstructural instabilitites such as lamellar microbuckling and micronecking. To describe such microstructural transformations the constitutive model needs to be augmented with appropriate criteria for the initiation of instabilities, and should account for plasticity-related localization phenomena. Even though these are decisive mechanisms for the large strain response of an oriented structure (single-crystal), we expect the model to be accurate enough for numerical studies on polycrystals.

The presented framework is general and the solution precedure can be followed for any choice of hyperelastic phase behavior. It is very possible that a numerical scheme will be needed to reach a solution for other material descriptions. Nevertheless, the neo-hookean behavior is an excellent approximation, pending on a judicious choise of material properties for the constituents.

5.1.2 Simulation of Plane-Strain Extension of Single-Crystals and Bicrystals

The effect of isolated deformation constraints on the deformation behavior of lamellar block copolymers was examined with plane-strain numerical calculations of the tensile behavior of oriented and bicrystal strip specimens, when grip constraints are imposed at the specimen ends.

The simulations have shown that the imposed extension on oriented material strips is accommodated by both shear and axial stretching, with relative contributions of shear and extension depending on the initial orientation as well as the imposed strain level. The grip boundary constraint and the specimen length have a very strong influence on the homogeneity of the deformation field. The spatial extent of the boundary influence depends strongly on the initial lamellae orientation and the specimen length.

For the case of bicrystal specimens, three bicrystal grain arrangements were examined. The resulting deformation patterns across the boundary and throughout the entire specimen are in excellent agreement with the experimental findings by Wanakamol and Thomas [51]. The nature and spatial extent of the grain boundary influence on the deformations of such bicrystal configurations strongly depends on the relative orientations of the neighboring grains and on the nature of the imposed loading. Micromechanical observations from the plane-strain extension tests on tensile strip specimens closely correlate to micro- and macrodeformation modes present during the extension of bicrystal strip speciens. The constitutive model was able to capture buckling instabilities which occur due to deformation incompatibilities at the grain boundary. A buckling criterion has not been rigorously implemented in the model, and due to the models inherent tendency to capture lower energy deformation modes, the finite element models used to calculate the deformation field within the asymmetric bicrystals exhibited hourglassing instabilities during the analysis.

5.1.3 Simulation of Plane-Strain Extension and Simple-Shear of Lamellar Polycrystal Aggregates

The analytical continuum constitutive model was utilized in 2D finite element based calculations to study the mechanical behavior of polycrystalline lamellar BCP microstructures under conditions of plane-strain deformation. 2D multigranular RVEs were developed, each containing 56 identically shaped hexagonal grains -an aggregate size sufficiently large to represent the material microstructure without being computationally expensive-, and the constitutive model was used to describe the behavior of the individual grains according to their specific microstructural orientation. Five different assignments were randomly cho-

sen for the inital grain orientations within RVEs, and two different types of macroscopic deformation were applied: plane-strain uniaxial extension, and plane-strain simple-shear.

The constitutive model is micromechanically/physically based, and thus it provides information both about the effective (homogenized) response at every material point, and about microstructural kinematic/stress quantities within each of the BCP's constituent phases, rubber (PB) and glass (PS). Therefore, a thorough investigation of both the macro- and microscopic stress and deformation field within a polycrystal RVE was possible, which motivates the development of a physically-based continuum constitutive description for the polycrystalline BCP material, and indicates the level of micromechanical detail needed for polycrystalline continuum modeling (whether, for example, kinking and grain size are necessary modeling quantities). The micromechanical deformation evolution in each grain was continuously monitored during the polycrytalline FE calculations. Deformation events occurring at the grain level, such as layer dilatation, shear, buckling, and rotation, were related to numerical and experimental macroscopic stress-strain characteristics such as the "yield" point and the gradual reduction in tangent stiffness, and compared to experimental SAXS data for the internal evolution of grain orientations. The physical validity of numerical predictions was verified by counter-examining contour plots of microdeformation and microstress fields at the length scale of individual grains. The contour snapshots show that the constitutive model is inherently able to capture complex intergranular interactions and characteristic local modes of micromechanical deformation -such as the synergy between lamellar buckling and interlayer shear within a grain- in a physicaly consistent manner, even though the analytical constitutive model is not informed about critical microstructural instabilities that drive such phaenomena. Contour plots and histograms of the evolving grain orientations agree both qualitatively and quantitatively with the corresponding trend of gradual grain tilting towards the loading axis up to a "'locking" tilt angle that has been observed in past x-ray studies. In adition, histograms of deformation gradient components, as these are calculated within the inividual grains, depict distributions which were both micromechanically realistic and in accord with the imposed macroscopic deformation gradient. The large, and increasing with deformation, variances observed for these distributions show that the simple Taylor/Sachs models, even though successful when describ-

ing polycrystal aggregates of metals, are innaccurate for materials with highly anisotropic single-crystal behavior.

The performance of the developed constitutive model in the presented analysis proves its utility as a powerful and very promising tool for finite element calculations on generic boundary value problems. However, the current model is developed for 2D plane-strain applications and should be extended to describe the mechanical behavior of a full 3D lamellar single-crystal and polycrystal morphology. The constitutive model can be used to predict the material behavior under different deformation histories, with RVEs containing larger grain polulations, and also up to macroscopic strains higher than in the present analysis with the help of remeshing techniques. Additional experimentation on polycrystalline BCP samples up to moderate strains is still needed to complete the study of lamellar BCP polycrystals, as the existing literature concentrates on the large strain behavior, when the microstructural order is completely destroyed due to layer fragmentation. In addition, and as described later, length-scale issues such as the effect of layer thickness (relative to the grain size) can now be revisited with multigranular RVEs containing both "homogenized" grains (grains described by the constitutive model), and grains with a discretely modeled lamellar microstructure. Finally, apart from being used to analyze existing microstructural configurations, the constitutive model can aid in designing/suggesting materials with application-specific optimal microstructures.

5.2 Future Directions

5.2.1 Constitutive Model for Single-Crystal Lamellar Structures

Extension to 3D lamellar structures The analytical model was developed for 2D plane-strain conditions and should be extended for 3D lamellar structures to study both oriented and polycrystalline 3D configurations. Also, plasticity-related aspects of the glassy layer deformation which lead to yielding, micronecking and eventual fragmentation of glassy layers for large extensions were not accounted for. A material model other than the hyperelastic Neo-Hookean, such as the Arruda-Boyce constitutive model for glassy polymers,

should be used to describe the elastic-plastic behavior of the glassy phase and the numerical RVEs should be augmentated with fracture criteria (namely with the element deletion capability) in order to capture plasticity related effects in the large-strain behavior of the BCP.

Microstructural Instabilities Plasticity related instabilities become important when loading is directed parallel to the BCP microstructure and the resulting deformation of glassy layers is maximized. In most cases however, the macroscopically observed nonlinearities are due to layer buckling. The current model does not account for this critical instability and should be improved with a layer buckling criterion. This can be accomplished either: *(i)* by comparing the calculated axial stress within the glassy layer, ${}^{g}\sigma_{ss}$, to a wave-length-dependent, critical axial stress value to trigger a buckling microstructural transition, or *(ii)* by assuming an initally buckled microstructure. The latter approach is described schematically in Fig. 5-1. The notional RVE is an assembly of two unequal limbs, each one being a fraction of the total bilayer RVE's length, L_o. The buckling wavelength is determined by the ratio of the chosen RVE length L_o versus the RVE thickness t_o. Each limb's initial orientation differs from that of the microstucture by a few degrees. With the approximation that the total RVE length L_o remains constant during deformation and the additional constraint for compatible layer deformation across the hinge section, the RVE geometry is fully defined. The analytical expression for the strain energy of the bilayer RVE as a function of the macroscopic deformation gradient and the initial RVE orientation has already been derived in this thesis. Then, the total strain energy of the buckled RVE is the sum of the strain energies stored in each limb, weighed by the relative limb ratios. The only unspecified quantity is the relative limb ratio of the buckled configuration, which also depends on the initial orientation of loading with respect to the microstructure. The optimal limb ratio minimizes the strain energy of the RVE. This last condition completes the set of equations that remain to be solved for a fully analytical description of the proposed configuration.

Parametric studies The continuum model can be used in parametric studies to investigate the influence the properties and the volume fraction of constituents have on the effective mechanical response and the deformation micromechanics of layered materials, both

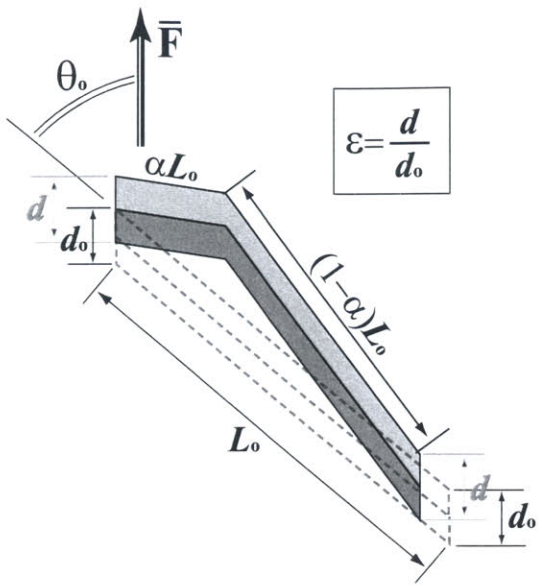

Figure 5-1: Bilayer RVE for the analytical derivation of a constituve model with a layer buckling capability.

for oriented and polycrystalline configurations. The continuum model treats the composite material as a homogeneous medium. Therefore, parametric studies can be performed with computationally simple, time efficient, single element calculations, and do not require discrete modeling and subsequent variations in the considered layered morphology. This is particularly convenient for materials where deformation-related nonlinearities such the glassy layer's micronecking and buckling instabilities are either physically absent or ignored in the analysis. Even though the analytical constitutive model does not account for such microstructural transformations its modeling capabilities are not limited to rigid microstructures. As observed in polycrystalline and bilayer calculations (as well as in oriented material calculations not reported here), the model was inherently capable to capture lower energy deformation modes. Thus, parametric studies for morphologies which experience the aforementioned microstructural transitions can still be carried out using the analytical constitutive model to charectirize the material's response, in a time- and computationally efficient manner without sacrificing any stuctural information, simply by introducing appropriate mesh imperfections in the corresponding micromechanical RVE. Such parametric studies can be used to identify, both qualitatitevely and quantitatively, how the interlayer property-contrast and the relative layer thickness (namely the volume fraction)

influence the deformation micromechanics or eliminate critical deformation instabilities at the microstructural level. Parametric studies are also cardinal for the design of novel materials and microstructures. Several nano-scale motion amplifies or auxetic materials are man-made structural arrangements that operate by exploiting certain deformation patterns. Parametric studies using the analytical model can be used to analyze and optimize the these mechanisms at the conseptual level before prototyping is finalized.

Structural Design Several new nano-devices, storage media, and coating layers are essentially oriented and polygranular BCP thin films, or structures that originate from BCP morphologies and still behave in a hyperelastic manner. The derived constitutive model can be used in numerical simulations to predict their structural behavior under the anticipated loading or deformation conditions during operation. Prior structural analysis using accurate an material description in FE modeling can lead to structural improvements and reduced production costs.

Cylindrical BCP morphologies The same framework can be applied to derive micromechanically based continuum constitutive models for hyperelastic materials with cylindrical morphologies. The set of equibirium and compatibility constraints imposed on the cylindrical interfaces between domains should in this case be expressed in cylindrical coordinates. The resulting system of equations can yield an analytical, closed-form solution for the non-affine mapping of the macroscopically applied deformations to the local deformations within the different constituent domains. Such physically-based continuum constitutive descriptions for materials with cylindrical microstructures, despite being derived for hyperelastic behaviors, can also model the mechanical response of fiber composites by approximating the rigidity of the reinforcemnt with an appropriately chosen stiffness contrast between the fibers and the matrix.

5.2.2 Simulation of Multigrain Configurations

Multigranular RVE Size Polygranular RVEs consisting of 56 hexagonal grains were developed to study the response of polycrystalline lamellar BCP configurations. The results were physically consistent, however, a slight anisotropy was induced by the chosen

honeycomb-topology of grain boundaries. RVEs consisting of a random grain tesselatations and perhaps of lager grain populations are expected to yield improved results for the anticipated isotropic response of the polycrystalline material. Furthermore, the polygranular RVE was developed for 2D plane-strain calculations. A full 3D analysis of polycrystalline lamellar BCP materials should be performed next, using 3D RVEs with grains randomly oriented and tesselated in space.

Continuum Constitutive Modelling of the Lamellar Polyrystal Response The polygranular RVE simulations have shown a large variation in the deformation and stress fields of individual grains throughout the RVE during the deformation. Therefore, the macroscopic deformation and stress fields cannot be mapped affinely to the corresponding fields in each individual grain. Conventional schemes such as the Taylor and Sachs models that average individual grain behavior exactly in this manner are physically incorrect and therefore very inaccurate in their predictions for the mechanical response of the polycrystalline aggregate. Polygranular RVE calculations describe in detail the preferred deformation mechanisms of individual grains and how these relate to grain orientation, anisotropy and neighboring grains, and provide insight on how these relate to grain orientation, anisotropy and continuum neighborhood, which can be used to develop physically-correct averaging models to map an external, macroscopically applied loading or deformation to the corresponding internal field of individual grains. Hybrid Taylor-Sachs models which affinely map macro- stress and deformation components to micro- stress and deformation fields can be a development in this direction, or averaging schemes that predict the effective tangent modulus at different levels of deformation based on the knowledge for the dominant micro-deformation mechanicsms by which grains respond at the given strains.

Grain Size Efects The effect of the grain size relative to the layer-thickness can be investigated with selective discrete modeling of layers within specific grains. The concept is illustrated in the polygranular RVE of Fig. 5-2. The oriented lamellar morphology of isolated grains within the RVEs is modelled discretely, while the remaining grains are assigned the mechanical behavior of lamellar BCP single-crystals, as this is described by the developed length-scale-independent analytical model. The aspect ratio of the lamellae within discretized grains can be varied in a consistent manner, for instance by reducing

layer thickness by half. The polygranular calculations will be repeated with identical traction or displacement boundary conditions imposed on the RVE in order to examine how the grain size influences the deformation mechanisms by which the selected grains and their neighbors will accommodate the imposed deformation/loading. In addition, by gradually increasing the number of discretely modeled grains we can investigate whether the grain size influences the effective mechanical response of polycrystalline lamellar BCPs by comparing results with polygranular RVE calculations where the grain behavior is fully assigned through the presented length-scale-independent constitutive model. It should be noted that the discretely modeled grains of Fig. 5-2 had initial orientations normal to the loading direction and responded by layer buckling and subsequent interlamellar rubber shear, similar to their homegenized grain counterparts, whose behavior was described by the derived analytical model. In the case however of discretely modeled grains, the buckling wavelength is determined by the layer thickness, while for the homogenized grains, the element size determines the size of opposite shearing domains within the particular grain. Finally, augmentation with variables that describe PS-layer fracture or element deletion are necessary to predict the onset of the "plastic-to-rubber" transition observed at the large strain behavior of polycrystals.

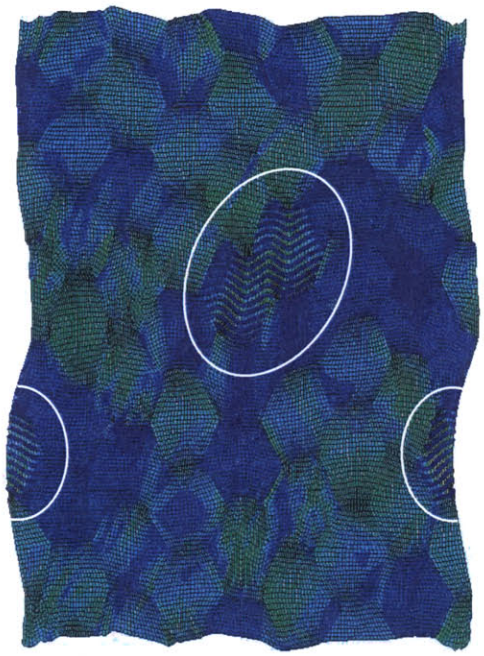

Figure 5-2: Logarithmic strain E_{22} contour from a multigranular RVE containing grains with discretely modeled lamellar microstructures (circled in the Figure). The RVE is deformed under plane-strain uniaxial extension along direction-2.

Bibliography

[1] G Holden. *Understanding Thermoplastic Elastomers*. Hanser, 2000.

[2] EL Thomas and RL Lescanec. Phase morphology in block copolymer systems. *Phyl. Trans. R. Soc. Lond. A*, 348:149–166, 1994.

[3] P Allan, RGC Arridge, F Ehtaiatkar, and MJ Folkes. The mechanical properties of an oriented lamella stock formed from an S-B-S block copolymer. *Journal of Physics D: Appl. Phys.*, 24(8):1381–1390, 1991.

[4] I Yamaoka and M Kimura. Effects of morphology on mechanical properties of a SBS triblock copolymer. *Polymer*, 34(3):4399–4409, 1993.

[5] Y Cohen, RJ Albalak, BJ Dair, MC Capel, and EL Thomas. Deformation of oriented lamellar block copolymer films. *Macromolecules*, 33(17):6502–6516, 2000.

[6] Y Cohen, M Brinkmann, and EL Thomas. Undulation, dilation, and folding of a layered block copolymer. *Journal of Chemical Physics*, 114(2):984–992, 2001.

[7] X Chen and JW Hutchinson. Thin film herringbone buckling patterns. *Mat. Res. Soc. Symp. Proc.*, 795, 2004.

[8] X Chen and JW Hutchinson. A family of herringbone patterns in thin films. *Scripta Materialia*, 50:797–801, 2004.

[9] SJ Singer. Buckling induced by dilative strain in two- and three-dimensional layered materials. *Physical Review E*, 62(3):3736–3746, 2000.

[10] L Qiao and KI Winey. Evolution of kink bands and tilt boundaries in block copolymers at large shear strains. *Macromolecules*, 33(3):851–856, 2000.

[11] DL Polis and KI Winey. Controlling kink band morphology in block copolymers: Threshold criteria and stability. *Macromolecules*, 31(11):3617–3625, 1998.

[12] C Daniel, IW Hamley, and K Mortensen. Effect of planar extension on the structure and mechanical properties of polystyrene-poly(ethylene-co-butylene)-polysryrene triblock copolymers. *Polymer*, 41:9239–9247, 2000.

[13] Y Cohen and EL Thomas. The effect of defects on the response of a layered block copolymer to perpendicular deformation: One-dimensional necking. *Macromolecules*, 36(14):5265–5270, 2003.

[14] DJ Read, RA Ducket, J Sweeney, and TCB McLeish. The chevron folding instability in thermoplastic elastomers and other layered materials. *Journal of Physics D: Appl. Phys.*, 32:2087–2099, 1999.

[15] TJ Hermel, SF Hahn, KA Chaffin, WW Gerberich, and SF Bates. Role of molecular architecture in mechanical failure of glassy/semicrystalline block copolymers: CEC vs CECEC lamellae. *Macromolecules*, 36(7):2190–2193, 2003.

[16] T Tzianetopoulou and MC Boyce. Micromechanics of PS/PB/PS triblock-copolymer films with lamellar morphology. In *Mat. Res. Soc. Symp. Proc.*, volume 788, Boston, December 2003. MRS.

[17] M Fujimura, T Hashimoto, and H Kawai. Structural-change accompanied by plastic-to-rubber transition of SBS block copolymers. *Rubber Chem. Techn.*, 51(2):215–224, 1978.

[18] T Hashimoto, M Fujimura, K Saijo, H Kawai, J Diamant, and M Shen. Strain-induced plastic-to-rubber transition of a SBS block copolymers and its blend with PS. *Amer. Chem. Soc. Adv. Chem. Ser.*, 176(2):257–275, 1979.

[19] R Seguela and J Prud'homme. Deformation mechanism of thermoplastic two-phase elastomers of lamellar morphology having a high volume fraction of rubbery microphase. *Macromolecules*, 14:197–202, 1981.

[20] RT Mayers. *Grains and Grain Boundaries in Lamellar Styrene–Butadiene Block Copolymers*. PhD dissertation, Massachusetts Institute of Technology, Department of Chemical Engineering, 1999.

[21] BL Cravalho, RL Lescanec, and EL Thomas. Grain boundary defects in block copolymer systems: Bulk and thin film results. *Macromolecular Symposia*, 98:1131–1146, 1995.

[22] MT Payne and CP Rader. Thermoplastic elastomers: A rising star. *In: Cheremisinoff,NP (Ed.) Elastomer Technology Handbook, CRC Press*, pages 557–595, 1993.

[23] RJ School. Markets for thermoplastic elastomers. *In: Cheremisinoff,NP (Ed.) Elastomer Technology Handbook, CRC Press*, pages 597–615, 1993.

[24] MJ Fasolka and AM Mayes. BLOCK COPOLYMER THIN FILMS: Physics and applications. *Annual Review of Materials Research*, 31:323–355, 2001.

[25] C Park, J Yoon, and EL Thomas. Enabling nanotechnology with self assembled block copolymer patterns. *Polymer*, 44:6725–6760, 2003.

[26] IW Hamley. Nanostructure fabrication using block copolymers. *Nanotechnology*, 14:R39–R54, 2003.

[27] SO Kim, HH Solak, MP Stoykovich, NJ Ferrier, JJ de Pablo, and PF Nealy. Epitaxial self-assembly on lithographically defined nanopatterned substrates. *Nature*, 424:411–414, 2003.

[28] K Amundson, E Helfand, DD Davis, X Quan, SS Patel, and SD Smith. Effect of an electric field on block copolymer microstructure. *Macromolecules*, 24:6546–6548, 1991.

[29] J DeRouchey, T Thurn-Albrecht, and TP Russell. Block copolymer domain reorientation in an electric field: An in-situ small-angle x-ray scattering study. *Macromolecules*, 37:2538–2543, 2004.

[30] GH Kim and YM Shkel. Polymeric composites tailored by electric field. *J. Mater. Res.*, 19(4):1164–1174, 2004.

[31] DY Godovsky. Device applications of polymer-nanocomposites. *Advances in Polymer Science*, 153:163–205, 2000.

[32] MJ Folkes and A Keller. The birefringence and mechanical properties of a 'single crystal' from a three-block copolymer. *Polymer*, 12(4):222–236, 1971.

[33] RGC Arridge and MJ Folkes. The mechanical properties of a single crystal of SBS copolymer-a novel composite material. *J. Phys. D: Appl. Phys.*, 5:344–358, 1972.

[34] RJ Albalak and EL Thomas. Microphase separation of block copolymer solutions in a flow field. *Journal of Polymer Science B: Polymer Physics*, 31(1):37–46, 1993.

[35] A Peterlin and FJ Balta-Calleja. Plastic deformation of polypropylene. III. Small-angle X-ray scattering in the neck region. *Journal of Applied Physics*, 40(11):4238–4242, 1969.

[36] HH Song, AS Argon, and RE Cohen. Morphology of highly textured high-density polyethylene. *Macromolecules*, 23:870–876, 1990.

[37] MB Bayly. Energy calculation concerning the roundness of folds. *Tectonophysics*, 24(4):291–316, 1974.

[38] AM Johnson. *Styles of Folding: mechanics and mechanisms of folding of natural elastic materials*. Elsevier North-Holland, 1977.

[39] K Kaiser and W Petch. Amplitude equations for the electrodynamic instability in nematic liquid crystals. *Phys. Rev. E*, 48(6):4510–4528, 1993.

[40] S Conti, A DeSimone, and G Dolzmann. Semisoft elasticity and director reorientation in stretched sheets of nematic elastomers. *Physical Review E*, 66(6):Art. No. 061710, 2002.

[41] L Qiao and KI Winey. Dynamics of kink bands in layered liquids: Theory and in situ saxs experiments on a block copolymer melt. *Macromolecules*, 34(22):7858–7867, 2001.

[42] CC Honeker, EL Thomas, RJ Albalak, DA Hajduk, SM Gruner, and MC Capel. Perpendicular deformation of a near-single-crystal triblock copolymer with a cylindrical morphology. 1. Synchrotron SAXS. *Macromolecules*, 33(25):9395–9406, 2000.

[43] CC Honeker and EL Thomas. Perpendicular deformation of a near-single-crystal triblock copolymer with a cylindrical morphology. 2. TEM. *Macromolecules*, 33(25):9307–9417, 2000.

[44] MD Nestorovic and N Triantafyllidis. Onset of failure in finitely strained layered composites subjected to combined normal and shear loading. *J. Mech. Phys. Solids*, 52(4):941–974, 2004.

[45] J Groenewold. Wrinkling of plates coupled with soft elastic media. *Physica A*, 298:32–45, 2001.

[46] ZY Huang, W Hong, and Z Suo. Nonlinear analyses of wrinkles in films on soft elastic substrates. *unpublished research*, 2004.

[47] CC Honeker and EL Thomas. Impact of morphological orientation in determining mechanical properties in triblock copolymer systems. *Chem. Mater.*, 8:1702–1714, 1996.

[48] M Ma, K Vijayan, A Hiltner, E Baer, and J Im. Thickness effects in microlayer composites of polycarbonate and poly(styrene-acrylonitrile). *Journal of Materials Science*, 25(4):2039–2055, 1990.

[49] JAW van Dommelen, DM Parks, MC Boyce, WAM Brekelmans, and FPT Baaijens. Micromechanical modeling of the elasto-viscoplastic behavior of semi-crystalline polymers. *Journal of the Mechanics and Physics of Solids*, 51(3):519–541, 2003.

[50] M Danielsson. *Micromechanics, macromechanics and constitutive modeling of the elasto-viscoplastic deformation of rubber-toughened glassy polymers*. PhD dissertation, Massachusetts Institute of Technology, Department of Mechanical Engineering, 2005.

[51] P Wanakamol. *Deformation Behavior of Cylindrical Block Copolymer Bicrystals: Pathway to Understanding Block Copolymer Grain Boundaries*. PhD dissertation, Massachusetts Institute of Technology, Department of Materials Science and Mechanical Engineering, 2005.

[52] SP Gido and EL Thomas. Lamellar diblock copolymer grain boundary morphology. 1. Twist boundary characterization. *Macromolecules*, 26:4506–4520, 1993.

[53] SP Gido and EL Thomas. Lamellar diblock copolymer grain boundary morphology. 2. Sherk twist boundary energy calculations. *Macromolecules*, 27:849–861, 1994.

[54] SP Gido and EL Thomas. Lamellar diblock copolymer grain boundary morphology. 4. Tilt boundaries. *Macromolecules*, 27:6137–6144, 1994.

[55] SP Gido and EL Thomas. Lamellar diblock copolymer grain boundary morphology. 3. Helicoid section twist boundarie energy. *Macromolecules*, 30:3739–3746, 1997.

[56] M.C.Boyce W.A.M. Brekelmans J.A.W. van Dommelen, D.M. Parks and F.P.T. Baaijens. Micromechanical modeling of the elasto-viscoplastic behavior of semi-crystalline polymers. *Journal of the Mechanics and Physics of Solids*, 51(3):519–541, 2003.